UNIVERSIDAD DE SEVILLA

DEPARTAMENTO DE FÍSICA APLICADA 1

CIRCUIT MODELING OF PERIODIC STRUCTURES

A dissertation submitted by
Carlos Molero Jiménez

Seville, October 2016

CIRCUIT MODELING OF PERIODIC STRUCTURES

Dissertation submitted by
Carlos Molero Jiménez

Supervisors:

_____	_____
Raúl Rodríguez Berral	**Francisco Luis Mesa Ledesma**

Candidate:

_____

Carlos Molero Jiménez

During the course of this work, the Ph.D student has receives financial support from the Spanish Ministry of Science and Innovation through a Research Scolarship (FPI grant) associated with the project TEC2010-16948:

- **Title**: Sistemas electromagnéticos avanzados para comunicaciones y aplicaciones médicas (advanced electromagnetic systems for communications and medical applications). **Financed by**: Spanish Ministry of Science and Technology and Feder funds. **Dates**: 01/01/2011 - 31/12/2013. **Head researcher**: Francisco Luis Mesa Ledesma

and through a research contract funded with project TEC2013-41913-P:

- **Title**: Modelado y aplicaciones de estructuras electromagnéticas periódicas para tecnologías emergentes (modelling and applications of periodic structures for emerging technologies). **Financed by**: Spanish Ministry of Science and Technology. **Dates**: 01/01/2014 - 31/12/2016. **Head researchers**: Francisco Luis Mesa Ledesma and Francisco Medina Mena

Durante la realización de este documento, que no es más que el resultado del trabajo de los últimos 5 años, me gustaría hacer especial mención a mis seres más cercanos:

Agradecer a mi padre su incesante lucha, a lo largo de su vida, por hacer que me interese por estudiar y aprender, no solo por la simple razón de encontrar un buen trabajo en un hipotético futuro, sino como medio fundamental para alcanzar la dignidad humana.

Agradecer a mi madre esa gran fortaleza que le caracteriza, inspiración necesaria para levantarme en mis peores momentos. Es, probablemente, la persona más fuerte que conozco.

Agradecer a mi hermano su espíritu crítico, que es bastante más refinado que el mío, y que me ha servido para pensar más allá cuando parecía que no era necesario.

Y agradecer, como no, a Clara el haberme escuchado y aguantado con paciencia durante estos últimos 3 años de grandes éxitos y fracasos. Agradecer su ejemplo como persona constante y trabajadora, ejemplo que he intentado seguir en este tiempo.

Copyright Credit

In the course of his Ph.D. program, the candidate has co-authored several publications in scientific journals. Therefore, a significant part of the original ideas and technical material presented in this thesis can be found in the following publications:

- R. Rodríguez-Berral, C. Molero, F. Medina and F. Mesa, *Analytical wideband model for strip/slit gratings with dielectrics slabs*, IEEE Trans. Microw. Theory Techn., vol. 60, pp. 3908-3918, Dec. 2012. ©2012 IEEE. (Chapters 1 and 2)

- C. Molero, R. Rodríguez-Berral, F. Mesa and F. Medina, *Analytical circuit model for 1-D periodic T-shaped corrugated surfaces*, IEEE Trans. Antennas Propag., vol. 62, pp. 794-803, Feb. 2014. ©2014 IEEE. (Chapters 1 and 3)

- C. Molero, R. Rodríguez-Berral, F. Mesa and F. Medina, *Dynamical equivalent circuit for 1-D periodic compound gratings*, IEEE Trans. Microw. Theory Techn., vol. 64, pp. 1195-1208, Apr. 2016. ©2016 IEEE. (Chapters 1 and 4)

- C. Molero, R. Rodríguez-Berral, F. Mesa, F. Medina, A. B. Yakovlev, *Wideband analytical equivalent circuit for 1-D periodic stacked arrays*, Phys. Rev. E, vol. 1, pp. 013306, Jan. 2016. ©2016 APS. (Chapter 5)

Acknowledgments, agradecimientos

Quisiera expresar mi gratitud a aquellas personas que me han acompañado, de una forma u otra, durante la realización de mi tesis doctoral.

En primer lugar, agradecer a *Raúl Rodríguez Berral* su labor como tutor de tesis durante estos 5 años. No solo me ha aportado ideas nuevas, explicaciones brillantes y discusiones interesantes, sino que ha cambiado por completo mi manera de pensar y de afrontar problemas.

Agradecer a *Francisco Mesa Ledesma* el haberme aceptado como su estudiante de doctorado, y su labor de supervisor. Destacar sus aportaciones científicas a esta tesis y su insistencia en el rigor a la hora de escribir textos científicos, exigencia que me ha hecho mejorar notablemente.

Agradecer a *Francisco Medina Mena* su dedicación, intensa, en mi formación como futuro investigador y sus brillantes contribuciones, muchas de ellas presentes en este documento. Agradecer enormemente su papel decisivo y fundamental en determinados momentos.

Agradecimientos a toda la familia de microonderos que han confluído junto a mí en el laboratorio de Microondas: *Armando, José Miguel, Rafael Florencio, Vicente Delgado, Alejandro*, y a todos aquellos que pasaron por laboratorio en cortos periodos de tiempo. Por supuesto, acordarme de *Juan* y *Paco*, de hidrodinámica, con quienes también he pasado buenos momentos.

Agradecer a todos los restantes miembros del grupo de Microndas que, de una forma u otra, me han ayudado y aceptado en el grupo: *Rafael R. Boix* (sin el cuál nunca hubiese sabido de la existencia de esta beca), *Vicente Losada*, *Manuel Freire* y *Ricardo Marqués*.

Acknowledgments to *Andrea Neto* and *Nuria Llombart* for accepting me as a visitor phd student in TU Delft, The Netherlands. I spent a quite fruitful time in the Tera-Hertz Sensing group, where I learnt a lot. Also thank my workmates in Delft: *Daniele, Erio, Alessandro, Ozan, Giorgio, Waqas, Sven, Shahab, Bea* and *María*. And of course, my office mate *Matteo*.

Agradecer finalmente a todos mis amigos y gente cercana, los cuales han sido también un gran apoyo a lo largo de esta aventura.

Science is not only compatible with spirituality; it is a profound source of spirituality. (La ciencia no solo es compatible con la espiritualidad; es una profunda fuente de espiritualidad.)

Carl Sagan

We may draw the very interesting and significant conclusion that electromagnetics involves a well-developed body intended for problems involving guided waves, resonant effects, coupling effects, etc., in which the structural dimensions are of the order of the wavelength, and that this body of techniques can be applied not only to the microwave frequency range, for which it was developed, but also for other frequency ranges and even other types when the basic conditions are appropriate

A. A. Oliner

Sacudimiento extraño
que agita las ideas,
como huracán que empuja
las olas en tropel;
murmullo que en el alma
se eleva y va creciendo,
como volcán que sordo
anuncia que va a arder;
deformes siluetas
de seres imposibles;
paisajes que aparecen
como a través de un tul;
colores que fundiéndose
remedan en el aire
los átomos de Iris,
que nadan en la luz;
ideas sin palabras,
palabras sin sentido;
cadencias que no tienen
ni ritmo ni compás;
memorias y deseos
de cosas que no existen;
accesos de alegría,
impulsos de llorar;
actividad nerviosa
que no halla en qué emplearse;
sin rienda que lo guíe
caballo volador;
Locura que el espíritu
exalta y enardece;
embriaguez divina
del genio creador...
¡Tal es la inspiración!

(Gustavo Adolfo Bécquer, Rimas y leyendas)

Contents

Introduction

The term *microwaves* refers to electromagnetic waves with frequencies ranging from 300 MHz to 300 GHz in the electromagnetic spectrum. The corresponding wavelengths associated with these frequencies in vacuum are 1 m and 1 mm respectively. The wavelength values comprised between 1 m and 1 mm are usually of the order of the size of structures and devices where microwaves propagate. This similarity in size makes the theoretical and mathematical treatment of microwave propagation be actually complex, unlike the propagation of waves at the optics regime, or below radio frequency.

From a circuit point of view, the understanding of high-frequency signals behavior has been a challenge until, practically, the end of the XIX century. In principle, for lower frequencies, voltage and current signals are considered to propagate *instanteneously* across the circuit, as long as the circuit dimensions are small in comparison with the wavelength of the signals. Under these circumstances Kirchhoff's circuit laws works properly. However, at microwaves and even at radio frequencies, the wavelength and the circuit size can usually have similar dimensions, and it occurs that the propagation of voltage and current signals is not *instanteneous* across the circuit. Consequently, voltage and current values also presents a *spatial variation* and Kirchhoff's laws become insufficient to describe the behavior of the circuit. It is worth mentioning that during the XIX century, there were several attemps to undertake the construction of an underwater cable to connect the United Kingdom and the United States [1]. Several attemps failed due to, among other factors, the non-existence of a clear model to describe the propagation of signals along a very long cable. Later,

O. Heaviside developed the current version of the transmission line model by deducing the telegrapher equations and introducing the outstanding concept of distributed circuit element [2].

From the point of view of the field analysis and wave propagation, the publication of Maxwell equations [3] and the corresponding unification of the electric and magnetic phenomena revealed than optics, radiowaves or microwaves are governed by the same principles. A priori, that means that any solution of a problem involving microwaves is obtained by *solving directly* Maxwell equations. By the beginning of the XX century problems involving the calculation of modal solutions in metallic tubes and the scattering field of waves after interacting with an obstacle were addressed [4]. Specifically, the calculation of modes inside bounded regions with a certain cylindrical symmetry brought in the concept of waveguides, due to the possibility of guiding energy from one point to another inside such bounded regions. The search of modal solutions for different types of waveguides was the main contribution to microwaves in the twenties and thirties of the XX century.

At that time, there was no clear connection between the circuit theory and the electromagnetic theory. S. A. Schelkunoff, at the end of the thirties, bridged both theories by means of the concept of impedance [5]. This concept was originally employed by O. Heaviside as the ratio between the voltage and the current in a RL circuit [4]. Schelkunoff, some decades later, developed and generalized the concept for some oscillatory systems. For instance, he defined the characteristic impedance of a transmission line, and the impedance of an electromagnetic field inside a waveguide, and discovered that there exist a relationship between them. In fact, he found that the description of the propagation along a transmission line and along a waveguide was analogous. In consequence, complex problems involving waveguides could be posed in terms of a transmission-line formalism. Although this equivalence was actually helpful for the comprehension of guiding problems, real waveguide problems used to incorporate some discontinuity regions inside. From the modal analysis of waveguides, researchers knew that the interaction between the propagating wave and

the discontinuity region gave rise to the excitation of higher-order modes which, provided their reactive nature, were localized around such a discontinuity. The concentration of the electromagentic energy in a certain limited region encounters certain analogy with the energy stored in capacitors and inductors. It was then suggested to model the discontinuity regions by means of networks formed by interconnections of capacitors and inductors. The description of the field propagation by distributed and lumped circuit elements was the origin of the Microwave Network Theory [6]. During the next years the main challenge was to find the appropriate topology and the proper values of the circuit elements for a given waveguide discontinuity geometry (this challenge remains nowadays). Among many researchers, one of the most prominent was N. Marcuvitz who found, through an elegant mathematical treatment, analytical topologies for a large variety of waveguide types and waveguide discontinuities. All this information is included in his reputed book *Waveguide handbook* [7].

The performance and efficiency of equivalent circuits and their reliability was actually good, although their use was always limited in frequency [8, 9]. The effort of researchers was then focused on the derivation of fully analytical circuit models. Circuit models with analytical expressions for all their elements facilitated enormously the calculation of solutions since computation was not available yet. In parallel, in the fifties of the XX century, the complexity of the waveguide geometries got increased due to the technical limitations of the classical prototypes (coaxial line, rectangular waveguide, circular waveguide). Novel topologies appeared at that time: the microstrip, the stripline, and the use of periodic structures.

Bonus attention will be paid in this thesis to the evolution of periodic structures and their application in Microwave Engineering. The study of periodic structures as guiding devices is a classical problem in physics. An excellent historical review is summarized in [10], written by Louis Brilloin. This book, in fact, presents an exhaustive study about the guiding properties of periodic structures, inspiring the first papers about guiding properties for microwaves [11, 12]. These papers describe the appearance of stopbands and passbands,

and the dispersion relation in terms of the Microwave Network Theory since the periodic extension of the structure can be represented by a cascade of an indefinite number of loaded transmission lines. Periodic structures, however, provide a larger variety of properties not only related with guidance. The history of the diffraction grating is a proof of it [13]. The diffraction grating has long been a subject of study due to the interesting properties when it interacts with the incident radiation. They exhibits a varying response in frequency as was originally reported by Rittenhouse [14] some centuries ago, or more recently (indeed an almost century ago) by Professor R. W. Wood, who discovered a surprising phenomenon that carries his name (Wood's anomaly) [15]. While the spectral properties of periodic gratings were originally reported in optics, applications in the millimeter range would be proposed several decades after.

The beginning of the extensive use of periodic structures for taking advantage of filtering properties goes back to the context of the cold war [16]. The control of the radar cross section of aircrafts was an emerging issue at the end of the fifties. According to "Foreword I" in Munk's book *Frequency selective surfaces* [17], Ed Kennaugh proposed a solution for the control of the radar cross section based on a device called "frequency selective surface" (FSS). FSSs are actually periodic structures, conceived as periodic distributions of slots perforated in a metallic screen or patches printed on a dielectric slab, and whose operation features are quite similar to the gratings mentioned above. That is, the behavior of the structure changes with frequency. This original proposal of Kennaugh inspired the further increment of the study of FSSs. It is worth highlighting the effort devoted by B. Munk during the sixties. In particular, he developed the mutual impedance approach for the analysis of FSSs. This technique tried to solve the problem of mutual couplings in arrays, since each single slot/patch feels the presence of, at least, their inmediate neighbours. The further progress and application of FSSs motivated the development and improvement of other analysis methods. For instance, the application of Floquet theorem [19] reduced the problem to the analisys of the unit cell of the array, which is analogous to a

waveguide problem. In addition, the formulation of the problem in the spectral domain also was a helpful step, since the periodic nature of the structures turned the convolutions form of the integral equation into an algebraic system. The formulation of the problem via the spectral domain was originally carried out by the group headed by R. Mittra, who also was a prominent researcher in the field of FSSs [18].

At the end of the last century, the discovery of extraordinary transmission (ET) in a FSS constituted by metallic holes at optics frequencies regained the study of FSSs [20]. The phenomenon of ET was actually surprising because it was found for wavelengths larger than the size of the holes. This result was in apparent contradiction with Bethe's theory [21], stated a half century before. The discovery of ET also at millimeter frequencies [22] excluded the first hypothesis to explain the phenomenon, based on the excitation of surface plasmons [20]. In addition, the numerical techniques developed for FSSs at millimeter ranges could be applied to study the ET. Provided the analogy between the unit-cell problem and a waveguide problem, and also the analogy between this last and the transmission-line theory, the problem could be posed from the perspective of the Microwave Network Theory. A first paper explaining ET from a circuit-model perspective was carried out in our research group [23]. This paper provides a simple and comprehensive interpretation of the phenomenon from the perspective of the circuit theory. The same authors developed another paper regarding 1-D periodic gratings instead of 2-D from the same circuit perspective [24], corroborating that under certain circumstances a new variant of ET is given in 1-D structure, called anomalous extraordinary transmission. The circuit models proposed in both papers were originally derived from an heuristic rationale. During the following years, a lot of effort was devoted to improve these models. Part of this improvement has been the main subject of the research detailed in the present dissertation.

In the present dissertation the main goal consists in the derivation of analytical circuit models for different types of 1-D periodic structures by a method based on the integral equation. As we mentioned before, to find a fully-analytical

equivalent circuit has been a challenge from the forties of the past century (as well as to obtain a wideband performance). The equivalent circuits which will be presented in this work are the result of previous attemps carried out by our research group. While, for the first proposed models, the topology of the circuit was intuitively proposed according to the geometry of the unit cell and the values of the circuit elements were extracted from simulations from commercial softwares, the following ones were incorporating improvements and were derived using some mathematical approaches. This increasing tendency has ended up in the resulting models and the corresponding concluding remarks presented in this thesis.

Thus, in Chapter 1 the techique to derive the equivalent circuits is described in detail. It is applied for 1-D periodic structures, although for 2-D periodic structures it can be applied in a similar manner. Single-slit gratings and compound gratings are analyzed by using a slit-array formulation. For the derivation of the model we assume the grating to be sandwiched by two semi-infinite dielectric susbtrates. Extensions to more complex environments are left for the following chapters. We will also present in the same chapter the strip-array formulation, which is adequate for slit gratings with large slit apertures. The obtaining of the circuits will be explained in detail, step by step, in order to see clearly the implicit physical insights.

In Chapter 2 the investigation is focused on the study of the scattering response of a periodic single slit- and strip-grating under TE and TM normal and oblique incidence. Their corresponding circuit models, derived in Chapter 1 assuming that the array is sandwiched by two semi-infinite dielectric slabs, are now extended to account for multilayer systems. Additionally, we will also consider a pair of coupled gratings, which, under certain symmetry conditions, can be studied from the perspective of a single grating by using an analysis based on even and odd excitations. It will be checked the excellent agreement shown by the circuit model in comparison with results provided by HFSS [25]. In particular, the appearance of some kind of resonances such as Wood's anomaly or anomalous extraordinary transmission are well catched by the model. Finally, a

discussion about the range of validity of the models is provided.

In Chapter 3, the scattering response of the well-known mushroom structure [26] under TM normal and oblique incidence is analyzed in depth. The mushroom periodic structure is actually a periodic corrugated surface. Its corresponding equivalent circuit will be used not only to check the excellent performance and the reliability to reproduce complex resonant behaviors but also as an efficient design tool. In order to corroborate this, an absorber is easily designed by filling the corrugations with a lossy silicon dielectric. The model also incorporate modifications in order to account for possible ohmic losses in the metallic surfaces. At the end of the chapter a brief discussion about the performance of the model is carried out.

Chapter 4 is devoted to the study of the scattering response of compound gratings under TM incidence. Periodic compound gratings contain more than one slit per period. The existence of two, three, or a more number of slit apertures per each period and its mutual coupling introduces a new type of resonant: the so-called phase resonance [27]. The appearance of phase resonance is accompanied with several phenomena whose study is quite interesting. The circuit model will provide an alternative explanation of phase resonance, and will allow us to undertand the associated complexity in a simple manner. The inclusion of ohmic and dielectric losses are incoporated in the model. Furthermore, it will also be checked that the model is capable to work accurately for frequencies close to the optic regime, by taking into account the properties of metals at these frequencies by the Drude model. This fact reveals that the Microwave Network Theory can be sucessfully extended to other frequency ranges under certain circumstances.

Finally, Chapter 5 shows an exhaustive study about the scattering properties of coupled slit gratings under TE and TM incidence. Departing from the model of a single slit grating, a Π topology is mathematically deduced to account for a pair of coupled gratings. These gratings can be geometrically different and be misaligned each other, but their period must coincide. Systems containing several gratings stacked will also be considered. From the circuit point of view, a

stack of gratings is readily modelled by cascading their corresponding Π circuits. A brief discussion about the limits of validity of the model is also provided.

Chapter 1

Circuit models: characterization of discontinuities for 1 – D periodic structures

1.1 Introduction

The interaction of electromagnetic waves with periodic arrangements of planar scatterers have been widely studied due to their interesting properties. They generally exhibit a varying response in frequency after being excited by an external radiation, reason for which they are also commonly known as Frequency Selective Surfaces (FSS) [17, 28, 29]. This chapter, and basically the whole dissertation, is fundamentally focused on the study of one-dimensional FSSs exposed to incoming plane waves from different incident angles. In particular we are mainly interested in the description of the reflected, transmitted and diffracted powers resulting from the interaction of the incident wave with the FSS. The FSSs under consideration here generally consists of a one-dimensional distribution of an infinite number of elements periodically spaced. The analysis of the response of an infinite number of elements periodically distributed can be addressed in terms of Floquet's theorem (interesting discussions about Floquet's

theorem are found in [30, 31]). Floquet's theorem states that the wave function, in this case the electric or magnetic field, evaluated at a given point of the structure concides with the value of the wave funtion if we move one period forward (also backward), but multiplied by a complex constant that indicates the phase shift between both points. The phase shift between both points is imposed by the incident wave in this case. Therefore, the function describing the fields along the periodic-structure plane is a "quasi-periodic" funtion, formed by the product between a *periodic function* and a complex *exponential factor*. In turn, the periodic-function contribution can be expressed as a Fourier series in terms of a sum of exponentials or *spatial harmonics*. The description of the fields by means of Floquet's theorem allows us to analyze the entire FSS considering one period only, namely, a *unit cell*. The unit cell contains just a single element and is bounded by periodic boundary conditions (PBC). Periodic boundary conditions account for the phase shift between the bottom and top walls of the unit cell, as well as the phase shift between the left and right vertical walls. Thus the original problem is reduced to solve a discontinuity problem inside a generalized waveguide bounded by PBC [33].

Waveguide discontinuity problems have been studied for decades. The first studies concerning discontinuities were carried out in the 1930's for diaphrams apertures inside waveguides [8, 9]. Basically, the discontinuity inside a homogeneus waveguide is a cross-sectional boundary condition at certain plane along the propagation axis, or it can be part of a junction between two waveguide regions [7]. It is well known that the interaction of an incoming wave with the discontinuity generates reflected and transmitted waves, as well as storage of reactive energy in the vicinity of the discontinuity [32]. Propagative fields along the generalized waveguide are described by harmonics whose cutoff frequency is lower than the working frequency. On the contrary, the reactive field close to the discontinuity is described by evanescent harmonics which decay exponentially, with their cutoff frequency being higher than the working frequency.

For many practical problems only the fundamental harmonic is propagative, consisting in some cases on a TEM wave with no field components along the

propagation direction. The propagation of such a TEM wave through a generalized waveguide admits a transmission line representation in terms of their associated voltage and currents [34, 35]. The remaining harmonics are evanescent and their corresponding fields are concentrated near the discontinuity region. The harmonics can be divided in two groups according to their TM (transverse magnetic) or TE (transverse electric) nature. The set of TM and TE harmonics form and orthonormal basis in the space bounded by the unit cell walls, and for waveguides with traslational symmetry, both sets are independent of each other. TM harmonics are actually field configurations with an electric-field component along the propagation (or longitudinal) direction. The excited evanescent TM harmonics have an excess of electric energy that is mostly localized in the vicinity of the discontinuity. This fact can be somehow identified with the electric energy stored in capacitors, so such an excess electric energy around the discontinuity region can be modeled as a regular capacitor in an equivalent circuit. The same rationale can be used for TE harmonics. They have a magnetic-field component directed along the longitudinal direction and thus we can find a similar connection between their excess magnetic energy associated with the energy stored in a regular inductor. On account of these equivalences, the discontinuity regions surrounded by reactive fields admit a description in terms of capacitors and inductors from a circuit point of view. These capacitors and inductors are interconnected forming a circuit network.

The use of circuit models is advantageous because the simple rules of the conventional circuit analysis can be applied to obtain the solution of complex problems. For instance a simple circuit modelling the propagation of the fundamental harmonic (represented by a transmission line) and the interaction and coupling of the rest of harmonics around the discontinuity (information included into lumped elements) is expected to work for frequencies below the first Wood's anomaly [15]. Beyond Wood's anomaly (also recognized as the onset of the first grating lobe), the propagative field is not uniquely represented by the fundamental harmonic but also by additional diffracted fields. That is, some evanescent harmonics associated to the near-field at lower frequencies

become propagative beyond the onset of the first grating lobe, so they also require a description by means of transmission lines. It is worth mentioning that the non-TEM nature of the additional propagative harmonics demands an *appropiate* definition of their associated *voltages* and *currents* in order to find a transmission line model [34].

In the present chapter, a rigorous method to obtain an equivalent circuit that reproduces the scattering properties of 1-D periodic structures will be developed. Thus, in the following sections we will deduce the equivalent circuit for three different types of unit cell problems. These unit cell problems are motivated by the structures analyzed in the rest of chapters. Analytical expressions will be given for all the circuit elements, which is a fundamental advantage compared with other models proposed in the literature.

1.2 Circuit model for a slit/strip-discontinuity problem in a waveguide

1.2.1 Motivation

The study of the problem concerning a slit- or strip-like discontinuity inside a waveguide is motivated by the analysis of the structures shown in Fig. 1.1. The figure shows the lateral view of four different types of a classical 1-D periodic gratings. For instance, the gratings in Fig. 1.1(a) and Fig. 1.1(b) are made of a periodic distribution of metal strips with narrow thickness. On the contrary, the gratings depicted in Fig. 1.1(c) and Fig. 1.1(d) comprise a periodic distributions of thick slits. All the structures in Fig.1.1 are periodic along the y direction, which will be called *periodicity direction*. Furthermore they are invariant along the *invariance direction*, x. The gratings are located at the interface between two semi-infinite dielectric media. This plane will be henceforth called *discontinuity plane*. Finally, the structures are excited by a TE- or TM-polarized incident

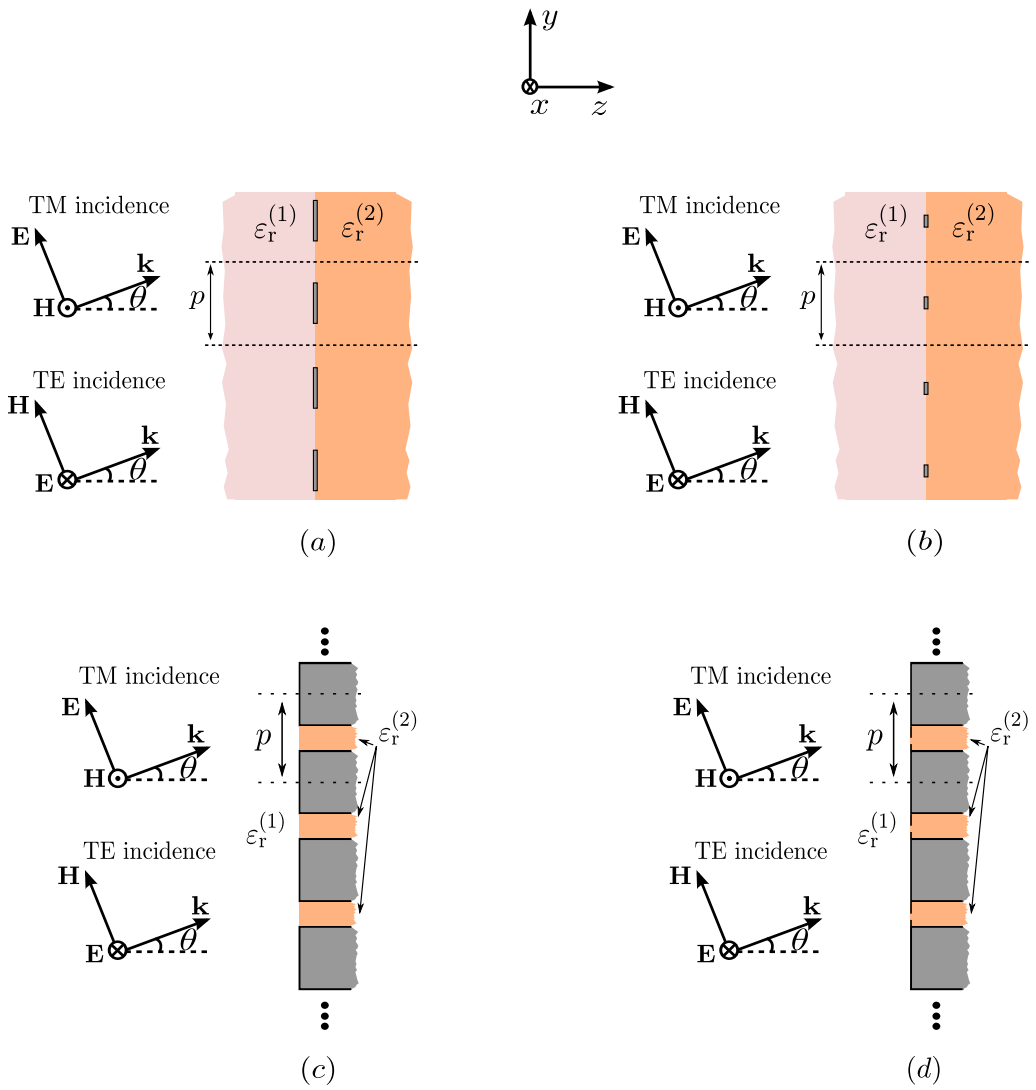

Figure 1.1: 1-D periodic gratings. (a): 1-D grating consisting on a periodic distribution slits in a thin metallic screen. (b): 1-D periodic grating consisting on a periodic distribution of thin metal strips. (c): 1-D periodic grating consisting on a periodic distribution of slits in a thin metallic screen. (d): Same as (c) but incorporating irises at the discontinuity plane.

plane wave. Throughout this dissertation, the incidence plane will always coincide with the YZ-plane (according to the coordinate system in Fig. 1.1).

The analysis of the structures in Fig. 1.1 is reduced to their corresponding unit cells, shown in Fig. 1.2. In a general context, the problem has been reduced to a waveguide discontinuity problem. At this point, we can distinguish

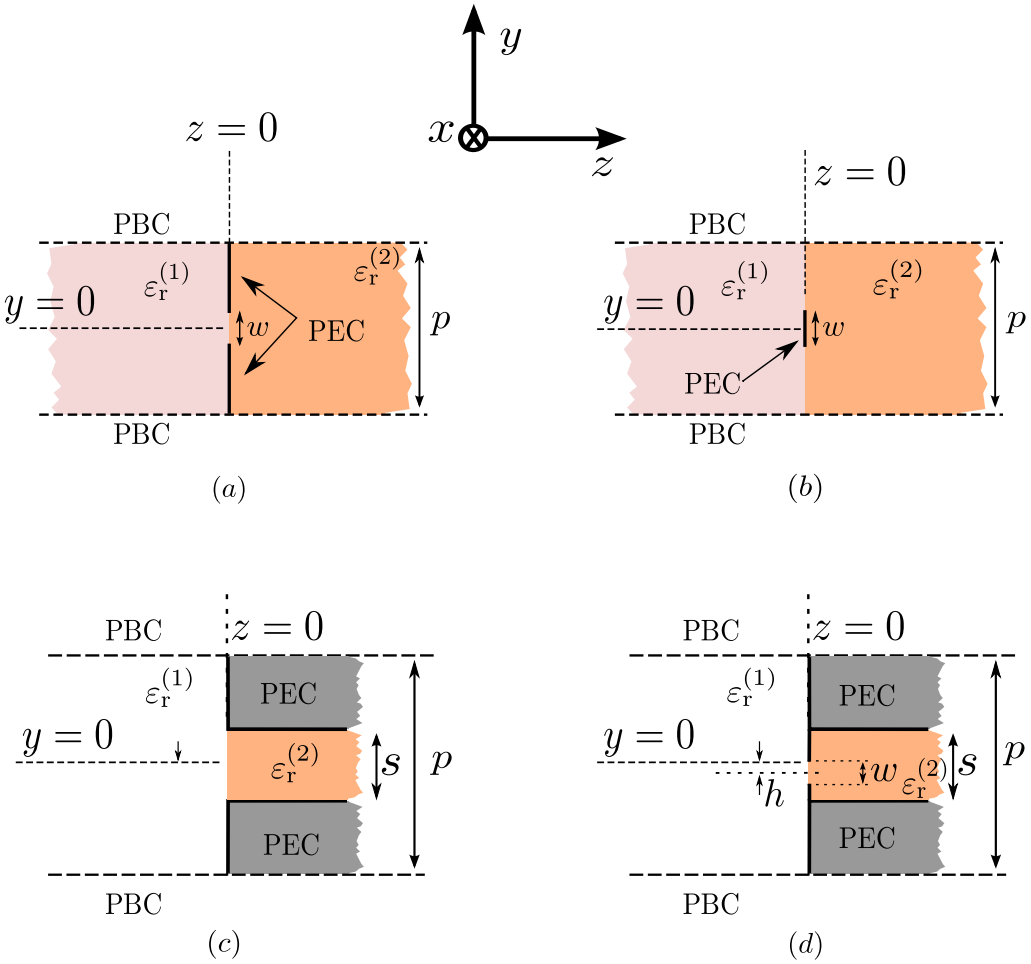

Figure 1.2: Unit cells corresponding to the structures in Fig.1.1. PBC denotes periodic boundary conditions. PEC denotes perfect electric conductor.

between two different discontinuity problems: the *slit-like discontinuity* problem, which takes place when the discontinuity consists of a small-sized slit aperture; namely the unit cell problems in Fig. 1.2(a), Fig. 1.2(c) and Fig. 1.2(d). On the contrary, Fig.1.2(b) corresponds to a *strip-like discontinuity* problem, where the discontinuity is actually a small-sized metal strip placed at the dielectric interface. In the following subsections, a circuit model to analyze the scattering response in both the strip- and slit-like discontinuity problems will be derived.

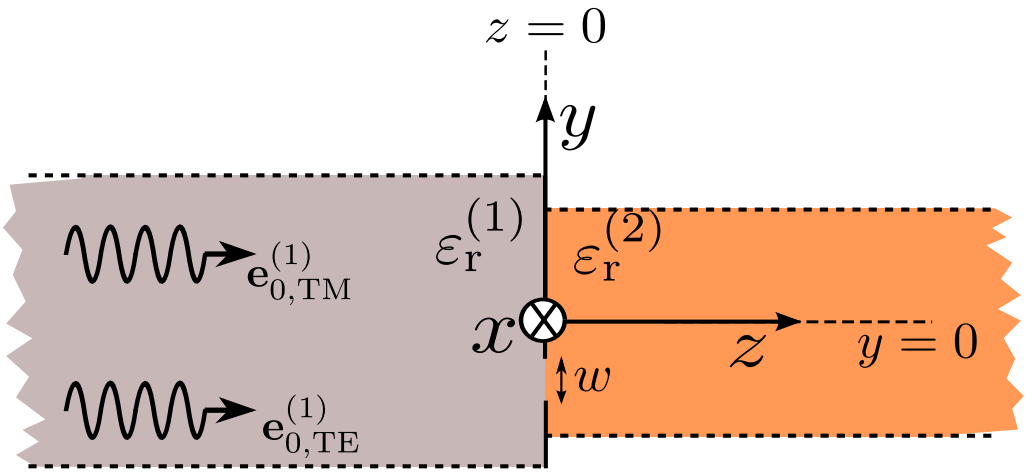

Figure 1.3: General problem concerning a slit discontinuity at the junction plane between two different waveguides.

1.2.2 Equivalent circuit for the slit discontinuity

In order to derive the equivalent circuit corresponding to a slit-discontinuity problem, we will consider the general structure depicted in Fig. 1.3, which includes all the cases shown in Fig.1.2. In this general problem, a slit discontinuity is located at the junction plane between two different and semi-infinite (along the propagation direction) homogeneus parallel-plate generalized waveguides. The lateral view shown in the figure is invariant along the x-direction. A TM or TE incident plane wave, coming from the left, meets the discontinuity plane at $z = 0$. For the scope of this dissertation, the transverse field profile of the incident wave will always coincide with the field profile of the fundamental mode supported by the left waveguide. The interaction of the incoming wave with the discontinuity plane generates reflected, transmitted and diffracted fields which can be described in terms of the modes supported by the corresponding waveguides.

Let us try to find the equivalent circuit of the structure in Fig. 1.3 assuming a TM-polarized incident wave. Owing to invariance along the x direction, the interaction of a TM-polarized plane wave with the discontinuity plane only excites TM modes. Thus, assuming an implicit time-harmonic dependence of the

type $\exp(\mathrm{j}\omega t)$, with ω being the angular frequency, the transverse electric field at the waveguide regions (1) and (2) can be expanded in terms of their respective TM modes:

$$\mathbf{E}^{(1)}(y,z) = \left[\mathrm{e}^{-\mathrm{j}\beta_0^{(1)}z} + R\mathrm{e}^{\mathrm{j}\beta_0^{(1)}z}\right]\mathbf{e}_{0,\mathrm{TM}}^{(1)}(y) + \sum_n{}' E_n^{(1)}\mathbf{e}_{n,\mathrm{TM}}^{(1)}(y)\mathrm{e}^{\mathrm{j}\beta_n^{(1)}z} \tag{1.1}$$

$$\mathbf{E}^{(2)}(y,z) = T\mathrm{e}^{\mathrm{j}\beta_0^{(2)}z}\mathbf{e}_{0,\mathrm{TM}}^{(2)}(y) + \sum_n{}' E_n^{(2)}\mathbf{e}_{n,\mathrm{TM}}^{(2)}(y)\mathrm{e}^{\mathrm{j}\beta_n^{(2)}z} \tag{1.2}$$

where $\sum_n{}' = \sum_{\forall n\neq 0}$ indicates that the summation includes all the modes except for the zeroth one, the amplitude of the impinging wave have been normalized to unity, R and T represent the reflection and transmission coefficient of the fundamental mode, $E_n^{(1)}$ and $E_n^{(2)}$ are the unknown normalized amplitudes of the nth mode at the waveguide regions (1) and (2), $\mathbf{e}_{n,\mathrm{TM}}^{(1)}$ and $\mathbf{e}_{n,\mathrm{TM}}^{(2)}$ are the corresponding transverse field profiles, and $\beta_n^{(1)}$ and $\beta_n^{(2)}$ represent the nth-order wavenumbers along the longitudinal direction given by

$$\beta_n^{(i)} = \sqrt{\varepsilon_{\mathrm{r}}^{(i)}k_0^2 - [k_n^{(i)}]^2} \qquad i = 1,2 \tag{1.3}$$

with $\varepsilon_{\mathrm{r}}^{(i)}$ being the relative permittivity in medium (i), k_0 the wavenumber in free-space and $k_n^{(i)}$ the cutoff wavenumber of a nth-order mode supported by the waveguide region (i). The modal profiles $\mathbf{e}_{n,\mathrm{TM}}^{(i)}(y)$ form an orthonormal basis for the waveguide region (i), so that

$$\int_\sigma \mathbf{e}_{n,\mathrm{TM}} \cdot \mathbf{e}_{m,\mathrm{TM}}^{*}\,\mathrm{d}\sigma = \delta_{n,m} \tag{1.4}$$

where σ is the integration domain, given by the dimensions of the waveguide cross-section (normal to the propagation direction). Due to the invariance along x, the integration domain σ is actually the distance between plates. The corresponding modal expansion for the magnetic field in regions (1) and (2) is expressed as follows:

$$\mathbf{H}^{(1)}(y,z) = Y_0^{(1)}(\mathrm{e}^{-\mathrm{j}\beta_n^{(1)}z} - R\mathrm{e}^{\mathrm{j}\beta_n^{(1)}})[\hat{\mathbf{z}} \times \mathbf{e}_{0,\mathrm{TM}}^{(1)}(y)] - \sum_n{}' E_n^{(1)}[\hat{\mathbf{z}} \times \mathbf{e}_{n,\mathrm{TM}}^{(1)}(y)] \tag{1.5}$$

$$\mathbf{H}^{(2)}(y,z) = Y_0^{(2)}T\mathrm{e}^{-\mathrm{j}\beta_n^{(1)}}[\hat{\mathbf{z}} \times \mathbf{e}_{0,\mathrm{TM}}^{(2)}(y)] + \sum_n{}' Y_n^{(2)}E_n^{(2)}[\hat{\mathbf{z}} \times \mathbf{e}_{n,\mathrm{TM}}^{(2)}(y)] \tag{1.6}$$

where we have made use of the nth-order TM admittance:

$$Y_n^{(i)} = \frac{\omega \varepsilon_{\mathrm{r}}^{(i)} \varepsilon_0}{\beta_n^{(i)}} \qquad i = 1, 2\,. \tag{1.7}$$

Let $\mathbf{E}_{\mathrm{s}}(\omega, y)$ be the electric field at the slit aperture. A priori, this field is not known but, under certain circumstances, its associated spatial profile is not expected to change significantly with frequency. In such case, we could approximate the field at the slit aperture as

$$\mathbf{E}_{\mathrm{s}}(\omega, y) = g(\omega)\mathbf{f}(y) \tag{1.8}$$

where we have factorized the frequency and spatial dependence. In principle, $\mathbf{f}(y)$ can be a complex function. Thus, at $z = 0$ we have

$$(1 + R)\mathbf{e}_{0,\mathrm{TM}}^{(1)} + {\sum_n}' E_n^{(1)} \mathbf{e}_{n,\mathrm{TM}}^{(1)} = \mathbf{E}_{\mathrm{s}}(\omega, y) \tag{1.9}$$

$$T\mathbf{e}_{0,\mathrm{TM}}^{(2)} + {\sum_n}' E_n^{(2)} \mathbf{e}_{n,\mathrm{TM}}^{(2)} = \mathbf{E}_{\mathrm{s}}(\omega, y) \tag{1.10}$$

where we have used the modal expansions in (1.1) and (1.2). The unknown coefficients of the field expansion in (1.1) and (1.2) are determined by the projection of the modes over the aperture field at $z = 0$,

$$\int_{\sigma_1} (1 + R)\mathbf{e}_{0,\mathrm{TM}}^{(1)} \cdot [\mathbf{e}_{0,\mathrm{TM}}^{(1)}]^* \mathrm{d}y = g(\omega) \int_{\mathrm{slit}} \mathbf{f}(y) \cdot [\mathbf{e}_{0,\mathrm{TM}}^{(1)}]^* \mathrm{d}y \tag{1.11}$$

$$\int_{\sigma_2} T\mathbf{e}_{0,\mathrm{TM}}^{(2)} \cdot [\mathbf{e}_{0,\mathrm{TM}}^{(2)}]^* \mathrm{d}y = g(\omega) \int_{\mathrm{slit}} \mathbf{f}(y) \cdot [\mathbf{e}_{0,\mathrm{TM}}^{(2)}]^* \mathrm{d}y \tag{1.12}$$

$$\int_{\sigma_1} E_n^{(1)} \mathbf{e}_{n,\mathrm{TM}}^{(1)} \cdot [\mathbf{e}_{n,\mathrm{TM}}^{(1)}]^* \mathrm{d}y = g(\omega) \int_{\mathrm{slit}} \mathbf{f}(y) \cdot [\mathbf{e}_{n,\mathrm{TM}}^{(1)}]^* \mathrm{d}y \tag{1.13}$$

$$\int_{\sigma_2} E_n^{(2)} \mathbf{e}_{n,\mathrm{TM}}^{(2)} \cdot [\mathbf{e}_{n,\mathrm{TM}}^{(2)}]^* \mathrm{d}y = g(\omega) \int_{\mathrm{slit}} \mathbf{f}(y) \cdot [\mathbf{e}_{n,\mathrm{TM}}^{(2)}]^* \mathrm{d}y\,. \tag{1.14}$$

Using the orthogonality of the modes, these expressions can be written as

$$(1 + R) = g(\omega)\tilde{f}_0^{(1)} \tag{1.15}$$

$$T = g(\omega)\tilde{f}_0^{(2)} \tag{1.16}$$

$$E_n^{(1)} = g(\omega)\tilde{f}_n^{(1)} \tag{1.17}$$

$$E_n^{(2)} = g(\omega)\tilde{f}_n^{(2)} \tag{1.18}$$

where, by definition,

$$\tilde{f}_n^{(i)} = \int_{\text{slit}} \mathbf{f}(y) \cdot [\mathbf{e}_{0,\text{TM}}^{(i)}(y)]^* \mathrm{d}y \qquad i = 1, 2\,. \tag{1.19}$$

From (1.15)-(1.18) we can deduce the following equalities:

$$T = (1+R)\frac{\tilde{f}_0^{(2)}}{\tilde{f}_0^{(1)}} \tag{1.20}$$

$$E_n^{(1)} = (1+R)\frac{\tilde{f}_n^{(1)}}{\tilde{f}_0^{(1)}} \tag{1.21}$$

$$E_n^{(2)} = (1+R)\frac{\tilde{f}_n^{(2)}}{\tilde{f}_0^{(1)}} \tag{1.22}$$

which will be quite helpful below. Now, we impose the continuity of the power flux through the slit aperture,

$$\hat{\mathbf{z}} \cdot \int_{\text{slit}} [\mathbf{E}_\text{s}(\omega, y)]^* \times \mathbf{H}^{(1)}(y, 0)\, \mathrm{d}y = \hat{\mathbf{z}} \cdot \int_{\text{slit}} [\mathbf{E}_\text{s}(\omega, y)]^* \times \mathbf{H}^{(2)}(y, 0)\, \mathrm{d}y\,. \tag{1.23}$$

Introducing the modal expansion of the magnetic field in (1.5) and (1.6), (1.23) is rewritten as

$$(1-R)Y_0^{(1)}[\tilde{f}_0^{(1)}]^* - \sum_n{}' E_n^{(1)} Y_n^{(1)} [\tilde{f}_n^{(1)}]^* = T Y_0^{(2)} [\tilde{f}_0^{(2)}]^* + \sum_n{}' E_n^{(2)} Y_n^{(2)} [\tilde{f}_n^{(2)}]^*\,. \tag{1.24}$$

Using the expressions in (1.20)-(1.22) in (1.24) we obtain

$$(1-R)Y_0^{(1)} - (1+R)\sum_n{}' Y_n^{(1)} \left|\frac{\tilde{f}_n^{(1)}}{\tilde{f}_0^{(1)}}\right|^2 = (1+R)Y_0^{(2)} \left|\frac{\tilde{f}_0^{(2)}}{\tilde{f}_0^{(1)}}\right|^2 - (1+R)\sum_n{}' Y_n^{(1)} \left|\frac{\tilde{f}_n^{(2)}}{\tilde{f}_0^{(1)}}\right|^2 \tag{1.25}$$

which, after some manipulations, leads to write the reflection coefficient as

$$R = \frac{Y_0^{(1)} - Y_0^{(2)} \left|\frac{\tilde{f}_0^{(2)}}{\tilde{f}_0^{(1)}}\right|^2 - \sum_n{}' Y_n^{(1)} \left|\frac{\tilde{f}_n^{(1)}}{\tilde{f}_0^{(1)}}\right|^2 - \sum_n{}' Y_n^{(1)} \left|\frac{\tilde{f}_n^{(2)}}{\tilde{f}_0^{(1)}}\right|^2}{Y_0^{(1)} + Y_0^{(2)} \left|\frac{\tilde{f}_0^{(2)}}{\tilde{f}_0^{(1)}}\right|^2 + \sum_n{}' Y_n^{(1)} \left|\frac{\tilde{f}_n^{(1)}}{\tilde{f}_0^{(1)}}\right|^2 + \sum_n{}' Y_n^{(1)} \left|\frac{\tilde{f}_n^{(2)}}{\tilde{f}_0^{(1)}}\right|^2}\,. \tag{1.26}$$

On the one hand, the admittances $Y_0^{(1)}$ and $Y_0^{(2)}$ in (1.26) can be identified as the characteristic admittances of the input and output transmission lines (both

with semi-infinite extension) where the fundamental modes propagate (impinging, reflected and transmitted waves). Furthermore, the factor $\left|\frac{\tilde{f}_0^{(2)}}{\tilde{f}_0^{(1)}}\right|$ indicates the coupling level between the incident and transmitted mode. From a circuit point of view, this factor can be identified with the turns ratio of an ideal transformer connected at the input of the line $Y_0^{(2)}$ [6]. On the other hand, after comparing (1.26) with the reflection-coefficient expression given in conventional transmission line theory [34], we can deduce an expression for the equivalent admittance met by the incident mode,

$$Y_{\text{eq}} = {\sum_n}' Y_n^{(1)} \left|\frac{\tilde{f}_n^{(1)}}{\tilde{f}_0^{(1)}}\right|^2 + {\sum_n}' Y_n^{(2)} \left|\frac{\tilde{f}_n^{(2)}}{\tilde{f}_0^{(1)}}\right|^2 \tag{1.27}$$

which includes the contribution of the remaining modes. The above expression consists of an infinite sum of modal admittances weighted by their corresponding factor. From a circuit point of view, each modal admittance can be identified with the characteristic admittance of a semi-infinite transmission line. The longitudinal wavenumber of a nth-order line is exactly the one of the corresponding mode (1.3). In addition, the weighting factor is recognized as the turns ratio of a transformer connected at the line input. Taking into account the above ideas, the equivalent circuit is schematically represented as a parallel connection of an infinite number of nth-order transmission lines in Fig. 1.4 through their respective transformers.

At this point it is important to mention that usually, most of modes contributing to the equivalent circuit are reactive; that is, their cutoff frequencies are far above the frequency of operation. Their respective transmission lines have purely imaginary characteristic admittances and their longitudinal wavenumbers are actually attenuation constants. When the operation frequency is higher than the cutoff frequency of a particular mode, this mode becomes propagative resulting in the appearance of a grating lobe. The onset of a nth grating lobe in a given dielectric region takes place when $\beta_n^{(i)} = 0$, so that the cutoff frequency

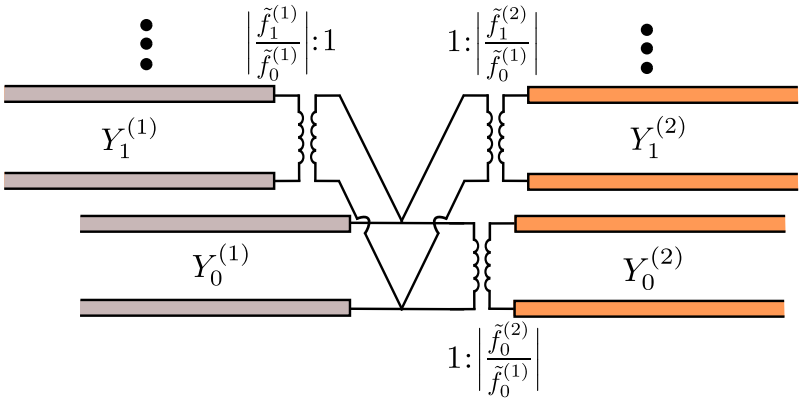

Figure 1.4: Illustration of the equivalent circuit derived for the general slit discontinuity in Fig. 1.3, consisting of an infinite number of transmission lines connected in parallel.

$f_n^{(i)}$ is calculated according to:

$$\beta_n^{(i)} = 0 \Rightarrow k_n^{(i)} = (\varepsilon_{\mathrm{r}}^{(i)})^{1/2} k_0; \qquad \Rightarrow \qquad f_n^{(i)} = \sqrt{\frac{1}{\mu_0 \varepsilon_0 \varepsilon_{\mathrm{r}}^{(i)}}} \frac{k_n^{(i)}}{2\pi}\,. \tag{1.28}$$

Modes with cutoff frequencies far above the operation frequency admit the following approximation:

$$\beta_n^{(i)} = -\mathrm{j} k_n^{(i)} \tag{1.29}$$

where we have used $k_n^{(i)} \gg k_0$ in (1.3). Introducing (1.29) in the TM-admittance expression (1.7) we obtain

$$Y_{n,\mathrm{ho}}^{(i)} = \mathrm{j}\omega \frac{\varepsilon_0 \varepsilon_{\mathrm{r}}^{(i)}}{k_n^{(i)}}\,, \tag{1.30}$$

expression that can be identified with the admittance of a regular capacitor, with

$$C_n^{(i)} = \frac{\varepsilon_0 \varepsilon_{\mathrm{r}}^{(i)}}{k_n^{(i)}} \tag{1.31}$$

being the capacitance associated with a nth-order mode in the medium (i). The label "ho" in (1.30) stands for *high order*, indicating that all the modes under the approximation in (1.29) are denoted as *high-order modes*. The parallel connection of all of them (according to the expression in (1.27)) results in a global

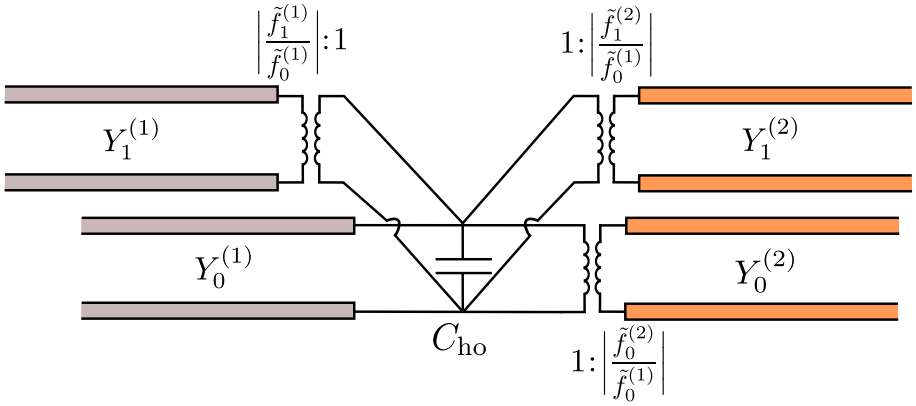

Figure 1.5: Example of the equivalent circuit for the slit-discontinuity problem assuming TM incidence and $N = 1$.

equivalent capacitor,

$$C_{\text{ho}} = \sum_{\forall n>N} \left(C_n^{(1)} \left| \frac{\tilde{f}_n^{(1)}}{\tilde{f}_0^{(1)}} \right|^2 + C_n^{(2)} \left| \frac{\tilde{f}_n^{(2)}}{\tilde{f}_0^{(1)}} \right|^2 \right). \tag{1.32}$$

The expression in (1.32) does not depend on frequency, so the infinite series can just be calculated once and stored. The parameter N denotes the number of modes excluded from the high-order group and are called *low-order modes*. In our experience, N can be taken as the number of propagative modes in the highest-permittivity medium at the highest frequency of interest, although in some situations it is also necessary to include the lowest-order evanescent mode. In any case, N is rarely higher than 2 or 3 for most practical cases. Finally, (1.27) is reduced to the following analytical expression,

$$Y_{\text{eq}} = \sum_{n=1}^{N} \left(Y_n^{(1)} \left| \frac{\tilde{f}_n^{(1)}}{\tilde{f}_0^{(1)}} \right|^2 + Y_n^{(2)} \left| \frac{\tilde{f}_n^{(2)}}{\tilde{f}_0^{(1)}} \right|^2 \right) + \text{j}\omega C_{\text{ho}} \tag{1.33}$$

whose corresponding equivalent circuit is depicted in Fig. 1.5.

An identical procedure to derive the equivalent circuit can be carried out for TE incidence. A TE-polarized plane wave impinging on the discontinuity plane only excites TE modes; hence, the electromagnetic field at both sides of

the discontinuity is expanded in terms of TE modes,

$$\mathbf{E}^{(1)}(y,z) = (\mathrm{e}^{-\mathrm{j}\beta_0^{(1)}z} + R\mathrm{e}^{\mathrm{j}\beta_n^{(1)}z})\mathbf{e}_{0,\mathrm{TE}}^{(1)}(y) + \sum_n{}' E_n^{(1)}\mathbf{e}_{n,\mathrm{TE}}^{(1)}(y)\mathrm{e}^{\mathrm{j}\beta_n^{(1)}z} \tag{1.34}$$

$$\mathbf{E}^{(2)}(y,z) = T\mathrm{e}^{-\mathrm{j}\beta_n^{(2)}z}\mathbf{e}_{0,\mathrm{TE}}^{(2)}(y) + \sum_n{}' E_n^{(2)}\mathbf{e}_{n,\mathrm{TE}}^{(2)}(y)\mathrm{e}^{-\mathrm{j}\beta_n^{(2)}z} \tag{1.35}$$

$$\mathbf{H}^{(1)}(y,z) = Y_0^{(1)}(\mathrm{e}^{-\mathrm{j}\beta_0^{(1)}z} - R\mathrm{e}^{\mathrm{j}\beta_n^{(1)}z})(\hat{\mathbf{z}}\times\mathbf{e}_{0,\mathrm{TE}}^{(1)}(y)) - \sum_n{}' Y_n^{(1)}E_n^{(1)}(\hat{\mathbf{z}}\times\mathbf{e}_{n,\mathrm{TE}}^{(1)}(y))\mathrm{e}^{\mathrm{j}\beta_n^{(1)}z} \tag{1.36}$$

$$\mathbf{H}^{(2)}(y,z) = Y_0^{(2)}T\mathrm{e}^{-\mathrm{j}\beta_n^{(2)}z}(\hat{\mathbf{z}}\times\mathbf{e}_{0,\mathrm{TE}}^{(2)}(y)) - \sum_n{}' Y_n^{(2)}E_n^{(2)}(\hat{\mathbf{z}}\times\mathbf{e}_{n,\mathrm{TE}}^{(2)}(y))\mathrm{e}^{-\mathrm{j}\beta_n^{(2)}z}\,, \tag{1.37}$$

with

$$\mathbf{e}_{n,\mathrm{TE}}^{(i)}(y) = \mathbf{e}_{n,\mathrm{TM}}^{(i)}(y)\times\hat{\mathbf{z}} \tag{1.38}$$

being the nth-order modal field profile associated with a nth-order TE mode and

$$Y_n^{(i)} = \frac{\beta_n^{(i)}}{\omega\mu_0} \tag{1.39}$$

the nth-order modal admittance associated with TE-polarized waves. The modal profiles $\mathbf{e}_{n,\mathrm{TE}}^{(i)}$ also form an orthonormal basis.

After following the same procedure as for TM incidence, an identical expression for the reflection coefficient as the one in (1.26) is obtained. Thus, the expression of the equivalent admittance of the circuit is the same in (1.27) but with TE admittances and with the transformers calculated according to

$$\tilde{f}_n^{(i)} = \int_{\mathrm{slit}} \mathbf{f}(y)\cdot[\mathbf{e}_{n,\mathrm{TE}}^{(i)}(y)]^*\mathrm{d}y\,. \tag{1.40}$$

This equivalent admittance Y_{eq} is also split into low- and high-order modes. High-order modes admit the approximation in (1.29), which after being introduced in the nth-order modal admittance for TE waves in (1.39), yields:

$$Y_{n,\mathrm{ho}}^{(i)} = -\mathrm{j}\frac{k_n^{(i)}}{\omega\mu_0}\,. \tag{1.41}$$

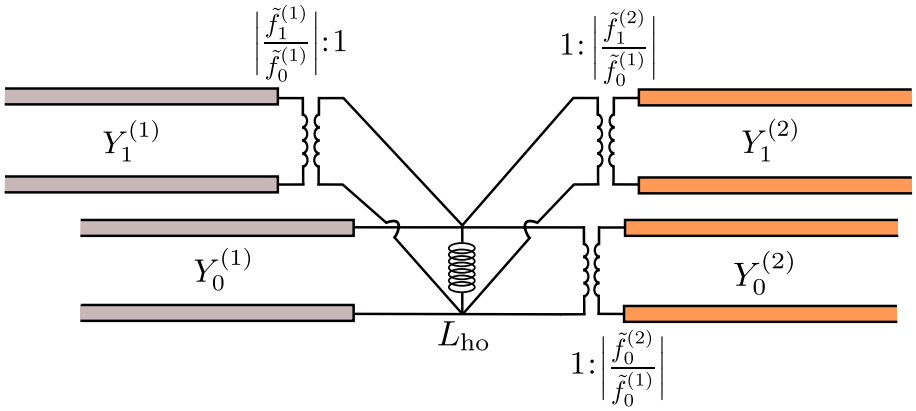

Figure 1.6: Example of the equivalent circuit for the slit-discontinuity problem assuming TE incidence and $N = 1$

The expression in (1.41) corresponds to the expression of an admittance associated with a regular inductor, thus we can define

$$L_n^{(i)} = \frac{\mu_0}{k_n^{(i)}}\,. \tag{1.42}$$

The parallel connection of an infinite number of inductors results in a global high-order inductor,

$$L_{\text{ho}} = \left[\sum_{\forall n>N}\left(\frac{1}{L_n^{(1)}}\left|\frac{\tilde{f}_n^{(1)}}{\tilde{f}_0^{(1)}}\right|^2 + \frac{1}{L_n^{(2)}}\left|\frac{\tilde{f}_n^{(2)}}{\tilde{f}_0^{(1)}}\right|^2\right)\right]^{-1}\,. \tag{1.43}$$

The expression in (1.43) is frequency-independent so it can be calculated once and stored. After introducing the L_{ho} inductance, (1.27) reduces to

$$Y_{\text{eq}} = \sum_{n=1}^{N}\left(Y_n^{(1)}\left|\frac{\tilde{f}_n^{(1)}}{\tilde{f}_0^{(1)}}\right|^2 + Y_n^{(2)}\left|\frac{\tilde{f}_n^{(2)}}{\tilde{f}_0^{(1)}}\right|^2\right) - \mathrm{j}\frac{1}{\omega L_{\text{ho}}} \tag{1.44}$$

whose equivalent circuit is schematically shown in Fig. 1.6.

1.2.3 Equivalent circuit for the strip discontinuity

The strip-like problem inferred from the unit cell configuration in Fig. 1.2(b) leads us to deal with the general situation shown in Fig. 1.7. In this figure, a lateral view of the junction between two waveguides is presented. A zero-thickness

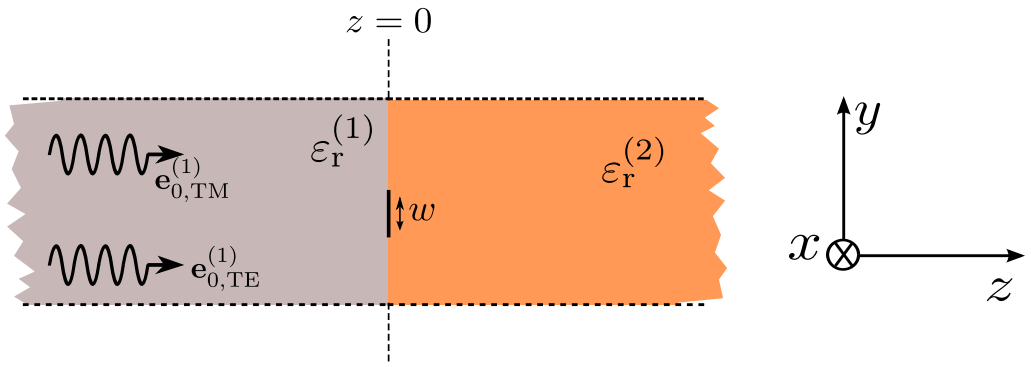

Figure 1.7: Lateral view of the strip-waveguide problem. Now the dimensions of the leftmost and rightmost waveguides are identical.

strip obstacle is placed at the junction plane. The cross-section remains invariant along the x-direction. The left and right waveguides are, for this problem, considered identical (except for the dielectric filling). The reason behind this decision concerns the orthonormality properties of the characteristic modes of each waveguide. We will check below that the method that we present to obtain the equivalent circuit requires the set of characteristic modes of both waveguides to be identical. Fortunately, the unit-cell problem in Fig. 1.2(b) satisfies this restriction. The starting point for the derivation is again the TM- and TE-field expansions. According to the aforementioned restriction, we now have

$$\mathbf{e}_{n,\mathrm{TM}}^{(1)}(y) = \mathbf{e}_{n,\mathrm{TM}}^{(2)}(y) = \mathbf{e}_{n,\mathrm{TM}}(y) \tag{1.45}$$

$$\mathbf{e}_{n,\mathrm{TE}}^{(1)}(y) = \mathbf{e}_{n,\mathrm{TE}}^{(2)}(y) = \mathbf{e}_{n,\mathrm{TE}}(y)\,. \tag{1.46}$$

Of course, the field profiles $\mathbf{e}_{n,\mathrm{TM}}$ and $\mathbf{e}_n$ form an orthonormal basis. Now, let $\mathbf{J}_{\mathrm{s}}(y)$ be the surface current density at the strip surface. Similar to the approximation used for the slit aperture field in the previous section, the spatial profile is assumed to be invariant with frequency, namely

$$\mathbf{J}_{\mathrm{s}}(y) = g(\omega)\mathbf{f}(y)\,. \tag{1.47}$$

The coefficients of the field expansion can be related to the surface current through the magnetic-field jump condition at the discontinuity plane (z = 0):

$$\mathbf{J}_{\mathrm{s}}(y) = \hat{\mathbf{z}} \times [\mathbf{H}^{(2)}(y) - \mathbf{H}^{(1)}(y)]\,. \tag{1.48}$$

Introducing the magnetic field expansions (1.5), (1.6) for TM incidence, or (1.36), (1.37) for TE incidence, into (1.48) we obtain

$$(1+R)Y_0^{(2)} - Y_0^{(1)}(1-R) = \tilde{f}_0 \tag{1.49}$$

$$(Y_n^{(2)} + Y_n^{(1)})E_n^{(i)} = \tilde{f}_n \qquad i = 1,2 \tag{1.50}$$

with

$$\tilde{f}_n = \begin{cases} \displaystyle\int_{\text{strip}} \mathbf{J}_\text{s} \cdot [\mathbf{e}_{n,\text{TM}}]^* \mathrm{d}y & \text{TM incidence} \\ \displaystyle\int_{\text{strip}} \mathbf{J}_\text{s} \cdot [\mathbf{e}_{n,\text{TE}}]^* \mathrm{d}y & \text{TE incidence} \end{cases} . \tag{1.51}$$

Combining (1.49) and (1.50), the nth-order coefficient is expressed in terms of the reflection coefficient as

$$E_n^{(i)} = \frac{\tilde{f}_n}{\tilde{f}_0} \frac{R(Y_0^{(1)} + Y_0^{(2)}) + Y_0^{(2)} - Y_0^{(1)}}{Y_n^{(1)} + Y_n^{(2)}} . \tag{1.52}$$

It is worth remarking again that the expressions in (1.49) and (1.50) are obtained because the set of charasteristic modes of both waveguides are identical (a nth-order mode, characteristic of the waveguide (1) is orthonormal to all the charasteristic modes of the waveguide (2) excepting, of course, the nth one). The projection of the fundamental mode over the surface-current profile in (1.49) would have given rise to

$$\tilde{f}_0^{(1)} = -(1-R)Y_0^{(1)} + T\int_\sigma \mathbf{e}_{0,\text{TM}}^{(2)} \cdot [\mathbf{e}_{0,\text{TM}}^{(1)}]^* \mathrm{d}y + {\sum_n}' E_n^{(2)} Y_n^{(2)} \int_\sigma \mathbf{e}_{n,\text{TM}}^{(2)} \cdot [\mathbf{e}_{0,\text{TM}}^{(1)}]^* \mathrm{d}y \, . \tag{1.53}$$

if both waveguides were different, and consequently, also their characteristic modes. The integral within the sum would not vanish, precluding the obtaining of the equivalent circuit. Note that the rightmost integral in (1.53) would only vanish if $\mathbf{e}_{n,\text{TM}}^{(1)} = \mathbf{e}_{n,\text{TM}}^{(2)}$, recovering the expression in (1.51).

Imposing now the electric-field boundary condition at the metallic surface of the strip,

$$\int_{\text{strip}} \mathbf{E}^{(1)}(y,0) \cdot [\mathbf{J}_\text{s}(y)]^* \mathrm{d}y = 0 \tag{1.54}$$

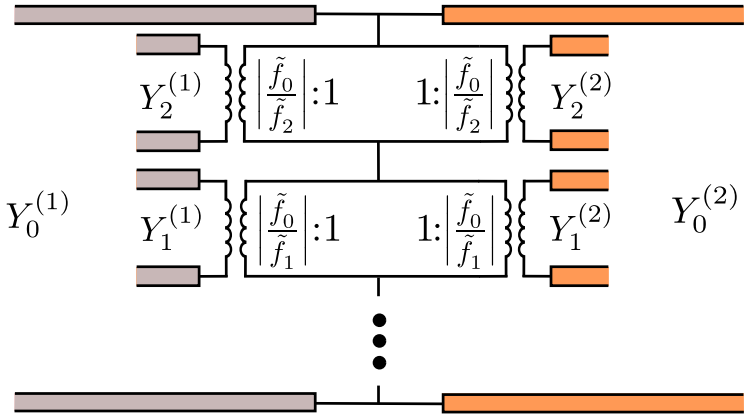

Figure 1.8: Equivalent circuit obtained for strip arrays. The equivalent impedance is now a series connection of pairs of admittances connected to their respective nth transformer.

and after introducing the corresponding field expansion in (1.54), we obtain

$$(1+R)\tilde{f}_0 + \sum_{\forall n\neq 0} E_n \tilde{f}_n = 0\,. \tag{1.55}$$

Introducing (1.52) into (1.55) and after some manipulations, the reflection coefficient is expressed in the following way:

$$R = \frac{Y_0^{(1)} - Y_0^{(2)} - \left[\sum_n{}' \frac{1}{Y_n^{(1)}+Y_n^{(2)}}\left|\frac{\tilde{f}_n}{\tilde{f}_0}\right|^2\right]^{-1}}{Y_0^{(1)} + Y_0^{(2)} + \left[\sum_n{}' \frac{1}{Y_n^{(1)}+Y_n^{(2)}}\left|\frac{\tilde{f}_n}{\tilde{f}_0}\right|^2\right]^{-1}} \tag{1.56}$$

where the equivalent impedance of the circuit can be identified as

$$Z_{\text{eq}} = \sum_n{}' \frac{1}{Y_n^{(1)} + Y_n^{(2)}}\left|\frac{\tilde{f}_n}{\tilde{f}_0}\right|^2. \tag{1.57}$$

From the expressions in (1.56) and (1.57) we deduce the topology of the equivalent circuit shown in Fig. 1.8. It consists of a series connection of an infinite number of pairs of parallel-connected transmission lines with characteristic admittances $Y_n^{(i)}$ and weighted by the factor $\left|\frac{\tilde{f}_n}{\tilde{f}_0}\right|$ (nth-order turns ratio of its associated transformers). Again, as in the previous subsection, the infinite series in

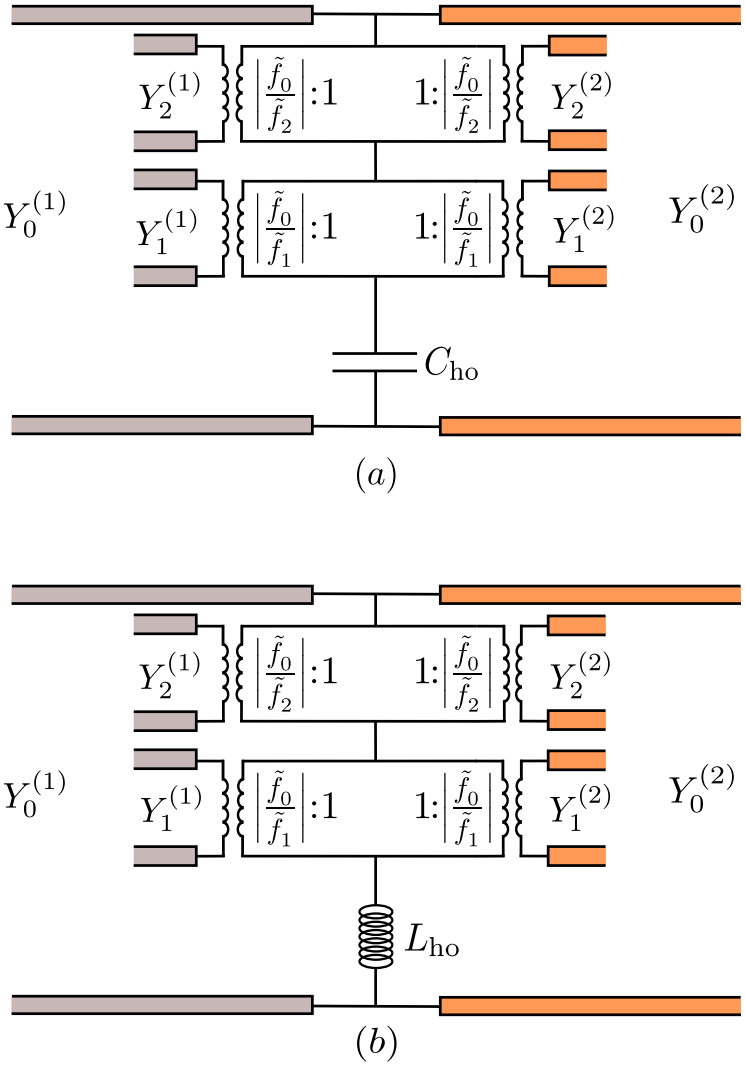

Figure 1.9: (a): Equivalent circuit obtained under TM incidence. (b): Equivalent circuit derived for TE incidence. $N = 2$ in both examples.

(1.57) can be split in two groups following the strategy of low- and high-order modes. The modal admittance of a nth high-order mode, after approximating its corresponding longitudinal wavenumber according to (1.29), is reduced to

$$Y_n^{(i)} = \begin{cases} \mathrm{j}\omega C_n^{(i)} & \text{TM incidence} \\ -\mathrm{j}\frac{1}{\omega L_n^{(i)}} & \text{TE incidence} \end{cases} \tag{1.58}$$

where $C_n^{(i)}$ and $L_n^{(i)}$ have already been calculated in (1.31) and (1.42) respectively. A high-order capacitance/inductance is defined in terms of the high-order modes,

$$C_{\text{ho}}^{(i)} = \left[\sum_{\forall n>N} \frac{1}{C_n^{(1)} + C_n^{(2)}} \left| \frac{\tilde{f}_n}{\tilde{f}_0} \right|^2 \right]^{-1} \qquad \text{TM incidence} \tag{1.59}$$

$$L_{\text{ho}}^{(i)} = \sum_{\forall n>N} \frac{L_n^{(1)}}{2} \left| \frac{\tilde{f}_n}{\tilde{f}_0} \right|^2 \qquad \text{TE incidence} \tag{1.60}$$

so that the expression in (1.57) is finally reduced to

$$Z_{\text{eq}} = \sum_{n=1}^{N} \frac{1}{Y_n^{(1)} + Y_n^{(2)}} \left| \frac{\tilde{f}_n}{\tilde{f}_0} \right|^2 + \frac{1}{\text{j}\omega C_{\text{ho}}} \qquad \text{TM polarization} \tag{1.61}$$

$$Z_{\text{eq}} = \sum_{n=1}^{N} \frac{1}{Y_n^{(1)} + Y_n^{(2)}} \left| \frac{\tilde{f}_n}{\tilde{f}_0} \right|^2 + \text{j}\omega L_{\text{ho}} \qquad \text{TE polarization} \tag{1.62}$$

where the parameter N indicates the number of low-order modes, calculated as the number of propagative modes in the highest-permitivity medium at the highest frequency of operation plus the first evanescent mode. It is worth mentioning that the profile functions appearing in (1.61) and (1.62) are generally different for each polarization. The equivalent circuit for both TM and TE incidence is shown in Fig.1.9.

1.3 Circuit model for a discontinuity involving three different waveguides

1.3.1 Motivation

Periodic gratings containing more than one slit per period are also quite interesting structures. In the literature, these kind of structures are commonly known as *compound gratings*. Specially our study will be focused on the analysis of the scattering properties associated with 1-D compound gratings consisting of a thick metallic screen with more than one slit per period. The present

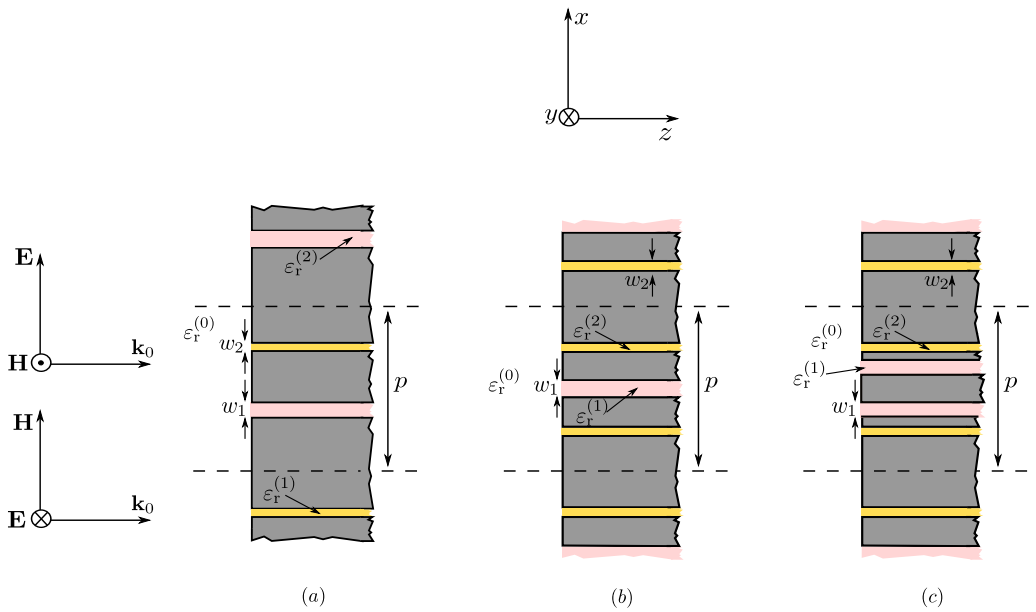

Figure 1.10: Compound grating structures (a): Compound grating with two different slits per period. (b): Compound grating with three slits per period symmetrically placed along the unit cell. (c): Compound gratings with four slits per period symmetrically placed. They all can be analyzed through a two-slits waveguide problem. Grey color represents metalized zones.

chapter will be only interested in obtaining the equivalent circuit for compound gratings whose unit cell is reducible to a discontinuity problem involving three different waveguides (in Chapter 4 we will extend the model for a larger number of slits per unit cell, based on the model for two slits per unit cell).Examples of structures having this property are sketched in Fig. 1.10. It will be discussed in Chapter 4 that the unit cell for gratings with three and four slits per period reduces to a two-slits problem under certain symmetry conditions. In this sense, a generalized unit-cell problem corresponding with the structures in Fig. 1.10 is shown in Fig. 1.11. The derivation of the corresponding equivalent circuit will be carried out in next subsection.

1.3.2 Equivalent circuit

The junction of three different-sized parallel-plate waveguides at $z = 0$ is depicted in Fig. 1.11. The lateral view shown in the figure remains invariant along

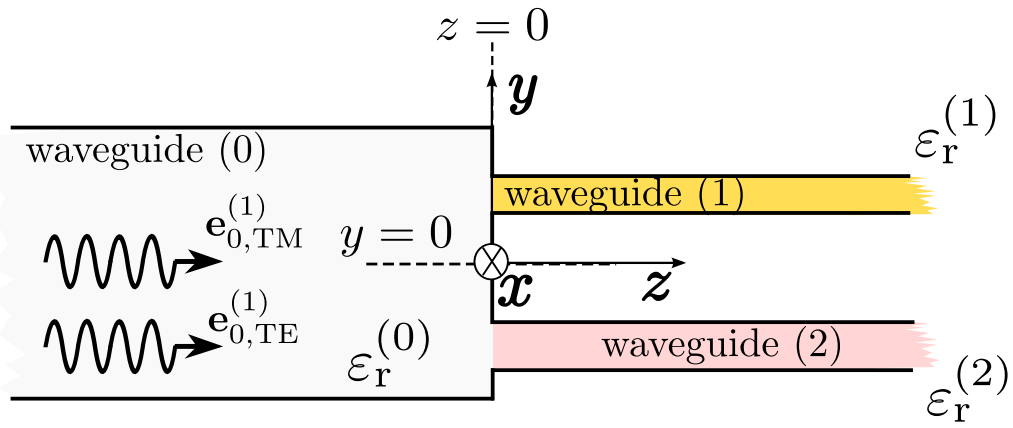

Figure 1.11: Generalized waveguide discontinuity problem corresponding to the unit cell of the structures in Fig.1.10.

the x-direction. The waveguide region at the left-hand side of the discontinuity plane ($z < 0$)will be called external region, labelled by the superscript (0). At the right-hand side of the discontinuity plane ($z > 0$), two waveguides make up the so called internal region, labelled (1) and (2). The size of these waveguides is considered to be small compared with the size of the external one. This fact allows us to approximate the description of the transverse components of the electromagnetic field inside such waveguides in terms of their fundamental TEM mode (if supported by the waveguide under consideration). Thus for $i = 1, 2$, these modes are given by

$$\mathbf{E}^{(i)}(y,z) = E_0^{(i)} \mathrm{e}^{-\mathrm{j}\beta_0^{(i)} z} \cdot \begin{cases} \mathbf{e}_{0,\mathrm{TM}}^{(i)} & \text{TM incidence} \\ \mathbf{e}_{0,\mathrm{TE}}^{(i)} & \text{TE incidence} \end{cases} \tag{1.63}$$

$$\mathbf{H}^{(i)}(y,z) = Y_0^{(i)} E_0^{(i)} \mathrm{e}^{-\mathrm{j}\beta_0^{(i)} z} \hat{\mathbf{z}} \times \begin{cases} \mathbf{e}_{0,\mathrm{TM}}^{(i)} & \text{TM incidence} \\ \mathbf{e}_{0,\mathrm{TE}}^{(i)} & \text{TE incidence} \end{cases} \tag{1.64}$$

with $E_0^{(i)}$ being the unknown amplitude of the fundamental mode propagating in waveguide (i). The wvanumber $\beta_0^{(i)}$ and the admittance $Y_0^{(i)}$ are those characteristic of a TEM plane wave,

$$\beta_0^{(i)} = \omega\sqrt{\varepsilon_{\mathrm{r}}^{(i)}\varepsilon_0\mu_0} \tag{1.65}$$

$$Y_0^{(i)} = \sqrt{\frac{\varepsilon_0\varepsilon_{\mathrm{r}}^{(i)}}{\mu_0}}\,. \tag{1.66}$$

In the external region (0), the transverse electromagnetic field is described in terms of the modes supported by its corresponding waveguide, which for TM incidence is

$$\mathbf{E}^{(0)}(y,z) = \left[\mathrm{e}^{-\mathrm{j}\beta_0^{(0)}z} + R\mathrm{e}^{\mathrm{j}\beta_0^{(0)}z}\right]\mathbf{e}_{0,\mathrm{TM}}^{(0)} + \sum_n{}' E_n^{(0)}\mathbf{e}_{n,\mathrm{TM}}^{(0)}\mathrm{e}^{\mathrm{j}\beta_n^{(0)}z} \tag{1.67}$$

$$\mathbf{H}^{(0)}(y,z) = \left[\mathrm{e}^{-\mathrm{j}\beta_0^{(0)}z} - R\mathrm{e}^{\mathrm{j}\beta_0^{(0)}z}\right]Y_0^{(0)}(\hat{\mathbf{z}}\times\mathbf{e}_{0,\mathrm{TM}}^{(0)}) - \sum_n{}' E_n^{(0)}Y_0^{(0)}(\hat{\mathbf{z}}\times\mathbf{e}_{n,\mathrm{TM}}^{(0)})\mathrm{e}^{\mathrm{j}\beta_n^{(0)}z} \tag{1.68}$$

where again, we have considered that the incident wave is the fundamental mode. For TE incidence we have

$$\mathbf{E}^{(0)}(y,z) = \left[\mathrm{e}^{-\mathrm{j}\beta_0^{(0)}z} + R\mathrm{e}^{\mathrm{j}\beta_0^{(0)}z}\right]\mathbf{e}_{0,\mathrm{TE}}^{(0)} + \sum_n{}' E_n^{(0)}\mathbf{e}_{n,\mathrm{TE}}^{(0)}\mathrm{e}^{\mathrm{j}\beta_n^{(0)}z} \tag{1.69}$$

$$\mathbf{H}^{(0)}(y,z) = \left[\mathrm{e}^{-\mathrm{j}\beta_0^{(0)}z} - R\mathrm{e}^{\mathrm{j}\beta_0^{(0)}z}\right]Y_0^{(0)}(\hat{\mathbf{z}}\times\mathbf{e}_{0,\mathrm{TE}}^{(0)}) - \sum_n{}' E_n^{(0)}Y_0^{(0)}(\hat{\mathbf{z}}\times\mathbf{e}_{n,\mathrm{TE}}^{(0)})\mathrm{e}^{\mathrm{j}\beta_n^{(0)}z}\,. \tag{1.70}$$

All the terms have been normalized to the amplitude of the impinging wave: $E_n^{(0)}$ is the nth-order modal amplitude and R represents the reflection coefficient associated with the fundamental mode. The expressions for the longitudinal wavenumbers $\beta_n^{(0)}$ and the modal admittances $Y_n^{(i)}$ are those in (1.3) and (1.7), (1.39) respectively. Note that (1.67),(1.68) and (1.69), (1.70) indicate that TM incidence only excites TM modes at the discontinuity plane, as well as TE incidence only excites TE modes, which is the case for 1-D structures where the incidence plane is normal to the invariance direction. Of course, the set of

modal profiles $\mathbf{e}^{(0)}_{n,\mathrm{TM}}$ and $\mathbf{e}^{(0)}_{n,\mathrm{TE}}$ form respectively an orthonormal basis of TM and TE fields in the external waveguide.

To proceed with the derivation of the circuit model, the aperture field at the discontinuity plane ($z = 0$) is assumed to have the following form:

$$\mathbf{E}_{\mathrm{s}} = \left[g_1(\omega)\mathbf{f}^{(1)}(y) + g_2(\omega)\mathbf{f}^{(2)}(y)\right]\ \hat{\mathbf{y}} \tag{1.71}$$

where the frequency and the spatial dependence of the fields are factorized, with $\mathbf{f}^{(i)}(y)$ being the proposed field pattern at the i-th slit aperture. This implies that the spatial field profiles at the apertures are considered independent of frequency, although their complex amplitudes g_1 and g_2 may vary strongly with frequency. The amplitudes g_1 and g_2 can readily be related to the coefficients of the modal expansion in the external region by projecting the modes over the aperture field. Thus, we obtain

$$(1 + R) = g_1(\omega)\tilde{f}^{(1)}_0 + g_2(\omega)\tilde{f}^{(2)}_0 \tag{1.72}$$

$$E^{(0)}_n = g_1(\omega)\ \tilde{f}^{(1)}_n + g_2(\omega)\ \tilde{f}^{(2)}_n \tag{1.73}$$

where

$$\tilde{f}^{(i)}_n = \int_{\text{slit } i} \mathbf{f}^{(i)}(y) \cdot [\mathbf{e}^{(0)}_{n,\mathrm{TM}}]^* \mathrm{d}y\,. \tag{1.74}$$

Also, the coefficients of the field in slits (1) and (2) are calculated according to

$$E^{(1)}_0 = g_1(\omega) \int_{\text{slit } 1} \mathbf{f}^{(1)} \cdot [\mathbf{e}^{(1)}_{0,\mathrm{TM}}]^* \mathrm{d}y = g_1(\omega)\tilde{S}^{(1)}_0 \tag{1.75}$$

$$E^{(2)}_0 = g_2(\omega) \int_{\text{slit } 2} \mathbf{f}^{(2)} \cdot [\mathbf{e}^{(2)}_{0,\mathrm{TM}}]^* \mathrm{d}y = g_2(\omega)\tilde{S}^{(2)}_0 \tag{1.76}$$

Let us writte the expressions in (1.72), (1.73), (1.75) and (1.76) in the following

way:

$$V_0 = V_1 + V_2 \tag{1.77}$$

$$E_n^{(0)} = V_1 \frac{\tilde{f}_n^{(1)}}{\tilde{f}_0^{(1)}} + V_2 \frac{\tilde{f}_n^{(2)}}{\tilde{f}_0^{(2)}} \tag{1.78}$$

$$E_0^{(1)} = V_1 \frac{\tilde{S}_0^{(1)}}{\tilde{f}_0^{(1)}} \tag{1.79}$$

$$E_0^{(2)} = V_2 \frac{\tilde{S}_0^{(2)}}{\tilde{f}_0^{(2)}} \tag{1.80}$$

where

$$V_0 = (1 + R) \tag{1.81}$$

$$V_1 = g_1(\omega)\tilde{f}_0^{(1)} \tag{1.82}$$

$$V_2 = g_2(\omega)\tilde{f}_0^{(2)}\,. \tag{1.83}$$

The next step in the derivation is to impose the continuity of the power flux through the slit apertures:

$$\hat{\mathbf{z}} \cdot \int_{\text{slit 1}} \mathbf{f}^{(1)}(y) \times \mathbf{H}^{(0)}(y,0)\,\mathrm{d}y = \hat{\mathbf{z}} \cdot \int_{\text{slit 1}} \mathbf{f}^{(1)} \times \mathbf{H}^{(1)}(y,0)\,\mathrm{d}y \tag{1.84}$$

$$\hat{\mathbf{z}} \cdot \int_{\text{slit 2}} \mathbf{f}^{(2)}(y) \times \mathbf{H}^{(0)}(y,0)\,\mathrm{d}y = \hat{\mathbf{z}} \cdot \int_{\text{slit 2}} \mathbf{f}^{(2)} \times \mathbf{H}^{(2)}(y,0)\,\mathrm{d}y\,. \tag{1.85}$$

Introducing (1.64) and (1.68) into (1.84) yields

$$(1-R)Y_0^{(0)}\tilde{f}_0^{(1)} - {\sum_n}' Y_n^{(0)} E_n^{(0)} \tilde{f}_n^{(1)} = Y_0^{(1)} E_0^{(1)} \tilde{S}_0^{(1)}\ . \tag{1.86}$$

Using (1.78) and (1.79), this last equation can be rewritten as

$$I_0 = \bar{Y}_0^{(1)} V_1 + \bar{Y}_{11} V_1 + \bar{Y}_{12} V_2 \tag{1.87}$$

with

$$\bar{Y}_{11} = \left| \frac{1}{\tilde{f}_0^{(1)}} \right|^2 {\sum_n}' Y_n^{(0)} |\tilde{f}_n^{(1)}|^2 \tag{1.88}$$

$$\bar{Y}_{12} = \frac{1}{\tilde{f}_0^{(1)}[\tilde{f}_0^{(2)}]^*} {\sum_n}' Y_n^{(0)} \tilde{f}_n^{(1)} [\tilde{f}_n^{(2)}]^* \tag{1.89}$$

$$\bar{Y}_0^{(1)} = \left| \frac{\tilde{S}_0^{(1)}}{\tilde{f}_0^{(1)}} \right|^2 Y_0^{(1)} \tag{1.90}$$

and where the I_0 current, is given by

$$I_0 = (1-R)Y_0^{(0)} \tag{1.91}$$

which represents the current associated with the fundamental mode at the discontinuity plane. Similarly, using (1.85) we can obtain

$$I_0 = \bar{Y}_0^{(2)}V_2 + \bar{Y}_{21}V_1 + \bar{Y}_{22}V_2 \tag{1.92}$$

with

$$\bar{Y}_{21} = \frac{1}{[\tilde{f}_0^{(1)}]^* \tilde{f}_0^{(2)}} \sum_n{}' Y_n^{(0)} [\tilde{f}_n^{(1)}]^* \tilde{f}_n^{(2)} \tag{1.93}$$

$$\bar{Y}_{22} = \left| \frac{1}{\tilde{f}_0^{(2)}} \right|^2 \sum_n{}' Y_n^{(0)} |\tilde{f}_n^{(2)}|^2 \tag{1.94}$$

$$\bar{Y}_0^{(2)} = \left| \frac{\tilde{S}_0^{(2)}}{\tilde{f}_0^{(2)}} \right|^2 Y_0^{(2)} \,. \tag{1.95}$$

Using (1.77) to eliminate V_2 in (1.87), (1.92), the following system of equations is achieved:

$$I_0 = V_1(\bar{Y}_0^{(1)} + \bar{Y}_{11} - \bar{Y}_{12}) + V_0\bar{Y}_{12} \tag{1.96}$$

$$I_0 = V_1\bar{Y}_{21} + V_0(\bar{Y}_0^{(2)} + \bar{Y}_{22} - \bar{Y}_{21}) \,. \tag{1.97}$$

so that (after eliminating V_1) I_0 and V_0 are related according to

$$I_0 = V_0 \left[\bar{Y}_{12} + (\bar{Y}_0^{(1)} + \bar{Y}_{11} - \bar{Y}_{12}) \frac{\bar{Y}_0^{(2)} + \bar{Y}_{22} - \bar{Y}_{21} - \bar{Y}_{12}}{\bar{Y}_0^{(1)} + \bar{Y}_{11} - \bar{Y}_{21} - \bar{Y}_{12}} \right] \tag{1.98}$$

where the equivalent load admittance met by the impinging wave is straighfordwardly derived by imposing the ratio $Y_{\text{eq}} = I_0/V_0$, so

$$Y_{\text{eq}} = \bar{Y}_{12} + (\bar{Y}_0^{(1)} + \bar{Y}_{11} - \bar{Y}_{12}) \frac{\bar{Y}_0^{(2)} + \bar{Y}_{22} - \bar{Y}_{21} - \bar{Y}_{12}}{\bar{Y}_0^{(1)} + \bar{Y}_{11} - \bar{Y}_{21} - \bar{Y}_{12}} \tag{1.99}$$

A priori, the complicated mathematical expression in (1.99) make it difficult to identify a simple topology. However, the complex-conjugate admittances $\bar{Y}_{12}$

and $\bar{Y}_{21}$ may become identical under certain circumstances. In these cases, the expression in (1.99) reduces to

$$Y_{\text{eq}} = Y_{12} + \left[\frac{1}{Y_{11} + \bar{Y}_0^{(1)}} + \frac{1}{Y_{22} + \bar{Y}_0^{(2)}} \right]^{-1} \tag{1.100}$$

where

$$Y_{12} = \bar{Y}_{21} = \bar{Y}_{12} \ , \qquad Y_{ii} = \bar{Y}_{ii} - Y_{12} \ . \tag{1.101}$$

It is important to remark that, as we will see in detail in Chapter 4, there are relevant practical situations in which $Y_{12} = Y_{21}$. Indeed, when the grating is illuminated by a normally-oriented wave, such condition is satisfied, and therefore the equivalent admittance in (1.100) can be used. This expression is fully

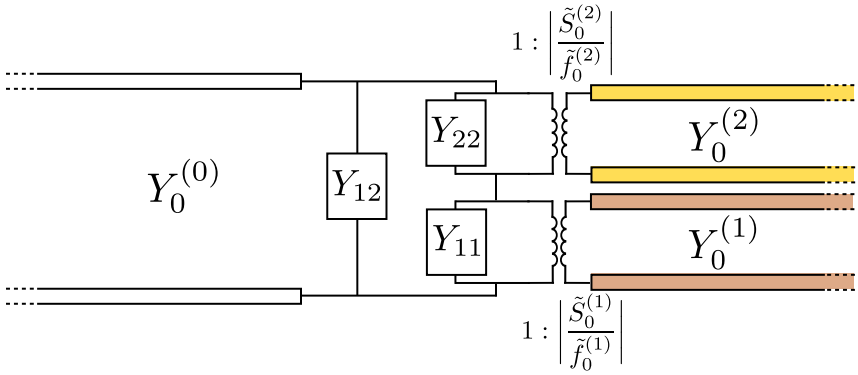

Figure 1.12: Topology of the circuit model derived for the discontinuity that couples the impinging wave (input line) to the slit transmission lines.

consistent with the circuit topology in Fig. 1.12. Again, the admittances Y_{11}, Y_{22} and Y_{12} are given by infinite series, which can be split into two contributions: low- and high-order elements. The longitudinal wavenumbers associated with high-order modes admits the approximation in (1.29). In consequence, their modal admittances become capactive admittances for TM incidence (1.31), and inductive admittances for TE incidence (1.42). A global capacitance/inductance

is obtained by the contribution of all the high-order modes. For TM incidence,

$$C_{12} = \frac{1}{\tilde{f}_0^{(1)}[\tilde{f}_0^{(2)}]^*} \sum_{\forall n>N} C_n^{(0)} \tilde{f}_n^{(1)}[\tilde{f}_n^{(2)}]^* \tag{1.102}$$

$$C_{ii} = \left|\frac{1}{\tilde{f}_0^{(i)}}\right|^2 \sum_{\forall n>N} C_n^{(0)} \left|\tilde{f}_n^{(i)}\right|^2 - C_{12}\,, \tag{1.103}$$

and for TE incidence,

$$L_{12} = \left[\frac{1}{\tilde{f}_0^{(1)}[\tilde{f}_0^{(2)}]^*} \sum_{\forall n>N} \frac{1}{L_n^{(0)}} \tilde{f}_n^{(1)}[\tilde{f}_n^{(2)}]^*\right]^{-1} \tag{1.104}$$

$$L_{ii} = \left[\left|\frac{1}{\tilde{f}_0^{(i)}}\right|^2 \sum_{\forall n>N} \frac{1}{L_n^{(0)}} |\tilde{f}_n^{(1)}|^2\right]^{-1} - L_{12} \tag{1.105}$$

with $i = 1, 2$. These global inductances and capacitances are frequency independent, so their respective infinite series are calculated once and stored. The equivalent admittance in (1.100) reduces to

$$Y_{ii} = Y_{ii}^{(\mathrm{lo})} + \begin{cases} \mathrm{j}\omega C_{ii} & \text{TM incidence} \\ -\mathrm{j}\dfrac{1}{\omega L_{ii}} & \text{TE incidence} \end{cases} \tag{1.106}$$

$$Y_{12} = Y_{12}^{(\mathrm{lo})} + \begin{cases} \mathrm{j}\omega C_{12} & \text{TM incidence} \\ -\mathrm{j}\dfrac{1}{\omega L_{12}} & \text{TE incidence} \end{cases} \tag{1.107}$$

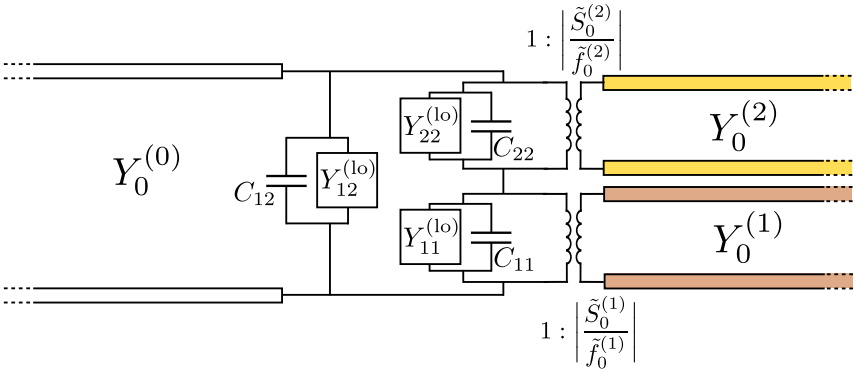

Figure 1.13: Circuit model in Fig. 1.12 but now showing the separate contribution of the low-order (lo), i.e., propagative or close to cutoff, modes and the frequency-independent capacitances that incorporate the global contribution of *all* the remaining high-order evanescent modes.

with $Y_{ij}^{(\mathrm{lo})}$ representing the low-order elements group, formed by a few modes according to

$$Y_{12}^{(\mathrm{lo})} = \frac{1}{\tilde{f}_0^{(1)}[\tilde{f}_0^{(2)}]^*} \sum_{n=1}^{N} Y_n^{(0)} \tilde{f}_n^{(1)} [\tilde{f}_n^{(2)}]^* \tag{1.108}$$

$$Y_{ii}^{(\mathrm{lo})} = \left| \frac{1}{\tilde{f}_0^{(i)}} \right|^2 \sum_{n=1}^{N} Y_n^{(0)} |\tilde{f}_n^{(i)}|^2 - Y_{12}^{(\mathrm{lo})} \,. \tag{1.109}$$

Finally, the equivalent circuit for both TM and TE incidence are sketched in Fig.1.13 and Fig.1.14.

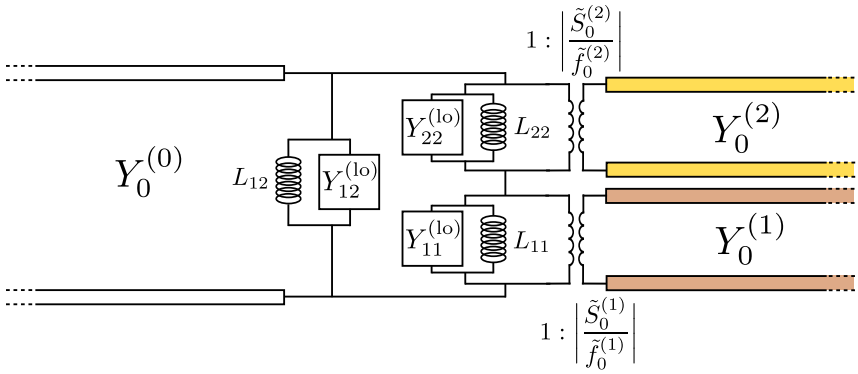

Figure 1.14: Circuit model in Fig.1.12 but now showing the separate contribution of the low-order (lo), i.e., propagative or close to cutoff, modes and the frequency-independent capacitances that incorporate the global contribution of *all* the remaining high-order evanescent modes.

Chapter 2

Thin strip/slit gratings loaded with dielectric slabs

2.1 Introduction

The analysis of the electromagnetic response of diffraction gratings has been a topic of interest for decades. To mention some applications, they can be used as selective frequency surfaces (FSSs) [17], polarizers [38, 39], artificial magnetic conductors [40], high-impedance surfaces [41], or partially reflective surfaces [42]. Some other examples of applications can be found in the terahertz regime [43, 44] and in the visible range [45–47]. In this chapter we will focus our study on the 1-D grating shown in Fig. 2.1. It consists of an infinite distribution of periodically-spaced lossless metal strips with zero thickness [37].

Some pioneering theoretical studies concerning this structure date back more than a century [48, 49]. These works detail the description of the diffractive field resulting from the interaction between a plane wave and an array of periodically distributed strips. In particular, early researchers paid much attention to an interesting property inherent to periodic structures: *Wood's anomaly* [15, 50]. According to the textual description given in [15], Wood's anomaly is a resonance phenomenon consisting of "*a drop from maximum illumination to minimum,*

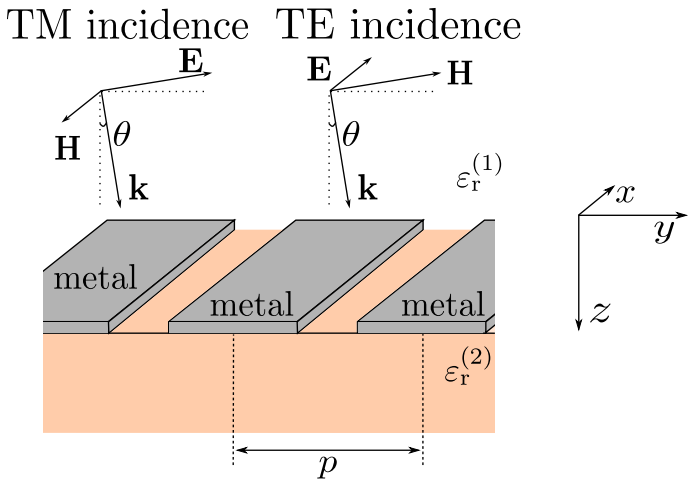

Figure 2.1: Sketch of a 1-D classical diffraction grating.

a drop certainly of from 10 to 1". In fact, such a drop from maximum illumination to minimum appears as a sudden and sharp variation in the spectrum. A first explanation about the phenomenon was reported in [50], associating its appearance with the excitation of grating lobes. At present, a modern explanation of Wood's anomaly is established, based on the appearance of surface waves supported by the gratings [51, 52]. For further information, a good discussion about Wood's anomaly is found in [53].

One-dimensional periodic gratings also exhibit other types of resonances associated to a high transmission response. We first highlight Fabry-Pérot resonances. Rigorously speaking, a Fabry-Pérot resonance is not a resonance inherent to the periodicity of the structure but rather to the thickness of the screen. In this sense, Fabry-Pérot condition requires the thickness of the grating to be close to an integer factor of $\lambda/2$ (λ is the wavelength of the mode propagating along the structure). Under these circumstances the grating can exhibit full transmission, even for gratings with subwavelength slits [54–56]. Thin gratings, on the contrary, do not fullfill the Fabry-Pérot condition unless they are supported by or printed on a sufficiently thick dielectric substrate. In these cases, the appearance of a Fabry-Pérot resonance is mainly related to the dielectric slab.

Another interesting resonant transmission phenomenon, discovered at the end of the last century, is the so-called *extraordinary optical transmission* (EOT) [20, 57]. EOT is, in contrast to Fabry-Pérot resonances, inherent to the periodic nature of the gratings. The phenomenon refers to the appearance, around a certain frequency, of a narrow and strong peak of transmission through an opaque screen periodically perforated with small holes. Moreover, it appears at wavelengths much larger than the dimensions of the holes, which in principle, would be in apparent contradiction with Bethe's predictions [21]. Originally the phenomenon was reported in the optics regime, as the response of a 2-D periodic structure of circular holes in a metallic screen. It was initially interpreted as the consequence of a constructive coupling between the incident wave and the surface plasmons supported by the grating [20, 57–60]. Surface plasmons are surface waves supported by metallic structures near the visible range, where the metal behaves as a plasma [61]. However the EOT phenomenon was also experimentally reported at millimeter frequencies in [22, 62], where the penetration of the magnetic field in metals is marginal, and therefore no surface plasmons can be excited. A new interpretation of extraordinary-transmission (ET) phenomena was then given, based on the surface waves (also called spoof plasmons) supported by the periodic structure under consideration [63]. At this point it is important to remark that extraordinary transmission, in the sense described above, can only be found in 2-D gratings composed of holes. For 1-D strip arrays the situation is slighly different, because extraordinary transmission is observed only when the incident field has its electric-field component directed along the periodicity direction. Additionally, the strips must necessarily be either thick or, on the contrary, the strips might be electrically thin but supported or printed on a thick dielectric substrate. Thus, in the context of 1-D thin gratings, extraordinary transmission has been called *anomalous extraordinary transmission* [150, 151].

In the microwave regime, extraordinary transmission and the rest of resonances previously mentioned can be accurately analyzed by full-wave diffraction models. Full-wave models provide accurate solutions in numerical form,

although in most cases, they are computationally expensive. An alternative way of addressing problems of this nature can be found in the microwave circuit theory. As outlined in the previous chapter, the analysis of a periodic structure is reduced to solve a discontinuity problem in a waveguide, interpreted as an equivalent circuit composed of lumped elements and transmission lines. A first equivalent circuit was proposed in the framework of extraordinary transmission through 2-D thin and thick screens with holes [23]. Following the guidelines given in [23], the problem of extraordinary transmission in 1-D gratings was also dealt with in [24], providing an heuristic circuit topology for both simple and compound gratings. An extension of the 1-D case is presented in [64, 65], which consider finite-thickness dielectric layers at both sides of the slit array. It is worth mentioning that the several circuit elements involved in the models reported in [23, 24, 64, 65] are not given in analytical form; that is, some circuit elements have to be calculated via numerical results extracted from an external full-wave simulator. Our contribution here will be consists of deriving a fully-analytical equivalent circuit for 1-D periodic structures of thin strips. Specifically, for the structure under consideration in the present chapter, we will use the analytical models developed in Sec. 1.2 of Chapter 1. These models were derived assuming semi-infinite dielectric media at both sides of the periodic array. Here we will also extend the use of the circuits to more complex situations involving stratified dielectric media at both sides of the grating. Numerous numerical results will be shown in order to check the performance of the model. Finally, at the end of the chapter we will explore the limits of validity of the circuit.

2.2 Equivalent circuit

The equivalent circuit for the structure of interest in Fig.2.1 is a particular case of the circuits derived in the previous chapter. A periodic grating as the one shown in Fig. 2.1 can be viewed from two different perspectives, depicted in Fig. 2.2(a) and Fig.2.2(b): the slit- and strip-like grating. The problem concerning gratings

with large strips is posed in terms of the slit-like problem, described in the previous chapter (small slit size). On the contrary, the problem concerning gratings with small strips is treated by the strip-like-grating approach, also described in the previous chapter. The reason behind this separation lies on the accuracy of the circuit models. As we will check at the end of the chapter, the models become more accurate as the slits/strips are smaller (in comparison with the operation wavelength).

Fig. 2.2(c) and Fig. 2.2(d) show the unit-cell problem corresponding to the slit- and strip-like grating. They both represent a waveguide discontinuity problem, where the geometry of the waveguides (1) and (2) is identical (except for the dielectric filling). The distance between the upper and lower walls of the waveguide is given by the period of the structure p, and the size of scatterer is denoted by w. Due to the periodicity of the grating and the excitation, the walls of both waveguides are periodic boundary conditions (PBC) so that the waveguides are actually generalized waveguides. These boundary conditions determine the specific expression of the modes and their cutoff wavenumbers. In fact, the modes of a generalized waveguide with PBC are commonly known as Floquet harmonics, which form an orthonormal basis. Mathematically, for the 1-D periodic case, they are expressed as

$$\mathbf{e}^{(1)}_{n,\mathrm{TM}} = \mathbf{e}^{(2)}_{n,\mathrm{TM}} = \frac{1}{\sqrt{p}} \mathrm{e}^{-\mathrm{j}k_n y}\hat{\mathbf{y}} \qquad \text{TM incidence} \tag{2.1}$$

$$\mathbf{e}^{(1)}_{n,\mathrm{TE}} = \mathbf{e}^{(2)}_{n,\mathrm{TE}} = \frac{1}{\sqrt{p}} \mathrm{e}^{-\mathrm{j}k_n y}\hat{\mathbf{x}} \qquad \text{TE incidence} \tag{2.2}$$

with $n \in \mathbb{Z}$. The cutoff wavenumber of a nth-order harmonic is given by the following expression,

$$k^{(1)}_n = k^{(2)}_n = k_n = \frac{2n\pi}{p} + k_\mathrm{t} \qquad n \in \mathbb{Z} \tag{2.3}$$

with k_t being the transverse component of the incident wavevector,

$$k_\mathrm{t} = (\varepsilon^{(1)}_\mathrm{r})^{1/2} \omega \sqrt{\varepsilon_0 \mu_0}\, \sin(\theta)\,. \tag{2.4}$$

As it was mentioned in the previous chapter, the incidence plane is always taken as the YZ-plane. In consequence, $\mathbf{k}_\mathrm{t}$ is directed along the y-direction in all cases.

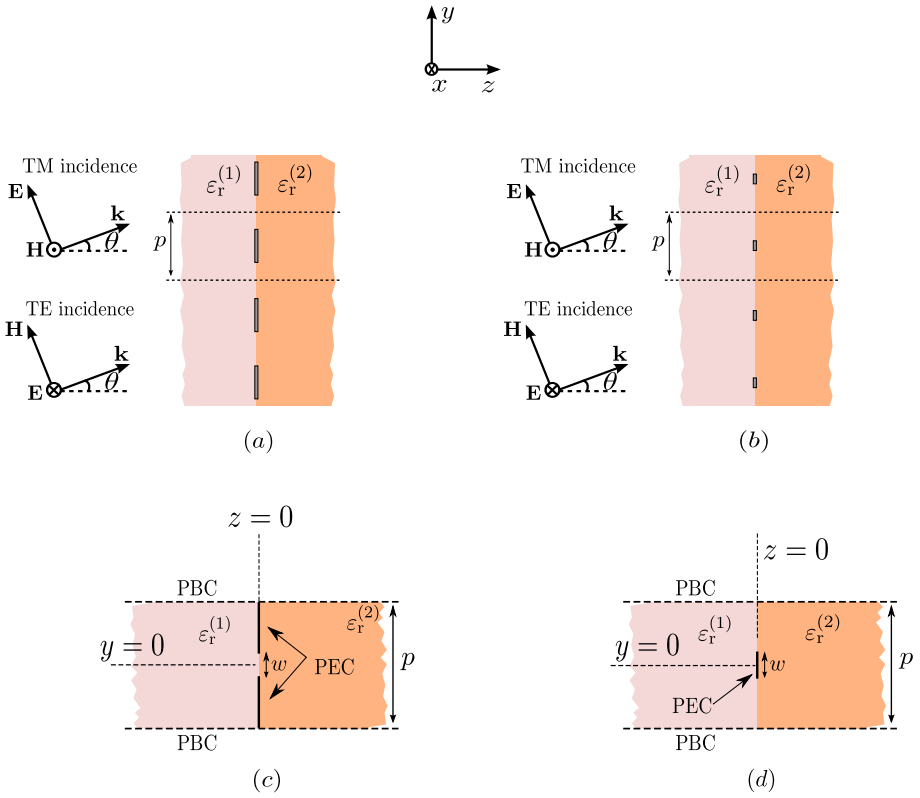

Figure 2.2: (a): slit-like grating. (b): strip-like grating. (c): unit cell corresponding to the grating in (a). (d): unit cell corresponding to the grating in (b).

2.2.1 1-D slit-like grating. Electric-field profile function

Let us begin by proposing an appropiate profile function for the electric field at the slit aperture. It is desirable that the function takes into account the edge behaviour of the field in the proximity of the strip edges. As is well known [31] the electric-field component parallel to the periodicity direction and perpendicular to the strip edge diverges as it approaches the border of the strip. On the contrary, electric-field components parallel to the strip edge tends to zero as they approach the edge of the strip.

Assuming first TM incidence, an appropiate function representing the field distribution would be:

$$\mathbf{f}(y) = \frac{2}{\pi}\frac{1}{\sqrt{1-(2y/w)^2}}\,\hat{\mathbf{y}} \qquad -w/2 < y < w/2 \tag{2.5}$$

with w being the slit width. The projection of a nth-order harmonic over the profile $\mathbf{f}(y)$ coincide with the nth-order Fourier transform due to the mathematical expression of the harmonics. Then, we have

$$\tilde{f}_n^{(1)} = \tilde{f}_n^{(2)} = \tilde{f}_n = \frac{2}{w\pi}\int_{-w/2}^{w/2} \frac{1}{\sqrt{1-(2y/w)^2}} \mathrm{e}^{-\mathrm{j}k_n y}\mathrm{d}y = J_0\big(k_n w/2\big) \tag{2.6}$$

so that the expression for the nth-order transformer is in this case

$$\frac{\tilde{f}_n}{\tilde{f}_0} = \frac{J_0\big(k_n w/2\big)}{J_0\big(k_\mathrm{t} w/2\big)}\,. \tag{2.7}$$

where $J_0(\cdot)$ is the zeroth-order Bessel function of the first kind. The parameter k_t plays here the role of the lowest-order cutoff wavenumber, obtained for $n = 0$ in (2.3).

For the case of TE incidence, the electric field component tends to zero as it approaches the edges of the strip. An appropiate profile in this case is

$$\mathbf{f}(y) = \frac{4}{\pi}\sqrt{1-(2y/w)^2}\,\hat{\mathbf{x}} \tag{2.8}$$

whose nth Fourier transform is expressed as

$$\tilde{f}_n = 2\frac{J_1\big(k_n w/2\big)}{k_n w/2} \tag{2.9}$$

with $J_1(\cdot)$ being the first-order Bessel function of the first kind. For this case the expression of the transformers is finally written as follows:

$$\frac{\tilde{f}_n}{\tilde{f}_0} = \frac{J_1\big(k_n w/2\big)}{J_1(k_\mathrm{t} w/2)}\frac{k_\mathrm{t}}{k_n} \tag{2.10}$$

Some other profile functions for reproducing the electric field at the slit aperture can be considered. For instance a constant aperture field could be used for TM incidence. However, this choice is expected to be less accurate because the edge singularities are not properly taken into account. The transformers would be given by

$$\frac{\tilde{f}_n}{\tilde{f}_0} = \frac{\mathrm{sinc}\big(k_n w/2\big)}{\mathrm{sinc}\big(k_\mathrm{t} w/2\big)}\,, \tag{2.11}$$

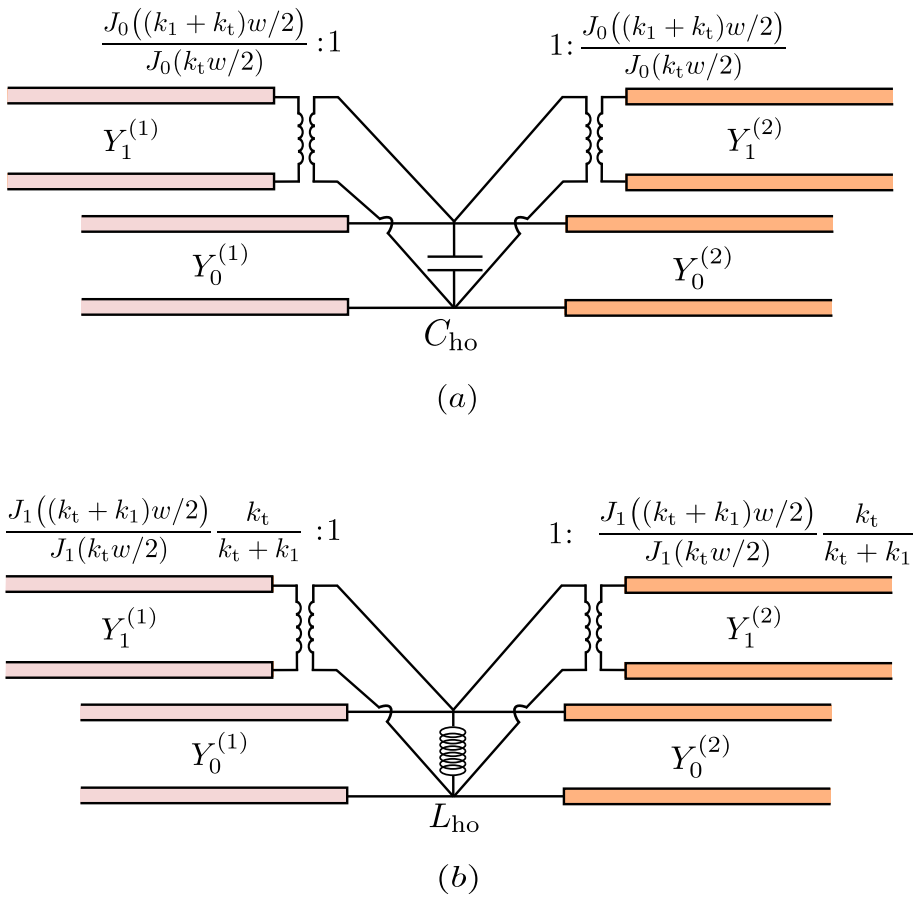

Figure 2.3: Equivalent circuit for slit gratings. (a): TM incidence using the profile function in (2.5). (b): TE incidence using the profile function in (2.8). Both circuits take the harmonic $n = 1$ as a low-order harmonic. The rest of the harmonics are all included in the lumped element.

where $\mathrm{sinc}(\cdot) = \frac{\sin(\cdot)}{(\cdot)}$ is the cardinal sine which corresponds to the Fourier transform of a rectangular function. This constant aperture field is not adequate to represent the electric field profile at the slit under TE incidence. The boundary conditions at the discontinuity force the electric field to become zero at the borders of the strip. The constant profile does not satisfy this condition and it could cause some numerical problems in the convergence of the series involved in the expressions of the circuit elements.

The choice of the electric-field profile functions given in (2.7) and (2.10) causes the equivalent circuits in Fig. 1.5 and Fig. 1.6 to become those in Fig. 2.3.

Note that the nth-order Fourier transforms of the profile function are real-valued, so that the turns ratio of the nth-order transformers become real quantities. Additionally the transformer associated to the zeroth-order harmonic in the region (2) disappears due to $\tilde{f}_0^{(1)} = \tilde{f}_0^{(2)} = \tilde{f}_0 \quad \Rightarrow \quad \dfrac{\tilde{f}_0^{(2)}}{\tilde{f}_0^{(1)}} = 1$.

2.2.2 1-D strip-like grating. Surface-current profile function

In order to determine an appropiate surface current profile needed for the strip-like case, it is also convenient to take into account the edge behaviour of the current at the border of the strip. A current component perpendicular to the strip edges becomes zero as it approaches the edge of the strips. On the contrary, a current component parallel to the strip edges shows a divengent behaviour at the edges. It suggests us to model the surface current for TE and TM incidence at the strip in terms of the functions already used in the slit case, but interchanged with respect to the polarization:

$$\mathbf{f}(y) = \frac{4}{\pi}\sqrt{1-(2y/w)^2}\,\hat{\mathbf{y}} \qquad \text{TM incidence} \tag{2.12}$$

$$\mathbf{f}(y) = \frac{2}{\pi}\frac{1}{\sqrt{1-(2y/w)^2}}\hat{\mathbf{x}} \qquad \text{TE incidence}\,. \tag{2.13}$$

Their corresponding nth Fourier transforms are thus

$$\tilde{f}_n = 2\frac{J_1\big(k_n w/2\big)}{k_n w/2} \qquad \text{TM incidence} \tag{2.14}$$

$$\tilde{f}_n = J_0\big(k_n w/2\big) \qquad \text{TE incidence}\,. \tag{2.15}$$

The constant profile could also be employed to model the surface current for the case of TE incidence. Note that for TM incidence the boundary conditions force the current to be null at the strip border. A constant profile does not fullfill this condition and the surface current would be discontinuous at the strip edge, which again leads to convergence problems. The equivalent circuit for both TM and TE incidence are sketched in Fig.2.4.

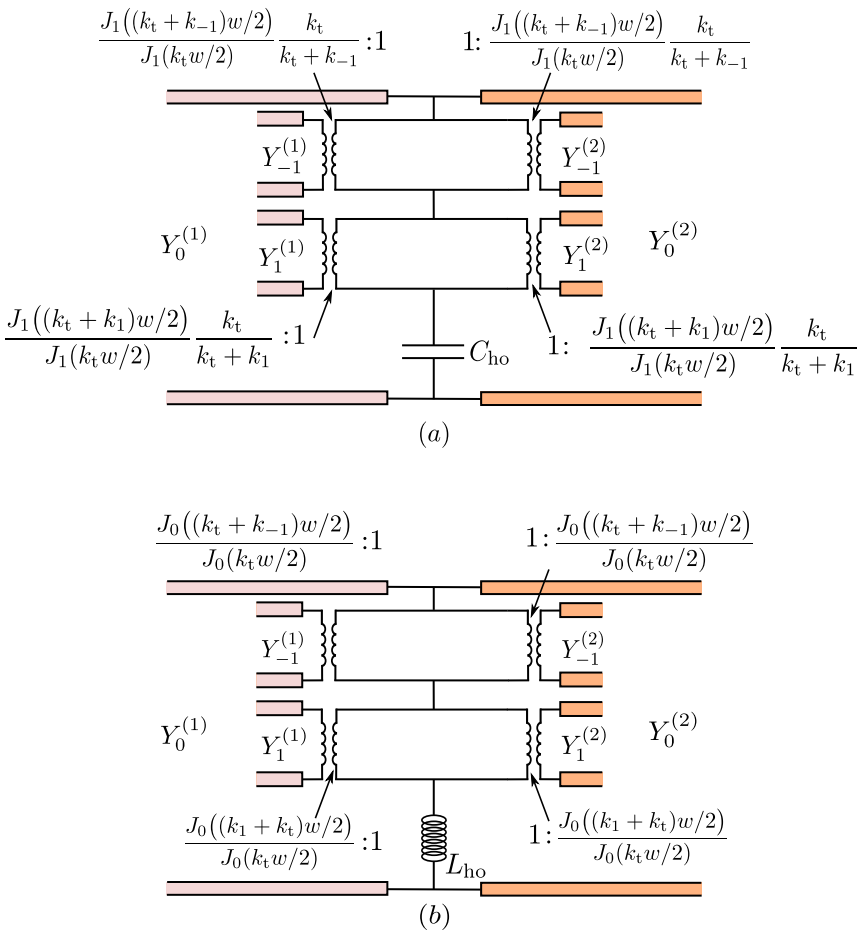

Figure 2.4: Equivalent circuit for strip gratings. (a): TM incidence using the profile function in (2.12). (b): Equivalent TE incidence using the profile function in (2.13). In both cases, the harmonics $n = 1, n = -1$ are considered low-order harmonics. The rest of the harmonics are included into the lumped element.

2.2.3 Dielectric slabs of finite thickness and grounded dielectric layers

Let us now extend the model to account for more complex structures involving dielectric layers. A schematic example is shown in Fig. 2.5, where the periodic array is embedded in stratified dielectric materials. The presence of finite-thickness dielectric slabs can readily be incorporated in our equivalent circuit, since the propagation of a plane wave through a stratified medium composed of

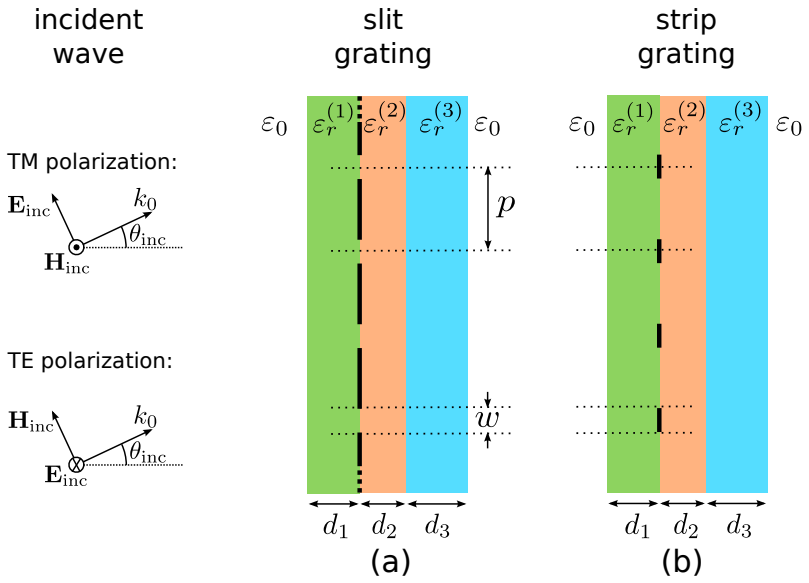

Figure 2.5: Schematic representation of the multilayer structure. TM and TE polarizations and oblique incidence of the impinging wave are considered. (a) Slit-like 1-D planar grating with an stratified medium. (b) Strip-like planar grating in the same stratified enviroment.

several dielectric layers admits a representation in terms of a cascade of transmission lines lengths. The presence of such a multilayer medium must be incorporated not only for the fundamental harmonic, but also for each harmonic taking part in the equivalent admittance, including high-order evanescent harmonics. Although the latter can be represented by a lumped capacitor or inductor, each single high-order harmonic is originally conceived in (1.27) and (1.57) as a transmission line with purely imaginary characteristic admittance, associated with evanescent fields that are mainly localized around the discontinuity. The original transmission-line representation associated with high-order harmonics allows us to proceed identically as in the case of low-order elements.

All of the above considerations necessarily demand for the modification of the expressions of the equivalent admittance and impedance in (1.27) and (1.57). According to standard transmission line theory, the admittances seen from the slit/strip discontinuity to the left and to the right are just the input admittances

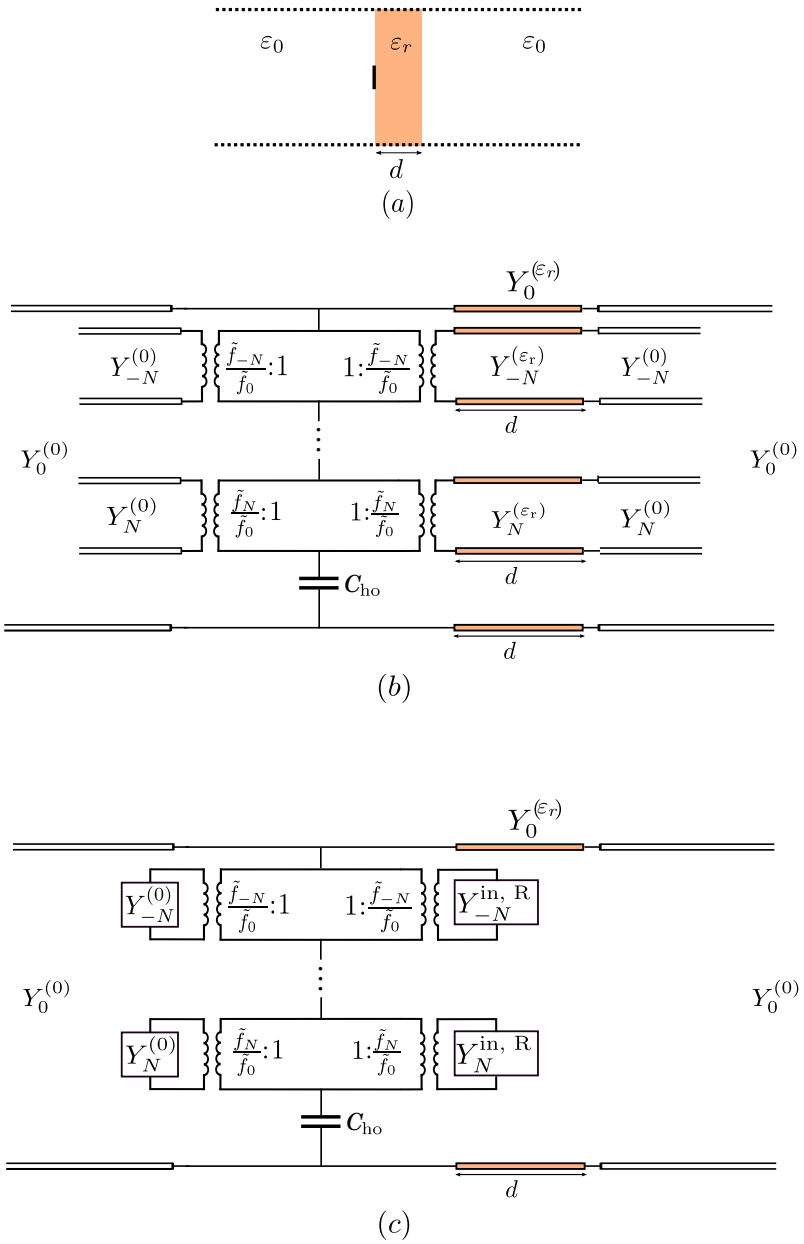

Figure 2.6: Equivalent network for a TM wave impinging obliquely from the left on a strip grating printed on a slab with relative permitivity ε_{r}. (a): Structure under analysis. (b): Equivalent network. The propagation of low-order harmonics through the dielectrics has been modelled by including the corresponding transmission line lengths. The capacitance C_{ho} is also affected by the presence of the stratified medium at the left side of the strip discontinuity. (c): The cascade of transmission lines can be replaced with its corresponding input admittance for each harmonic.

seen from the grating plane at both sides. Thus both expressions can be rewritten in this context as follows:

$$Y_{\text{eq}} = \sum_n{}' (Y_n^{\text{in, L}} + Y_n^{\text{in, R}}) \frac{\tilde{f}_n^2}{\tilde{f}_0^2} \qquad \text{Slit grating} \tag{2.16}$$

$$Z_{\text{eq}} = \sum_n{}' \frac{1}{Y_n^{\text{in, L}} + Y_n^{\text{in, R}}} \frac{\tilde{f}_n^2}{\tilde{f}_0^2} \qquad \text{Strip grating} \tag{2.17}$$

where $Y_n^{\text{in, L}}$ and $Y_n^{\text{in, R}}$ are the input admittances seen from the slit/strip discontinuity to the left and to the right, respectively.

As an example we will consider the case of a TM-polarized plane wave impinging on a strip grating. The grating is printed on a dielectric substrate of thickness d and relative permitivity ε_{r}, as shown in Fig. 2.6(a). The corresponding equivalent circuit has also been depicted in Fig. 2.6(b) and Fig. 2.6(c). Note that low-order elements incorporate the corresponding length of transmission line associated with the propagation of their corresponding harmonics through the different dielectric layers. In consequence, the nth input admittance to the right side from the discontinuity $Y_n^{\text{in, R}}$ can be written as

$$Y_n^{\text{in, R}} = Y_n^{(\varepsilon_{\text{r}})} \frac{Y_n^{(0)} + \text{j} Y_n^{(\varepsilon_{\text{r}})} \tan(\beta_n^{(\varepsilon_{\text{r}})} d)}{Y_n^{(\varepsilon_{\text{r}})} + \text{j} Y_n^{(0)} \tan(\beta_n^{(\varepsilon_{\text{r}})} d)} \tag{2.18}$$

according to transmission line theory. At the left side of the strip discontinuity there is only free-space, so that the corresponding nth input admittance $Y_n^{\text{in, L}}$ coincides with the nth admittance of the harmonic in this medium, $Y_n^{(0)}$.

For the case of high-order harmonics, the general expression in (2.18) (same for high- and low-order elements) can be simplified by introducing the approximation in (1.29) into the modal admittance expressions. This leads to the following expression for the global high-order capacitance:

$$\frac{1}{C_{\text{ho}}} = \frac{2}{\varepsilon_0 \tilde{f}_0^2} \sum_{n=N+1}^{\infty} \tilde{f}_n^2 \, k_n \left[1 + \varepsilon_{\text{r}} \frac{1 + \varepsilon_{\text{r}} \tanh(k_n d)}{\varepsilon_{\text{r}} + \tanh(k_n d)} \right]^{-1} \tag{2.19}$$

where the second member of the right-hand side of the equation indicates that the high-order capacitance is also affected by the presence of the multilayer. If the dielectric slab is thick enough, $\tanh(k_n d) \approx 1$.

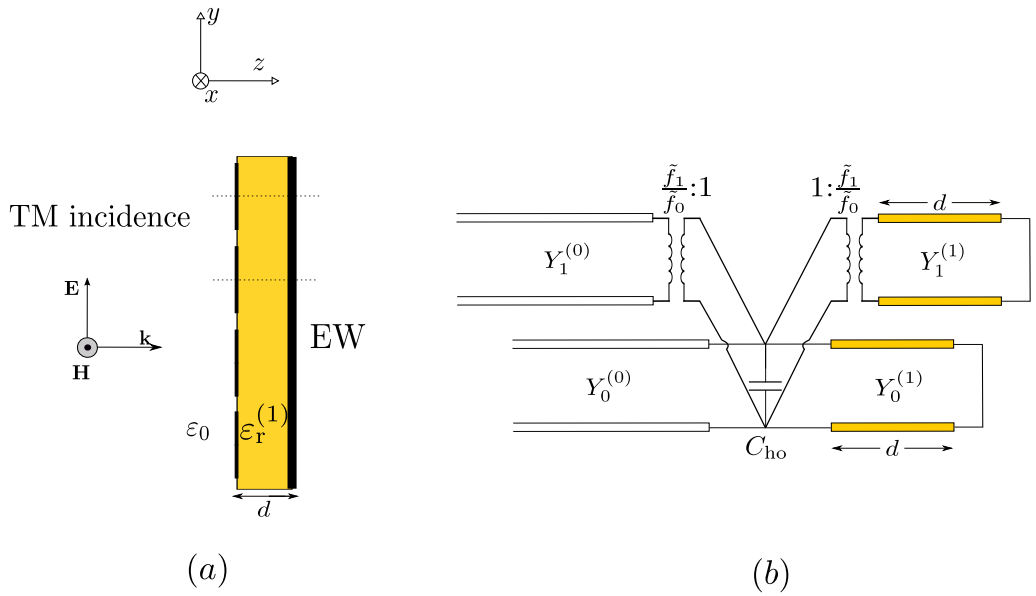

Figure 2.7: (a): Structure formed by a slit grating printed grounded dielectric slab of ε_1 embedded in vacuum. TM normal incidence is impinging on the structure. (b): Equivalent circuit considering $N = 1$ low-order harmonic. The transmission lines are of length d are short-terminated. The lumped element C_{ho} also is also affected by the presence of the electric wall.

Note that this result could also be extended to structures having a grounded dielectric slab. In that case, the corresponding transmission line section associated with the propagation of each harmonic through the grounded dielectric layer is then terminated with a short-circuit. In Fig. 2.7(a) an example is shown considering a slit grating printed on a grounded dielectric slab. The equivalent circuit, depicted in Fig. 2.7(b) has been considered to include the $N = 1$ low-order elements. The expression of the nth-order input admittance to the right side of the discontinuity is obtained by translating the short-circuit through its corresponding transmission-line section, namely

$$Y_n^{\text{in, R}} = -\text{j}Y_n^{(1)} \cot(\beta_n^{(1)} d)\,. \tag{2.20}$$

At the left side of the discontinuity the nth input admittance coincides with the nth-order admittance of the wave in vacuum,

$$Y_n^{\text{in, L}} = Y_n^{(0)}\,. \tag{2.21}$$

These expressions for the input admittances at each side are applied for both low- and high-order elements. After introducing (1.29), the contribution of all high-order elements (at both sides of the discontinuity) is given by

$$Y_{\mathrm{ho}} = \mathrm{j}\omega C_{\mathrm{ho}} = \mathrm{j}\omega \frac{2\varepsilon_0}{\tilde{f}_0^2} \sum_{n=N+1}^{\infty} \frac{\tilde{f}_n^2}{k_n} \left[1 + \varepsilon_{\mathrm{r}}^{(1)} \coth(k_n d)\right] \tag{2.22}$$

where the influence of the ground plane on the equivalent capacitance is given by the $\coth(\cdot)$ function. Note that for thick dielectrics $\coth(k_n d) \to 1$, indicating that the reactive field around the slit aperture does not reach the electric wall, and therefore the high-order capacitor can be calculated assuming two semi-infinite dielectric slabs.

2.3 Numerical results and discussion

The proposed analytical model has been developed on the basis of a certain number of assumptions concerning the width of slits (or strips) and the field distribution (current distribution) on those slits (strips). Moreover, some decisions have to be considered before generating numerical results concerning the number of TE/TM harmonics of relatively low order that must be explicitly retained in the formulation (the remaining infinite higher order harmonics are accounted for by the lumped elements). Although these issues have been treated in detail in [65], the main difference between the model reported in [65] and the model derived here lies in the development of a fully analytical circuit-like model (the lumped parameters in [65] were extracted from a numerical calculation for a single frequency point). Here we have provided analytical formulas for all the relevant parameters, and it is necessary to check the accuracy of such formulas. However the physical considerations about the number of modes that have to be retained to account for the (possibly) complex frequency-dependent behaviour of the fields at the dicontinuity are exactly the same as in [65]. The criterion here (it was also mentioned in the previous chapter) is to retain all the

TE/TM harmonics that operate above cutoff plus the first evanescent higher order mode. Since the cutoff frequencies of the TE/TM harmonics are known in advance, this task can readily be implemented in a computer code. For comparison purposes, a method of moments (MoM) in the spectral domain has been applied to solve the electric-field/surface-current integral equations for the slit/strip arrays. A sufficient number of entire domain basis functions that include the edge behavior have been employed to ensure high accuracy and fast convergence. The MoM data will then be considered as virtually "exact".

In order to have a global idea about the performance of the model, a first structure under study is shown in Fig. 2.8(a), which consists of a strip grating printed on a grounded dielectric slab illuminated by a normally-incident TE polarized wave. Our aim is to show the importance of selecting an appropiate number of low-order elements to obtain accurate results. Traditionally this kind of structures are dealt with in an approximate manner by using a lumped inductor to account for the reactive field around the discontinuity and a transmission line section terminated in short circuit to represent the grounded dielectric slab. Note that inside the dielectric slab, this simplified model accounts for the propagation of the TEM harmonic only, but it does not consider the influence of the ground plane on the lumped element. Thus this representation ignores the possibility of high-order mode interaction of the grating with the ground plane. Under this assumption, the model is expected to work properly if there are not higher-order progagative harmonics inside an electrically thick slab or the value of w is extremely small. Significant differences can be found between such a simple analytical model and exact numerical calculations if the frequency of operation is close or higher than the cutoff frequency of the first high-order harmonic inside the dielectric slab. Certainly this effect cannot be taken into account by simple quasi-static models. If we make $N = 0$ in our formulation, our model reduces to a quasi-static model similar to the aforementioned simpler approach. Actually, with $N = 0$ in our formulation we still keep the influence of the ground plane on the *quasi-static* inductance characterizing the discontinuity. However this quasi-static model does not account for the

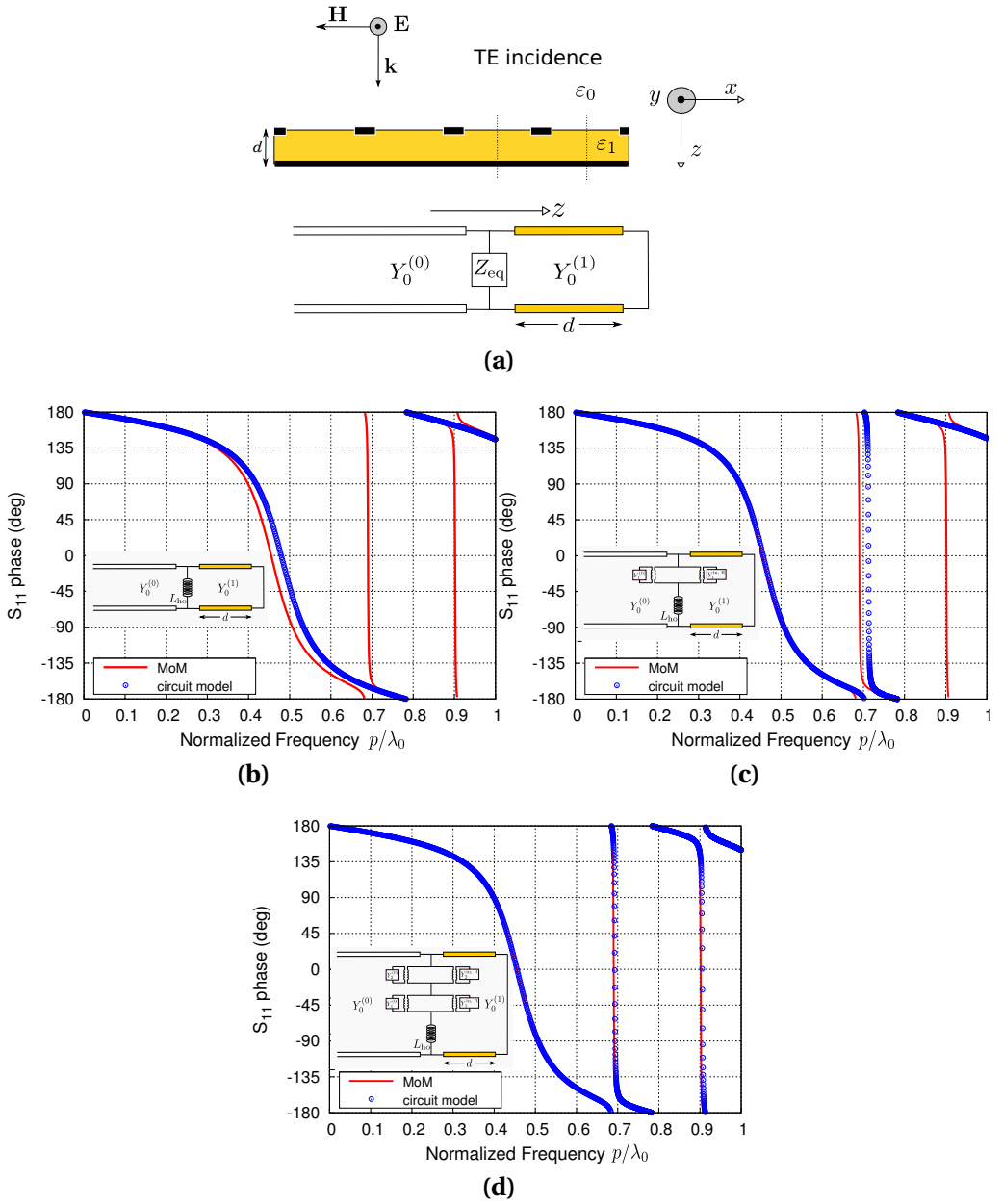

Figure 2.8: (a). Structure under analysis together with the equivalent circuit showing a general shunt impedance $Z_{\rm eq}$. The rest of graphs shows the phase of the reflection coefficient. Structure parameters: $w = 0.1p$, $\varepsilon_{\rm r} = 10.2$, $d = 0.2p$. (b): $N = 0$. (c): $N = 1$. (d): $N = 2$.

coupling through propagative harmonics at higher frequencies. To clarify this point we show in Figs. 2.8(b) – (d) the reflection coefficient versus the normalized frequency in terms of p/λ_0, with λ_0 being the wavelength in vacuum. The number of low-order modes, N, is different in each plot. Since the amplitude of the reflection coefficient is unity due to the presence of the ground plane, we plot the phase of the reflection coefficient. Although the quasi-static ($N = 0$) model gives accurate results up to $p/\lambda_0 = 0.3$, noticeable differences can be appreciated above that frequency. Indeed, the results provided by the quasi-static model are qualitatively incorrect for $p/\lambda_0 > 0.6$. If $N = 2$ ($N = 2$ indicates that we are taking as low-order harmonics those with $n = 1, -1$ and $n = 2, -2$; for normal incidence, pairs of harmonics with opposite sign form a single mode), the analytical model perfectly captures the details of the phase behaviour up to the frequency of the onset of the first grating lobe. The model is still valid above that frequency but, in such a case, the magnitude of the specular reflection coefficient is not unity.

A second study concerning the accuracy of the model in terms of the profile function is presented in Fig. 2.9(a) which shows the transmission coefficient versus the normalized frequency, p/λ_0, for a slit grating under TM incidence. The transmission coefficient for TE incidence on a strip grating is shown in Fig. 2.9(b). Two profile functions have been considered: the edge singular profile in (2.5) and the constant profile function whose Fourier transform is given by (2.11). Results obtained with the MoM and with both profiles are included in each plot in order to check the accuracy of the model for different profile functions. In general, the model is less accurate when using the constant profile. The deviations of the results given by such a profile with respect to the 'exact' MoM results becomes clearer as the slit/strip width increases. The reason lies in the better description of the edge behaviour of the field/current given by the edge-singular profile. However the use of this function also has some limitations due to the frequency-dependence of the field/current distribution at the slit/strip for higher frequencies. These limitations will be studied in detail in next section. It is worth noting that the transmission/reflection spectra obtained for

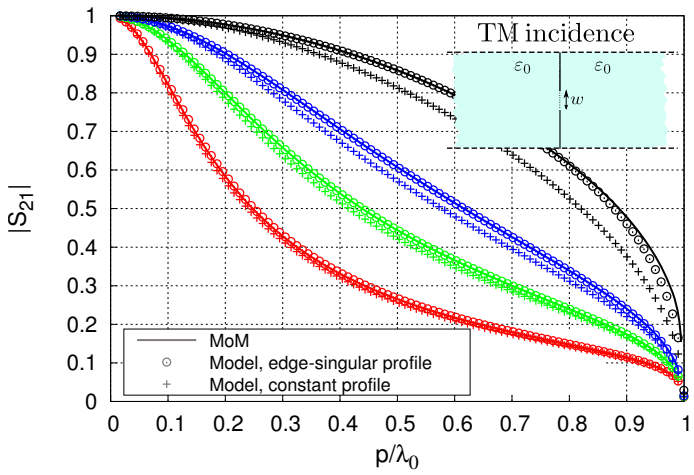

(a)

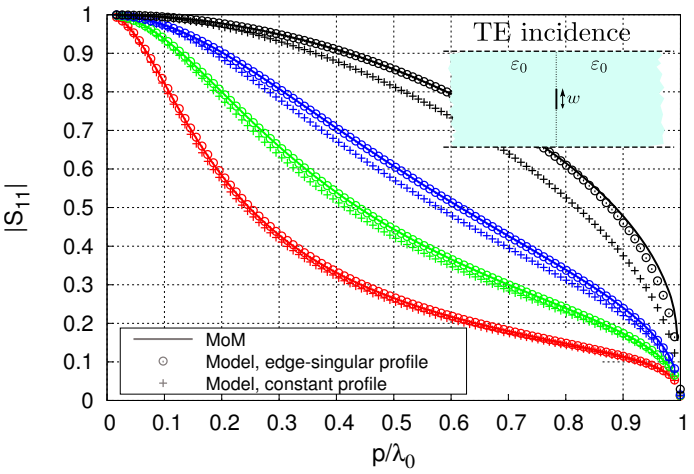

(b)

Figure 2.9: Transmission/reflection coefficient versus normalized frequency. (a): Slit grating in vacuum under normal TM incidence. (b): describes the reflection coefficient obtained under TE incidence for strip gratings. Line and points in red denote $w = 0.02p$, line and points in green denote $w = 0.1p$, line and points in blue denote $w = 0.2p$ and line and points in black denote $w = 0.4p$.

TM/TE incidence coincide for cases having the same slit/strip size. This is a direct consequence of Babinet's principle [43, 44].

A third example is analyzed in Fig.2.10 which shows, for different incidence angles, the phase of the reflection coefficient versus the normalized frequency

for strip/slit gratings printed on a grounded dielectric slab with the structures parameters defined in the caption of the figure. The MoM numerical results are also shown, and the comparison with the analytical results shows an excellent agreement for all the cases. It is well known that, as frequency increases, these structures present a near-zero phase for the reflection coefficient (namely artificial magnetic conductor behaviour) in a given frequency range. In the normal incidence case considered in Fig.2.10(b), this behaviour occurs around $p/\lambda_0 \approx 0.52$ for the strip grating under TE illumination. This behaviour remains basically the same for the oblique incidence results shown in Fig.2.10(c) – Fig.2.10(d). For the high-frequency portion of the spectrum, the phase exhibits a faster and more complicated variation with frequency, specially for oblique incidence.

As a last example and in order to obtain a global idea about the performance of the model, we have included in Fig.2.11 several illustrative color maps. These maps show the magnitude of the transmission coefficient for the configuration depicted in Fig.2.11(a) as a function of the normalized frequency p/λ_0 and the angle of incidence. The left plot in Fig.2.11(b) has been generated with the analytical model described in this chapter corresponding to a TM wave incidence on a grating of narrow slits sandwiched between two different slightly lossy dielectric slabs. The numerically generated results (MoM) have been plotted in the right plot of Fig.2.11(b). We can observe that both plots are almost identical. The drawn spectra are very complex for frequencies beyond $p/\lambda_0 > 0.4$ due to the presence of the dielectric slabs. Note that one of the dielectric slabs has a high permitivity, which implies it supports propagative high-order harmonics favoring the appearance of complex spectra. It is worth mentioning that due to the analytical nature of the model, all the results were generated in a few seconds. Similar plots for TE illuminated slit-like planar metal grating are shown in Fig.2.11(c). A wider slit is considered here in order to enhance the high transmission frequency regions. Once again the agreement between the numerical results and the analytical data is very good. Specifically, in these figures a narrow high transmission peak in the frequency range going from $p/\lambda_0 \approx 0.47$ to

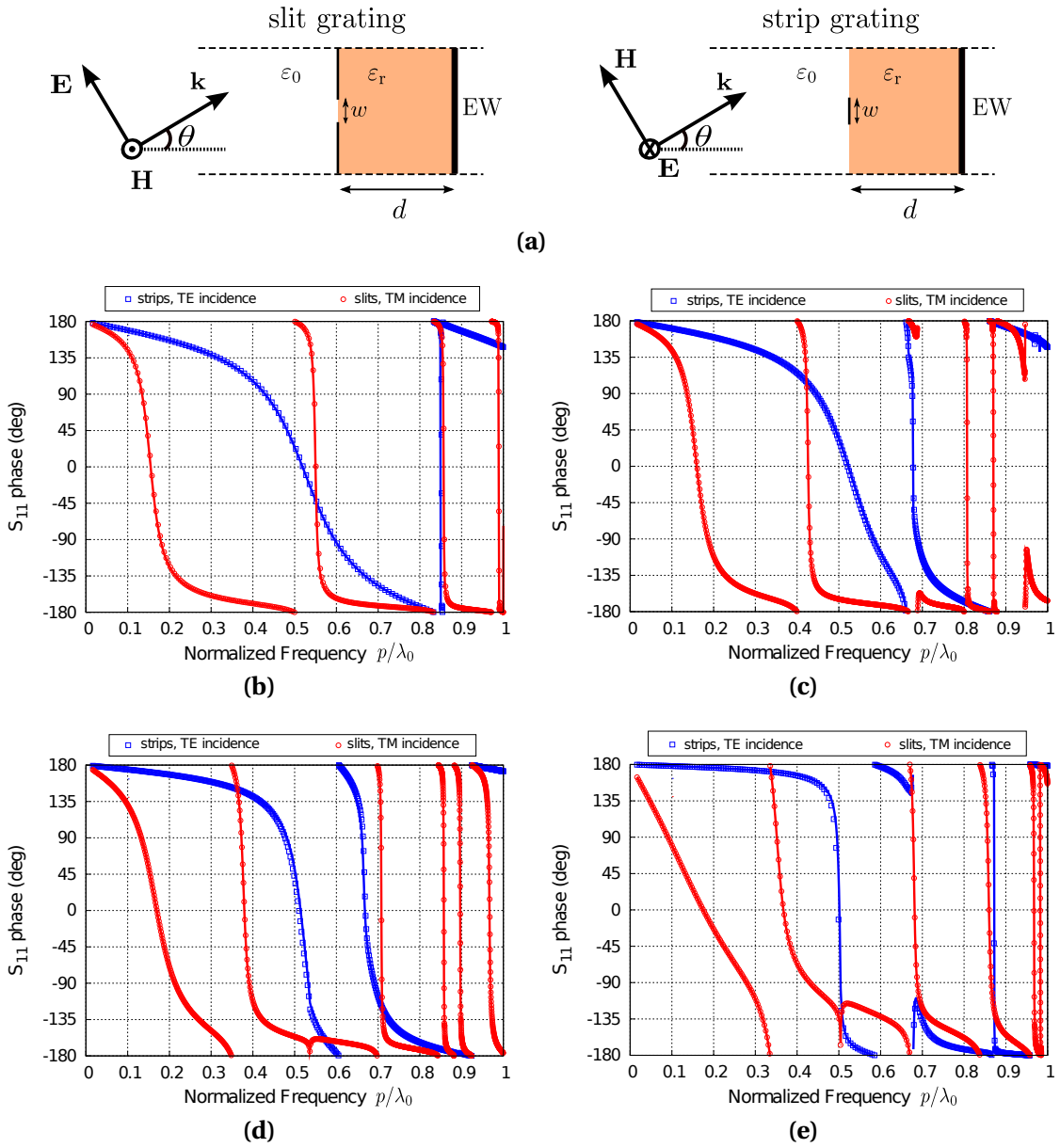

Figure 2.10: . Phase of the reflection coefficient for a strip grating under TE incidence and a slit grating under TM incidence, both printed on a grounded dielectric slab (a). Solid lines: results provided by a MoM numerical code. Circles and squares: results obtained with our circuit model. Structure parameters: $w = 0.1p$, $d = 0.3p$, $\varepsilon_r = 4$. (b) Incidence angle $\theta = 0^o$. (c) Incidence angle $\theta = 30^o$, (d) Incidence angle $\theta = 60^o$. (e) Incidence angle $\theta = 80^o$.

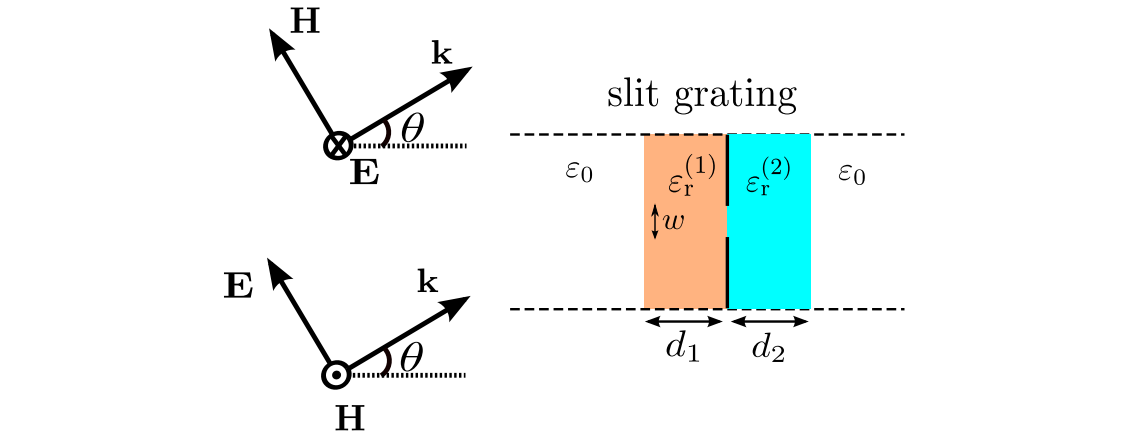

(a)

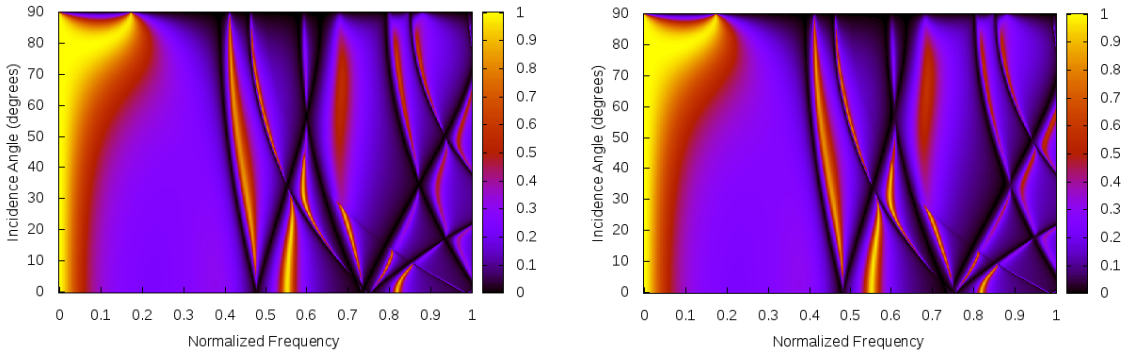

(b)

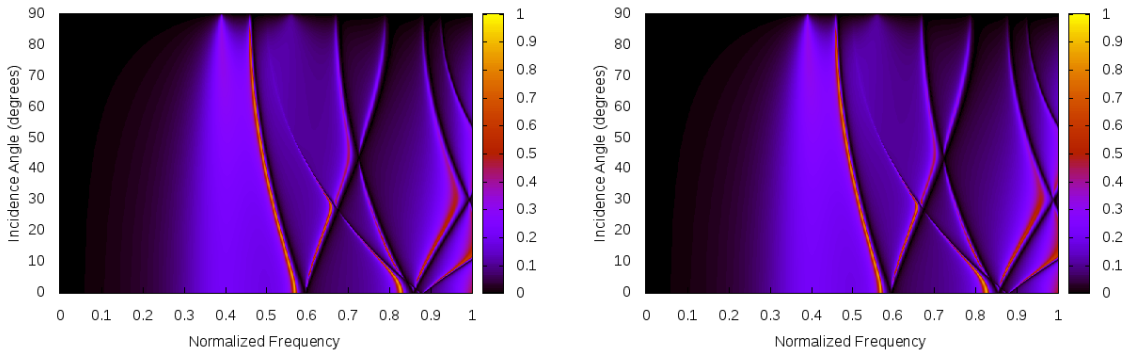

(c)

Figure 2.11: (a) Structure under analysis. (b) Magnitude of the transmission coefficient under TM incidence for a slit grating $w = 0.1p$. (c) Magnitude of the transmission coefficient under TE incidence for a slit grating $w = 0.2p$. They both are embedded between two dielectric layers with $\varepsilon_{\mathrm{r}}^{(1)} = 2.2$ and $\varepsilon_{\mathrm{r}}^{(2)} = 10.2$, and $d_1 = 0.4p$ and $d_2 = 0.2p$. Both dielectric layers are lossy with $\tan(\delta) = 0.001$. Left plot shows the results obtained with the circuit model and right plots show MoM results. Normalized frequency is p/λ_0 being λ_0 the wavelength in vacuum.

$p/\lambda_0 \approx 0.6$ can be clearly appreciated. Right after this peak, a transmission zero appears (Fano-like resonances). This is the so-called anomalous extraordinary transmission [150]. For this polarization and grating geometry, low transmission regions rather than transmission peaks should be expected in the absense of electrically thick dielectric layer. It is the presence of dielectric slabs what introduces the possibility of having transmission peaks.

2.4 Range of application of the equivalent circuits.

Although the accuracy shown by the equivalent circuits in the previous examples is actually good, the obtaining of the model is based on the assumption of a specific frequency-independent spatial profile. This assumption can be appropiate for wavelengths much larger than the slit/strip widths. When the working wavelength is similar to the slit/strip width, the dependence of the field/current distribution with frequency should not be ignored and, consequently, the precision of the equivalent circuit deteriorates. Also, the chosen profile functions are symmetric with respect to the horizontal middle plane of the slit/strip. Rigorously speaking, the electric field/current at the slit/strip discontinuity is symmetric under normal incidence. However this symmetry breaks down for oblique incidence so that the use of a symmetric function to reproduce the field/current profile at the discontinuity is expected to be less accurate for oblique incidence.

The aim here is to investigate the limits of validity of the equivalent circuit in terms of the slit/strip size. For that purpose, we will represent below the transmission coefficient of slit/strip arrays surrounded by a homogeneus media or embedded by stratified dielectric media. In all cases we will compare with results from a MoM code, considered "exact". After exploring several results, a generalized criterion for the range of application of the equivalent circuit of a given structure under a particular incident polarization will be established.

2.4.1 Validity of the equivalent circuit for TM incidence.

We will begin with the case of TM incidence on slit gratings. In Fig. 2.12 the transmission coefficient of two different structures is plotted versus normalized frequency for normal incidence. For the structure depicted in the left of Fig.2.12(a), which consists of a slit grating in vacuum, the normalized frequency is defined in terms of the wavelength in vacuum. The right picture in Fig.2.12(a) shows a slit grating in a stratified environment. Here, the normalized frequency is defined in terms of the wavelength in the highest permittivity medium. In fact, this last definition of normalized frequency is the general criterion (for vacuum, it reduces to the definition in the left pictures). We observe in Fig.2.12(b) that the results provided by the circuit model and by the MoM are in good agreement for frequencies up to $w/\lambda \approx 0.4$ in all cases. The left column of results in Fig. 2.12(b) show the transmission coefficient in vacuum for two different values of w. Beyond $w/\lambda_0 = 0.4$ the results obtained using both methods deviate slighly. This deviation is also appreciated in the right column plots (to a lesser degree), obtained for gratings embedded between two different dielectric layers. In these plots the differences between both results are significant beyond $w/\lambda \approx 0.5$ with λ the wavelength in the highest-permittivity medium, $\lambda = \lambda_0/(\varepsilon_{\mathrm{r}}^{(2)})^{1/2}$. It is worth mentioning that we have also checked that the additional dielectric layers with are not in contact with the array do not have a relevant effect on the validity limits found above.

Next, a similar study is carried out for TM normal incidence on strip gratings. The same structures as in Fig. 2.12 are taken into account, replacing the slit aperture with a metal strip as shown in Fig. 2.13(a). The transmission coefficient is again represented versus normalized frequency. For the strip array in vacuum, this normalized frequency is defined in terms of the wavelength in vacuum. However, for the grating in a multilayered environment we have now used the *effective* wavelength, λ_{eff}. The effective wavelength is calculated via the effective permittivity, which is the average of the permittivities of the dielectric

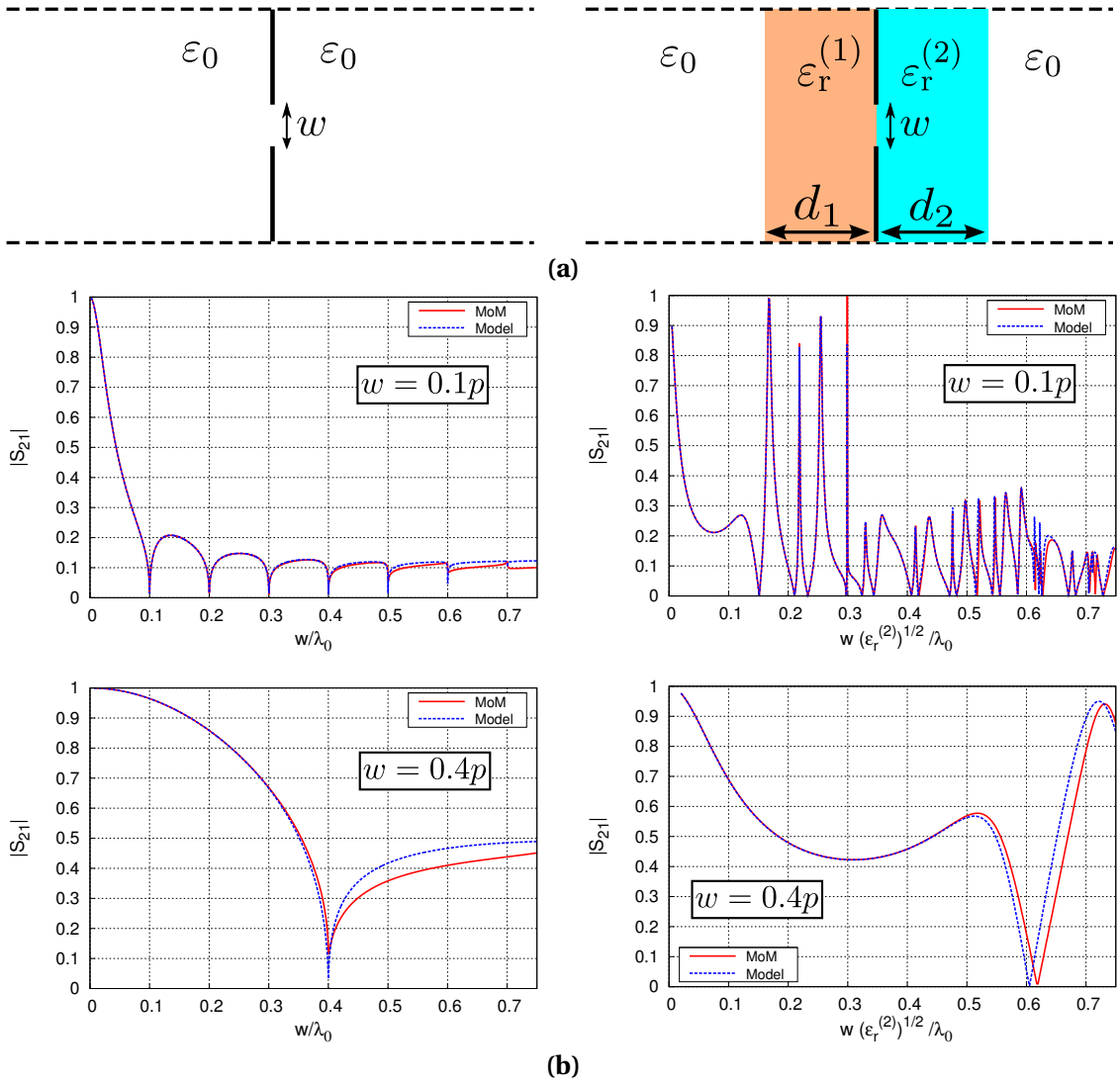

Figure 2.12: Transmission coefficient versus normalized frequency under TM normal incidence for two different values of w. (a): Two different structures are considered. The left picture represents the slit grating inmmersed in vacuum. For this case, the normalized frequency is defined in terms of the wavelength in vacuum. The rigth picture represents a slit grating in a multilayered structure, with $d_1 = d_2 = 0.2p$, $\varepsilon_r^{(1)} = 4$, $\varepsilon_r^{(2)} = 9$. The normalized frequency is obtained in terms of the wavelength in the highest-permittivity medium. (b): Transmission coefficient.

media at both sides of the strip array,

$$\varepsilon_{\text{eff}} = \frac{\varepsilon_{\text{r}}^{\text{L}} + \varepsilon_{\text{r}}^{\text{R}}}{2} \tag{2.23}$$

where the indexes L and R refer to the the materials at the left and at the right of the strip array. It is remarkable that the criterion to normalize the frequency for this case is different comparing to the slit-grating case. This criterion was taken after observing a large number of results involving strip gratings embedded in several layered environments under TM normal incidence, concluding that, the as we will check below, the model works properly for frequencies up to $w/\lambda_{\text{eff}} = 0.6 - 0.7$.

The transmission coefficients represented in the plots in Fig. 2.13(b) by the circuit model and the MoM code are in good agreement up to $w/\lambda_{\text{eff}} \approx 0.6 - 0.7$. This good agreement is even better for the layered structure. In this case, some differences start to be appreciated for $w/\lambda_{\text{eff}} \approx 0.7$, although the agreement between both results beyond 0.7 is still good. It is also worth remarking that the presence of additional dielectric media does not seem to modify the limit of validity.

According to the limit of validity deduced for both slit and strip gratings, it seems that the strip model is more accurate. To better illustrate this fact, Fig. 2.14 represents results provided by both the slit- and strip-grating for the same structure. A TM-polarized plane wave impinges normally on the structure depicted in Fig. 2.14(a). The corresponding transmission coefficient obtained from each equivalent circuit is plotted in Fig. 2.14(b)-(f) for different slit widths versus the normalized frequency p/λ_0. The slit model is accurate for slit widths much smaller than the period. On the other hand, the strip circuit shows a better accuracy for slit widths close to the period (small strip width). The most interesting result is, perhaps, that plotted in Fig. 2.14(d), where the slit (and the strip) occupies half unit cell. The figure confirms that the strip equivalent circuit is more accurate. In fact, the model for strip gratings provides accurate results for frequencies beyond $p/\lambda_0 = 0.8$ whereas the slit model starts to deviate for frequencies around $p/\lambda_0 = 0.4$. Some further discussions on the fact that for TM

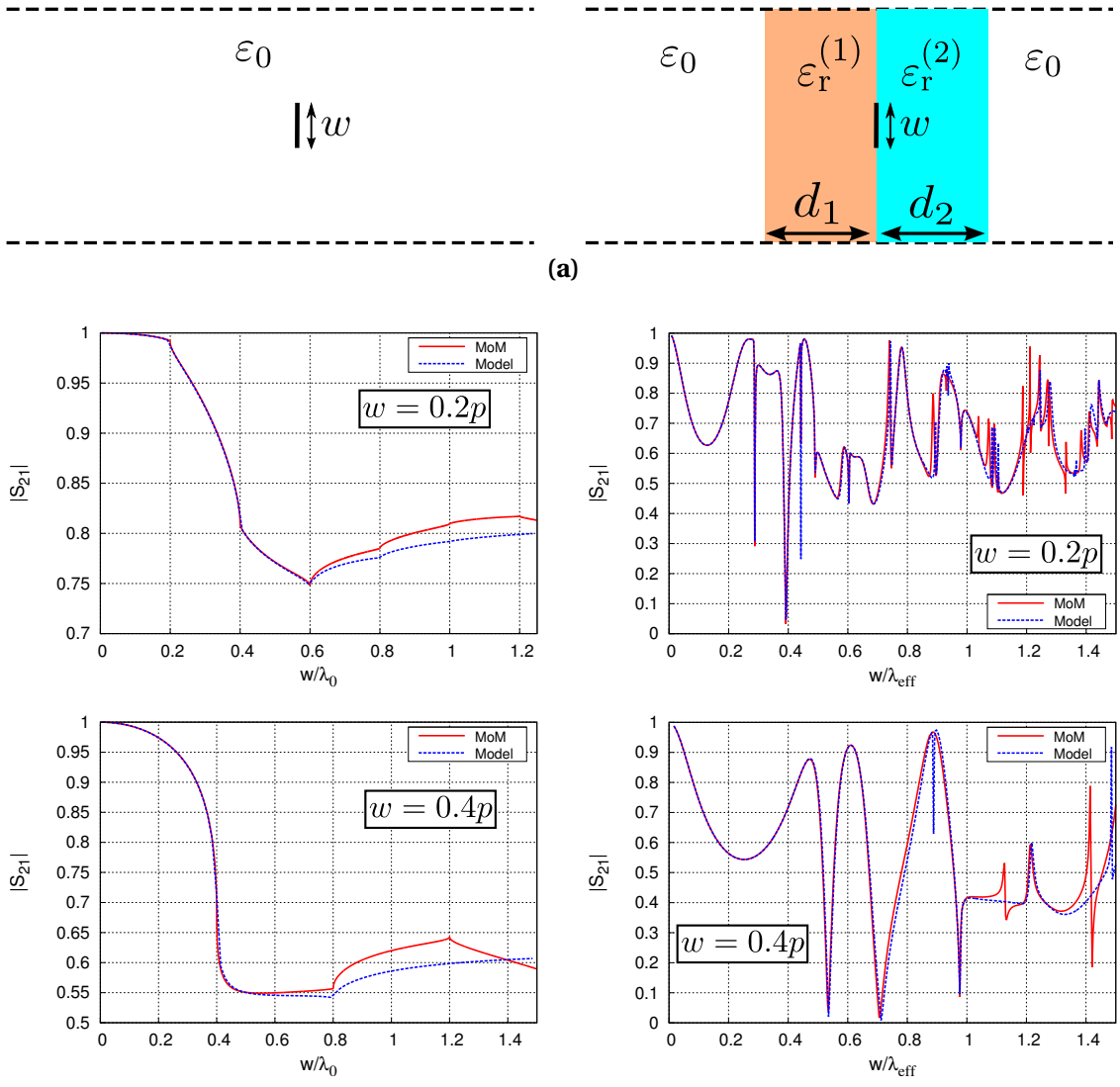

Figure 2.13: Same as Fig. 2.12 but for strip gratings. Now, the normalized frequency is defined in terms of an effective wavelength (see main text). (a): Structure under analysis. (b): Transmission coefficient.

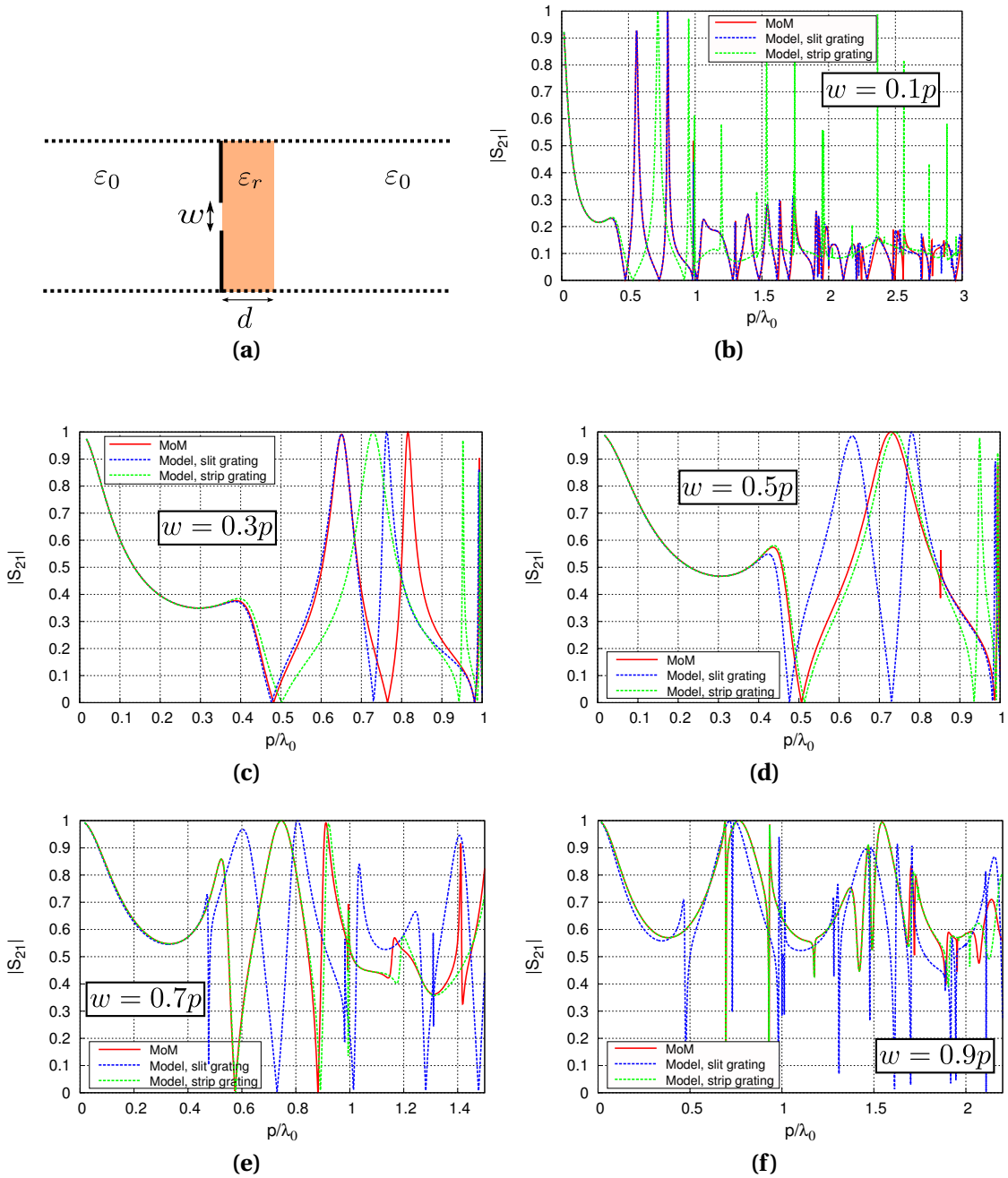

Figure 2.14: Comparison between the transmission coefficient obtained by using both the slit and the strip models for the structure in (a) under TM normal incidence. Relative permittivity of the dielectric slab is $\varepsilon_{\mathrm{r}} = 10.2$. The slit/strip widths are shown in the corresponding plots, (b)–(f).

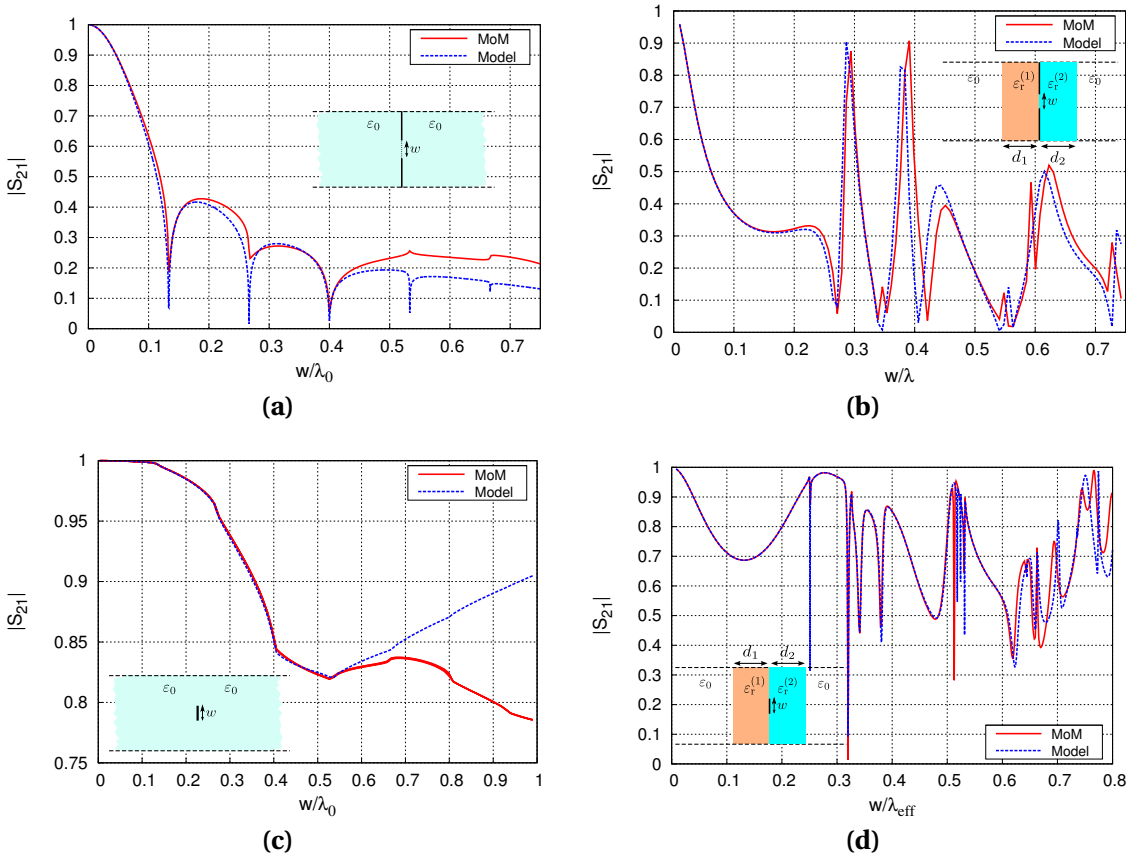

Figure 2.15: Oblique TM incidence with $\theta = 30^o$. (a): Slit grating in vacuum with $w = 0.2p$. (b): Slit grating in a multilayered structure with $w = 0.2p$, $d_1 = d_2 = 0.2p$, $\varepsilon_r^{(1)} = 4$, $\varepsilon_r^{(2)} = 9$ and $\lambda = \lambda_0/(\varepsilon_r^{(2)})^{1/2}$. (c): Same as (a) but for strip grating. (d): Same as (b) but for strip grating.

incidence the strip model has a wider range of application than the slit model will be given in section 2.4.3. It is also important to mention that the most accurate model in each example provides reliable results, at least, up to frequencies around $p/\lambda_0 \approx 0.8$.

Our final comparison study is for the case of TM-oblique incidence. Fig.2.15 shows some results for different structures including slit and strip gratings. We always consider $w = 0.2p$ and $\theta = 30^o$. As it was mentioned above, the degree of accuracy is expected to be less than for normal incidence due to the lack of symmetry of the field/current distributions. According to the results obtained

for the case of slit gratings under normal incidence, we deduced a limit of validity of $w/\lambda \approx 0.4$ in the worst case, where λ is the wavelength in the highest-permittivity medium forming the dielectric interface. For oblique incidence we observe that this limit is reduced to half its value. That is, the equivalent circuit can reliably reproduce results up to frequencies around $w/\lambda = 0.2$ but the deterioration is not dramatic before frequencies of about $w/\lambda \approx 0.4$. The equivalent circuit for strip gratings show a wider application range. We observe that the results are reliable at least for normalized frequencies w/λ_{eff} around $0.5 - 0.6$. This validity limit is slightly less than the limit found for normal incidence.

2.4.2 Validity of the equivalent circuit for TE incidence.

In general, the conclusions extracted for TM incidence can be applied here because the profile functions used are the same. That is, the equivalent circuit for TE incidence on slit (strip) gratings uses the same profile function as for TM incidence on strip (slit) gratings, and therefore the same degree of accuracy is expected.

In order to corroborate these predictions several results are shown in Fig.2.16 for slit gratings. From the plots showing results in vacuum (those at the left in Fig. 2.16), we can deduce the same limit of validity as for case of TM incidence on strip gratings, $w/\lambda_0 = 0.6$. For a slit grating printed at the interface of a multilayered structure under TE incidence, similar conclusions as for the case of TM incidence on strip arrays can be extracted.

Regarding TE incidence on strip gratings, two different structures are shown in Fig. 2.17. The left plots deal with the case of a strip grating in vaccum. The right plots show results obtained in a multilayered structure. From both plots we can obtain the same conclusions as in the case of TM incidence on slit gratings. The general limit of good accuracy in that case was found to be $w/\lambda \leq 0.4$, with λ being the wavelength in the highest-permittivity medium forming the interface where the grating is printed. For TE incidence on strip gratings such a limit also applies.

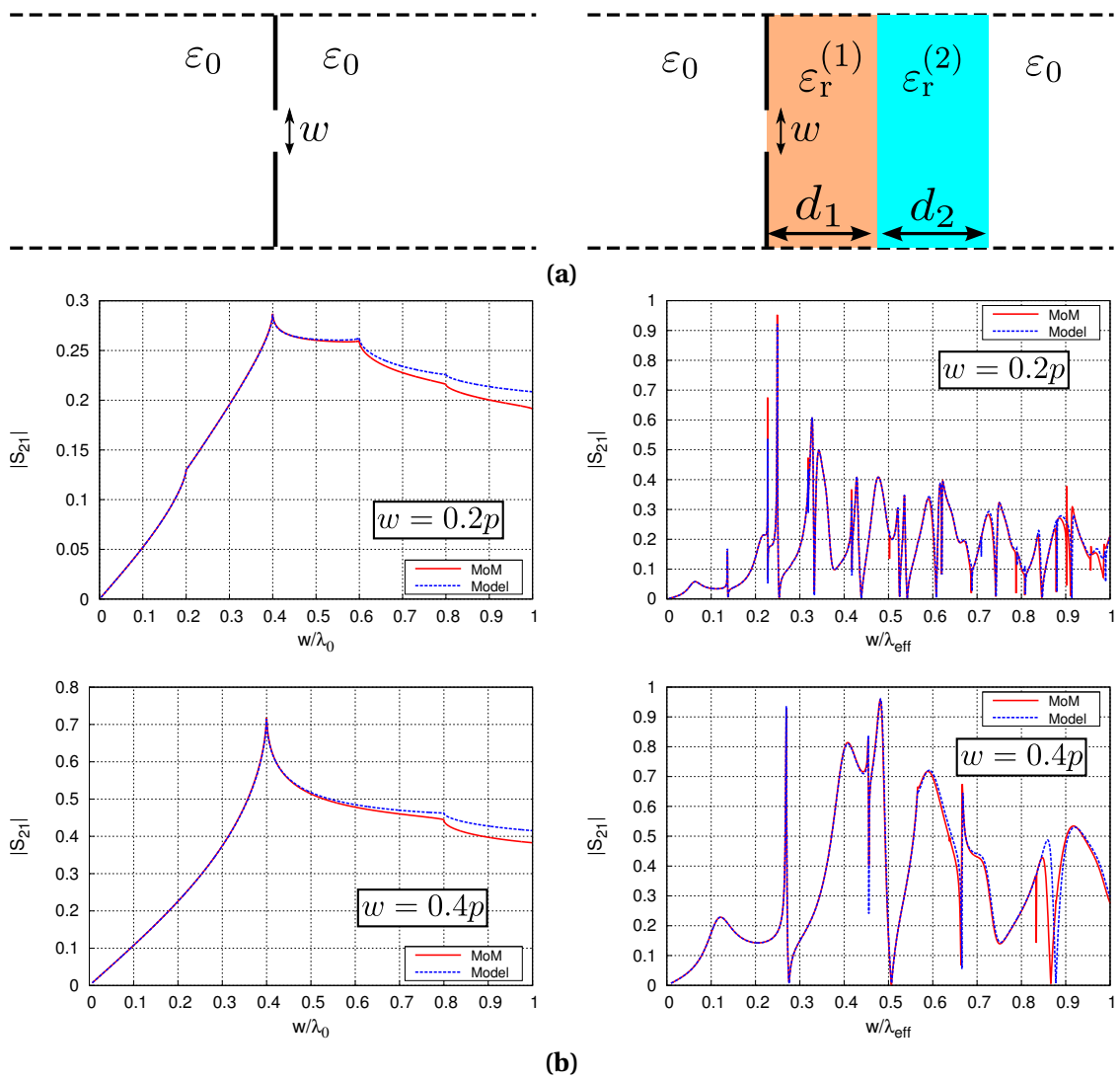

Figure 2.16: (a): Slit gratings under TE normal incidence. Parameters of the multilayer: $\varepsilon_r^{(1)} = 4$, $\varepsilon_r^{(2)} = 9$, $d_1 = d_2 = 0.2p$. (b): Transmission coefficient versus effective wavelength.

For oblique incidence, after making a similar study (not included here) as the one presented in Fig. 2.15, we conclude that the model for strip gratings is accurate up to frequencies around $w/\lambda = 0.2$ whereas for slit gratings, the model is accurate up to $w/\lambda_{\text{eff}} = 0.5 - 0.6$. These conclusions are actually "dual" to those obtained in the previous subsection for TM oblique incidence, which is

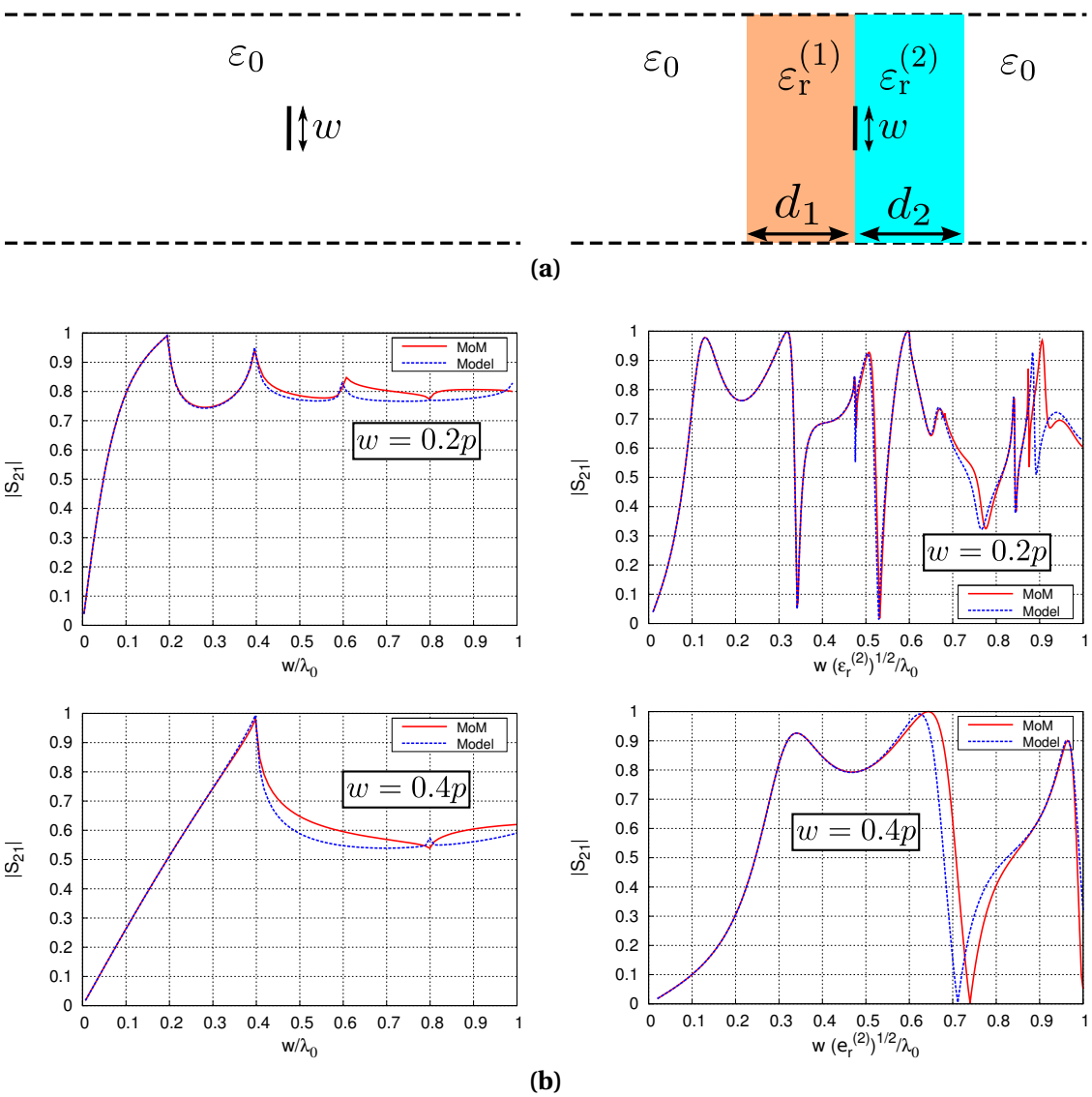

Figure 2.17: Same as Fig.2.13 but for TE incidence.

somehow expected since the slit aperture field profile here is similar to the strip current profile for TM incidence, and viceversa.

2.4.3 Discussion about the different range of validity of the strip and slit models

We have checked in section 2.4.1 above that for TM incidence the strip-like model has a wider application range than the slit model. In this section we will try to provide some further insight into this different performance of the two models. First, Fig. 2.18 shows the TM reflection coefficient obtained using both models as a function of the strip width at two different frequency values. For the sake of simplicity, the case of a free-standing grating under normal TM incidence is considered. The results provided by the model are compared against those obtained from the MoM, which can be considered exact. For the case shown in Fig. 2.18(a) the frequency is $f = 0.75 f_1$, with f_1 being the onset frequency of the first higher-order mode (first grating lobe). It can be observed in this plot that the strip model provides reliable results for virtually any strip width, whereas the slit model results deteriorate for strips narrower than 30% of the period (corresponding to slits wider than 70% of the period). In the high-frequency case shown in Fig. 2.18(b), already in the diffraction regime ($f = 1.5 f_1$), it is similarly observed that the strip model is more robust. Indeed, it can provide reliable results for strip widths up to $w_{\text{strip}} \approx 0.5p$, whereas the slit model results already start to deviate at $w_{\text{strip}}/p \approx 0.7$, i.e., for slits wider than 30% of the unit cell.

Since the main assumption in the derivation of the models is that the strip current and the slit field profiles are independent of frequency, the observed difference in the performance of both models seems to indicate that, for TM incidence, the actual slit aperture field profile shows a stronger tendency to vary with frequency than the strip current profile. In order to explore this, we resort to our MoM implementation, where for each frequency value the aperture field

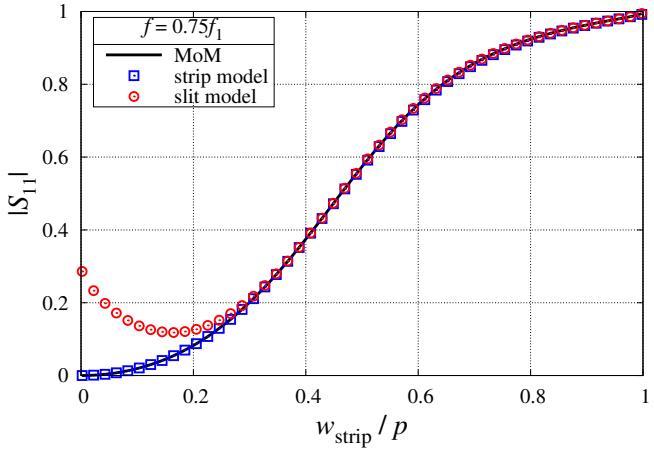

(a)

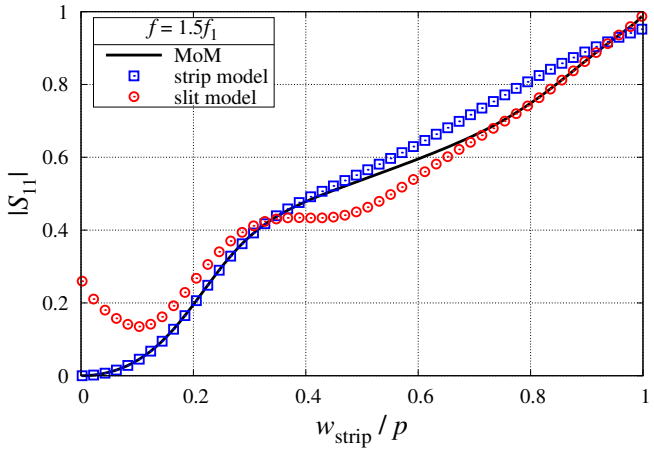

(b)

Figure 2.18: Reflection coefficient versus normalized strip size for a free-standing grating. The results obtained using both the strip and slit circuit models are compared against those provided by the MoM. (a): $f/f_1 = 0.75$ with f_1 the onset frequency of the first grating lobe. (b): $f/f_1 = 1.5$.

at the slit and the surface current in the strip are expanded into a linear combination of basis functions as

$$J_{\text{MoM}}(\omega, y) = \frac{4}{\pi} \sum_{n=0}^{\infty} A_n(\omega) U_n(2y/w) \sqrt{1-(2y/w)^2} \quad \text{strip formulation} \tag{2.24}$$

$$E_{\text{MoM}}(\omega, y) = \frac{2}{\pi} \sum_{n=0}^{\infty} A_n(\omega) \frac{T_n(2y/w)}{\sqrt{1-(2y/w)^2}} \quad \text{slit formulation .} \tag{2.25}$$

Note that the zero-th order terms in the above expansions correspond to the profiles used in the circuit models. The magnitude of the coefficents in the expansions, $A_n(\omega)$, provides information about the relevance of the corresponding basis function in the actual strip current or slit aperture field profiles. Thus, Fig. 2.19 shows the frequency behavior of the first three basis functions coefficients in both the strip and the slit MoM formulations (the odd terms in the expansions are not excited in this case due to symmetry). In order to have a significant comparison, the strips/slits in the considered grating occupy half of the unit cell. As it can be observed in Fig. 2.19(a), for the strip formulation the relevance of the second-order basis function is quite low in all the frequency range shown, which extends up to the onset frequency of the second grating lobe. This means that the strip current profile is approximately constant and equal to the profile of the zero-th order basis function, which is indeed the current profile assumed in the cicuit model. On the contrary, Fig. 2.19(b) shows that in the slit formulation the second-order basis function for the aperture field becomes comparatively much more relevant, and its relative weight in the aperture field expansion varies considerably with frequency. In consequence, the profile of the electric field at the slit aperture exhibits a significant frequency dependence.

A qualitative argument for the above behavior can be given as follows. The magnetic field at the left-hand side of the discontinuity can be written in terms of the modal expansion

$$\mathbf{H}(y,z) = Y_0^{(0)}(1-R)\mathbf{h}_{0,\mathrm{TM}} - {\sum_n}' Y_n^{(0)} E_n \mathbf{h}_{n,\mathrm{TM}}\,. \tag{2.26}$$

If the operation frequency approaches the onset of the n-th grating lobe, the corresponding TM modal admittance,

$$Y_n^{(0)} = \frac{\varepsilon_0 \omega}{\beta_n} \tag{2.27}$$

diverges since β_n approaches zero. According to the slit formulation in chapter 1, the E_n coefficients are given by

$$E_n = (1+R)\frac{\tilde{f}_n}{\tilde{f}_0}\,, \tag{2.28}$$

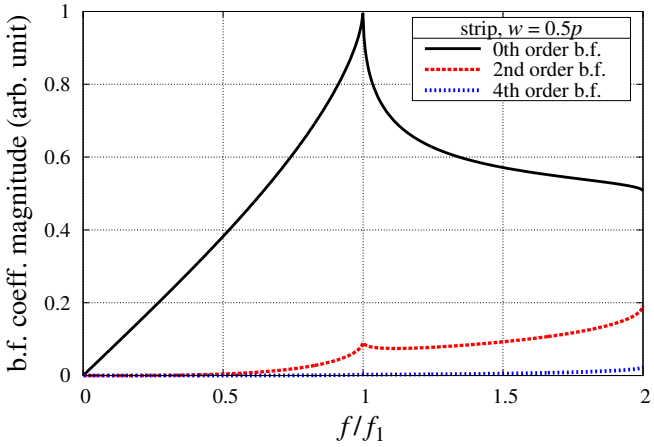

(a)

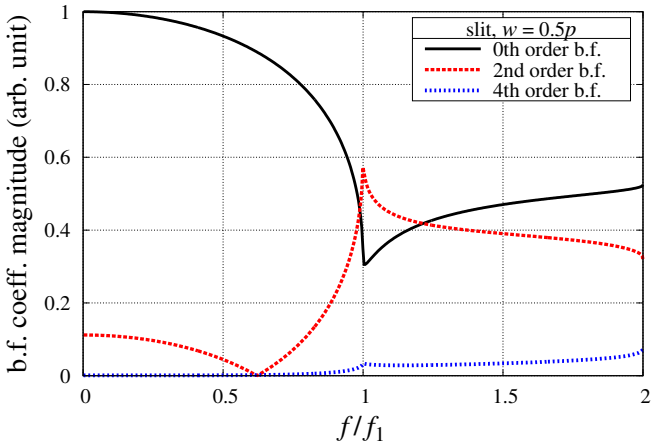

(b)

Figure 2.19: Magnitude of the lowest-order basis functions coefficients ($n = 0, 2, 4$) versus frequency for a free-standing strip grating with $w = 0.5p$. (a): MoM strip formulation. (b): MoM slit formulation.

and therefore (2.26) takes the form

$$\mathbf{H}(y,z) = Y_0^{(0)}(1-R)\,\mathbf{h}_{0,\mathrm{TM}} - (1+R)\sum_n{}' Y_n^{(0)}\frac{\tilde{f}_n}{\tilde{f}_0}\,\mathbf{h}_{n,\mathrm{TM}}\,, \tag{2.29}$$

where $\tilde{f}_n$ represents the projection of the slit aperture field profile over the n-th modal field. On the other hand, using the strip formulation the coefficients can

be written as

$$E_n = -\frac{\tilde{f'}_n}{\tilde{f'}_0}\,\frac{RY_0^{(0)}}{Y_n^{(0)}} \tag{2.30}$$

which leads to

$$\mathbf{H}(y,z) = Y_0^{(0)}(1-R)\,\mathbf{h}_{0,\mathrm{TM}} + RY_0^{(0)}\sum_n{}'\,\frac{\tilde{f'}_n}{\tilde{f'}_0}\,\mathbf{h}_{n,\mathrm{TM}}\,, \tag{2.31}$$

where $\tilde{f'}_n$ denotes the projection of the strip current profile over the n-th modal field. It can be observed that the $\tilde{f}_n/\tilde{f}_0$ factors in (2.29) are multiplied by the higher-order modal admittances $Y_n^{(0)}$, but that is not the case in (2.31). In order to keep the coefficients in the modal expansion finite, the $\tilde{f}_n/\tilde{f}_0$ factors in the slit formulation have to somehow compensate for the singular behavior of the modal admittances, and thus they exhibit a more pronounced frequency dependence than the $\tilde{f'}_n/\tilde{f'}_0$ coefficients in the strip formulation.

Finally, it should be mentioned that a completely similar analysis can be carried out for the dual case of free-standing gratings under TE incidence, leading to similar arguments about the wider application range of the slit model in that case.

2.5 Conclusions

A circuit model has been derived for the analysis of the scattering properties of a single slit grating embedded in a leyered dielectric environment. Two different models have been presented, one for narrow slit and one for narrow strip gratings. Fully-analytical expressions are derived for all the circuit elements. The circuit elements are split into low- and high-order elements, where low-order elements have mostly a propagative nature and high-order elements are purely reactive. In practice, only a few low-order elements are considered, whereas the rest of high-order elements are accounted for by a global high-order lumped element. The agreement between results provided by the models and by an in-house method of moments is excellent both for normal and oblique incidence within a wide frequency band. An exhaustive study has determined that the

model provides reliable results for normalized frequencies up to $w/\lambda = 0.2$ in the worst case, with w being the slit/strip width and λ the wavelength in the highest-permittivity medium. In the most favourable case, the model is accurate up to normalized frequencies of $w/\lambda_{\text{eff}} = 0.8$, with λ_{eff} being the effective wavelength, calculated using the average value of the permittivity of the dielectric layers in contact with the grating.

Chapter 3

1-D periodic T-shaped corrugated surfaces

3.1 Introduction

Corrugated conducting surfaces have long been employed in microwave and antenna engineering for their unique and special electromagnetic properties. This kind of surfaces can act as guiding systems for bound surface waves and leaky waves, as well as artificial magnetic conductors in the framework of the scattering of plane waves. The control of the features of the bound and scattered waves by the manipulation of the geometry of the corrugations is one of the main adventages provided by corrugated surfaces.

The study of corrugated surfaces is a classical topic in the microwaves field. Pioneer researchers focused their study of these structures on the propagation characteristics along corrugated planes [67–70], corrugated cylindrical waveguides [68, 69, 71] or corrugated rectangular waveguides [72]. Corrugated surfaces were first applied in the design on hybrid-mode horns antennas [73–75] due to, among other properties, the anisotropic propagation features exhibited

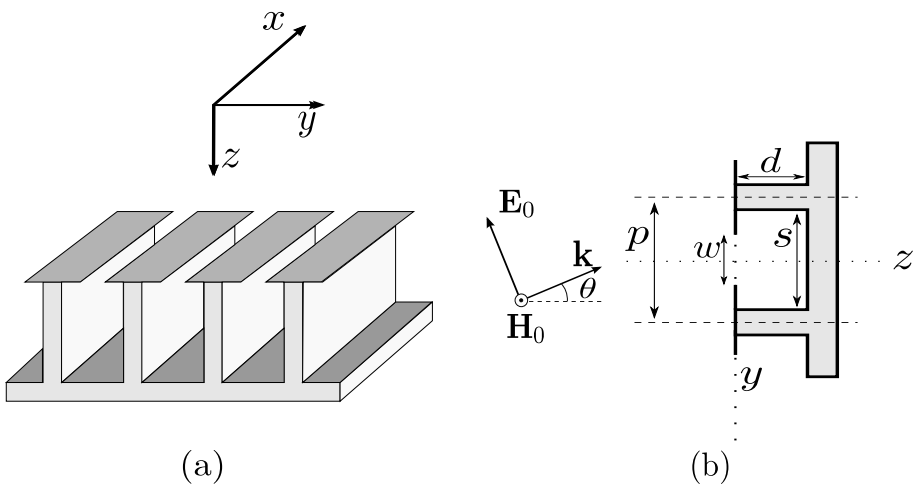

Figure 3.1: (a): Three-dimensional view of a 1D periodic corrugated-surface prototype. (b): Cross-sectional view of the same structure.

by waves supported by them. The anisotropic characteristics in corrugated surfaces comes from the existence of a particular direction where the wave propagation along the surface is suppressed whereas enhanced in a different direction. These anisotropic properties in corrugated surfaces and many other structures inspired a more general classification reported in [76, 77], where the concept of soft and hard surfaces is proposed for surfaces that suppress and enhance the wave propagation, respectively. Soft and hard surfaces can both be defined in terms of an equivalent surface impedance.

Periodic corrugated surfaces can also be applied to manipulate the scattering behavior of an incident plane wave. First researchers on this topic paid attention to the effect of corrugations on the field scattered from perfectly conducting circular cylinders with transverse corrugations [78–80]. This problem was posed for the design of low-blockage feed-support struts in reflector antennas [81]. In the optics range, planar corrugated surfaces are applied in [82] to exploit the field enhancement at certain zones of the structure by manipulating the scattering properties of the incoming plane wave.

The basic geometry of a 1-D periodic corrugated surface is depicted Fig.3.1. As was mentioned above, corrugated surfaces are mainly applied as guiding structures and to tailor the scattering features when they are excited by external

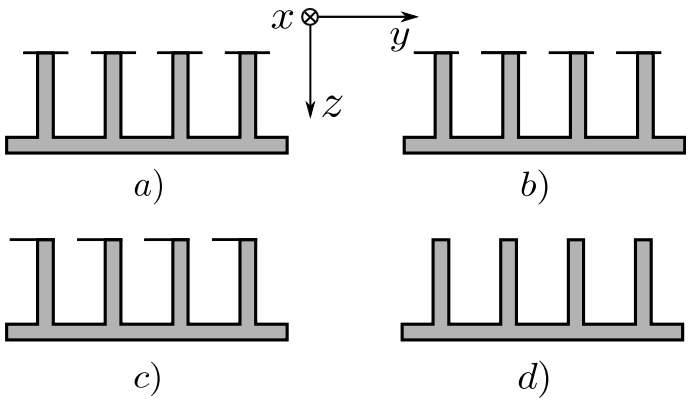

Figure 3.2: Cross section of the different types of corrugated planar surfaces analyzed in this chapter. a): T-shaped corrugated structure with a symmetrically centered slit aperture. b): T-shaped corrugated structure with a non symmetrical slit position. c): T-shaped corrugation with the maximum slit displacement. d): Classical corrugated plane. The structures are periodic along the y direction and invariant along the x direction. ©2014 IEEE

plane waves. Similar to other periodic structures, they can exhibit frequency bands allowing the wave propagation (passbands) and frequency bands suppressing the wave propagation (stopbands) [12, 35]. Moreover, corrugated surfaces also behave as artificial magnetic conductors (AMC) at certain frequency bands. AMC condition is attained when a plane wave impinging on the structure is reflected with a near-zero phase shift. By tailoring adequately the structure parameters of corrugated surfaces, the stopband and AMC properties can simultaneously be achieved at approximately the same frequency band. This particular result has been efficiently applied in the fabrication of low-profile antennas [26, 83, 84]. The idea of overlapping both phenomena (in frequency) was first reported in [26] where both properties appear naturally at the same frequency band. Although there are some counterexamples in the literature demostrating that the stopband and AMC properties are actually independent of each other in 2-D periodic structures [85], it can be demostrated that certain configurations of planar corrugated surfaces at subwavelength frequencies exhibit both AMC and stopbands simultaneously (models proposed in [26]).

In this chapter we focus on in the analysis of the scattering properties of the structures depicted in Fig.3.2. These same configurations have been treated and

reported in [86] where the scattered field is calculated by solving the integral equation using the method of moments. The results provided in that paper are very accurate but require an important computational effort. Some previous works as [87] and [88] addressed the scattering problem by replacing the corrugated surface by an impedance boundary condition. Of course the computational cost is reduced considerably, but the applicability of this method imposes restrictions on the geometrical parameters of the structure. In a recent paper [89], the symmetric T-shaped corrugated structure shown in Fig. 3.2(a) is analyzed. A simple formula is derived (with certain parameters to be fitted) using the transverse resonance technique to calculate the phase of the reflection coefficient when the structure is illuminated by an obliquely-incident wave. This formula works properly for narrow corrugations but fails in predicting the behaviour of the structure if the groove size is similar to the period. An enhanced theory was reported in [90] by the same author but it is valid only for the case of the simpler corrugation shown in Fig.3.2(d).

Here we propose an alternative way to analyze 1-D planar corrugated structures by using an equivalent circuit approach. This approach was also previously adopted in [91], but for the analysis of the classical corrugated structure in Fig.3.2(d) only. As far as we know, there are not many works in the literature using the circuit-model approach to analyze corrugated surfaces. Note that the basic details concerning the characterization of the discontinuity have already been described in Chapter 1. In the present chapter, and following [23, 65], we extend the model to more complex cases including stratified dielectrics and ohmic losses. Several results for TM incidence (it interacts strongly with the structure, in contrast to TE incidence) will be plotted, comparing them with the models provided in [89], [91], an in-house method of moments and ANSYS HFSS. Some possible applications of 1-D corrugated surfaces will also be proposed after an efficient and fast design by using the equivalent circuit. Finally, the limits of validity of the model will be discussed.

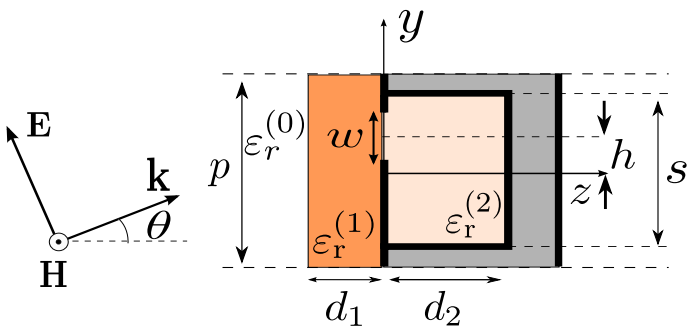

Figure 3.3: General unit cell of any of the structures shown in Fig. 3.2 including a cover slab and a cavity dielectric filling. Structural parameters: period a, groove size s, slit width w, slit displacement h, external slab thickness d_1, corrugation depth d_2, relative permittivity of the dielectric in the cavity $\varepsilon_r^{(2)}$, relative permittivity in the external slab $\varepsilon_r^{(1)}$, external relative permittivity $\varepsilon_r^{(0)}$, incidence angle θ. ©2014 IEEE

3.2 Analytical circuit model

3.2.1 Lossless grating

The T-shaped corrugated structures under consideration in this work are those shown in Fig.3.2, including also the possible presence of a dielectric cover. The whole structure extends indefinitely along the x direction, which makes the structure be one-dimensional (1-D) periodic along the y-direction. A plane wave with TM polarization impinges on the structure, exciting electric currents on the metallic surfaces. The response of the structure under TE incidence will not be treated in the present chapter because the structure practically behaves as a perfect electric wall, and thus no interesting phenomena are observed. Due to the periodic nature of the structure, Floquet theory allows us to restrict the analysis to the unit cell of period p shown in Fig. 3.3 (it should be noted that all the configurations sketched in Fig.3.2 are particular cases of the generalized unit cell depicted in Fig.3.3).

An equivalent circuit for thick metal gratings has already been derived in Chapter 1, section 1.2.1, where the problem is interpreted as a waveguide junction. Two different waveguides are clearly distinguished in Fig.3.3. The external region, denoted by the superscript (1) ($z < 0$), is a generalized parallel-plate

waveguide with periodic boundary conditions at its upper and lower boundaries. The modal profiles $\mathbf{e}^{(1)}_{n,\mathrm{TM}}$ of the characteristic modes in this region are actually Floquet harmonics and are formally those described in (2.1). The cut-off wavenumber of a particular nth-order harmonic is given by (2.3). A dielectric overlay can eventually be placed in this region above the corrugations at $-d_1 < z < 0$. The cavity or internal region, denoted by (2), is a parallel-plate waveguide with electric-wall boundary conditions at the top and bottom walls, and short-circuited at its right end ($z = d_2$). The modal profile of its charasteristic modes is now expressed as

$$\mathbf{e}^{(2)}_{2n,\mathrm{TM}} = \sqrt{\frac{(2-\delta_{2n,0})}{s}}\cos(k^{(2)}_{2n}y)\hat{\mathbf{y}} \tag{3.1}$$

$$\mathbf{e}^{(2)}_{2n+1,\mathrm{TM}} = \sqrt{\frac{2}{s}}\sin(k^{(2)}_{2n+1}y)\hat{\mathbf{y}} \tag{3.2}$$

with

$$k^{(2)}_q = \frac{q\pi}{s} \qquad q \in \mathbb{N} \tag{3.3}$$

and where (3.1) represents even modes of the cavity, whereas (3.2) represents odd modes of the cavity. They all together form an orthonormal basis.

The equivalent admittance expression for this kind of slit-discontinuity problems in (1.27) must now incorporate the presence of the dielectric interfase at a distance $-d_1$ and also the presence of the electric wall at d_2. This is readily done by considering the input admittances seen from the slit discontinuity to the left- and to the right-hand side. In this way we obtain

$$Y_{\mathrm{eq}} = \sum_{|n|\geq 1}^{\infty} Y_n^{\mathrm{in,\,L}} \left|\frac{\tilde{f}^{(1)}_n}{\tilde{f}^{(1)}_0}\right|^2 + \sum_{n=1}^{\infty} Y_n^{\mathrm{in,\,R}} \left|\frac{\tilde{f}^{(2)}_{2n}}{\tilde{f}^{(1)}_0}\right|^2 \tag{3.4}$$

where the admittances $Y_n^{\mathrm{in,\,L/R}}$ denote the admittance of the nth harmonic/mode at the left/right of the slit aperture. Specifically, at the left-hand side there is a dielectric interface between the finite-thickness slab with $\varepsilon_{\mathrm{r}}^{(1)}$ and the semi-infinite dielectric medium with $\varepsilon_{\mathrm{r}}^{(0)}$. Thus the nth admittance seen from the slit grating is calculated as

$$Y_n^{\mathrm{in,\,L}} = Y_n^{(1)}\frac{Y_n^{(0)} + \mathrm{j}Y_n^{(1)}\tan(\beta_n^{(1)}d_1)}{Y_n^{(1)} + \mathrm{j}Y_n^{(0)}\tan(\beta_n^{(1)}d)}\,. \tag{3.5}$$

At the right-hand side of the discontinuity, there is a grounded dielectric layer of thickness d_2. The input admittance associated with a nth-order mode in this medium is

$$Y_n^{\text{in, R}} = -\text{j}Y_n^{(2)} \cot(\beta_n^{(2)} d_2)\,. \tag{3.6}$$

The series in (3.4) is composed of low- and high-order harmonics/modes. Low-order elements keep their full dynamical frequency dependence on the admittance expression. On the contrary, the combination of high-order modes/harmonics gives rise to the following global capacitance:

$$C_{\text{ho}} = \sum_{n=N+1}^{\infty} C_n^{(1)} \frac{\varepsilon_{\text{r}}^{(1)} + \varepsilon_{\text{r}}^{(0)} \tanh(k_n^{(1)} d_1)}{\varepsilon_{\text{r}}^{(0)} + \varepsilon_{\text{r}}^{(1)} \tanh(k_n^{(1)} d_1)} \left[\frac{\tilde{f}_n^{(1)}}{\tilde{f}_0^{(1)}}\right]^2 + 2 \sum_{n=M}^{\infty} C_n^{(2)} \coth(k_n^{(2)} d_2) \left[\frac{\tilde{f}_n^{(2)}}{\tilde{f}_0^{(1)}}\right]^2 \tag{3.7}$$

with $C_n^{(i)} = \dfrac{\varepsilon_0 \varepsilon_{\text{r}}^{(i)}}{k_n^{(i)}}$. This infinite series does not depend on the incidence angle or the frequency, and thus it can be calculated only once and stored. The numbers N and M denote the number of low-order harmonics/modes respectively. At this point, we need to choose the electric-field profile function. For this slit-discontinuity problem we can again use the field profile chosen in the previous chapter for TM incidence (2.5), but centered at the middle plane of the slit aperture,

$$\mathbf{f}(y) = \frac{2/\pi}{\sqrt{1 - \left(\dfrac{2(y-h)}{w}\right)^2}} \hat{\mathbf{y}}\,. \tag{3.8}$$

The corresponding projections over the harmonics and modes give rise to the following expressions:

$$\tilde{f}_n^{(1)} = \sqrt{\frac{1}{p}} J_0\big(k_n^{(1)} w/2\big) \text{e}^{-\text{j}k_n^{(1)} h} \tag{3.9}$$

$$\tilde{f}_{2n}^{(2)} = \sqrt{\frac{2 - \delta_{2n,0}}{s}} J_0\big(k_{2n}^{(2)} w/2\big) \cos(k_{2n}^{(2)} h) \tag{3.10}$$

$$\tilde{f}_{2n+1}^{(2)} = \sqrt{\frac{2}{s}} J_0\big(k_{2n+1}^{(2)} w/2\big) \sin(k_{2n+1}^{(2)} h) \tag{3.11}$$

with $J_0(\cdot)$ being the zeroth-order Bessel function of the first kind. With the help of (3.9), (3.10) and (3.11), the equivalent admittance of the circuit model is given

by

$$Y_{\text{eq}} = \sum_{|n|\geq 1}^{\infty} Y_n^{\text{in, L}} \left| \frac{J_0(k_n^{(1)} w/2)}{J_0(k_{\text{t}} w/2)} \right|^2 + \frac{2p}{s} \sum_{n=1}^{\infty} Y_{2n}^{\text{in, R}} \left[\frac{J_0(k_{2n}^{(2)} w/2)}{J_0(k_{\text{t}} w/2)} \cos(k_{2n}^{(2)} h) \right]^2 + \frac{2p}{s} \sum_{n=1}^{\infty} Y_{2n+1}^{\text{in, R}} \left[\frac{J_0(k_{2n+1} w/2)}{J_0(k_{\text{t}} w/2)} \sin(k_{2n+1}^{(2)} h) \right]^2 \quad (3.12)$$

where k_{t} denotes the lowest-order cutoff wavenumber in the external region. We observe the scaling factor $\frac{2p}{s}$ appearing in (3.12) for the admittances of the internal region. It basically consists of a ratio involving the dimensions of each waveguide. We can redefine the characteristic admittances of the lines in the internal region as

$$\bar{Y}_q^{(2)} = \frac{2p}{s} Y_q^{(2)} . \quad (3.13)$$

This scaled definition is in agreement with the classical definition of the characteristic admittance in terms of the ratio between the equivalent voltage and current associated with the fields of the mode under consideration [34]. That is, after defining the equivalent voltage and current of an individual mode, the scaling factor appears in a natural way in the expression of its associated characteristic admittance. In our method, this scaling factor is implicit in the transformer expressions. Of course, when the waveguide regions (1) and (2) are identical, the scaling factor disappears after normalizing to the size of any of the guides. The fundamental mode propagating in the internal region also incorporates its corresponding scaling factor. According to the expression in (1.26) and using (3.9) and (3.10), the zeroth-order transformer is given by

$$\left| \frac{\tilde{f}_0^{(2)}}{\tilde{f}_0^{(1)}} \right|^2 = \frac{p}{s} \frac{1}{\left| J_0(k_{\text{t}} w/2) \right|^2} . \quad (3.14)$$

The scaling factor $\frac{p}{s}$ allows us to redefine the characteristic admittance of their associated transmission line as

$$\bar{Y}_0^{\text{in, R}} = \frac{p}{s} Y_0^{\text{in, R}} . \quad (3.15)$$

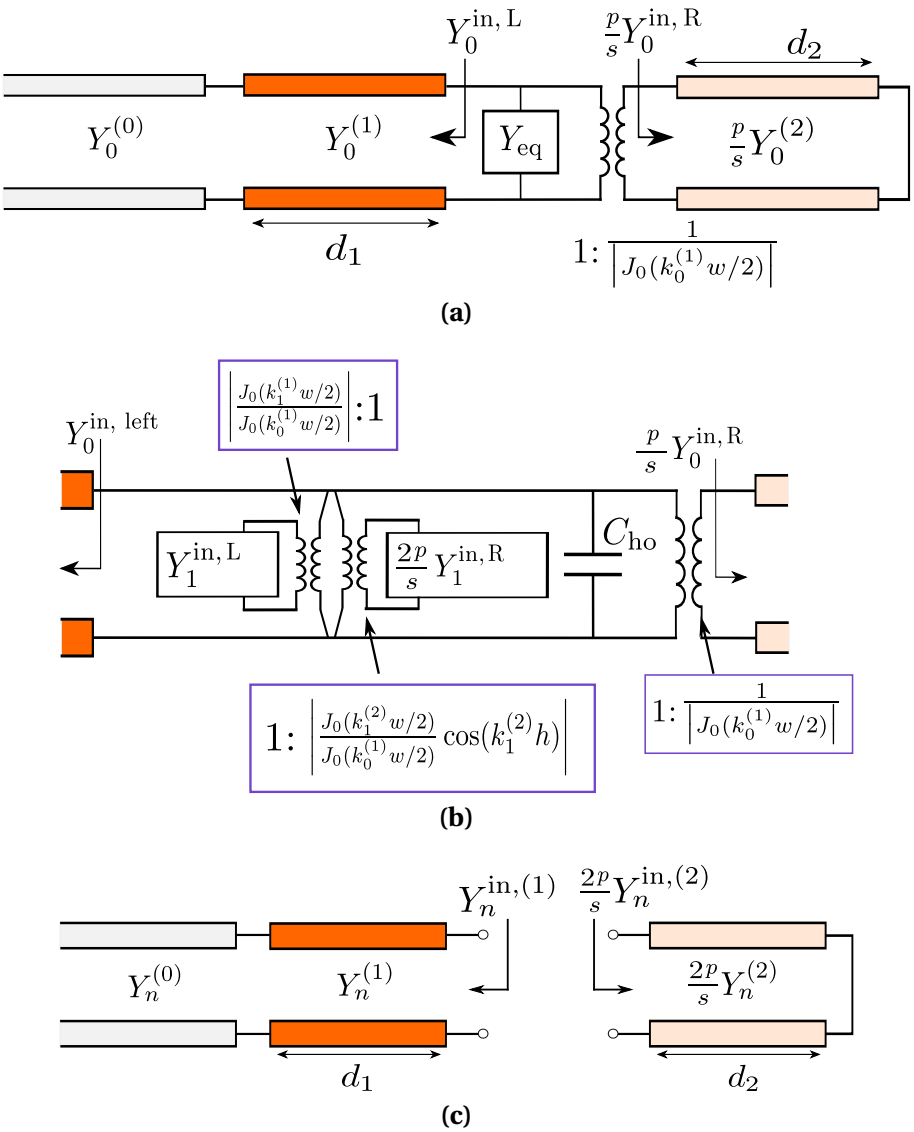

Figure 3.4: (a) Equivalent circuit of the periodic structure under analysis. (b) Topology of the equivalent admittance Y_{eq} that represents the high-order harmonics and modes excited at the slit discontinuity. (c) Definition of the input admittances in Y_{eq}.

With the help of these new definitions, the final topology of the equivalent circuit is shown in Fig.3.4.

3.2.2 Resistive overlay

If the dielectric overlay [medium (1)] is lossy (this is an interesting situation if the structure is intended to be used as an absorber), its permittivity is complex and can be written as $\hat{\varepsilon}^{(1)} = \varepsilon_0 \hat{\varepsilon}_{\mathrm{r}}^{(1)}$ with

$$\hat{\varepsilon}_{\mathrm{r}}^{(1)} = \varepsilon_{\mathrm{r}}^{(1)}(1 - \mathrm{j}\tan\delta) - \mathrm{j}\frac{\sigma_1}{\omega\varepsilon_0} \tag{3.16}$$

where $\tan(\delta)$ represents the dielectric loss tangent and σ_1 the conductivity of the medium. The complex longitudinal wavenumber of the n-th harmonic in this medium is then given by

$$\hat{\beta}_n^{(1)} = \sqrt{\hat{\varepsilon}_{\mathrm{r}}^{(1)} k_0^2 - [k_n^{(1)}]^2}\,. \tag{3.17}$$

The complex values of the relative permittivity and the wavenumber given in (3.16) and (3.17) must now be taken into account to obtain the associated complex characteristic admittance in this lossy medium,

$$\hat{Y}_n^{(1)} = \frac{\hat{\varepsilon}_{\mathrm{r}}{}^{(1)} k_0}{\eta_0 \hat{\beta}_n^{(1)}}\,. \tag{3.18}$$

A completely similar treatment applies in case the dielectric filling the cavity is lossy.

3.2.3 Ohmic losses in the cavity walls

For completeness, ohmic losses in the cavity walls are also incorporated in the model. Since the metallic materials usually employed in the fabrication of practical structures are good conductors, the conventional strong skin-effect approximation is used here. The effect of losses in the lateral walls at $y = \pm s/2$, the back wall at $z = d_2$, and the periodic slit screen are considered separately. In

any case, an additional approximation is made that conductor ohmic losses are attributed to propagative modes only.

Ohmic losses in the lateral walls cause the wavenumbers of the parallel plate waveguide modes to become complex. Their quantitative impact is obtained via the well-known perturbation method [34], which provides not only a resistive but also an inductive contribution due to the penetration of the magnetic field into the metal (the inductive contribution is usually negligible, but may become noticeable for very high frequencies and/or very narrow cavities). Thus, the complex wavenumber of each modal transmission line in the cavity can now be written as

$$\hat{\beta}_n^{(2)} = \sqrt{(\beta_n^{(2)})^2 + (\Delta\beta_n)^2} \tag{3.19}$$

where $\beta_n^{(2)}$ is the propagation constant calculated in the lossless case, and $(\Delta\beta_n)^2$ is the contribution of the ohmic losses obtained by the perturbation method [34],

$$(\Delta\beta_n)^2 = (2 - \delta_{n,0})(1 - \mathrm{j})\frac{\delta_s}{s}\varepsilon_{\mathrm{r}}^{(2)}k_0^2 \tag{3.20}$$

with $\delta_s = \sqrt{2/\omega\mu_0\sigma_{\mathrm{m}}}$ being the skin depth and σ_{m} the conductivity of the metal. The complex characteristic admittance of the corresponding nth-order transmission line, $\hat{Y}_n^{(2)}$, is obtained using (3.18) but with $\varepsilon_{\mathrm{r}}^{(2)}$ and $\hat{\beta}_n^{(2)}$.

Concerning ohmic losses in the back wall of the cavity, its effect is introduced by placing an imperfect short-circuit load at the end of the modal transmission lines. Assuming strong skin effect, the value of the admittance of this load is given directly by the surface admittance [34],

$$Y_s = \frac{1}{2}(1 - \mathrm{j})\sigma_{\mathrm{m}}\delta_s \tag{3.21}$$

which is the same for all the cavity modes.

For the two previous cases of lateral walls and back wall it has been possible to account approximately for the effect of ohmic losses individually for each mode in the cavity, and then it is straightforward to compute the corresponding input admittances seen at the slit aperture. These input admittances incorporate the combined effect of the lateral and back wall losses and are obtained

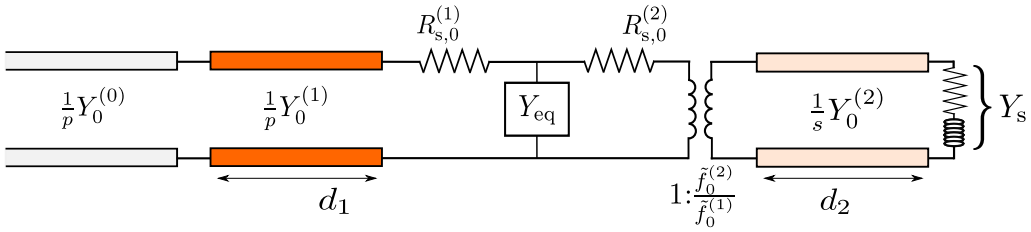

Figure 3.5: Equivalent circuit of the periodic structure under analysis with ohmic losses.

by transforming the imperfect load Y_s along the lossy transmission line with wavenumber $\hat{\beta}_n^{(2)}$ and characteristic admittance $\hat{Y}_n^{(2)}$, thus giving the following expression that substitutes (3.6):

$$\hat{Y}_n^{\text{in, R}} = \hat{Y}_n^{(2)} \frac{Y_s + \mathrm{j}\hat{Y}_n^{(2)} \tan(\hat{\beta}_n^{(2)} d_2)}{\hat{Y}_n^{(2)} + \mathrm{j} Y_s \tan(\hat{\beta}_n^{(2)} d_2)} \,. \tag{3.22}$$

Finally, for ohmic losses in the slit screen, since all modes and harmonics couple together at the slit discontinuity, it is not easy to find an approximate analytical expression that accounts for the effect of each individual mode. However, an heuristic reasoning suggests to model approximately the resistive screen by a similar equivalent surface admittance as that used in the back wall case, but excluding now the contribution corresponding to the aperture. Thus, this ohmic effect is here taken into account as a series resistance connected to each transmission line (propagative modes/harmonics), whose value is given by

$$R_{\mathrm{s},n}^{(1)} = \frac{p-w}{p} \frac{1}{\sigma_{\mathrm{m}} \delta_s} \tag{3.23}$$

$$R_{\mathrm{s},n}^{(2)} = 2(1-\delta_{n,0}) \frac{p}{s} \frac{s-w}{s} \frac{1}{\sigma_{\mathrm{m}} \delta_s} \,. \tag{3.24}$$

The resulting final equivalent circuit is schematically shown in Fig.3.5.

3.3 Numerical Results

In the derivation of our equivalent circuit model, a given electric field profile at the slit aperture was assumed. For the strip/slit gratings studied in Chapter 2,

this approximated profile was proven to give sufficient accuracy, even in the oblique incidence case. This fact suggests that the same profile could also work properly for both the symmetric and the non-symmetric planar T-shaped corrugated structures. In this latter case, the asymmetry is partly considered in our analysis by the inclusion of odd modes in the proposed modal expansion for the cavity. An additional approximation in our study is that the effect of higher order harmonics/modes is accounted for by a global lumped capacitance. Hence, due to the existence of such approximations, the accuracy of our model needs to be validated against some independent numerical results. This validation is next carried out by comparing our results with the data obtained from an in-house full-wave MoM numerical code that uses several basis functions for the electric field at the slit (for our purposes, this carefully implemented MoM is considered "exact"). With the aim of exploring how other previously proposed equivalent-circuit models behave with respect to our equivalent-circuit approach in terms of accuracy, robustness and range of applicability, our results are also compared with those computed from the formula provided in [89, Eq.27] (henceforth called Kehn's formula) and with those obtained following Woo's circuit reported in [91]. The examples showing ohmic losses are compared with simulations obtained with HFSS.

3.3.1 Comparison with MoM and Kehn's formula

A first comparison is shown in Fig. 3.6, where the phase of the reflection coefficient is plotted versus frequency for three different configurations (see the caption for the structure parameters). The slit aperture is symmetrically placed, so there is no contribution of the odd modes inside the cavity in our model. As expected, as frequency increases, the structure departs from the low-frequency electric wall behavior to achieve a near-zero phase of the reflection coefficient (the well known artificial magnetic conductor, AMC, or high-impedance surface) in a given frequency range. This can be understood as the "quarter-wave

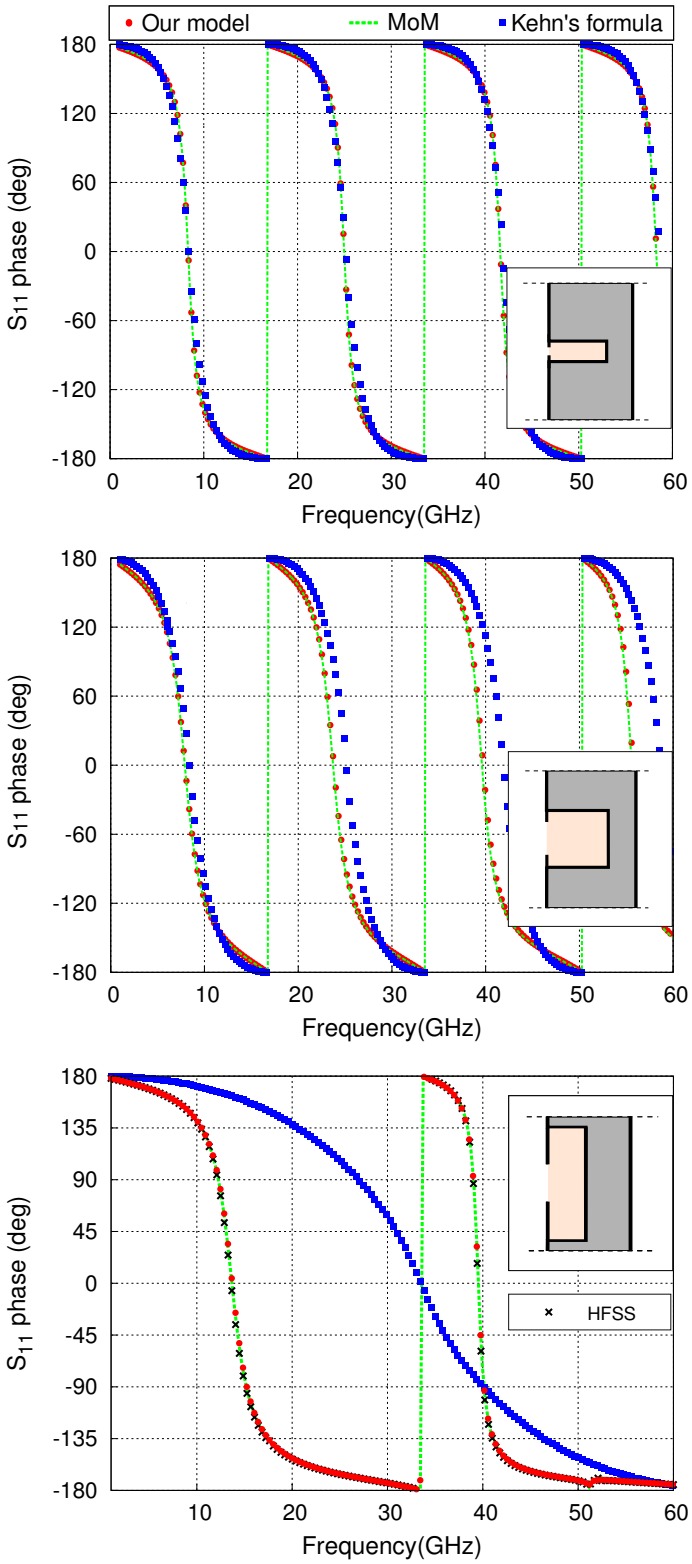

Figure 3.6: Phase of the reflection coefficient vs. frequency for three different configurations. Top: $p = 1\,\text{mm}$, $s = 0.25\,\text{mm}$, $w = 0.75s$, $d_2 = 4\,\text{mm}$, $h = 0\,\text{mm}$, $\varepsilon_\text{r}^{(1)} = 1$, $\varepsilon_\text{r}^{(2)} = 5$, $\theta = 30°$, in our model $N = 2$, $M = 1$. Center: same as top, except $s = 0.5\,\text{mm}$, $w = 0.2s$. Bottom: $p = 5\,\text{mm}$, $s = 4\,\text{mm}$, $w = 0.2s$, $d_2 = 1\,\text{mm}$, $h = 0\,\text{mm}$, $\varepsilon_\text{r}^{(1)} = 1$, $\varepsilon_\text{r}^{(2)} = 5$, $\theta = 10°$. In our model, $N = 2$, $M = 2$.

transformer" effect caused by the transmission line corresponding to the fundamental TEM mode inside the groove [the transmission line (2) shown in Fig.3.4(a)]. Rigorously, the magnetic wall condition occurs at a frequency slightly lower than that for which $\frac{p}{w}Y_0^{\text{in, right}} = 0$, since this admittance has to compensate for the capacitive admittance Y_{eq} introduced by the high-order modes/harmonics excited at the slit discontinuity so that $\frac{p}{w}Y_0^{\text{in, right}} + Y_{\text{eq}} = 0$. In the case shown at the top of Fig. 3.6, the agreement between the three sets of data (our equivalent circuit, the MoM, and Kehn's formula in [89, 90]) is very good in all the frequency range shown. However, in this case, the groove width is electrically small in the considered frequency range ($s/\lambda_0 \leq 1/20$, with λ_0 being the free-space wavelength) and the slit aperture is relatively wide with respect to the groove ($w/s = 3/4$). Hence, the high-order modes excited at the discontinuity are not expected to have a relevant effect (Khen's formula was derived neglecting the effect of high order modes). In the case shown at the central panel of Fig. 3.6, the groove has been enlarged to half the size of the unit-cell period ($s/p = 1/2$), and the slit aperture has been narrowed to 20% of the groove size ($w/s = 1/5$). In this situation, Kehn's formula clearly deviates from the MoM numerical results as frequency increases, whereas the results provided by our circuit model remain remarkably accurate. With the set of dimensions chosen in the bottom panel in Fig. 3.6, Kehn's formula is not capable of reproducing the correct behavior of the phase of the reflection coefficient. The reason behind such a poor behavior of Kehn's expression is related to the relatively small value of the corrugation depth. Under these circumstances, the implicit assumption in Kehn's model linking the phase evolution to the existence of Fabry-Pérot resonances along the z-direction is no longer valid. Our model makes no assumption in this regard but takes into account analytically the influence of high order cavity modes, which turns out to be essential in this situation. Indeed, the cutoff frequency of the first high order mode inside the cavity is 33.54 GHz. At this frequency, the admittance of this high order mode diverges, giving rise to a short-circuit in the equivalent admittance associated with the discontinuity. This fact is perfectly captured by our model, in good agreement with MoM, but seems to

be ignored by other simplified equivalent circuits. (In order to show a validation of our MoM code, HFSS results are also included in this last plot. The agreement between MoM and HFSS results is similarly good for all the cases without ohmic losses studied.)

3.3.2 Classical corrugated surface. Comparison with Woo's circuit model

Fig.3.7 shows results for the classical corrugated surface recently studied in [91] by means of an analytical circuit model (here called Woo's circuit model). Actually, for the case of TM incidence, the circuit model in [91] resembles the one proposed by some of the authors in [24] for transmission slit structures. The purpose of Fig. 3.7 is to compare the predictions of the model in [91] with the new proposal in the present chapter. The top plot shows the phase of the reflection coefficient when the groove size is 1/10 of the unit cell period. As expected, our circuit approach gives accurate results, which agree very well with MoM data, due to the small electrical size of the aperture. Woo's circuit model also provides acceptable agreement with MoM numerical code results, although slightly less precise. It should be reminded that Woo's model considers only the TEM mode inside the cavity; i.e., the reactive field is ignored. Hence, as the groove size grows, the accuracy of this model is expected to worsen, as observed in the bottom plot of Fig.3.7 even in the low frequency regime. In this last case, the groove size is now 4/10 of the period and its electrical size is not negligible at the high end of the studied frequency spectrum, thus raising a non-negligible reactive field inside the cavity. Although our model does account for the reactive field excited in the discontinuity, its numerical results are not expected to be very accurate at high frequencies where the width of the cavity is not electrically small (@45 GHz, $s/\lambda_0 = 3/10$) and the approximation for the aperture field in (3.8) is not sufficiently valid.

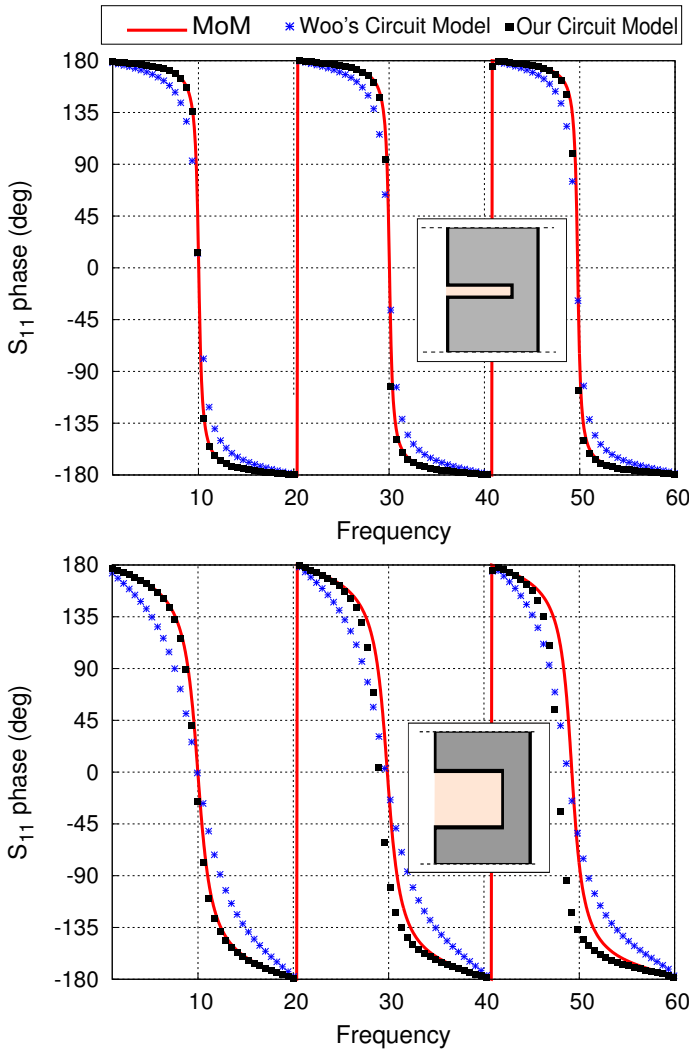

Figure 3.7: Phase of reflection coefficient vs. frequency for two different configurations. Top: $p = 5\,\text{mm}$, $s = 0.5\,\text{mm}$, $w = s$, $d = 3\,\text{mm}$, $h = 0\,\text{mm}$, $\varepsilon_\text{r}^{(1)} = 1$, $\varepsilon_\text{r}^{(2)} = 6$, $\theta = 0°$, in our model $N = 1$, $M = 1$. Bottom: same as top, except $s = 2\,\text{mm}$ and $M = 2$.

3.3.3 T-shaped corrugated structure beyond the onset of the first grating lobe

An interesting example is shown in Fig. 3.8, where the magnitude and phase of the reflection coefficient is plotted versus frequency for a T-shaped and non-symmetric corrugated structure. Since an obliquely incident plane wave impinges on the corrugated surface, purely specular reflection is expected only below approximately $34\,\mathrm{GHz}$, the onset frequency at which the $n = -1$ harmonic

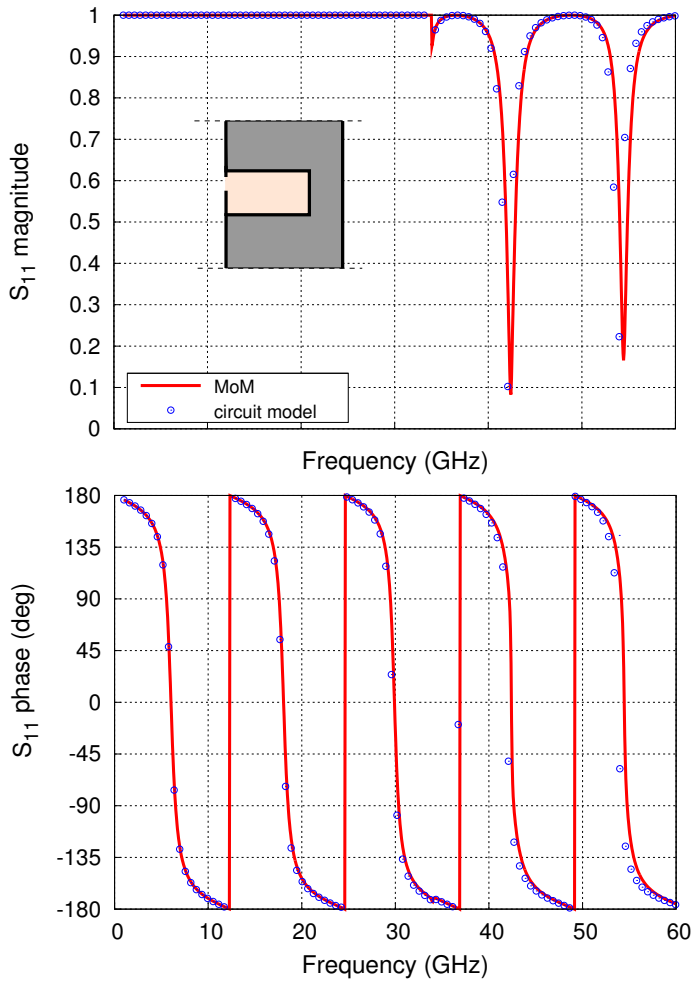

Figure 3.8: Magnitude (top) and phase (bottom) of the reflection coefficient vs. frequency for a structure with $p = 5\,\mathrm{mm}$, $s = 1\,\mathrm{mm}$, $w = 0.5\,\mathrm{mm}$, $d_2 = 5\,\mathrm{mm}$, $h = 0.1$, $\varepsilon_\mathrm{r}^{(1)} = 1$, $\varepsilon_\mathrm{r}^{(2)} = 6$, $\theta = 50°$. In our model, $N = 2$, $M = 1$. The frequency swept in the top plot has been removed, but it is exactly the same as the one used for the bottom plot.

becomes propagative. Above that onset frequency, the reflected power is carried away by the two propagative harmonics ($n = 0, -1$) outside the cavity. As frequency increases, the power ratio transferred to each propagative harmonic varies. The top plot in Fig. 3.8 shows that, around 42 and 54 GHz, the fraction of the reflected power channeled into the zero-order harmonic is very low. In certain frequency bands centered at these two frequencies, most of the power is then "diffracted" to the $n = -1$ harmonic, thus preventing specular reflection. This behavior can readily be understood in terms of our circuit model, as explained next. In the bottom plot of Fig. 3.8, it can be observed that the reflection phase is close to zero at these two reflectivity minima. Indeed, the minima occur when the corrugation depth d_2 is below but close to $7/4\lambda_0^{(2)}$ and $9/4\lambda_0^{(2)}$, with $\lambda_0^{(2)}$ being the wavelength of the TEM (zero-order) mode inside the cavity. At these frequencies the zero-order mode input admittance, $\frac{p}{w}Y_0^{\text{in, R}}$, is inductive and small (recall that $\frac{p}{w}Y_0^{\text{in, R}} = 0$ when the corrugation depth is an odd multiple of $\lambda_0^{(2)}/4$). Hence, the $\frac{p}{s}Y_0^{\text{in, R}}$ admittance can compensate for the small capacitive admittance introduced by evanescent harmonic/modes excited at the slit discontinuity (namely, $\frac{p}{s}Y_0^{\text{in, R}} + \tilde{Y}_{\text{eq}} \approx 0$, where $\tilde{Y}_{\text{eq}}$ stands for the equivalent admittance excluding the effect of the $n = -1$ propagative harmonic). Under these circumstances, the load met at $z = 0$ by the impinging signal in the circuit model is just the real admittance of the $n = -1$ propagative harmonic. If this real admittance is close to the characteristic admittance of the input transmission line ($Y_0^{(0)}$ in this case), there will be good matching and most of the impinging power is transferred to the $n = -1$ propagative harmonic (this matching is found to be better at 41.2 GHz than at 52.7 GHz). At approximately 49 GHz, the whole power returns again along the input line since, at this frequency, $d_2 = 2\lambda_0^{(2)}$ and then $Y_0^{\text{in},(2)} = \infty$, causing a short circuit in the corresponding equivalent circuit. It should be noted that the groove size was chosen small enough to avoid the excitation of propagative modes inside the cavity in the considered frequency range ($s/\lambda_0^{(2)} < 1/2$). Thus, the present structure could be used in applications where specular reflections are not desired. Finally, it should be pointed out that the

numerical results provided by our approach and the MoM agree very satisfactorily, showing a slight deviation at high frequencies as a consequence, once again, of the limitations introduced by the assumed electric field profile. This satisfactory agreement has also been found for other incident angles, even for the limiting case of grazing incidence.

3.3.4 T-shaped corrugated structure with narrow grooves: high-impedance-surface behavior

Previously it has been discussed that the possible application of the T-shaped corrugated structure as a high impedance surface (HIS, obtained when it behaves as an AMC) can be related to corrugation depths satisfying the condition $d_2 \approx (2m+1)\lambda_0^{(2)}/4$. However, this HIS behavior can also be obtained in a different way by using wide and shallow grooves to make that the first propagative mode inside the cavity appears at a frequency lower than that of the first AMC condition (this situation requires $s > 2d_2$). At this point it is convenient to recall that the TM modal admittances grow to infinity as the frequency approaches any of the corresponding modal cutoff frequencies. Thus, for frequencies lower than the cutoff frequency of a given high order mode, the corresponding modal admittance is capacitive and can be as high as desired. For wide and shallow grooves, it implies that, at some frequency below the cutoff of the first high order mode inside the cavity, the capacitive admittance of the high order modes can compensate for the inductive admittance associated with the zero-order TEM standing wave inside the cavity (so that the admittance of the resulting LC tank is zero). For that frequency, the corrugated structure resonates and behaves as a magnetic conductor (open circuit). This situation is reported in Fig.3.9, which shows the phase of the reflection coefficient versus the normalized frequency for two different configurations. In the top plot, a symmetric structure is analyzed. Since odd high order modes inside the cavity are not considered due to symmetry, the onset of the first high order mode takes place at $s/\lambda_0^{(2)} = 1$. A near-zero phase is observed at $d_2/\lambda_0^{(2)} \approx 0.052$, corresponding to $s/\lambda_0^{(2)} \approx 0.466$.

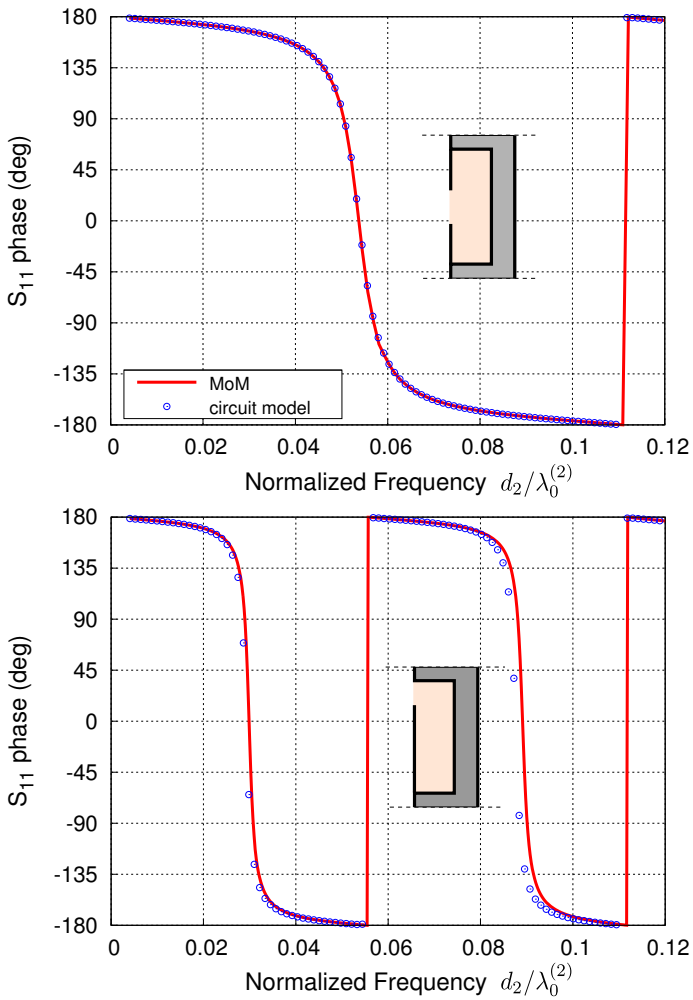

Figure 3.9: Phase of reflection coefficient vs. frequency for two different configurations. Top: $p = 5\,\text{mm}$, $s = 4.5\,\text{mm}$, $w = 0.5\,\text{mm}$, $d_2 = 0.5\,\text{mm}$, $h = 0\,\text{mm}$, $\varepsilon_\text{r}^{(1)} = 1$, $\varepsilon_\text{r}^{(2)} = 5$, $\theta = 30°$. Bottom: Same as top, except $h = 2\,\text{mm}$. $N = 1$, $M = 2$. ©2014 IEEE

The bottom plot shows results obtained for an asymmetric structure with the slit fully displaced. In this case, the onset of the first odd high-order mode is half lower than that of the first even high-order mode, which causes the HIS behavior to be found also at a lower frequency ($d_2/\lambda_0^{(2)} \approx 0.0284$, corresponding to $s/\lambda_0^{(2)} \approx 0.255$). It is interesting to note that these HIS behaviors occur when the groove size is roughly $\lambda_0^{(2)}/2$ and $\lambda_0^{(2)}/4$, respectively. This is consistent with a possible alternative view [84] that considers the propagation of the TEM mode

along the vertical y direction inside the cavity, with the screen and the back wall now forming the parallel-plate waveguide. Under this standpoint, the structure is expected to behave as an AMC when either the upper (seen from the slit aperture) or the lower TEM line is roughly a quarter wavelength long.

3.3.5 Design of an absorber

The AMC behavior of the T-shaped planar corrugated structure discussed above can also be used to design a very thin narrow-band absorber. The underlying reasoning is based on the familiar idea that the electric field is maximum at the aperture under resonance condition, and therefore it may be strongly dissipated by placing a resistive overlay with the appropriate conductivity on top of the corrugations. In principle, this appropriate value of conductivity can be found by matching the real part of the input admittance of the resistive overlay (terminated with an open circuit) to the characteristic admittance of the input transmission line, namely,

$$Y_0^{(0)} = \mathrm{Re}\Big[Y_0^{\mathrm{in,\,L}}\Big] = \mathrm{Re}\Big[\mathrm{j}\hat{Y}_0^{(1)}\tan(\hat{\beta}_n^{(1)}d_1)\Big] \ . \tag{3.25}$$

Assuming that the resistive slab is electrically thin, the above condition leads to

$$Y_0^{(0)} \approx \mathrm{Re}\left[\mathrm{j}\,\frac{\omega\varepsilon_0\hat{\varepsilon}_{\mathrm{r}}^{(1)}}{\hat{\beta}_n^{(1)}}\,\hat{\beta}_n^{(1)}d_1\right] = \sigma_1 d_1 \ . \tag{3.26}$$

However, it should be noted that the condition (3.26) has been obtained considering only the effect that the resistive overlay has on the zeroth-order harmonic. Certainly, the higher-order harmonics will also be affected, and their corresponding admittances in the model also contribute with a real (resistive) part. In other words, the value of the overlay conductivity in (3.26) provides optimum absorption as long as the total field inside the resistive slab is well accounted for by the zeroth-order harmonic field, thus neglecting the strong inhomogeneity of the field in the aperture region. Nevertheless, the value of the conductivity obtained from the proposed coarse matching condition (3.26) can be used as an initial guess in an optimization procedure to enhance the

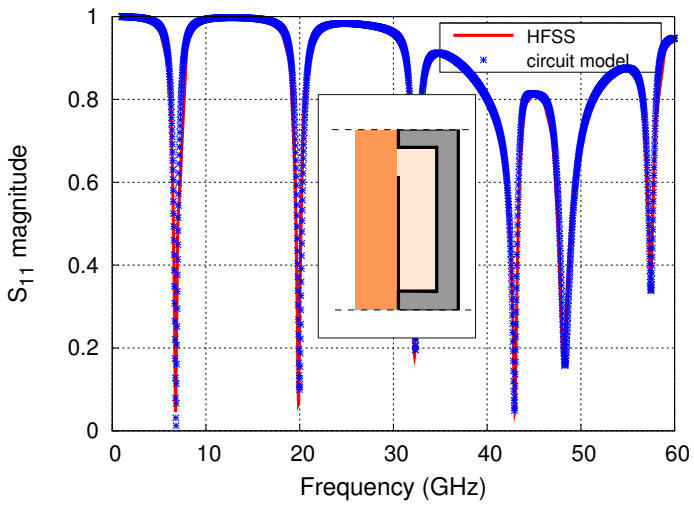

Figure 3.10: Magnitude of reflection coefficient vs. frequency. Structure parameters: $p = 5\,\text{mm}$, $s = 4.5\,\text{mm}$, $w = 0.5\,\text{mm}$, $d_1 = 0.5\,\text{mm}$, $d_2 = 0.5\,\text{mm}$ $h = 2\,\text{mm}$, $\varepsilon_{\text{r}}^{(0)} = 1$, $\varepsilon_{\text{r}}^{(1)} = 12$, $\varepsilon_{\text{r}}^{(2)} = 5$, $\theta = 0°$, $\sigma_1 = 1.088\,\text{S/m}$, $N = 2$, $M = 3$. ©2014 IEEE

level of absorption. Here it should be pointed out that the very fast numerical nature of our circuit model makes it particularly suitable for this optimization procedure. An example under normal incidence is given in Fig.3.10, where the initial conductivity value given by (3.26) was $\sigma_1 = 5.308\,\text{S/m}$, and the final overlay conductivity that provides the good levels of absorption shown in the figure is $\sigma_1 = 1.088\,\text{S/m}$ (the relative permittivity of the cover layer is taken as $\varepsilon_r^{(1)} = 12$ to simulate a silicon substrate). Strong dissipation is observed at certain narrow frequency bands where an AMC resonance condition exists, as expected. These bands alternate with broad bands of high reflection when the frequency is far from the mentioned resonance conditions.

If the incidence angle of the impinging plane wave varies, the admittances of the lines in the model change and so does the optimal value of the conductivity. In order to study this issue, Fig.3.11 shows an incidence angle scanning for different slab thicknesses at the maximum-dissipation frequency (6.34 GHz). For each substrate thickness, the conductivity of the resistive cover layer has been

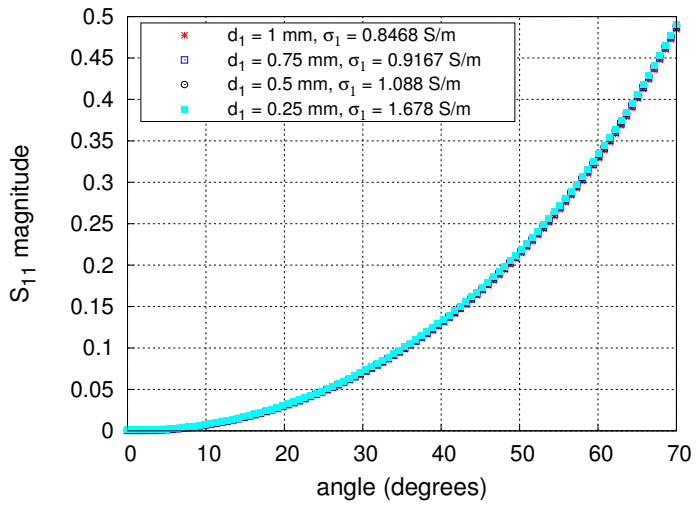

Figure 3.11: Magnitude of the reflection coefficient vs. incidence angle. Structure parameters: $p = 5\,\text{mm}$, $s = 4.5\,\text{mm}$, $w = 0.5\,\text{mm}$, $d_2 = 0.5\,\text{mm}$, $h = 2\,\text{mm}$, $\varepsilon_\text{r}^{(0)} = 1$, $\varepsilon_\text{r}^{(1)} = 12$, $\varepsilon_\text{r}^{(2)} = 5$, Freq $= 6.34\,\text{GHz}$, $N = 1$, $M = 1$. ©2014 IEEE

optimized to obtain minimum reflection at normal incidence. It can be observed how the absorption deteriorates as the incidence angle increases. Nevertheless, the reflection coefficient magnitude is kept below 0.1 (-20 dB) for angles up to around 35°. Thus, for incidence between -35° and 35°, a reflection level below -20 dB is expected. Fig. 3.11 also shows the remarkable fact that the angular variation of the reflection coefficient is almost independent of the overlay thickness.

3.3.6 Lossy grating

As a last example, the accuracy of our equivalent circuit to model a cavity with ohmic losses is studied. In most practical cases, the cavity is usually fabricated with a good conductor and an almost negligible effect of dissipation is expected. In the present example, a lossy conductor is used in order to increase the influence of the ohmic losses. In Fig. 3.12 the reflection coefficient is plotted versus frequency when an oblique plane wave impinges on an asymmetric T-shaped corrugated structure. The dissipation level is low except around the frequencies

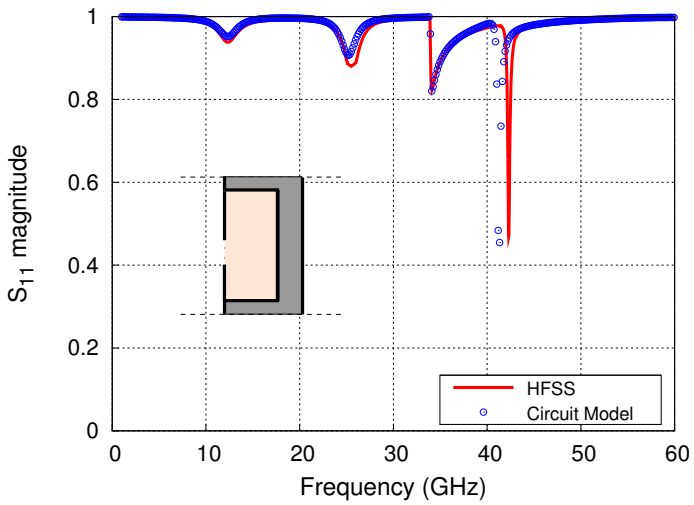

Figure 3.12: Magnitude of the reflection coefficient vs. normalized frequency. Structure parameters: $p = 5\,\text{mm}$, $s = 3\,\text{mm}$, $w = 0.6\,\text{mm}$, $d_2 = 1\,\text{mm}$, $h = -0.6\,\text{mm}$, $\varepsilon_\text{r}^{(1)} = 1$, $\varepsilon_\text{r}^{(2)} = 6$, $\theta = 50°$, $\sigma_\text{m} = 10^6\,\text{S/m}$, $N = 2$, $M = 2$. ©2014 IEEE

for which the structure behaves as an AMC. At these particular frequencies, the reactive admittances of the corresponding equivalent circuit cancel out, resulting in a purely resistive equivalent admittance. Beyond 34 GHz, the structure works in the first grating-lobe regime and the power is split into both propagative harmonics ($n = 0$, $n = -1$), making the effect of losses difficult to visualize. The comparison between our model and HFSS is good for low frequencies and deteriorates at higher frequencies because of the limitations of the model.

3.4 Limits of validity of the model

In the present section we will study the limits of validity of the equivalent circuit for the structure considered in this chapter. In the previous chapter, a study concerning the accuracy of the model in terms of the slit size was carried out. Now, we will extend the study to the analysis of the accuracy of the model in terms of the position of the slit, given by the parameter h, and the proximity of the back electric wall to the slit aperture plane, represented by d. In principle,

setting the slit at a non-symmetric position with respect to the horizontal middle plane of the unit cell introduces a non-negligible odd contribution in the field at the discontinuity, even for normal incidence. We will now check if this effect is properly taken into account by the profile in (3.8), which is symmetric with respect to the middle plane of the slit, but non-symmetric with respect to the horizontal middle plane of the unit cell. The position of the electric wall also influences the slit-aperture field, specially when the wall is close enough to the slit-aperture plane.

3.4.1 Influence of the position of the slit

As a first example, we consider the results plotted in Fig.3.13, which show three different plots for three different positions of the slit aperture (3 different values of h). The structure is immersed in vacuum and TM normal incidence is assumed. Due to the full reflection exhibited by these kind of structures, the phase of the reflection coefficient is plotted versus the normalized frequency. The frequency has been normalized in terms of the wavelength in vacuum. At this point it is important to highlight that following the criterion to normalize the frequency used in the previous chapter for TM incidence on slit gratings (w/λ, with λ being the wavelength in the highest permittivity medium), the conclusions obtained for the case in vacuum could readily be extended to more complex cases with different dielectric media at both sides of the discontinuity. On account on this, we only show results in vacuum in this section. The plot in Fig. 3.13(a) have been obtained for $h = 0$. Results from the MoM and the circuit model are almost identical up to $w/\lambda_0 = 0.6$. Beyond this frequency some differences can be clearly appreciated. The plots in Fig.3.13(b) and Fig.3.13(c), obtained for $h = 0.15p$ and $h = 0.35p$ respectively, show some differences between both kind of results around $w/\lambda_0 \approx 0.4$. In addition, there is not a perfect matching in the results beyond $w/\lambda_0 = 0.2$ in both cases although the differences are minor. It is worth mentioning that according to the structure parameters of the structure (see the caption of the figure), the maximum value allowed

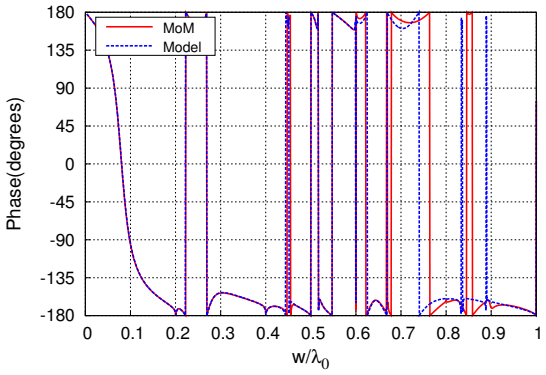

(a) $h = 0\,\text{mm}$

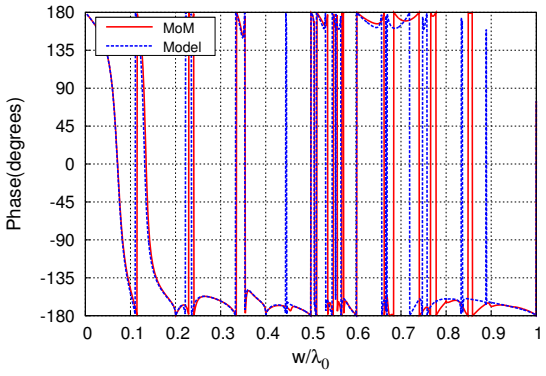

(b) $h = 0.15p$

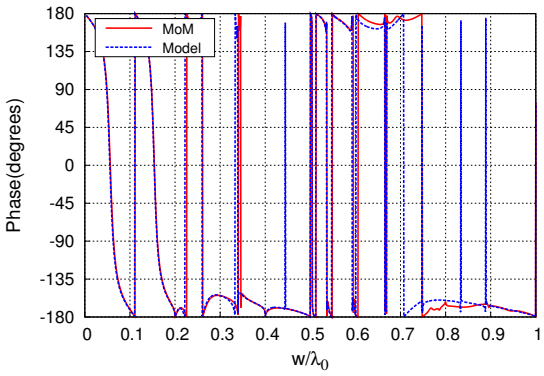

(c) $h = 0.35p$

Figure 3.13: Phase of the reflection coefficient versus normalized frequency for TM normal incidence in vacuum. Structure parameters: $p = 5\,\text{mm}$, $s = 4.5\,\text{mm}$, $w = 1\,\text{mm}$, $d = 1\,\text{mm}$.

for h is $h = 0.35p$ (larger values would place the slit at the same height than the vertical walls of the metallic waveguide), so we can conclude that the model works accurately even up to $w/\lambda_0 = 0.4$ in the most extreme case (highest value allowed for h). Of course this limit is increased, up to $w/\lambda_0 = 0.6$, if the slit is symmetrically placed with respect the horizontal middle plane of the unit cell, $h = 0$.

3.4.2 Influence of the back electric wall

The results discussed above have been obtained for a groove depth (distance between the back electric wall and the slit discontinuity) of $d = 0.2p$. At this position the influence of the electric wall over the field at the slit aperture is expected to be negligible. However, this influence should not be neglected if the wall is closer to the slit-aperture plane. In this sense, in Fig.3.14 we have plotted the phase of the reflection coefficient of a normally-impinging TM plane wave for different groove depths when the structure has the slit centered ($h = 0$, left column) and the structure has the slit at $h = 0.35p$ (right column). The groove depths chosen are, from top to bottom, $d = 0.4p, 0.1p, 0.02p$ in both columns. As expected, the top plots keep the limit of validity deduced in the previous case when the influence of the wall was considered negligible. The middle plots (both right and left), on the contrary, show a deterioration of the results at lower frequencies. The left figure, obtained for a centered slit, begins to deteriorate beyond $w/\lambda_0 = 0.4$ whereas the right figure, with the slit in a non-symmetric position with respect to the horizontal middle plane, shows accurate results up to $w/\lambda_0 = 0.2$. Similar conclusions can be extracted from the bottom plots so that it is clear that the presence of the electric wall affects the field at the slit in these cases. Anyhow, in the worst case and under normal incidence, we observe that the model provides accurate results up to $w/\lambda_0 = 0.2$. In fact, we can also add that the model provides reliable results, in the most extreme case, up to $w/\lambda_0 = 0.4$, and up to $w/\lambda_0 = 0.6$ for the structure with the slit symmetrically placed.

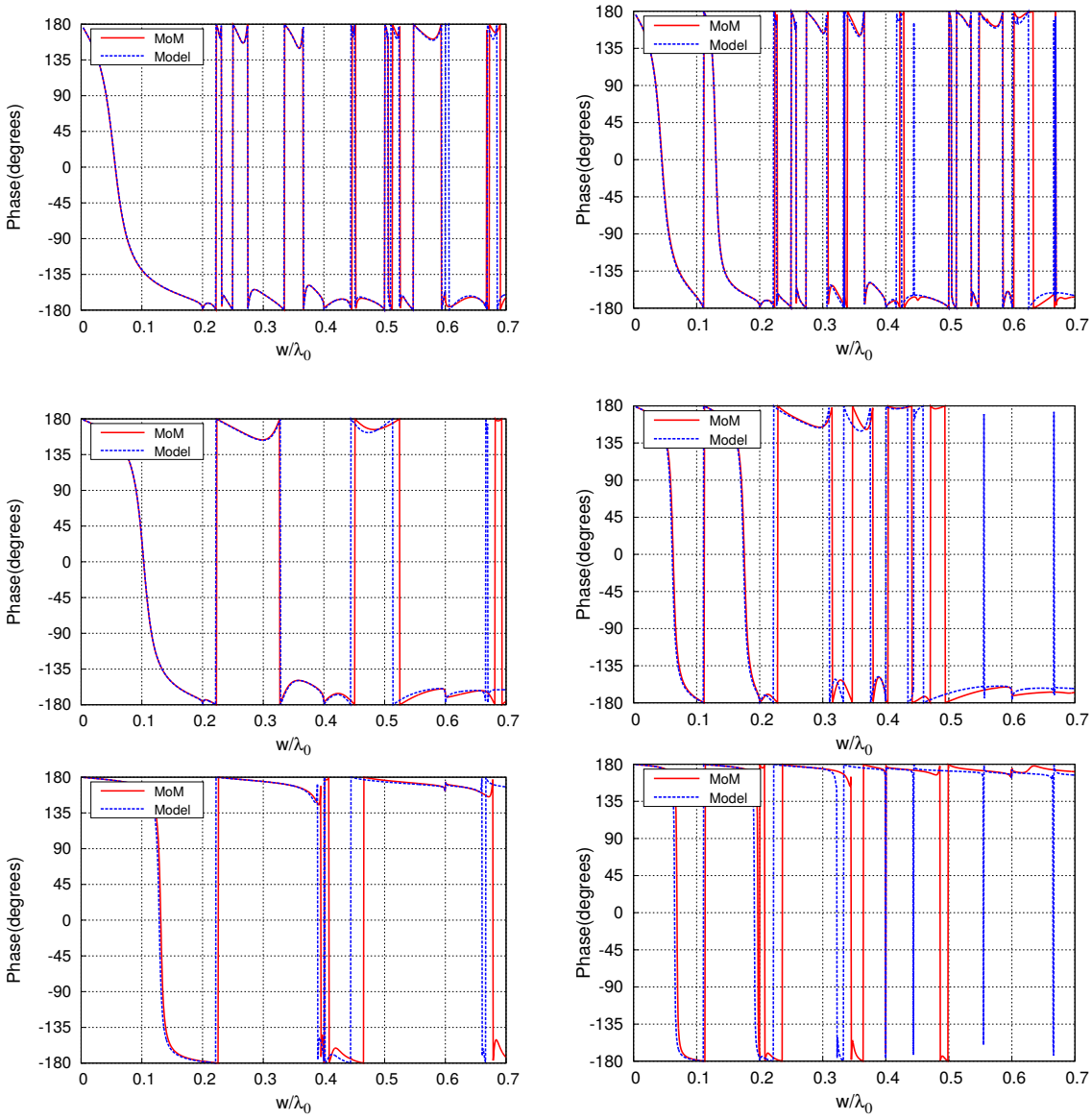

Figure 3.14: Phase of the reflection coefficient versus normalized frequency for TM normal incidence. Structure parameters: $p, s, w, \varepsilon_{\mathrm{r}}^{(1)}, \varepsilon_{\mathrm{r}}^{(2)}$ are identical those used in Fig.3.13. The left column shows results obtained for $h = 0$ mm. The right column shows results for $h = 0.35p$. From top to bottom: $d = 0.4p, 0.1p, 0.02p$ in both columns.

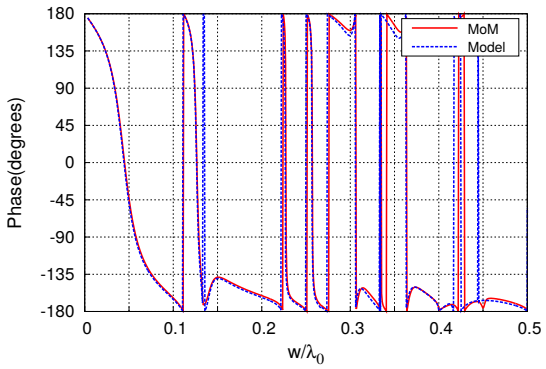

(a) $d = 0.4p$

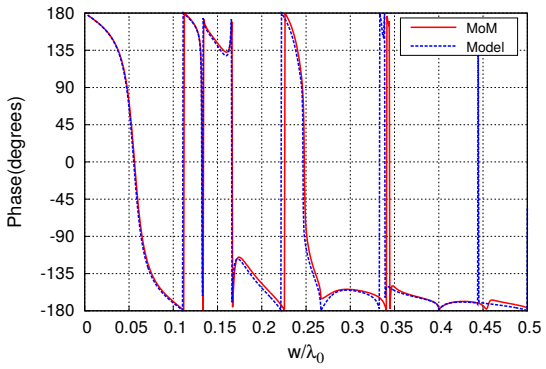

(b) $d = 0.2p$

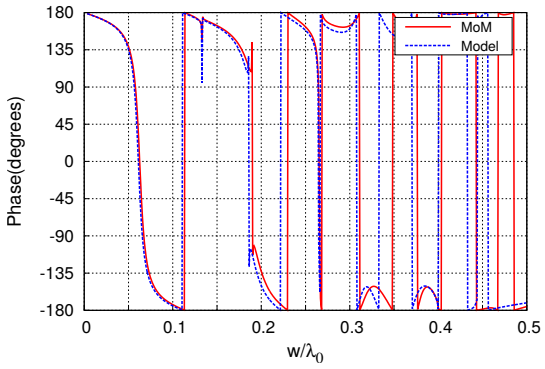

(c) $d = 0.1p$

Figure 3.15: Phase of the reflection coefficient for TM oblique incidence. Structure parameters: $p, s, w, \varepsilon_{\mathrm{r}}^{(1)}, \varepsilon_{\mathrm{r}}^{(2)}$ are identical to those used in Fig.3.13. $h = 0.35p$ and $\theta = 30^o$.

3.4.3 Influence of the incidence angle

Finally, some results are shown for oblique incidence at $\theta = 30^o$ in Fig. 3.15. Three different groove depths are considered for the case of $h = 0.35p$. From top to bottom, they are $d = 0.4p, 0.2p, 0.1p$. The top and middle plots show a good agreement up to frequencies around $w/\lambda_0 = 0.3$, which coincides with half the limit deduced above for normal incidence. The bottom plot also shows reliable results up to $w/\lambda_0 \approx 0.3$. In this sense we can conclude that, for oblique incidence, reliable results are obtained up to $w/\lambda_0 = 0.3$ in all cases, although, of course, the level of accuracy improves slighly as the groove depth is longer. All these conclusions can be extended to more complicated cases considering different dielectric slabs at both sides of the discontinuity if, as we have mentioned above, the normalization of the frequency is carried out according to the criterion employed in the previous chapter for TM incidence on slits gratings.

3.5 Conclusions

A novel equivalent circuit approach has been presented to deal with the scattering of a TM-polarized plane wave obliquely incident on a 1-D periodic T-shaped corrugated surface with an overlay. The key features of our approach are that the topology of the circuit is deduced rigorously from an integral equation formulation and that closed-form expressions are given for all the circuit parameters. This last feature makes that the computational cost required by the present approach is very low, which can be very advantageous for design and/or optimization purposes. The numerical results obtained with the present circuit model have been compared with a rigorous full-wave MoM method and with the HFSS simulator, as well as with other circuit approaches previously reported in the literature. The agreement is quite good with MoM and HFSS for relatively narrow slits even well beyond the diffraction regime, deteriorating slightly as the electrical size of the corrugation aperture increases. An additional advantage of our

approach comes from the fact that the equivalent circuit allows for a straightforward understanding of the underlying physics of some relevant phenomena in terms of circuital and transmission line concepts. This provides us with the capability of predicting new interesting configurations with potential practical applications. Some of the possible applications that have been discussed in this chapter are an electrically thin high-impedance surface, a structure that avoids specular reflection, and a very thin narrow-band absorber. The equivalent circuit approach has also been extended to incorporate the effect of ohmic losses in the cavity walls.

Chapter 4

1-D Periodic Compound Gratings.

4.1 Introduction

The study of the scattering response of periodic compound gratings has attracted much attention due to their interesting properties. Compound gratings refers to gratings that have more than one scatterer per period. In particular, in the present chapter we will deal with thick gratings having several slits per period. The study of thick compound gratings was linked to their *superdirectivity* properties in the field of passive antennas in the last century [92]. The superdirectivity concept, however, has been known for many decades [94–96] and denotes an arbitrary ultra-directive sharp beam given in a finite-sized radiation system. Based on previous analysis on planar structures with periodically perforated cavities [97–101], the work in [102] predicts that the scattered field from a structure formed by a finite number of slotted cylinders exhibits superdirectivity at certain frequencies. According to the result in [102], in [92] a similar study about superdirectivity was carried out in metal thick and planar screens with 1-D rectangular and different-sized corrugations. In that work the appearance of superdirectivity was directly related to the excitation of a particular resonance, appearing where the fields in different cavities differs in π radians. Such a resonance phenomenon is accompanied with a strong magnetic-field enhancement

inside the resonant cavities. This particular resonance is the so-called *phase resonance* [27].

Phase resonance, mainly given in structures containing several individual resonators, is exhibited when, at least, two of these resonators resonate between them [102]. For instance, a particular case of such resonant structure is a corrugated surface with different cavities, as the one reported in [92]. Further studies concluded that corrugated surfaces consisting of periodic gratings comprising several identical corrugations per period also show phase resonance. In [27] an exhaustive study about phase resonance is carried out in gratings having several rectangular corrugations per period, also called *reflection* compound grating. Assuming a TM plane wave impinging normally on the structure, citeFanitno01 explores the connection between the number of slits per unit cell and the number of phase resonances excited along a wide frequency band. The study determined that, for a symmetrical unit cell with identical slits, at least three grooves are required to excite a phase resonance. According to this, compound gratings having one or two identical slits per period will not support phase resonances. Following the line in [27], a in-depth study about the influence of the geometry of the compound-grating unit cell on phase resonances is reported in [103]. Phase resonances are also studied in detail when the gratings are exposed to obliquely-incidence radiation [104]. The possible practical interest of phase resonances is not linked only to superdirectivity. At frequencies far below the first grating lobe, phase resonance is manifested in lossy compound gratings as a strong absorption peak [105]. No clear interpretations are found in the literature about this surprising phenomenon (a 60%-absorption peak can be achieved in copper-gratings).

Transmission compound gratings also present interesting properties linked to phase resonances. Transmission compound gratings are, for the scope of this chapter, thick metallic gratings having several slits per period. In transmission

compound gratings, phase resonance is theoretically reported [106–108] and experimentally measured [109–111] as a narrow transmission dip inside a Fabry-Pérot (FP) transmission band. These spectral properties in transmission gratings have been exploited in two-slit compound gratings at optical frequencies. As was mentioned above, compound gratings with two identical slits do not exhibit phase resonance [112, 113]. On the contrary, gratings with two different slits per period [114, 115] or two identical slits per period exposed to obliquely-incident radiation [116] do exhibit phase resonance.

In this chapter we will study in detail the rich phenomenology associated with compound gratings. Most of the theoretical studies reported in the papers cited above addressed the compound-grating problem in terms of a mode-matching method. Mode matching provides accurate numerical results but it is computationally demanding. In the literature, previous heuristic circuit models were proposed in [24, 117] in order to explain extraordinary transmission (which also appears in compound gratings). The circuit elements of the circuit were obtained via external full-wave simulations, and they do not work properly beyond the onset of the first grating lobe. In order to extend the use of the circuit model to a wider range of frequencies, here we present an equivalent circuit derived from the electric field integral equation. In fact, this derivation was explicitally developed in Chapter 1 for a compound grating whose unit cell is reducible to a two-slit discontinuity problem. The approach provides fully-analytical and self-consistent expressions for all the circuit elements, including the dynamical behaviour of the structure. The derivation of such a circuit is now extended to compound gratings having a higher number of slits per period, symmetrically and non-symmetrically distributed along the unit cell of the structure. We will also briefly consider the case of oblique incidence, giving a solution for the problem although not providing an explicit topology for the circuit model. Ohmic losses will be included in the model by using the strong skin effect of the approximation already used for T-shaped corrugations in Chapter 3. Finally, we will also include the plasma behaviour of metals in the circuit model, in order to reproduce the scattering properties of compound gratings

operating in THz/infrared regime. Many comparisons with commercial solvers are provided, both for frequency ranges far below and above the onset of the first grating lobe. Finally, a brief discussion about the limits of validity of the model is also added at the end of the present chapter.

4.2 Compound grating whose unit cell is reducible to a two-slit discontinuity problem.

In the present section we will deal with 1-D compound gratings whose unit cell reduces to the two-slit discontinuity problem previously analyzed in Chapter 1. This kind of gratings includes not only compound gratings with two slits per period, but also gratings with three and four slits per period when they satisfy some symmetry restrictions; namely, the slit distribution must be symmetrical with respect to the middle plane of the unit cell (slits located at opposite positions with respect to the middle plane must be identical, and the incidence of the plane wave must be normal). These conditions ensure that the field distribution at slits located at opposite positions with respect the horizontal middle plane of the unit cell are identical. This fact allows us to reduce the analysis to a half unit-cell problem, thus reducing the three- and four-slit discontinuity problem to a two-slit discontinuity problem. The restriction concerning the incident direction of the impinging plane wave is also necessary for the case of compound grating with two slits per period. In fact, this restriction is crucial in order to derive the equivalent circuit, as it was advanced in Chapter 1, in order to satisfy the condition in (1.101). Summarizing, the model obtained in Chapter 1 is valid for gratings with two slits per period, which may be different and can be arbitrarily distributed along the unit cell, and for gratings with three and four slits per period simmetrically distributed within the unit cell. In all cases, the incidence must be normal.

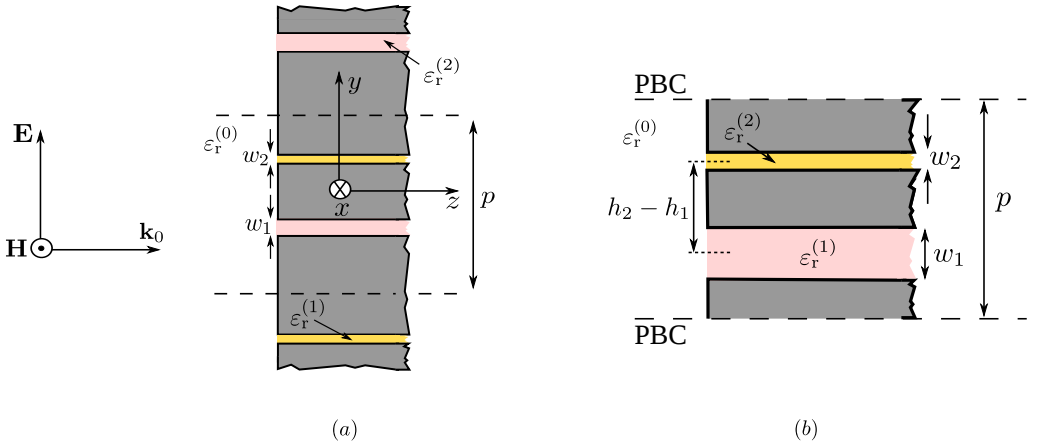

Figure 4.1: (a): Structure to be characterized. The discontinuity is constituted by two different slits. (b): Corresponding unit cell.

4.2.1 Equivalent circuit for 1-D compound gratings with two slits per period. Characterization of the discontinuity

We will first particularize the equivalent circuit in Fig. 1.12 for the compound grating with two slits per period. The structure under consideration is shown in Fig. 4.1(a), and its corresponding unit cell is sketched in Fig. 4.1(b). The unit cell shows a general situation, where the metallic structure has two slits with different sizes. The center of each slit is separated h_1 and h_2 from the horizontal middle plane of the unit cell, so that the distance between the center of both slits is $h_2 - h_1$. The external region, denoted by (0), is bounded by PBC (generalized waveguide), so that the field in this region can be represented in terms of Floquet harmonics. At this point, it is important to remark that only TM incidence will be considered in the present chapter. The interaction of TM waves with the structure provides a rich phenomenology associated with the scattered fields whereas TE waves barely interact with the structure. Then, the proper set of modes for the external region is described by the following orthonormal basis of TM Floquet harmonics,

$$\mathbf{e}_{n,\mathrm{TM}}^{(0)} = \frac{1}{\sqrt{p}} \mathrm{e}^{-\mathrm{j}k_n y}\, \hat{\mathbf{y}}\,. \tag{4.1}$$

On the other hand, the internal region involves the metallic structure. Both slits, which might be filled with a dielectric substrate, are actually parallel-plate waveguides bounded by perfect electric conductors. Due to the assumed small size of the slits with respect the operation wavelength, the field inside can be described in terms of the fundamental or TEM mode supported by each waveguide. Introducing the appropiate normalization constants, the modal profile of the TEM mode for each waveguide is given by

$$\mathbf{e}_{0,\mathrm{TM}}^{(i)} = \frac{1}{\sqrt{w_i}} \qquad i = 1, 2\,. \tag{4.2}$$

Now, let the electric field distribution at each slit aperture be represented by a constant profile; that is,

$$\mathbf{E}_{\mathrm{s}}(\omega, y) = g_1(\omega)A_1 + g_2(\omega)A_2, \tag{4.3}$$

with A_i being the field profile corresponding to slit (i) and defined for the interval $-w_i/2 + h_i < y < w_i/2 + h_i$. Therefore, the specific expression in (1.74) corresponding to the projection of a nth-order harmonic $\mathbf{e}_{n,\mathrm{TM}}^{(0)}$ over the field profiles A_i are

$$\tilde{f}_n^{(i)} = \frac{A_i w_i}{\sqrt{p}} \operatorname{sinc}(k_n w_i/2)\mathrm{e}^{\mathrm{j}k_n h_i} \qquad i = 1, 2 \tag{4.4}$$

with $\operatorname{sinc}(\cdot)$ being the cardinal sine function. Analogously, the expressions in (1.75) and (1.76) involve the projection of the TEM mode over the field profile at each aperture. Assuming the profile in (4.3), we now have

$$S_0^{(i)} = A_i\sqrt{w_i} \qquad i = 1, 2\,. \tag{4.5}$$

Using (4.4) and (4.5), the turn ratios of the transformers previously defined for the admittance expressions in (1.88), (1.89), (1.90), (1.93), (1.94) and (1.95) now

become

$$\left|\frac{\tilde{f}_n^{(i)}}{\tilde{f}_0^{(i)}}\right|^2 = \mathrm{sinc}^2(k_n w_i/2) \qquad i=1,2 \tag{4.6}$$

$$\frac{\tilde{f}_n^{(1)}[\tilde{f}_n^{(2)}]^*}{\tilde{f}_0^{(1)}[\tilde{f}_0^{(2)}]^*} = \mathrm{sinc}(k_n w_1/2)\mathrm{sinc}(k_n w_2/2)\mathrm{e}^{\mathrm{j}k_n(h_1-h_2)} \tag{4.7}$$

$$\frac{\tilde{f}_n^{(2)}[\tilde{f}_n^{(1)}]^*}{\tilde{f}_0^{(2)}[\tilde{f}_0^{(1)}]^*} = \mathrm{sinc}(k_n w_1/2)\mathrm{sinc}(k_n w_2/2)\mathrm{e}^{-\mathrm{j}k_n(h_1-h_2)} \tag{4.8}$$

$$\left|\frac{\tilde{S}_0^{(i)}}{\tilde{f}_0^{(i)}}\right|^2 = \frac{p}{w_i} \qquad i=1,2\,. \tag{4.9}$$

From (4.7) and (4.8) we construct Y_{12} and Y_{21} according to the expressions in (1.89) and (1.93). Although the nature of the individual nth-order transformers in (4.7) and (4.8) is complex, it can be demostrated that for Y_{12},

$$\begin{aligned} Y_{12} &= {\sum_n}' Y_n^{(0)}\mathrm{sinc}(k_n w_1/2)\mathrm{sinc}(k_n w_2/2)\mathrm{e}^{\mathrm{j}k_n(h_1-h_2)} \\ &= 2\sum_{n=1}^{\infty} Y_n^{(0)}\mathrm{sinc}(k_n w_1/2)\mathrm{sinc}(k_n w_2/2)\cos[k_n(h_1-h_2)] \end{aligned} \tag{4.10}$$

resulting in a purely real admittance. Proceeding identically with Y_{21} we finally obtain the same result, satisfying $Y_{12} = Y_{21}$. This condition is fullfilled because the admittances become real-valued functions, which come from the consideration of normal incidence. This would not have been possible for oblique incidence. The expression in (4.9) shows a ratio between the dimensions of both waveguides. Actually, such a factor can be used to redefine the characteristic admittances of the lines that model the propagation of the TEM mode inside the slits. As discussed in the previous chapter, this factor is in agreement with the classical definition of the characteristic admittances for transmission lines in terms of their associated voltages and currents. The equivalent circuit can finally be represented as the one in Fig. 4.2, where the elements are those in (1.102), (1.103), (1.108) and (1.109), which are calculated by introducing the corresponding expressions of the transformers.

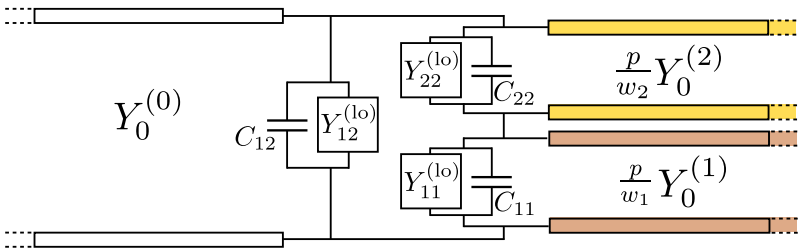

Figure 4.2: Equivalent circuit for the discontinuity shown in Fig. 4.1. The characteristic admittances of the lines have been adequately scaled.

4.2.2 1-D compound gratings with three and four slits per period. Characterization of the discontinuity

As mentioned above, the unit cell of compound gratings with three and four slits per period must be symmetrical with respect to its horizontal middle plane in order to be analyzed as a two-slit discontinuity problem. In Fig. 4.3(a) and Fig. 4.3(b) both structures are shown. Their corresponding two-slit unit cells are depicted in Fig. 4.3(c) and Fig. 4.3(d). Due to the symmetry with respect to $y = 0$, and the normal incidence, the external region is now bounded by virtual electric walls. It is then interpreted as a parallel-plate waveguide whose plates are separated $p/2$. The field in this region is described in terms of the modes of such a waveguide, whose nth-order modal profiles are now described as

$$\mathbf{e}_{n,\mathrm{TM}}^{(0)} = \sqrt{\frac{4 - 2\delta_{n,0}}{p}} \cos(k_n y) \tag{4.11}$$

with $k_n = \frac{2n\pi}{p}$. The internal region is identical as the one described for the previous case, although it is important to remark that for the compound grating with three slits per period, the waveguide (1) is, for the resulting unit cell in Fig.4.3(c), $w_1/2$ wide and its center is placed at $h_1 = 0$. Assuming the electric field in (4.3) at the slit aperture plane, the projection of the modes over such a profile is written

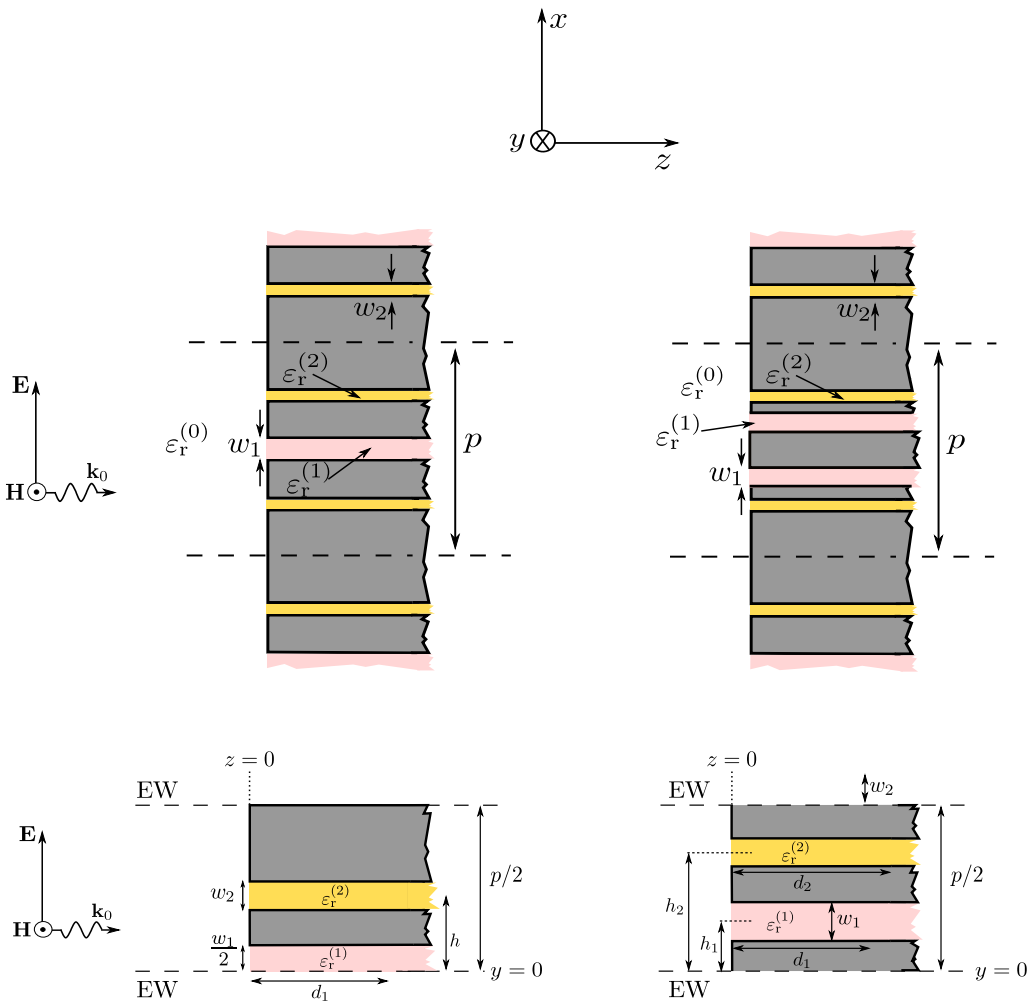

Figure 4.3: (a): Three-slit compound grating. (b) Four-slit compound grating. (c) and (d) represent the half unit cell for the three- and four-slit compound grating respectively.

for the three-slit compound grating as follows:

$$\tilde{f}_n^{(1)} = A\sqrt{\frac{4-2\delta_{n,0}}{p}}\operatorname{sinc}(k_n w_1/2)\cos(k_n h_1) \tag{4.12}$$

$$\tilde{f}_n^{(2)} = B\sqrt{\frac{4-2\delta_{n,0}}{p}}\operatorname{sinc}(k_n w_2/2)\cos(k_n h_2) \tag{4.13}$$

$$\tilde{S}_0^{(1)} = A\sqrt{\frac{w_1}{2}} \tag{4.14}$$

$$\tilde{S}_0^{(2)} = B\sqrt{w_2}\,. \tag{4.15}$$

In consequence, the transformer ratios can be expressed in the following way:

$$\left|\frac{\tilde{f}_n^{(i)}}{\tilde{f}_0^{(i)}}\right|^2 = 4\,\mathrm{sinc}^2(k_n w_i/2)\cos^2(k_n h_i) \qquad i = 1,2 \tag{4.16}$$

$$\frac{\tilde{f}_n^{(1)}\,\tilde{f}_n^{(2)}}{\tilde{f}_0^{(1)}\,\tilde{f}_0^{(2)}} = 4\,\mathrm{sinc}(k_n w_1/2)\mathrm{sinc}(k_n w_2/2)\cos(k_n h_1)\cos(k_n h_2) \tag{4.17}$$

$$\left|\frac{\tilde{S}_0^{(1)}}{\tilde{f}_0^{(1)}}\right|^2 = \frac{p}{w_1} \tag{4.18}$$

$$\left|\frac{\tilde{S}_0^{(2)}}{\tilde{f}_0^{(2)}}\right|^2 = \frac{p}{2w_2} \tag{4.19}$$

where $h_1 = 0$. The scaling factor "2" appearing in (4.19) refers to the ratio between the dimensions of the unit cell, $p/2$ and the waveguide (2), w_2.

For the four-slits compound grating, the above expressions are identical excepting (4.14) and, consequently, (4.18) because the size of the slit (1) is w_1. Thus,

$$\tilde{S}_0^{(1)} = A\sqrt{w_1} \tag{4.20}$$

and

$$\left|\frac{\tilde{S}_0^{(1)}}{\tilde{f}_0^{(1)}}\right|^2 = \frac{p}{2w_1}\,. \tag{4.21}$$

The equivalent circuit is identical to the one in Fig. 4.2 but considering the corresponding scaling factors for the characteristic admittances of the lines.

4.2.3 Complete model for the reflection and transmission lossless structures

Once the equivalent circuit of the discontinuity that couples the impinging wave to the slits is known, the complete models for both the reflection and transmission structures are obtained quite straightforwardly. For a reflection grating such as, for example, that sketched in Fig. 4.4, we just have to incorporate the termination of the slits into the model. This is achieved simply by placing a short-circuit termination at the corresponding distance from the discontinuity

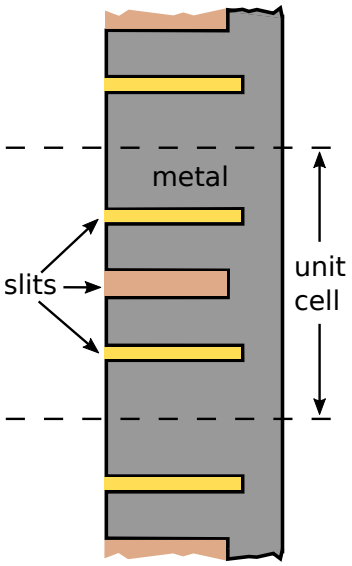

Figure 4.4: . Sketch of a reflection three-slit structure.

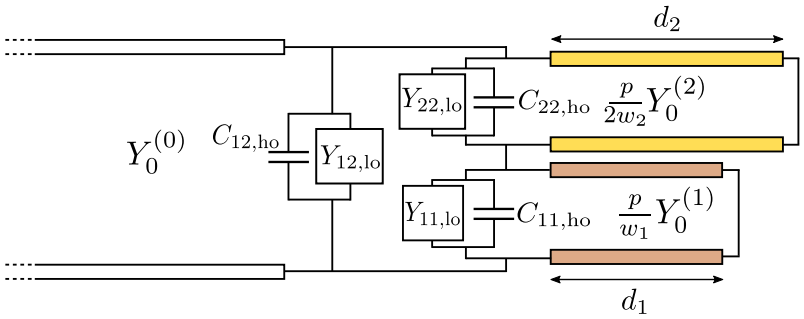

Figure 4.5: Complete circuit model for a reflection compound grating such as that in Fig.4.4. ©2016 IEEE

in each slit transmission line, as shown in Fig. 4.5. The equivalent load admittance met by the impinging wave is then given by

$$Y_{\mathrm{eq}} = Y_{12} + \left[\frac{1}{Y_{11} + \frac{p}{w_1}Y_{\mathrm{in}}^{(1)}} + \frac{1}{Y_{22} + \frac{p}{2w_2}Y_{\mathrm{in}}^{(2)}}\right]^{-1} \tag{4.22}$$

where $Y_{\mathrm{in}}^{(i)}$ is the input admittance to the short-circuited length of transmission line corresponding to slit i, namely,

$$Y_{\mathrm{in}}^{(i)} = -\mathrm{j}Y_0^{(i)}\cot(\beta_0^{(i)}d_i) \tag{4.23}$$

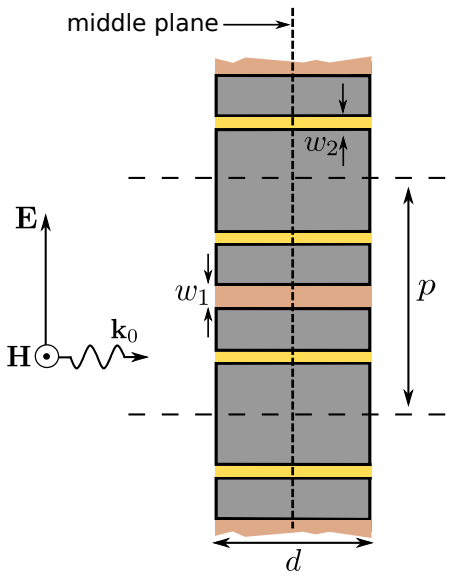

Figure 4.6: Sketch of a transmission compound grating with three slits per period distributed symmetrically in the unit cell. The structure is symmetric with respect to the middle plane. ©2016 IEEE

with

$$\beta_0^{(i)} = k_0\sqrt{\varepsilon_{\mathrm{r}}^{(i)}} \tag{4.24}$$

being the wavenumber of the i-th slit TEM mode. The reflection coefficient is finally obtained using standard transmission line theory as

$$R = \frac{Y_0^{(0)} - Y_{\mathrm{eq}}}{Y_0^{(0)} + Y_{\mathrm{eq}}}\,. \tag{4.25}$$

For the case of a transmission grating such as that sketched in Fig. 4.6, we can take advantage of the symmetry of the structure with respect to the vertical middle plane of the screen to decompose the problem into even- and odd-excitation half problems [24]. For the even excitation case, the middle plane behaves as a virtual magnetic wall. This magnetic wall condition at the middle of the screen translates into open circuit terminations of the slit transmission lines at a distance $d/2$ from the discontinuity (d is the screen thickness). For the odd excitation case, the middle plane behaves as a virtual electric wall, corresponding to short-circuit terminations. Taking into account these considerations, the circuit models for the even- and odd-excitation half problems are

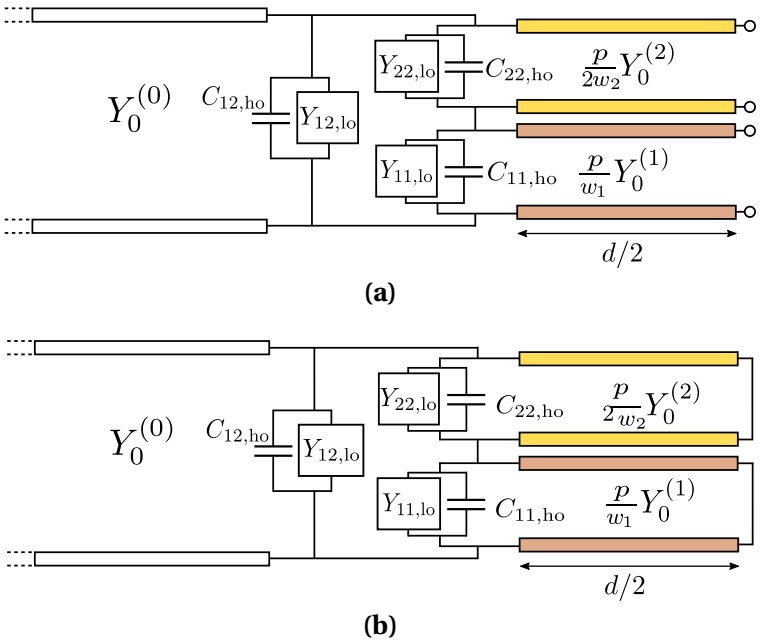

Figure 4.7: Circuit models for the (a) even and (b) odd excitation of the transmission structure in Fig. 4.6. The models differ in the open/short circuit terminations of the slit transmission lines at a distance $d/2$, which correspond to the middle plane behaving as a virtual magnetic/electric wall. ©2016 IEEE

depicted in Fig.4.7. The equivalent load admittance for the even/odd excitation circuits, $Y_{\mathrm{eq}}^{(\mathrm{e/o})}$, is thus given by (4.22), but replacing the input admittances with the ones corresponding to the circuits in Fig.4.7, namely,

$$Y_{\mathrm{in}}^{(i)} = \mathrm{j}Y_0^{(i)} \times \begin{cases} \tan(\beta_0^{(i)} d/2) & \text{even excitation} \\ -\cot(\beta_0^{(i)} d/2) & \text{odd excitation} \,. \end{cases} \tag{4.26}$$

The reflection coefficients for the even/odd excitations half problems are then computed from

$$S_{11}^{(\mathrm{e/o})} = \frac{Y_0^{(0)} - Y_{\mathrm{eq}}^{(\mathrm{e/o})}}{Y_0^{(0)} + Y_{\mathrm{eq}}^{(\mathrm{e/o})}} \,. \tag{4.27}$$

Finally, the reflection and transmission coefficients for the complete structure

are obtained as

$$R = \frac{1}{2}(S_{11}^{(\mathrm{e})} + S_{11}^{(\mathrm{o})}) \tag{4.28}$$

$$T = \frac{1}{2}(S_{11}^{(\mathrm{e})} - S_{11}^{(\mathrm{o})})\,. \tag{4.29}$$

4.2.4 Introduction of losses

Material losses are separately considered (as usual) as dielectric losses in the media filling the slits and ohmic losses in the metallic screen. The dielectric losses are accounted for by simply taking their corresponding complex-valued permittivities:

$$\hat{\varepsilon}_{\mathrm{r}}^{(i)} = \varepsilon_{\mathrm{r}}^{(i)}(1 - \mathrm{j}\tan\delta^{(i)}) \tag{4.30}$$

where $\tan\delta^{(i)}$ is the dielectric loss tangent of the medium inside slit i. From a practical point of view, dielectric losses are rigorously incorporated in the model by introducing the complex permittivities into the expressions of the slit characteristic admittances and wavenumbers.

Although high-conductivity metals behave almost as perfect conductors at microwave frequencies, ohmic losses may be significant at the frequencies of interest when resonances appear. In order to incorporate ohmic losses in the present circuit model, the basic ideas in Chapter 3 can similarly be applied here. In brief, the slits are now considered lossy parallel plate waveguides with complex wavenumbers which, under the good conductor approximation and strong skin effect conditions, are given by

$$\hat{\beta}_0^{(i)} = \beta_0^{(i)}\sqrt{1 + (1 - \mathrm{j})\delta_{\mathrm{s}}/w_i} \tag{4.31}$$

where $\beta_0^{(i)}$ is the wavenumber for the lossless structure and $\delta_{\mathrm{s}} = \sqrt{2/\omega\mu_0\sigma}$ is the skin penetration depth into the metallic walls (σ is the screen conductivity). Assuming a three-slit grating, the characteristic admittances of the slit transmission lines are then obtained considering that

$$\hat{Y}_0^{(i)} = \frac{[\hat{\varepsilon}_{\mathrm{r}}^{(i)}]^{1/2}}{\eta_0} \qquad i = 1, 2\,. \tag{4.32}$$

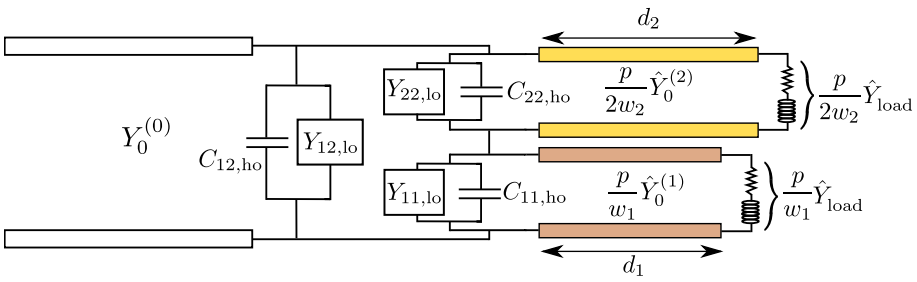

Figure 4.8: Sketch of the circuit model for a lossy reflection grating, showing the complex load admittances at the termination of the slit lines. ©2016 IEEE

For a transmission grating, ohmic losses are introduced in the model just by replacing $Y_0^{(i)}$ and $\beta_0^{(i)}$ with their corresponding complex values $\hat{Y}_0^{(i)}$ and $\hat{\beta}_0^{(i)}$ in (4.26). In the case of a reflection grating, the losses at the bottom wall of the slits can also be accounted for by terminating the slit transmission line with imperfect short loads, as sketched in Fig.4.8. Including these loads is important because high current density levels can appear in the short-circuit termination of the slits at resonance. Under strong skin effect, the values of the load admittances are given by

$$\frac{p}{w_1}\hat{Y}_{\mathrm{load}} = \frac{p}{w_1 Z_{\mathrm{s}}} \quad ; \qquad \frac{p}{2w_2}\hat{Y}_{\mathrm{load}} = \frac{p}{2w_2 Z_{\mathrm{s}}} \tag{4.33}$$

where

$$Z_{\mathrm{s}} = \frac{1+\mathrm{j}}{\sigma\delta_{\mathrm{s}}} \tag{4.34}$$

is the surface impedance of the metal. In consequence, the input admittances in (4.23) have to be replaced with

$$Y_{\mathrm{in}}^{(1)} = \frac{p}{w_1}\hat{Y}_0^{(1)}\frac{\hat{Y}_{\mathrm{load}}^{(1)} + \mathrm{j}\hat{Y}_0^{(1)}\tan(\hat{\beta}_0^{(1)}d_1)}{\hat{Y}_0^{(1)} + \mathrm{j}\hat{Y}_{\mathrm{load}}^{(1)}\tan(\hat{\beta}_0^{(1)}d_1)} \,. \tag{4.35}$$

where we have considered arbitrarily the slit (1).

It should be pointed out that the above considerations account for ohmic losses in all the slit walls, but not in the metallic surfaces out of the slits. This effect could be approximately introduced by adding appropriate resistors. However, as already mentioned above, this contribution can be neglected for good

conductors (e.g., metals at microwave frequencies) since ohmic losses are significant only under specific resonance conditions where most of the power is dissipated inside the slits.

4.2.5 Extension of the equivalent circuit for THz/infrared frequencies.

In the previous section we have described the introduction of ohmic losses in the equivalent circuit. The approximation used in terms of the DC conductivity is valid for good conductors in the microwave regime. However for THz/infrared frequencies, metallic materials become dispersive and the approximations based on a fixed finite DC conductivity becomes inaccurate. A better description of the electromagnetic response of metals at these frequencies is given by the well-known *Drude model* [61], which considers that the metal behaves as a gas of free electrons moving in a fixed background of positive ion cores. The response of a metallic material to an incoming radiation is described by the following frequency-dependent complex permittivity (Drude permittivity):

$$\varepsilon_{\mathrm{r}}^{\mathrm{Drude}}(\omega) = \varepsilon_{\infty} - \frac{\omega_{\mathrm{p}}^2}{\omega^2 - \mathrm{j}\gamma\omega} \tag{4.36}$$

with ω_{p} being the plasma angular frequency, γ the collision frequency, and ε_{∞} a dielectric constant accounting for residual polarization. A particular metal is characterized by its own plasma and collision frequency [119]. For the scope of this work, $\varepsilon_{\infty} = 1$.

Introducing the properties of the metals into the circuit model, the electrical features of the metallic walls of each groove are described by the Drude permittivity [see Fig. 4.9(a)]. Generally, the modes supported by this kind of parallel-plate waveguides are different to the modes supported by a waveguide delimited by perfect electric conductors (especially at higher frequencies). We are interested in finding the propagation constant of the fundamental TM mode,

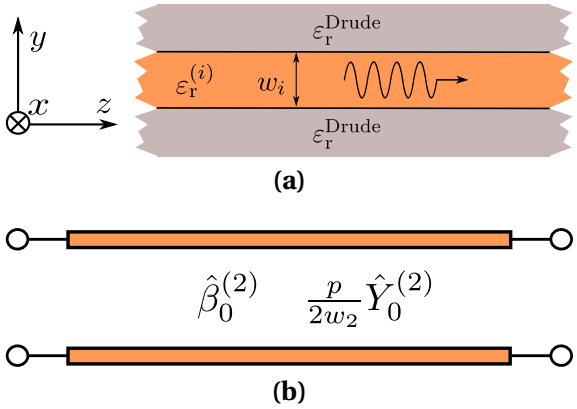

Figure 4.9: (a): Sketch of a plane wave propagating within a parallel-plate waveguide bounded by a Drude material. (b): Equivalent transmission-line, in this case, particularized for the slit 2.

which is obtained after solving the next system of equations [34],

$$\varepsilon_{\mathrm{r}}^{\mathrm{Drude}} k_{\mathrm{y}}^{(i)} \tan(k_{\mathrm{y}}^{(i)} w_i/2) = \varepsilon_{\mathrm{r}}^{(i)} k_{\mathrm{y}}^{\mathrm{Drude}} \tag{4.37}$$

$$\varepsilon_{\mathrm{r}}^{(i)} k_0^2 - [k_{\mathrm{y}}^{(i)}]^2 = \varepsilon_{\mathrm{r}}^{\mathrm{Drude}} k_0^2 - [k_{\mathrm{y}}^{\mathrm{Drude}}]^2 \tag{4.38}$$

where $k_{\mathrm{y}}^{(i)}$ and $k_{\mathrm{y}}^{\mathrm{Drude}}$ represents the transverse component of the wavevector at the media (i) and the metal respectively. The equation in (4.37) is a trascendental equation whose solution can be found numerically by using, for intance, the Muller root-finding method [120]. Once the transverse component of the wavevector is found, its associated propagation constant is calculated according to

$$\beta_0^{(i)} = \sqrt{\varepsilon_{\mathrm{r}}^{(i)} k_0^2 - [k_{\mathrm{y}}^{(i)}]^2}\,. \tag{4.39}$$

As a first approximation, this propagation constant is introduced into the conventional TM-admittance expression,

$$\hat{Y}_0^{(i)} = \frac{\sqrt{\varepsilon_{\mathrm{r}}} k_0}{\eta_0 \hat{\beta}_0^{(i)}}\,. \tag{4.40}$$

Thus, having $\hat{\beta}_0^{(i)}$ and $\hat{Y}_0^{(i)}$, an equivalent transmission can be defined, as shown in Fig. 4.9(b). This transmission line is therefore a generalized version of the lossy line defined in the previous section.

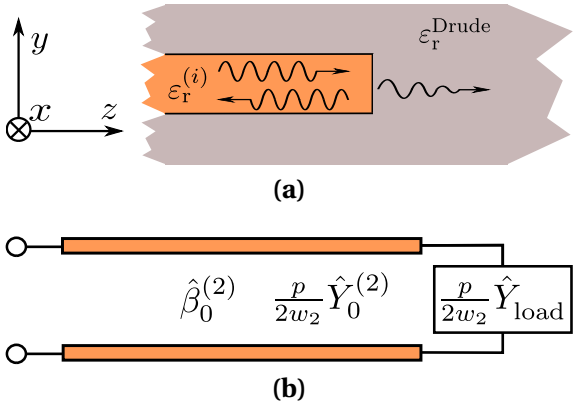

Figure 4.10: (a): Sketch of the back wall found by the propagating wave. (b): transmission-line representation for the slit 2.

The plasma properties of the bottom wall (case of reflection grating) must also be taken into account in the equivalent circuit. This wall can be modelled by using a proper surface admittance [see Fig.4.10(a)], which to a first approximation is described according to

$$\hat{Y}_{\text{load}} = \frac{[\varepsilon_r^{\text{Drude}}]^{1/2}}{\eta_0}\,. \tag{4.41}$$

At lower frequencies, $\omega/\gamma << 1$ in (4.36), so that

$$\varepsilon_r^{\text{Drude}} \approx -\text{j}\frac{\gamma\omega_p}{\omega} = -\text{j}\frac{\sigma}{\varepsilon_0\omega} \tag{4.42}$$

with σ being the DC conductivity of the metal. Introducing this permittivity into (4.41), it reduces to

$$\hat{Y}_{\text{load}} = \frac{\sigma^{1/2}}{\eta_0(\omega\varepsilon_0)^{1/2}} = \frac{1-\text{j}}{2}\sigma\delta_s = \frac{1}{Z_s} \tag{4.43}$$

which coincides with the expression obtained in the previous section.

4.2.6 Equivalent circuit for a compound gratings with more than four slits per period.

This subsection presents the generalization of the circuit model to structures with a higher number of slits in the irreducible unit cell or half unit cell problem. Consider, for instance, a structure with five slits per period distributed symmetrically within the unit cell. The corresponding generalized waveguide discontinuity associated with the half unit cell problem is depicted in Fig. 4.11. By following the same line of reasoning as in Chapter 1 for the voltages at the ports, we will have

$$V_0 = V_1 + V_2 + V_3 \tag{4.44}$$

and for the current at the input port we now have the following three equations with a similar structure as (1.87) and (1.92):

$$I_0 = \left[\bar{Y}_{11} + \frac{p}{w_1} Y_0^{(1)}\right] V_1 + \bar{Y}_{12} V_2 + \bar{Y}_{13} V_3 \tag{4.45}$$

$$I_0 = \bar{Y}_{12} V_1 + \left[\frac{p}{2w_2} \bar{Y}_{22} + Y_0^{(2)}\right] V_2 + \bar{Y}_{23} V_3 \tag{4.46}$$

$$I_0 = \bar{Y}_{13} V_1 + \bar{Y}_{23} V_2 + \left[\bar{Y}_{33} + \frac{p}{2w_3} Y_0^{(3)}\right] V_3 \,. \tag{4.47}$$

The obtaining of the above three equations comes from imposing the continuity of the power flow at each slit aperture, similarly as was proceeded in Chapter 1. Now consider the topology shown in Fig. 4.12, which is the natural extension of

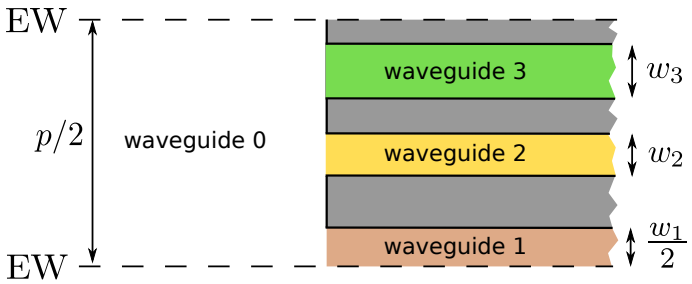

Figure 4.11: (a) Generalized waveguide discontinuity problem associated with the half unit cell of a structure with five slits per period and symmetric unit cell.

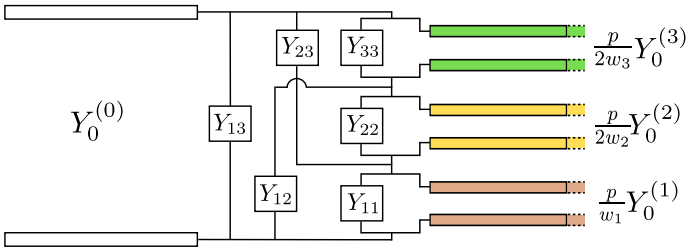

Figure 4.12: Topology of the equivalent circuit for a structure in which the irreducible unit cell or half unit cell problem has three slits. ©2016 IEEE

the topology previously derived in Chapter 1. In this equivalent circuit we can distinguish three coupling orders: a first coupling order represented by the Y_{12} and Y_{23} admittances, which accounts for the interaction between adjacent slits (nearest neighbors); a second order coupling represented by Y_{13} (second nearest neighbor interaction); and a zero-th order coupling (self reaction) associated with the Y_{ii} admittances. The current flowing downward through a longitudinal cut placed at the height of the transmission line corresponding to slit 1 can be written as

$$I_0 = Y_{13}V_0 + Y_{12}(V_1 + V_2) + \left[Y_{11} + Y_0^{(1)}\right] V_1 \ . \tag{4.48}$$

Similarly, the current flowing through longitudinal cuts at slits 2 and 3 are

$$I_0 = Y_{13}V_0 + Y_{12}(V_1 + V_2) + Y_{23}(V_2 + V_3) + \left[Y_{22} + Y_0^{(2)}\right] V_2 \tag{4.49}$$

$$I_0 = Y_{13}V_0 + Y_{23}(V_2 + V_3) + \left[Y_{33} + Y_0^{(3)}\right] V_3 \ . \tag{4.50}$$

Substituting (4.44) into these last three equations and identifying them with (4.45), (4.46), and (4.47), respectively, we obtain

$$Y_{13} = \bar{Y}_{13} \tag{4.51}$$

$$Y_{12} = \bar{Y}_{12} - Y_{13} \tag{4.52}$$

$$Y_{23} = \bar{Y}_{23} - Y_{13} \tag{4.53}$$

$$Y_{11} = \bar{Y}_{11} - Y_{12} - Y_{13} \tag{4.54}$$

$$Y_{22} = \bar{Y}_{22} - Y_{23} - Y_{12} - Y_{13} \tag{4.55}$$

$$Y_{33} = \bar{Y}_{33} - Y_{23} - Y_{13} \ . \tag{4.56}$$

In other words, the admittance Y_{ij} of a given element in the circuit is given by the corresponding barred admittance, $\bar{Y}_{ij}$, minus the admittances of all the elements of higher order coupling that cover the ij element between their connections.

At the light of the above derivation, the generalization to a compound grating whose irreducible unit cell or half unit cell problem comprises N_s slits is rather straightforward. The topology of the circuit model is the natural extension of that in Fig. 4.12, with N_s coupling levels (from 0 to $N_\mathrm{s}-1$). The barred admittances are defined as

$$\bar{Y}_{ij} = 2\sum_{n=1}^{\infty} Y_n^{(0)} \mathrm{sinc}(k_n^{(0)} w_i/2)\mathrm{sinc}(k_n^{(0)} w_j/2)\cos[k_n^{(0)}(h_i - h_j)] \tag{4.57}$$

for structures with non-symmetrical unit cell, and

$$\bar{Y}_{ij} = 2\sum_{n=1}^{\infty} Y_n^{(0)} \mathrm{sinc}(k_n^{(0)} w_i/2)\mathrm{sinc}(k_n^{(0)} w_j/2)\cos(k_n^{(0)} h_i)\cos(k_n^{(0)} h_j) \tag{4.58}$$

for structures with symmetrical unit cell (in this case, if the unit cell has an odd number of slits, in the above formula the h parameter of the central slit is taken as zero, and its w parameter corresponds to half its width). The admittances of the elements in the equivalent circuit are given by ($i \leq j$)

$$Y_{ij} = \bar{Y}_{ij} - \sum_{n,m} Y_{nm} \tag{4.59}$$

$$\text{with } n \leq i\ , m \geq j\ , (n,m) \neq (i,j)\ .$$

4.3 Numerical results

4.3.1 Structures far below the first grating lobe

The present subsection will be devoted to the study of three-slit compound gratings at frequencies far below the onset of the first grating lobe. The same phenomenology that will be explained here is also found in the two- and four-slit

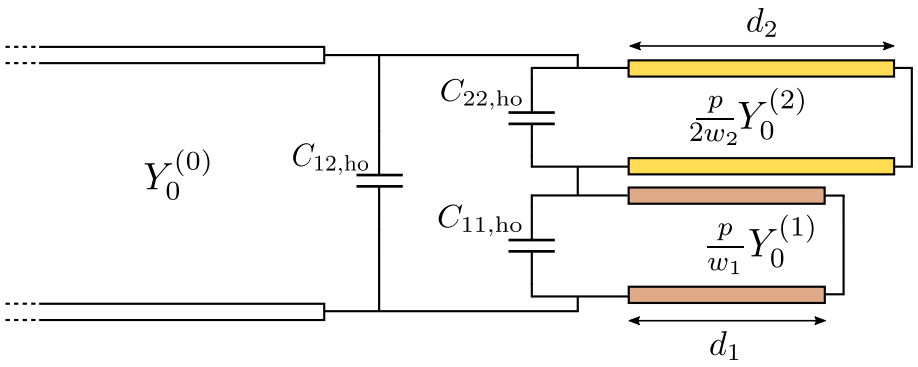

Figure 4.13: Quasi-static circuit model.

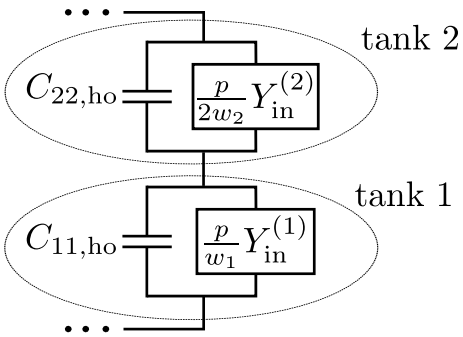

Figure 4.14: Second branch of the circuit, showing two resonators connected in series. Each resonator, formed by a capacitance and the input admittance of the slit transmission line, is labeled as tank 1 or tank 2.

compound gratings. Since the model deduced for the present chapter is topologically more complex than those presented in the previous chapters, we will first introduce a simple discussion of its main characteristics and behavior for frequencies far below the onset of the first grating lobe. At low frequencies, the admittances Y_{ii} and Y_{ij} are well described by their quasi-static approximations, corresponding to purely capacitive admittances whose capacitances are given by(1.102) and (1.103), with $N = 0$. Under this circumstance, the resulting equivalent circuit (shown in Fig.4.13) will be referred to as “quasi-static”.

The elements $C_{11,\mathrm{ho}}$ and $C_{22,\mathrm{ho}}$ are actually the edge capacitances of the slit grooves, which are accounted for by the short-terminated transmission lines. Note that the model in Fig.4.13 corresponds to a reflection compound grating, which will be subject of study in the present subsection. The shunt connection

between each edge capacitance and the input admittance of its corresponding short-terminated line can be recognized as an individual resonator. The rightmost branch (henceforth second branch) of the circuit in Fig. 4.13 is schematically represented in Fig. 4.14, showing both resonators (or tanks). At lower frequencies, the shorted line of each tank behaves as a small inductance (high inductive susceptance), so that the whole tank has an inductive nature. As the frequency increases, the inductive contribution of the tank decreases, whereas the capacitance increases. At certain frequency, it is expected both reactive contributions to be equal, giving rise to the resonance of the tank. Beyond the resonance frequency, the resonator becomes capacitive.

Let us now consider the series connection of both tanks shown in Fig. 4.14. At lower frequencies, the inductive nature of both tanks results in a global inductive impedance of this second branch. In the frequency range between between the resonance frequencies of the two tanks (in general, the individual resonances are found at different frequency values), one of them has already become capacitive whereas the other one is still inductive. In consequence, a series resonance may take place at some frequency value within that frequency range. This series resonance (short circuit) is actually the phase resonance of the circuit. It is important to note that the coupling capacitance C_{12} in the leftmost branch does not play a decisive role in the phase resonance mechanism, and therefore it will not be considered in the discussions presented next about phase resonances.

A first example is shown in Fig. 4.15. These numerical results correspond to a lossless and symmetric reflection compound grating having three slits per period and excited by a TM-polarized and normally incident wave. The phase of the reflection coefficient is plotted versus the frequency (its magnitude is unity). The phase resonance can be recognized in the curve as an abrupt and sudden variation of the phase of the reflection coefficient around 12.1 GHz. The appearance of such a strong and sudden variation within a very narrow band can

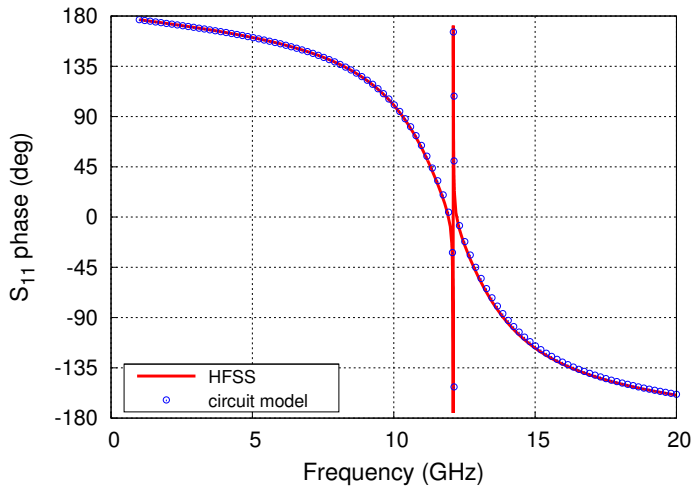

Figure 4.15: Phase of the reflection coefficient versus frequency. Structure parameters: $p = 10\,\text{mm}$, $w_1 = w_2 = 0.8\,\text{mm}$, $d_1 = d_2 = 5.7\,\text{mm}$, $h = 1.6\,\text{mm}$.

be explained in terms of the frequency evolution of the impedances in the second branch, as mentioned above. Thus, the frequency evolution of the reactances of the two tanks is plotted in Fig. 4.16(a). Additionally, the equivalent reactance associated with the series connection of both tanks is also shown in this figure (in green). The phase resonance takes place at the frequency where this last curve crosses zero (short circuit), which, as expected, appears at an intermediate frequency between the individual resonance frequency of both tanks.

Phase resonances are usually accompanied with a *magnetic field enhancement* [27], which consists of a strong increase of the magnetic field inside the grooves. From a circuit point of view, the magnetic field behavior inside the grooves is directly related to the current flowing into the transmission lines. As shown in Fig. 4.16(b), at phase resonance these currents tend to be considerably larger than the current flowing through the input line $Y_0^{(0)}$ (which is related to the magnetic field of the incident and reflected waves). In order to give an appropriate and simple interpretation of the current enhancement, let us consider the sketch in Fig. 4.17. At phase resonance the second branch behaves as a short circuit and there is a current flowing through it whose value is twice the current associated to the impinging wave. In contrast, we observe in Fig. 4.16(a)

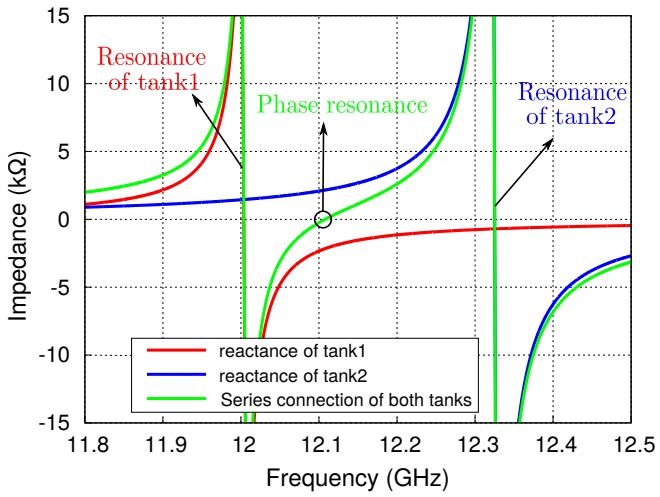

(a)

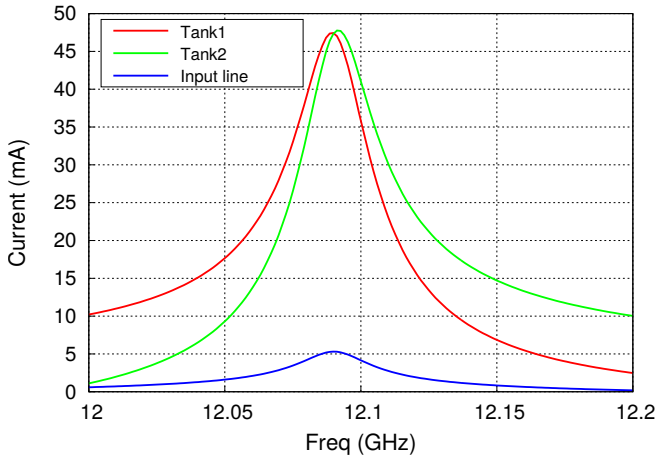

(b)

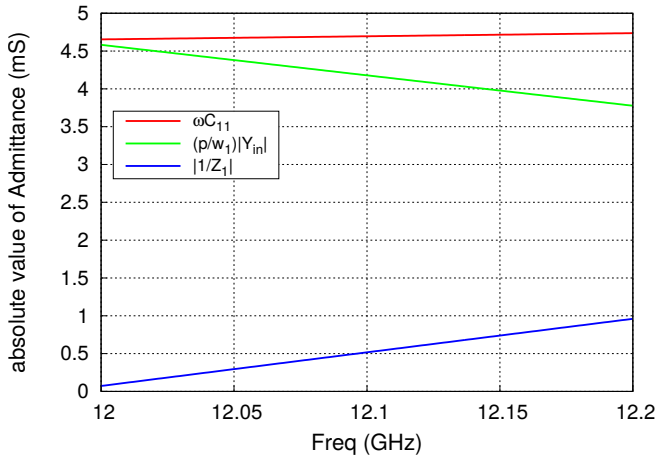

(c)

Figure 4.16: (a): Frequency evolution of the reactive impedances in the phase resonance region. (b): Current flowing into each transmission line around the phase resonance frequency. (c): Susceptances associated with tank 1. Structure parameters: same as inFig.4.15.

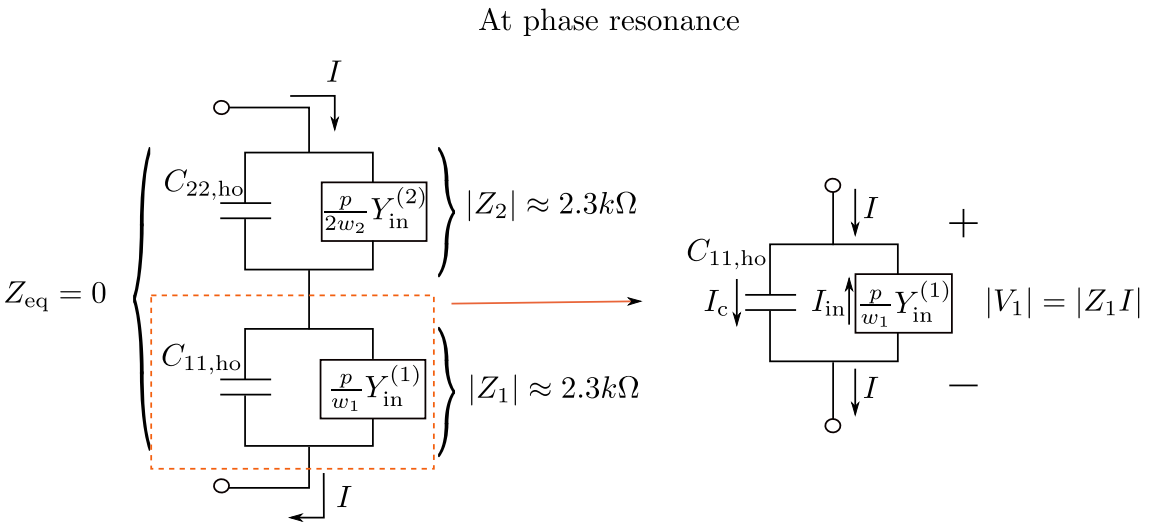

Figure 4.17: Representation of the equivalent circuit and the value of the $|Z_1|$ and $|Z_2|$ reactances at phase resonance.

that each individual tank has a relatively big equivalent impedance (the reactance of both tanks is around $2.5k\Omega$). The voltage associated with each tank is therefore expected to be very high (of course, the voltages in the two tanks have opposite phase since the total voltage in the branch is zero). Focusing on tank 1, whose equivalent impedance has been denoted as Z_1 in Fig.4.17 and numerically represented in Fig.4.16(c), the voltage between its terminals is calculated as $V_1 = Z_1 I$. Its impedance, Z_1, is actually the result of a shunt connection between a capacitor and an input impedance [see for intance Fig.4.14]:

$$\frac{1}{Z_1} = \mathrm{j}\left(\omega C_{11,\mathrm{ho}} - \frac{p}{w_1}|Y_{\mathrm{in}}^{(1)}|\right) \tag{4.60}$$

From Fig.4.16(a), we realize that Z_1 has already become capacitive at phase resonance. Additionally. from Fig.4.16(c), we check that

$$\frac{1}{|Z_1|} \approx \frac{1}{9}\omega C_{11,\mathrm{ho}} \tag{4.61}$$

$$\frac{1}{|Z_1|} \approx \frac{1}{8}\frac{p}{w_1}|Y_{\mathrm{in}}^{(1)}|\,. \tag{4.62}$$

Since $I = V_1/Z_1$, multiplying the right and left member of (4.61) by V_1 we deduce that

$$I \approx \frac{1}{9}\mathrm{j}\omega C_{11,\mathrm{ho}} V_1 \qquad \Rightarrow \qquad |I_{\mathrm{c}}| \approx 9|I| \tag{4.63}$$

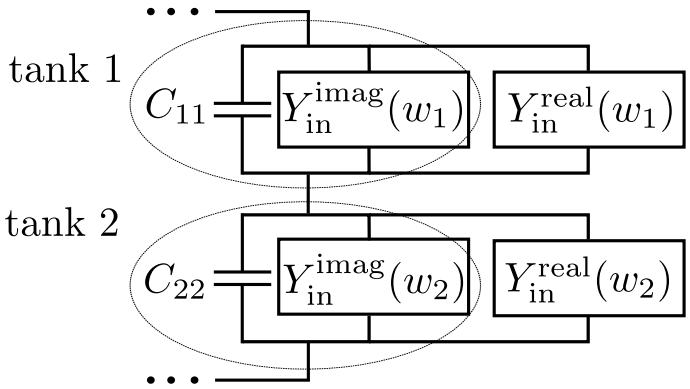

Figure 4.18: Second branch of the circuit including ohmic losses. Ohmic losses are represented by a third element in each tank $Y_{\text{in}}^{\text{real}}(w_i)$.

with I_{c} being the current flowing through the capacitive admittance. Similarly, it can be deduced from (4.62) that

$$|I| \approx \frac{1}{8}\frac{p}{w_1}|Y_{\text{in}}^{(1)}||V_1| \qquad \Rightarrow \qquad |I_{\text{in}}| \approx 8|I| \tag{4.64}$$

with I_{in} being the current flowing through the input impedance seen from the aperture plane. This current is the one related to the magnetic field inside the grooves, which is, according to (4.64) and Fig.4.16(b), about 8 times greater than the current in the branch I. It is worth mentioning that the currents I_{c} and I_{in} satisfy Kirchhoff's rule,

$$I = I_{\text{c}} + I_{\text{in}} \ , \tag{4.65}$$

but, since they have opposite sign (due to the opposite signs of the reactances of the circuit elements they flow through), I_{c} and I_{in} might therefore be several order of magnitude greater than I. An identical rationale can be used to explain the current enhancement in tank 2, also shown in Fig.4.16(b).

The current-enhancement phenomenon could be exploited to obtain a high absorption if we consider a lossy grating instead of a lossless one. The appropriate equivalent circuit for this case is the one drawn in Fig. 4.8. Now the resonators forming the second branch include a non-negligible resistive contribution (see Fig. 4.18) which is responsible for the absorption. The degree of absorption can readily be controlled by tuning this equivalent resistances varying

the geometrical parameters of the unit cell. Indeed for some unit-cell geometries most of the incoming power is efficiently absorbed.

An illustrative example of a compound grating designed to be an efficient absorber is shown in Fig.4.19(a) and Fig.4.19(b), where we have plotted the reflection coefficient, both in magnitude and phase, obtained from a lossy grating with three slits per period under TM normal incidence. The phase-resonance frequency is well recognized in Fig.4.19(b) as the sudden variation in the curve at approximately 12.2 GHz. In the magnitude plot, phase resonance is recognized as a remarkable reflection dip. Note that the absorption level obtained is quite stricking taking into account that the grating material is copper. However it can readily readily understood in terms of an impedance-matching problem between the admittance of the input transmission line, $Y_0^{(0)}$, and the equivalent admittance Y_{eq}. Specifically, the impedance-matching problem can be analyzed in terms of the behavior of the second branch of the equivalent circuit. Thus the reactances and resistances in each resonator are plotted in Fig.4.19(c) and Fig.4.19(d) respectively. The evolution of the reactances in Fig.4.19(c) gives rise to a series resonance between both resonators at a frequency close to 12.2 GHz (zero-crossing of the green line). At this same frequency, the real values of the resistances associated with each individual tank in Fig.4.19(d) are 265 Ω and 122 Ω. The total resistance of the second branch (there is no reactance at phase resonance) is $265+122 = 388\,\Omega$. This value of the resistor matches the characteristic impedance of the input line $Z_0^{(0)} = 377\,\Omega$, so that

$$R = \frac{388 - 377}{388 + 377} \approx 0.014 \tag{4.66}$$

is the expected value of the reflection coefficient of the incident wave. Practically no power is reflected, but it is dissipated in the lossy walls of the grooves. The reflection dip is quite narrow due to the narrow-band nature of the phase resonance, associated to the strong frequency-dependence of the impedances forming the branch at this frequency range.

The frequency dependence of the equivalent resistances/reactances become

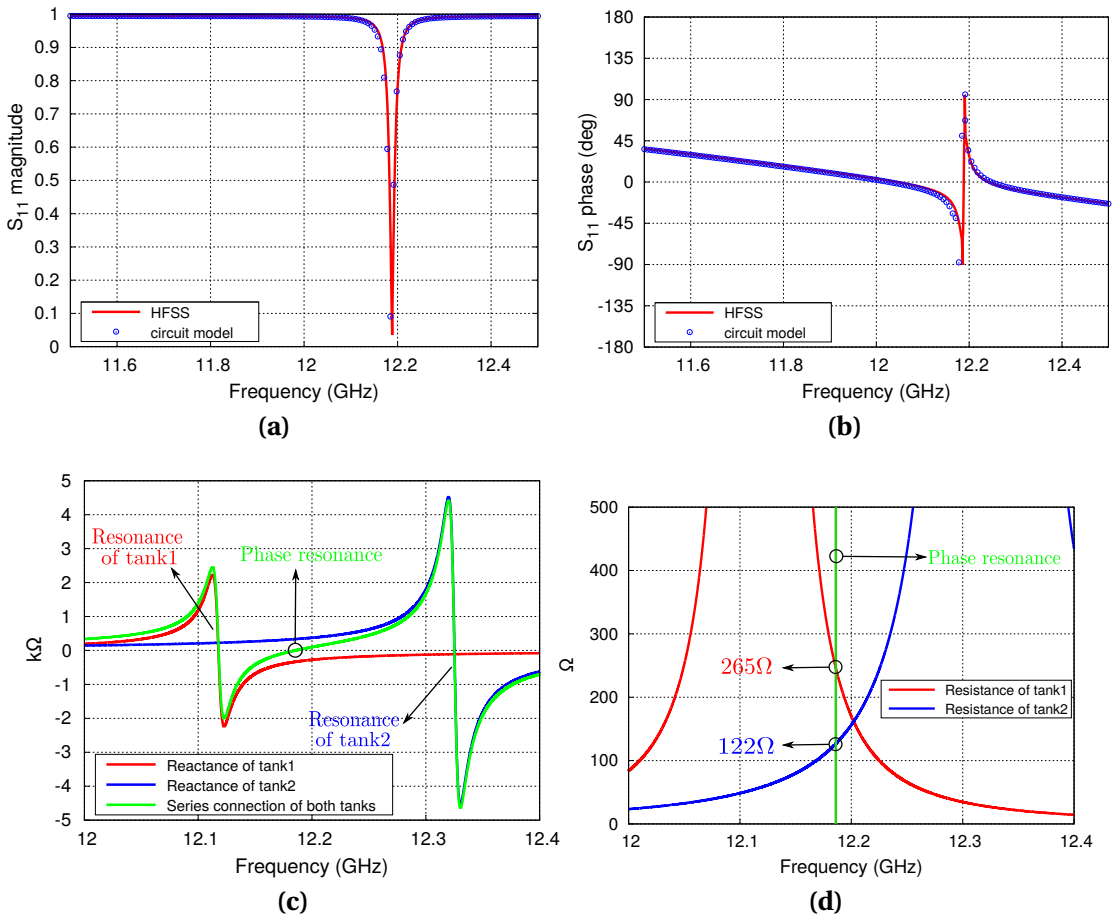

Figure 4.19: (a): reflection coefficient versus frequency in a three-slit compound grating fabricated with a lossy metal. (b): phase of the relfection coefficient. (c): evolution of the reactive impedances in the second branch. The different resonances are also indicated. (d): evolution of the resisitive impedances of each tank. Their values are explicitally indicated at the phase resonance. Structure paramaters: $p = 10\,\text{mm}$, $w_1 = w_2 = 0.8\,\text{mm}$, $d_1 = 5.7\,\text{mm}$, $d_2 = 5.641\,\text{mm}$, $h = 1.6\,\text{mm}$, $\sigma = 5.8 \cdot 10^7\,\text{S/m}$.

smoother in frequency regions far from the resonance frequency of each individual tank. The smooth variation in frequency of the equivalent resistances and reactances would facilitate a wider absorption band. However, we will also check that the matching deteriorates irremediably, thus affecting the performance of the absorber. In order to have a quantitative idea concerning this issue, an example is given in Fig. 4.20. We took the structure in Fig. 4.15, but

modifying d_1 from 5.7 mm to 5 mm and considering ohmic losses (copper). The different groove depths moves away the resonance frequency of the tank. We observe in Fig.4.20(c) and Fig.4.20(d) that, both frequencies differ in more than 1 GHz. Under these circumstances, the resistive contribution of the tanks at phase resonance is quite small, and causes a strong mismatching, as shown in Fig. 4.20(e).The resulting reflection dip is shown in Fig. 4.20(a). The bandwidth has been enlarged in comparison with the previous case, but the absorption efficiency is actually poor.

A last example is depicted in Fig. 4.21, which considers a reflection compound grating with three equidistant and identical slits per period. A grating with equidistant slits can actually be analyzed as a single-slit grating problem (cases in the previous chapters). No phase resonance is expected to appear, so from the point of view of the circuit of the present chapter, it should happen that the individual resonance frequencies associated with both resonators coincide. In Fig.4.21(a) and Fig.4.21(b) the corresponding magnitude and phase of the reflection coefficient are plotted versus frequency. No sharp variation in frequency is appreciated in the phase curve. For instance, the highest absorption level is reached at the frequency where the phase crosses the zero axis, associated with a quarter-of-a-wavelength resonance. The reflection coefficient is practically unity along the entire frequency band of interest, as a consequence of a strong mismatching between the resistive contribution of tanks and the input transmission line, as can be inferred from the behaviour of the impedances in Fig. 4.21(c) and Fig. 4.21(d). Finally we remark the excellent agreement between the numerical results provided by the model and the numerical results from HFSS in all cases.

Phase resonance also appears in the infrared range. A proof of that is the result illustrated in Fig. 4.22, where we have reproduced the reflection coefficient for a three-slit compound grating under an impinging TM-polarized plane wave. The dimensions of the unit cell have been adequately scaled in order to use the quasi-static version of the circuit model at the frequency band of interest. The metallic parts of the grating are described by the Drude model. In this

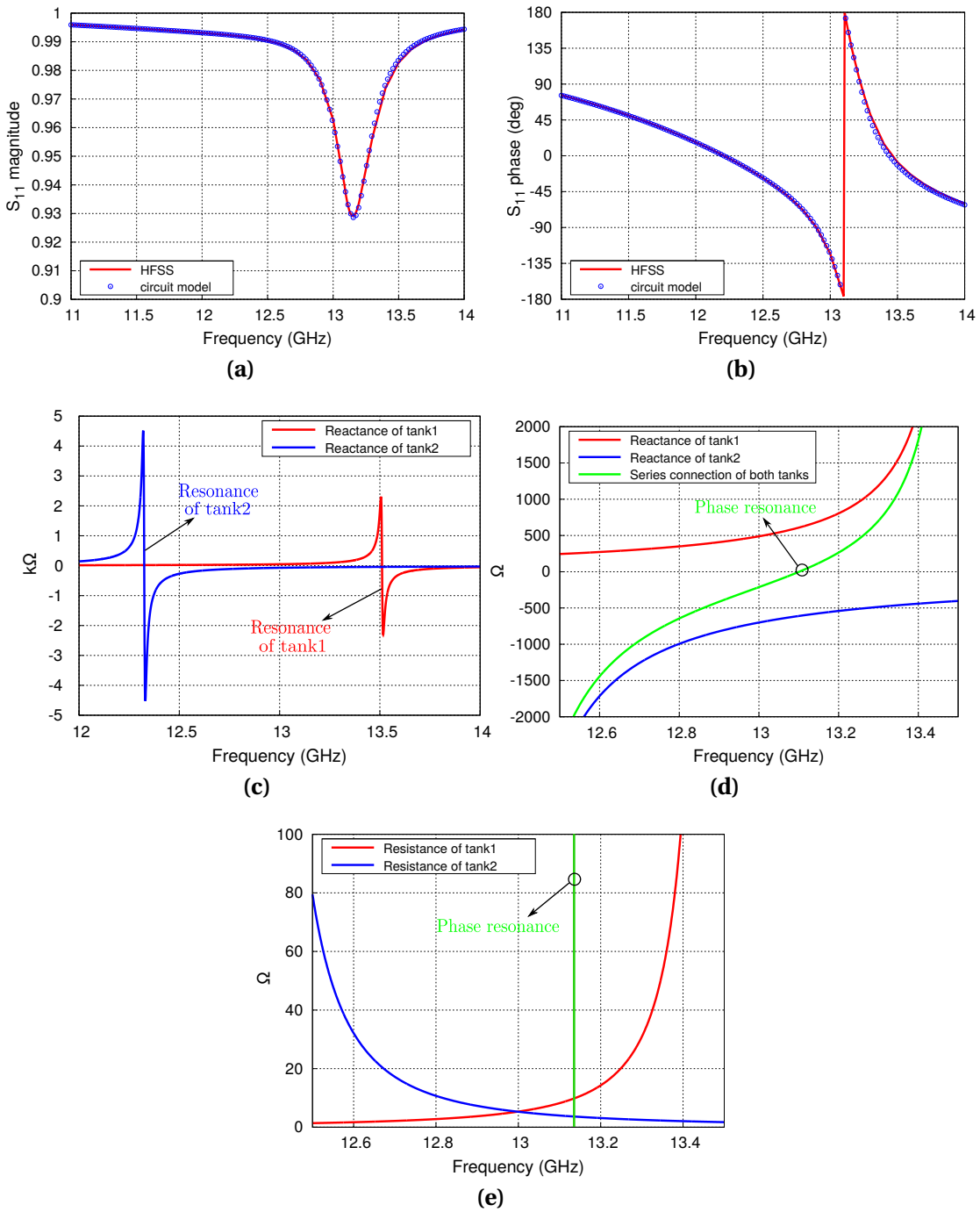

Figure 4.20: (a): reflection coefficient versus frequency in a three-slit compound grating fabricated with a lossy metal. (b): phase of the reflection coefficient. (c): evolution of the reactive impedances in the second branch. (d): zoom of the plot showing the evolution of the reactances. This zoom is made in order to see clearer the frequency of phase resonance. (e): evolution of the resistive impedances in the second branch. Structure parameters: $p = 10\,\text{mm}$, $w_1 = w_2 = 0.8\,\text{mm}$, $d_1 = 5\,\text{mm}$, $d_2 = 5.7\,\text{mm}$, $h = 1.66\,\text{mm}$, $\sigma = 5.8 \cdot 10^7\,\text{S/m}$.

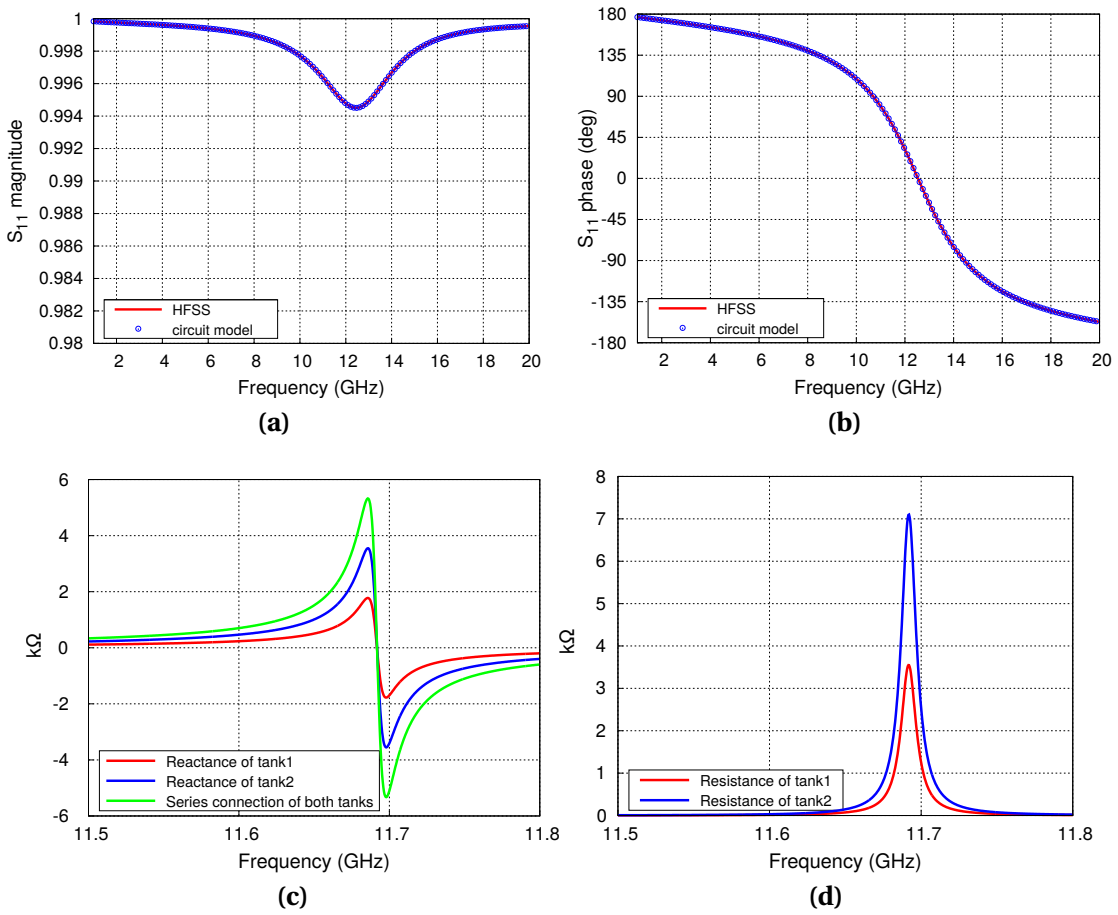

Figure 4.21: (a): reflection coefficient versus frequency in an equidistant three-slit compound grating fabricated with a lossy metal. (b): phase of the reflection coefficient. (c): evolution of the reactive impedances in the second branch. (d): evolution of the resistive impedances in the second branch. Structure parameters: $p = 10\,\text{mm}$, $w_1 = w_2 = 0.8\,\text{mm}$, $d_1 = d_2 = 5.7\,\text{mm}$, $h = 3.33\,\text{mm}$, $\sigma = 5.8 \cdot 10^7\,\text{S/m}$.

case, we have selected the Drude parameters of silver, extracted from [119]. It is demonstrated experimentally in that document that, for the range of interest in Fig. 4.22, the theoretical values of the Drude model reproduce well the experimental properties of silver. In addition, at this range, the penetration depth of the fields in the metal is less than 20 nanometers, so the field penetrating through the lateral walls in one of the grooves do not reach the adjacent groove. In Fig.4.22 three curves are plotted versus frequency. The red solid line presents

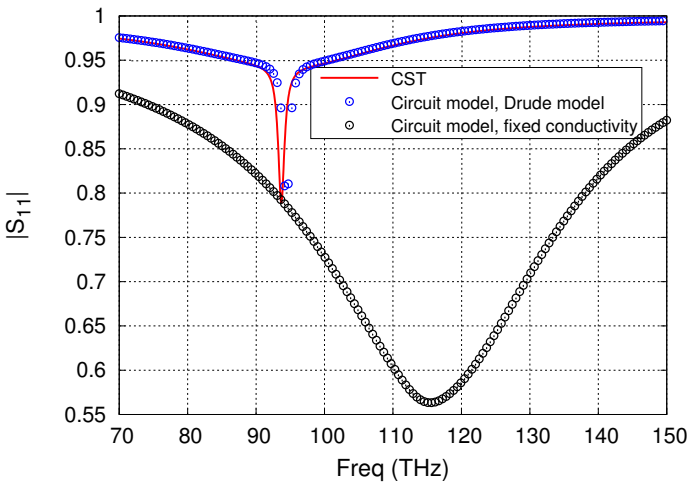

Figure 4.22: Reflection coefficient versus frequency for a three-slit compound grating of silver. at the tera hertz regime. The 'exact' results have been extracted from CST. The results from the model have been obtained by using the Drude model for the metals and by using a fixed-conductivity. Structure parameters: $p = 1\,\mu$m, $d_1 = d_2 = 0.57\,\mu$m, $w_1 = w_2 = 0.08\,\mu$m, $h = 0.2\,\mu$m. Drude parameters of silver: $\omega_p = 1.3914 \cdot 10^{16}$ rad/s, $\gamma = 3.2258 \cdot 10^{13}$ Hz. Fixed conductivity used: $\sigma = 5.13 \cdot 10^7$ S/m.

the results obtained from CST, where a Drude material can be readily considered by introducing its corresponding collition and plasma frequencies. The points represent the results provided by the circuit model. Blue points corresponds to the reflection coefficient calculated considering the Drude model in our circuit. The black points are the reflection coefficient, also provided by the equivalent circuit, but using the approximated model for lossy and good conductors (valid in the millimeter-wave range). The fixed-conductivity value for silver has been calculated at low frequency using the expression in (4.42), after introducing the Drude parameters of silver. The differences between both models are significant. The circuit that uses the Drude model agrees satisfactorily with the results provided by CST. On the contrary, the results from the model with fixed conductivity clearly deviate. In conclusion, the figure confirms the importance of accounting for the plasma behavior of metals at high frequencies.

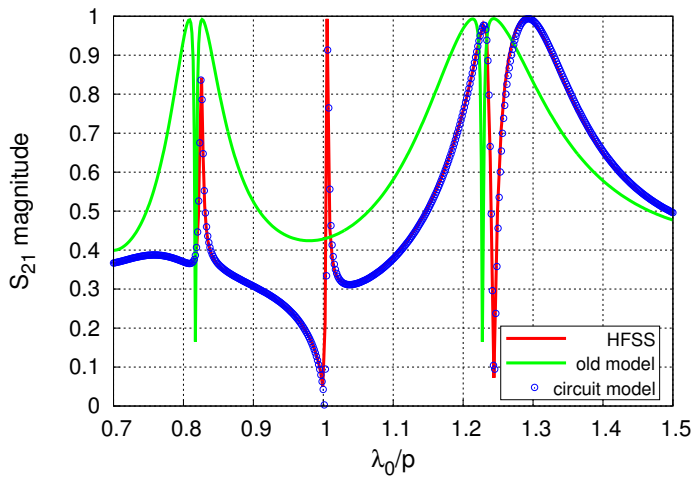

Figure 4.23: Comparison of the transmission coefficients (magnitude) computed with HFSS (red solid line) with the quasi-static [24] (old circuit) predictions (green solid line) and with the dynamical circuit in this paper (blue circles). The considered structure is the three slits per period compound grating analyzed in [24, Fig.5]. Dimensions: period, $p = 10$ mm; metal slab thickness, $d = 11.4$ mm, $w_1 = w_2 = 0.8$ mm and separation between the centers of the slits of 1.6 mm. ©2016 IEEE

4.3.2 Structures close or beyond the first grating lobe.

This section presents some results to check the validity and accuracy of the proposed dynamical model for compound gratings at frequencies close or beyond the first grating lobe, as well as the advantages of this model over the previously reported quasi-static version [24]. The quasi-static version is adequate to study the phenomena occurring at frequencies whose associated wavelength is much larger than the dimensions of the unit cell. On the contrary, the dynamic character of the structure at frequencies close to the onset of the first grating lobe makes the quasi-static circuit reported in [24] and the equivalent circuit here derived different from each other. The derivation of the quasi-static model was heuristic and it is limited to grating configurations having structure parameters much smaller than the operation wavelength. The dynamical features introduced systematically by our approach will allow the model to cover situations beyond the onset of the first grating lobe.

In order to appreciate the limits of the quasi-static model and the capabilities of the dynamical one, a first example considering the transmission-like compound gratings analyzed in [24, Fig. 5] is presented. In that paper it was shown that the quasi-static model was suitable to explain the existence of narrow transmission dips inside the Fabry-Pérot transmission bands for transmission compound gratings based on groups of three or more slits per period (normal incidence case). This phenomenon is closely related to the so-called classical electromagnetically induced transparency. In [24, Fig. 5] it could be seen that the quantitative agreement between the heuristic circuit model predictions and full-wave simulations (HFSS) was quite good for the FP resonance occurring at frequencies for which $\lambda_0/p \approx 2.5$, with λ_0 being the free space wavelength. However, the quantitative agreement significantly deteriorates as the operation frequency approaches the onset of the diffraction regime ($\lambda_0/p \lesssim 1$). A detailed exploration of this frequency range for the three slits per period structure in [24, Fig. 5] is now shown in Fig.4.23. In this figure numerical (HFSS) results are compared with the predictions of the quasi-static model [24] (old model) and with the dynamical model introduced in the present chapter. From the figure it is clear that the quasi-static model still predicts the existence of the transmission dip in the middle of the Fabry-Pérot resonance ($\lambda_0/p \approx 1.23$), but its quantitative accuracy is very poor. In contrast, the results obtained with the dynamical model are indistinguishable from numerical data. This good matching is caused by the incorporation of the frequency-dependent behavior of the capacitances in the model, which is quite relevant in that frequency region. These capacitances exhibit a singular behavior around the Rayleigh-Woods (RW) frequency ($\lambda_0/p = 1$), in such a way that an extraordinary transmission peak followed by a Rayleigh transmission zero (Fano-like resonance) is predicted. This fact is in perfect agreement with the numerical calculation (see region around $\lambda_0/p = 1$ in Fig.4.23) but it is completely lost by the quasi-static model. The results provided by the quasi-static model above the diffraction threshold ($\lambda_0/p < 1$) are completely meaningless, while the data computed with the dynamical model perfectly match the HFSS results within the diffraction region. The above results

show then that the dynamical circuit model is advantageous when used at relatively high frequencies to characterize transmission-like compound gratings, and it is indispensable for frequencies around and above the first RW anomaly.

The case of lossless reflection gratings is of interest in the context of the present section because many interesting properties appear in the diffraction regime. For lossless structures within the *sub-diffraction* regime, nothing relevant is observed in the magnitude of the reflection coefficient; although its phase experiences fast variations around certain frequency points (phase resonance studied in the previous section dedicated to the grating at frequencies far below the onset of the first grating lobe). We observed a very good agreement with the results from HFSS assuming quasi-static capacitors because the frequency of interest is far below the onset of the first grating lobe. However if the operation frequency is sufficiently close to the onset of any high-order mode, the corresponding previously-taken static capacitor should now incorporate a frequency-dependent contribution associated with the involved TM mode. This contribution is singular at cutoff and explains, in the frame of the circuit model, the observation of perfect specular reflection at the RW anomaly frequency points. (Specular reflection is the reflection corresponding to the zero order impinging mode according to the terminology of the equivalent waveguide problem used in this chapter and also in Chapter 1.) Note that RW anomalies of the grating correspond to the onset of TM modes in the waveguide model. Thus, perfect specular reflection at RW anomalies is trivially explained, in the frame of the circuit model, by the singular behavior of the frequency-dependent capacitors. Moreover, the model also accounts for the transfer of power to the successive diffraction orders by means of additional transmission lines that are shunt-connected to the capacitors. For lossless conductors and below the onset of the first grating lobe, it is obvious that the magnitude of the specular reflection coefficient must be unity. However, above the first RW frequency, the specular reflection coefficient drastically drops because a significant part of the impinging power is transferred to non-specular grating lobes. This is what happens with simple gratings (case studied in Chapter 3 for gratings containing one

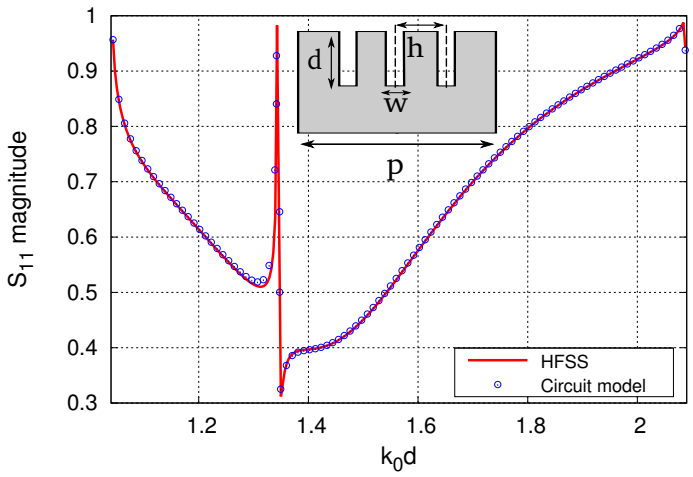

(a)

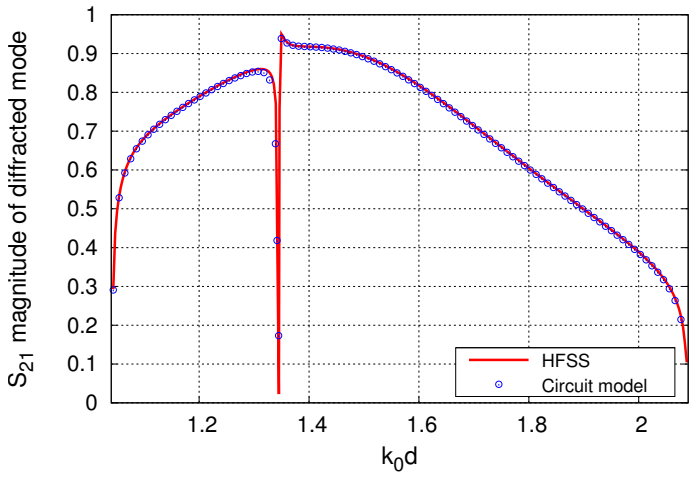

(b)

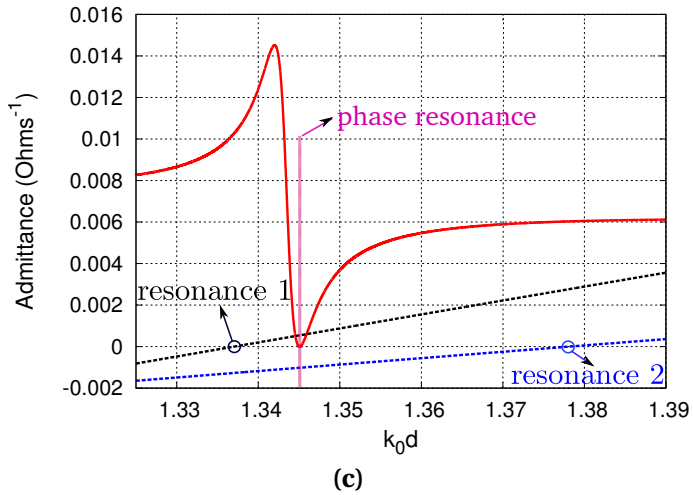

(c)

Figure 4.24: (a) Magnitude of S_{11} (specular efficiency) for the three slits per period compound reflection grating considered in [27, Fig. 2(b)] (see inset for unit cell). Normalized dimensions: $p/d = 6.0$, $w/d = 0.30$, $h/d = 0.50$. (b) Transmission to the first diffraction order (magnitude). (c) Dashed lines: Imaginary parts of the admittances associated with the resonant circuits involved in the modeling of the two independent slits. Solid line: real part of the overall equivalent admittance loading the input transmission line [see Eq. (4.22)].

slit per period) in all the frequency span between any two successive RW points. However, in the case of compound gratings, narrow peaks of perfect specular reflection have been reported at some intermediate frequencies between RW anomalies [27, 103]. These peaks were attributed to the existence of phase resonance phenomena. Our circuit model can also provide a simple explanation to this effect. In the case of a lossless system involving three slits per period, the pertinent equivalent circuit is the one in Fig. 4.5. The results provided by HFSS and our dynamical circuit model for the specular efficiency pattern of a the three-slit per period reflection compound grating analyzed in [27, Fig. 2(b)] are shown in Fig. 4.24(a). The transmission from the impinging wave to the first diffraction order is plot in Fig. 4.24(b). Normalized frequency is used as in [27]. Very good agreement between analytical and numerical data can be observed. Similar good agreement has been verified with the curve reported in [27, Fig. 2(b)], which was obtained using a mode-matching scheme. Note that a perfect specular reflection peak appears at about $k_0 d = 1.35$. This peak is associated with the existence of a zero of the real part of the equivalent admittance [see (4.22)] loading the transmission line that represents the impinging uniform plane wave. This zero always appears in the range of frequencies defined by the resonances of the individual resonators composed by the short-circuited slits with their associated external edge capacitances. These resonances are highlighted in Fig.4.24(c) with circles and correspond to the points where the imaginary parts of the overall admittances (dashed lines) associated with slits 1 and 2 are null. The real part of (4.22) is represented in the same figure as a solid line. It can be observed that this quantity vanishes at around $k_0 d = 1.35$. Therefore, at certain frequency point, all the impinging power is specularly reflected and no transfer of power to grating lobes is allowed, as it was numerically predicted in [27]. Our circuit model provides a simple explanation for this fact.

As previously examined, our model can also deal with lossy materials (metal and dielectric). In Fig.4.25 it is plotted the magnitude and phase of the reflection coefficient of the structure studied in Fig. 4.24 but including metal losses (aluminium is considered in this example). Note that normalized frequency values

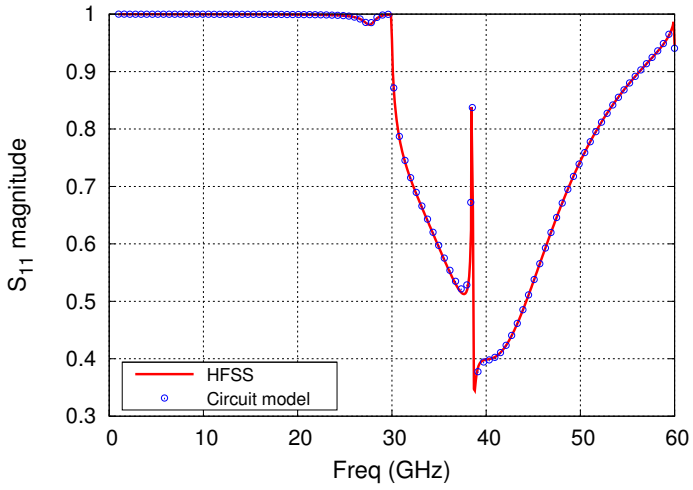

(a)

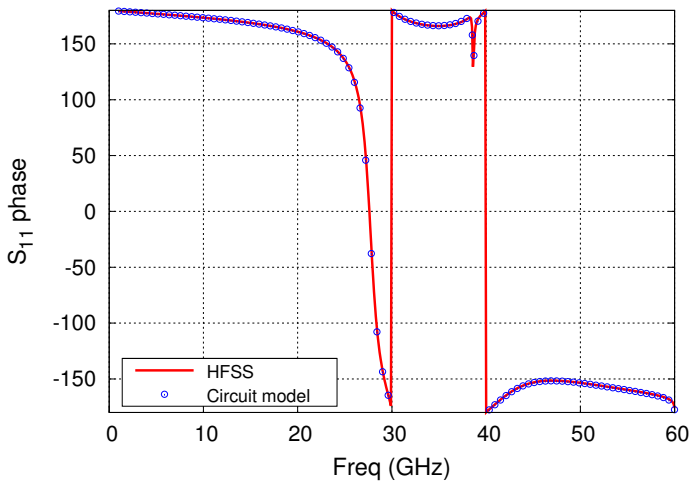

(b)

Figure 4.25: (a): Magnitude of the reflection coefficient versus frequency. (b): Phase of the reflection coefficient versus frequency. Structure parameters: $p = 10\,\text{mm}$, $w_1 = w_2 = 0.8\,\text{mm}$, $d_1 = 5.641\,\text{mm}$, $d_2 = 5.7\,\text{mm}$, $h = 1.6\,\text{mm}$, $\varepsilon_\text{r}^{(1)} = \varepsilon_\text{r}^{(2)} = 1$, $\sigma(\text{Al}) = 3.8\times10^7\,\text{S/m}$. ©2016 IEEE

cannot be used in this case. A specific choice has been done for the dimensions (maintaining their relative values) and thus a specific frequency range must be explored. It can be appreciated that circuit-model and numerical (HFSS) results agree very well over the whole analyzed frequency band. As it can be observed in Fig. 4.25(a), the specular reflection peak is greatly affected by metal losses (the magnitude of S_{11} is now about 0.84 instead of 1). It can also be recognized a small transmission dip in the magnitude of S_{11} close to the onset of the diffraction regime. This dip is related to both phase resonance and extraordinary transmission and it is again accurately reproduced with our dynamical circuit model. In this example the phase of the reflection coefficient has also been plotted in Fig.4.25(b) to show the good performance of our model even for phase calculations.

The analytical model described in Sect. 4.2.6 has been used to reproduce the data reported in [103, Fig. 2a] (five slits per period). These data are shown in Fig.4.26(a) (note that normalized frequencies are used, as in [103]). Agreement with full-wave computations is very good and the two expected specular reflection points are reproduced very accurately. The reason for the existence of those points can be appreciated in Fig.4.26(b), where two zeros of the real part of the loading equivalent admittance can be clearly noticed. Note that those zeros are again around the resonance region of the three slits of the irreducible unit cell. The equivalent circuit allows us to predict again the existence of such zeros and then perfect specular reflection peaks.

As a final example, in Fig.4.27 it is studied the transmission compound grating with experimental data reported in [109]. This figure clearly shows that our model matches the measured transmission coefficients very accurately. For the given values of the groove depth, the two explored frequency regions plotted in Figs. 4.27(a) and (b) correspond to FP-like resonances which could have been reasonably reproduced with the quasi-static model reported in [24]. Nevertheless, the dynamical-circuit results shown in these figures show a better quantitative matching.

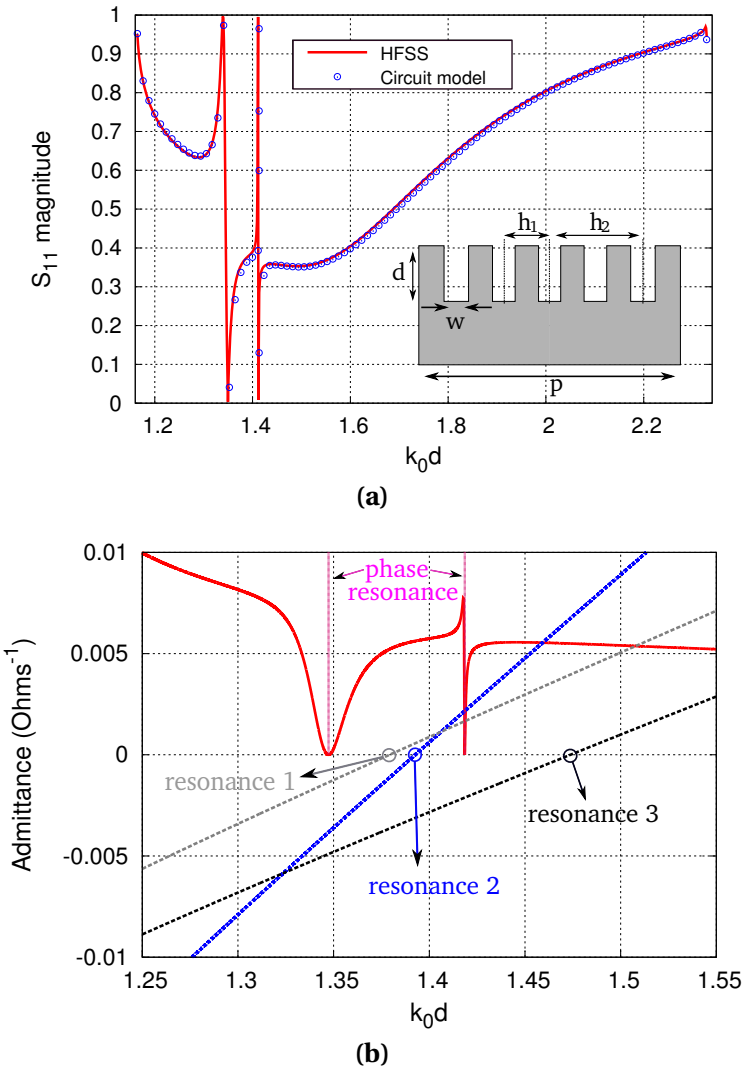

Figure 4.26: Results obtained for a compound grating with five identical slits per period. (a): Magnitude of the reflection coefficient; (b): Imaginary parts (dashed lines) of the admittances of the individual independent slits and real part (solid line) of the admittance loading the input transmission line. Dimensions: $p = 10.0\,\text{mm}$, $w_1 = w_2 = w_3 = 0.37\,\text{mm}$, $d_1 = d_2 = d_3 = 1.852\,\text{mm}$, $h_2 = 2h_1 = 1.37\,\text{mm}$. ©2016 IEEE

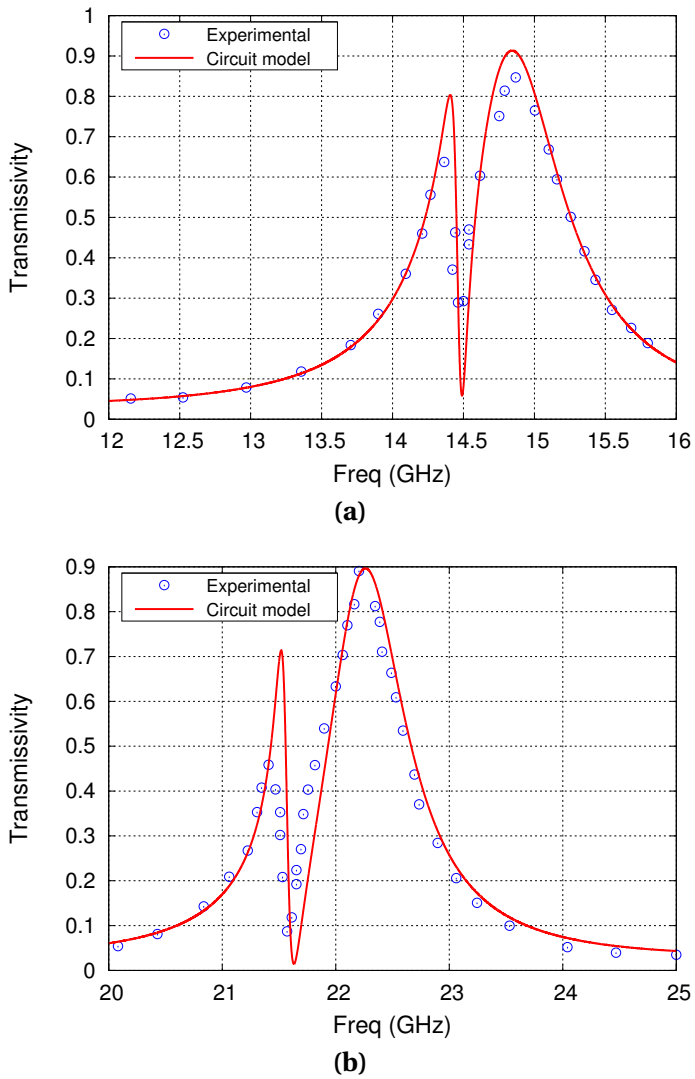

Figure 4.27: Transmissivitty versus frequency for two different FP bands of the compound grating experimentally studied in [109]. Red solid line corresponds to the analytical results and the circles are samples of the experimental results in [109]. Structure parameters: $p = 10\,\text{mm}$, $w_1 = w_2 = 0.5\,\text{mm}$, $d_1 = d_2 = 9.9\,\text{mm}$, $h = 3.375\,\text{mm}$, $\varepsilon_\text{r}^{(1)} = \varepsilon_\text{r}^{(2)} = 1$, $\sigma = 3.816 \cdot 10^7$ S/m. ©2016 IEEE

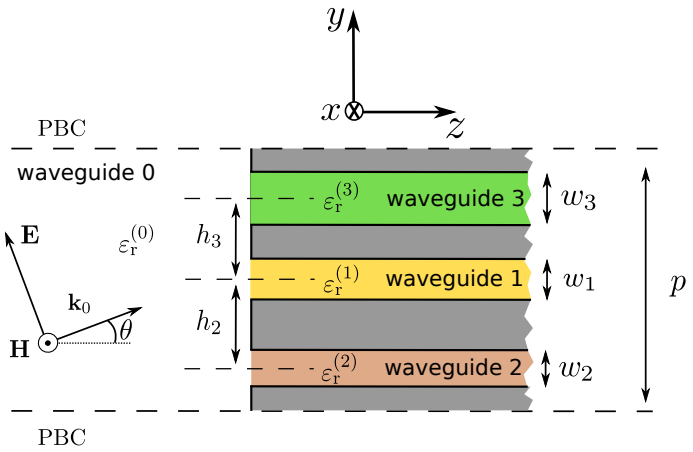

Figure 4.28: Sketch representing the unit cell of a general non-symmetric compound grating with three slits per period.

4.4 Compound gratings under oblique incidence.

Thus far, we have analyzed several geometries of compound gratings, both in transmission and reflection, and both symmetric or non-symmetric with respect the horizontal middle plane of the unit cell. However, all the above cases has been examined under normal incidence. Normal incidence provides several advantages for its analysis in contrast to oblique incidence. For instance the unit cell of a compound grating symmetric with respect the horizontal middle plane can be reduced to its half, reducing the number of slits for the analysis, and therefore lowering the complexity of the problem. Under oblique incidence, however, this reduction cannot be carried out. Furthermore, there also exists an additional disadvantage for oblique incidence. As it will be checked next, the condition involving the coupling terms, $Y_{ij} = Y_{ji}$, is not satisfied and in consequence, a topology for the equivalent circuit cannot be derived.

Let us focus our attention to the compound grating depicted in Fig. 4.28. The figure represents a discontinuity problem inside a generalized waveguide, bounded by periodic boundary conditions (PBC). Now the discontinuity is formed by three different slits distributed along the discontinuity plane. Note that the unit cell has similar features to the unit-cell problem posed for the case of 5 (or 6) slits per period symmetrically distributed under normal incidence, Fig. 4.11.

In principle it is suggested to address the problem in a similar way. Let next function be the electric field at the discontinuity plane,

$$E_{\mathrm{s}} = g_1(\omega)A_1 + g_2(\omega)A_2 + g_3(\omega)A_3 \tag{4.67}$$

with A_1 a constant slit profile at the central slit, and A_2 and A_3 the slit profile at the lower and upper slits respectively. The transverse fields on the external region, also denoted as "waveguide 0", are represented by a Floquet expansion of harmonics,

$$\mathbf{E}(y,z) = \left[(\mathrm{e}^{-\mathrm{j}\beta_0^{(0)}z-\mathrm{j}k_{\mathrm{t}}y} + R\mathrm{e}^{\mathrm{j}\beta_0^{(0)}z-\mathrm{j}k_{\mathrm{t}}y}) + \sum_n{}' E_n \mathrm{e}^{\mathrm{j}\beta_n^{(0)}z-\mathrm{j}k_n y}\right]\mathrm{e}^{\mathrm{j}k_{\mathrm{t}}y}\,\hat{\mathbf{y}} \tag{4.68}$$

$$\mathbf{H}(y,z) = \left[(\mathrm{e}^{-\mathrm{j}\beta_0^{(0)}z-\mathrm{j}k_{\mathrm{t}}y} - R\mathrm{e}^{\mathrm{j}\beta_0^{(0)}z-\mathrm{j}k_{\mathrm{t}}y})Y_0^{(0)} - \sum_n{}' E_n Y_n^{(0)} \mathrm{e}^{\mathrm{j}\beta_n^{(0)}z-\mathrm{j}k_n y}\right]\mathrm{e}^{\mathrm{j}k_{\mathrm{t}}y}\,(-\hat{\mathbf{x}}) \tag{4.69}$$

with $Y_n^{(0)} = \dfrac{\varepsilon_{\mathrm{r}}k_0}{\eta_0\beta_n^{(0)}}$ the TM modal admittance and $k_{\mathrm{t}} = \varepsilon_{\mathrm{r}}^{(0)}k_0\sin(\theta)$ the transverse component of the incident wavevector. The field inside the grooves is represented by the TEM propagating mode,

$$\mathbf{E}^{(i)} = E^{(i)}\mathrm{e}^{-\mathrm{j}\beta_0^{(i)}z}\hat{\mathbf{y}}; \qquad \mathbf{H}^{(i)} = E^{(i)}Y_0^{(i)}\mathrm{e}^{-\mathrm{j}\beta_0^{(i)}z}(-\hat{\mathbf{x}}) \tag{4.70}$$

with $i = 1, 2, 3$.

After imposing the boundary conditions to be satisfied by the electric and magnetic field at the discontinuity plane, a system of three equations is obtained, similar to the one formed by (4.45), (4.46) and (4.47):

$$I_0 = \left[\bar{Y}_{11} + \frac{1}{\left|\tilde{f}_0(w_1)\right|^2}\frac{p}{w_1}Y_0^{(1)}\right]V_1 + \bar{Y}_{12}V_2 + \bar{Y}_{13}V_3 \tag{4.71}$$

$$I_0 = \bar{Y}_{21}V_1 + \left[\bar{Y}_{22} + \frac{1}{\left|\tilde{f}_0(w_2)\right|^2}\frac{p}{w_2}Y_0^{(2)}\right]V_2 + \bar{Y}_{23}V_3 \tag{4.72}$$

$$I_0 = \bar{Y}_{31}V_1 + \bar{Y}_{32}V_2 + \left[\bar{Y}_{33} + \frac{1}{\left|\tilde{f}_0(w_3)\right|^2}\frac{p}{w_3}Y_0^{(3)}\right]V_3 \tag{4.73}$$

with

$$V_0 = V_1 + V_2 + V_3 \tag{4.74}$$

$$V_i = g_i(\omega) w_i \tilde{f}_0(w_i) \qquad i = 1,2,3 \tag{4.75}$$

$$I_0 = (1-R)p \tag{4.76}$$

$$\bar{Y}_{ii} = \sum_n{}' \, Y_n^{(0)} \left| \frac{\tilde{f}_n(w_i)}{\tilde{f}_n(w_i)} \right|^2 \tag{4.77}$$

$$\bar{Y}_{ij} = \sum_n{}' \, Y_n^{(0)} \frac{\tilde{f}_n(w_i)\big[\tilde{f}_n(w_j)\big]^*}{\tilde{f}_0(w_i)\big[\tilde{f}_0(w_j)\big]^*} \tag{4.78}$$

$$\tilde{f}_n(w_i) = \mathrm{sinc}\big([k_n + k_\mathrm{t}]w_i/2\big)\mathrm{e}^{\mathrm{j}(k_n+k_\mathrm{t})h_i} \qquad i = 1,2,3\,. \tag{4.79}$$

Notice that the cross terms $\bar{Y}_{ij}$ and $\bar{Y}_{ji}$ are different in general. In particular they are related as

$$\bar{Y}_{ij} = [\bar{Y}_{ji}]^*\,. \tag{4.80}$$

According to the problem of five slits, the system of equations formed by (4.45), (4.46) and (4.47) contained six different admittances, since the cross terms were identical, $\bar{Y}_{ij} = \bar{Y}_{ji}$. This result allowed us to deduce the topology of the equivalent circuit depicted in Fig.4.12. Now, the condition in (4.80) precludes deducing expressions similar to those in (4.51)-(4.56), which is crucial to derive a corresponding topology. Thus, the way of proceeding will consist of solving directly the system of equations formed by (4.71)-(4.73), and the equivalent admittance will be found after imposing the ratio between the current and voltage at the discontinuity, $Y_\mathrm{eq} = \dfrac{I_0}{V_0}$.

Following the steps in Sec. 4.2.3, the reflection and transmission grating can readily be accounted for. For the reflection compound grating, a ground plane is placed at a certain distance from each slit aperture. Therefore, we use the input admittance seen from the slit aperture $\dfrac{p}{w_i}Y_\mathrm{in}^{(i)}$ instead of the admittance of the TEM wave $\frac{p}{w_i}Y_0^{(i)}$

$$Y_\mathrm{in}^{(i)} = -\mathrm{j}\frac{p}{w_i}Y_0^{(i)}\cot(\beta_0^{(i)}d)\,. \tag{4.81}$$

with d being the groove depth. The transmission grating is solved by superposing the solutions obtained after applying even/odd excitation. The admittances

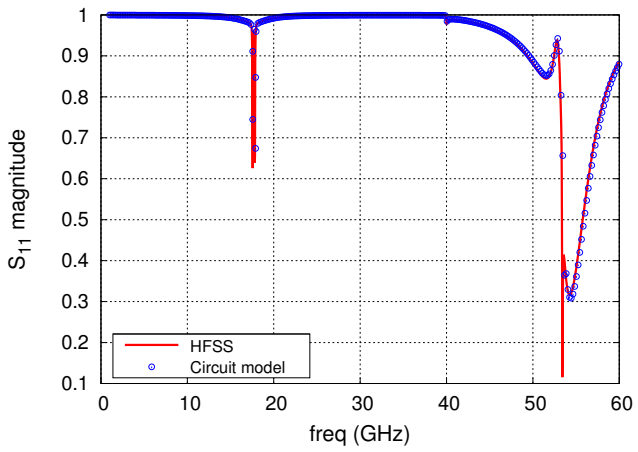

(a)

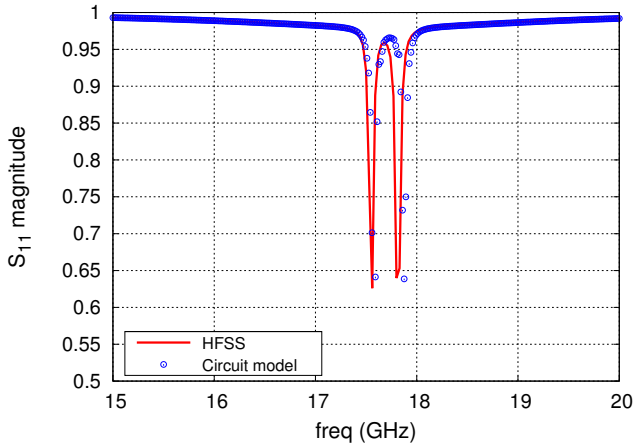

(b)

Figure 4.29: (a): Reflection coefficient versus frequency for a reflection grating containing 3 slits per period under TM oblique incidence. (b): Detail of the phase-resonance region. Structure parameters: $p = 5\,\text{mm}$, $w_1 = w_2 = w_3 = 0.25\,\text{mm}$, $d_1 = d_2 = d_3 = 4\,\text{mm}$, $h_2 = -0.75\,\text{mm}$, $h_3 = 0.75\,\text{mm}$, $\varepsilon_\text{r}^{(0)} = \varepsilon_\text{r}^{(1)} = \varepsilon_\text{r}^{(2)} = \varepsilon_\text{r}^{(3)} = 1$, $\sigma = 5.8 \cdot 10^7\,\text{S/m}$, $\theta = 30^o$.

to be used in each analysis are written as

$$Y_{\text{in, even}} = \text{j}\frac{p}{w_i} Y_0^{(i)} \tan(\beta_0^{(i)} d/2) \tag{4.82}$$

$$Y_{\text{in, odd}} = -\text{j}\frac{p}{w_i} Y_0^{(i)} \cot(\beta_0^{(i)} d/2) \tag{4.83}$$

with d screen thickness. The transmission and reflection coefficients are finally

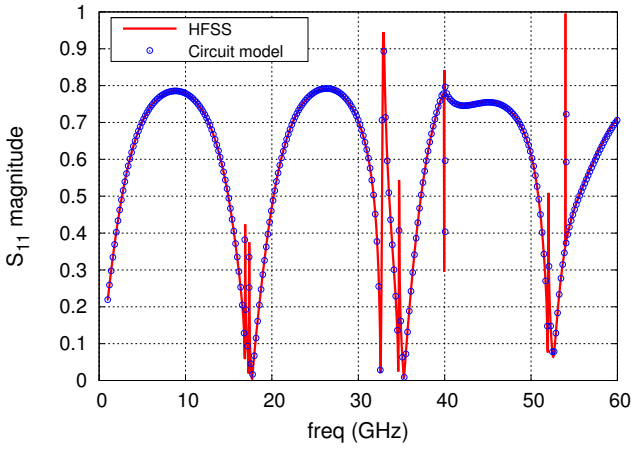

(a)

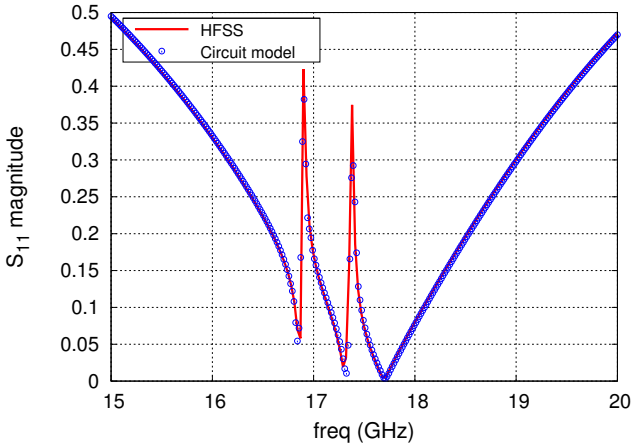

(b)

Figure 4.30: (a): Transmission coefficient versus frequency for a transmission grating containing three slits per period under TM oblique incidence. (b): Detail of the phase-resonance region. Structure parameters: $p = 5\,\text{mm}$, $w_1 = w_2 = w_3 = 0.5\,\text{mm}$, $d_1 = d_2 = d_3 = 4\,\text{mm}$, $h_2 = -1\,\text{mm}$, $h_3 = 1\,\text{mm}$, $\varepsilon_\text{r}^{(0)} = \varepsilon_\text{r}^{(1)} = \varepsilon_\text{r}^{(2)} = \varepsilon_\text{r}^{(3)} = 1$, $\sigma = 5.8 \cdot 10^7\,\text{S/m}$, $\theta = 30^o$.

expressed as

$$S_{11} = \frac{1}{2}(S_{11}^{\text{even}} + S_{11}^{\text{odd}}) \tag{4.84}$$

$$S_{21} = \frac{1}{2}(S_{11}^{\text{even}} - S_{11}^{\text{odd}})\,. \tag{4.85}$$

The inclussion of ohmic losses and the extension of the model to higher frequency regimes as THz or infrared can be carried out as described in Sec. 4.2.4

and Sec. 4.2.5.

As a final example, two more cases are analyzed in Fig. 4.28 and Fig. 4.30. In Fig. 4.28(a) we have plotted the reflection coefficient of a reflection lossy grating with three slits per period. A TM plane wave impinges with $\theta = 30^o$. Below the frequency of the first grating lobe the grating is highly reflective, except for a narrow frequency range exhibiting two consecutive reflection dips. Both dips, zoomed in Fig. 4.28(b) are expected according to [104]. It is important to remark that the gratings have identical slits. However, the reactive field at each slit aperture is different in general from each other. The interaction between those fields allows for the appearance of two phase resonances. If the plane wave impinges normally to the discontinuity plane, phase resonance appears just at a single frequency, due to the equality between the fields in the upper and lower slits. Similar arguments can be applied to the transmission compound grating, whose response in frequency is plotted in Fig. 4.30 versus frequency. The agreement with results from HFSS is excellent in both cases, even beyond the onset of the first grating lobe.

4.5 Range of validity of the model

In the previous section we have checked that the performance of the equivalent circuit is very good, even for frequencies beyond the onset of grating lobes. In the present section we will try to explore the limits of validity of the model in terms of the normalized frequency w/λ. For the derivation of the model we have always neglected the reactive field inside the slits. Therefore, we will check the influence of the geometry of the cavities on the range of validity. In principle, we expect that this approximation becomes inaccurate when the operation wavelength is comparable to the slit widths.

A first result is shown in Fig. 4.31, where the reflection coefficient of three different geometries of the three-slit compound grating is plotted versus normalized frequency. The only difference between these three gratings lies in their slit widths. Specifically, Fig. 4.31(a) represents results obtained for $w_1 = w_2 =$

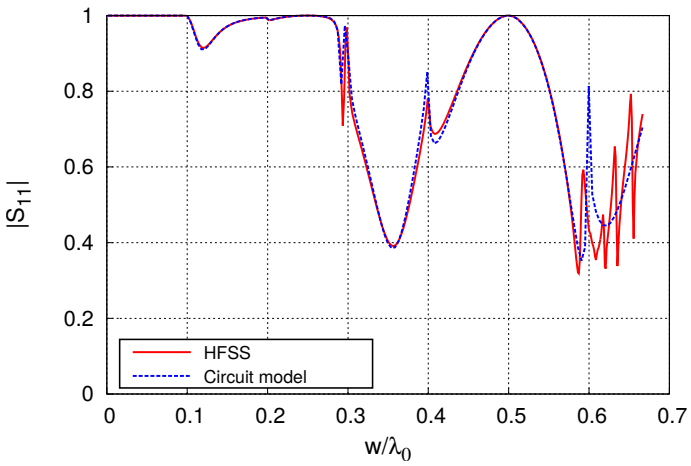

(a) $w_1 = w_2 = 0.5\,\text{mm}$

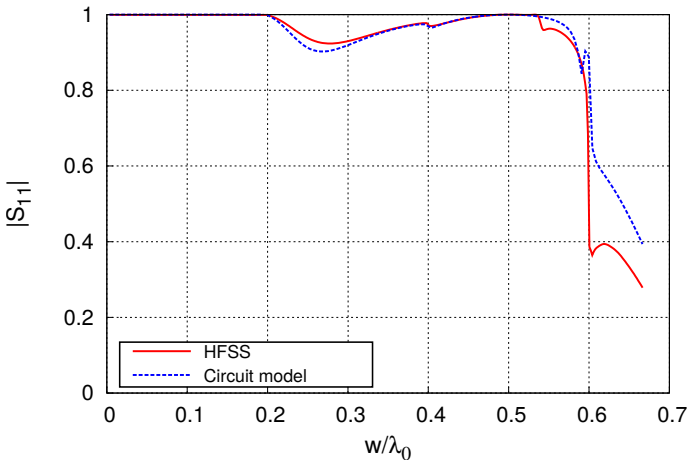

(b) $w_1 = w_2 = 1\,\text{mm}$

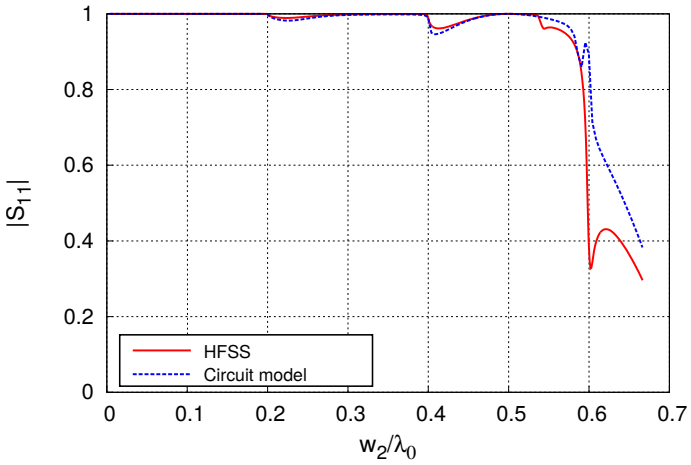

(c) $w_1 = 0.5\,\text{mm}$, $w_2 = 1\,\text{mm}$

Figure 4.31: Reflection coefficient for three different geometries of the reflection compound gratings with three slits per period under TM normal incidence. Common parameters: $p = 5\,\text{mm}$, $d_1 = 1\,\text{mm}$, $d_2 = 1\,\text{mm}$, $h_2 = 1.5\,\text{mm}$, $\varepsilon_\text{r}^{(0)} = \varepsilon_\text{r}^{(1)} = \varepsilon_\text{r}^{(2)} = 1$.

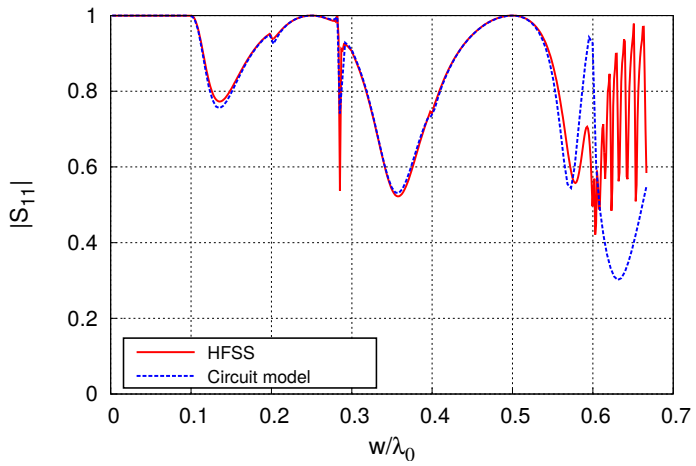

(a) Five slits: $h_1 = 0\,\text{mm}$, $h_2 = 0.8\,\text{mm}$, $h_3 = 1.6\,\text{mm}$

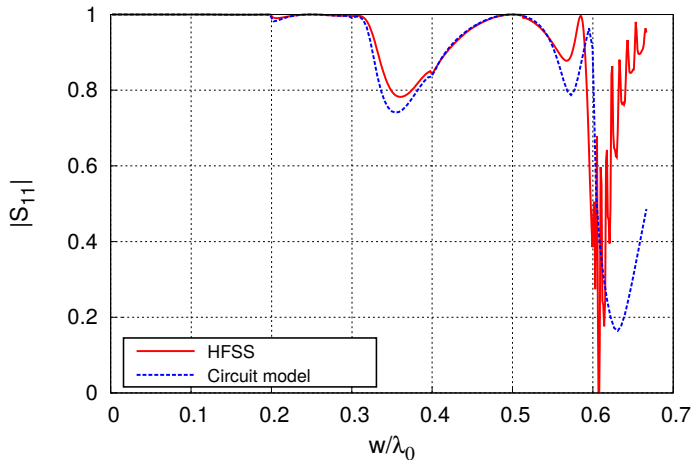

(b) Six slits: $h_1 = 0.5\,\text{mm}$, $h_2 = 1.2\,\text{mm}$, $h_3 = 2\,\text{mm}$

Figure 4.32: Reflection coefficient for two different reflection compound gratings under TM normal incidence, with five and six slits per period respectively. Common parameters: $p = 5\,\text{mm}$, $w_1 = w_2 = w_3 = 0.5$, $d_1 = 1\,\text{mm}$, $d_2 = 1\,\text{mm}$, $d_3 = 1\,\text{mm}$, $\varepsilon_\text{r}^{(0)} = \varepsilon_\text{r}^{(1)} = \varepsilon_\text{r}^{(2)} = \varepsilon_\text{r}^{(3)} = 1$.

$0.5\,\text{mm}$, Fig.4.31(b) shows results provided by the grating with $w_1 = w_2 = 1\,\text{mm}$, and finally Fig. 4.31(c) shows the reflecion coefficient of a grating with $w_1 = 0.5\,\text{mm}$ and $w_2 = 1\,\text{mm}$. We observe in all cases that there exists a very good agreement between the results provided by the circuit model and HFSS up to

$w/\lambda_0 = 0.5$. In Fig.4.31(c) the normalization has been carried out in terms of the wider slit, w_2. It is worthy to note that, according to the structure parameters in the caption of the figure, $w/\lambda_0 = 0.5$ corresponds to a frequency of 300 GHz for the case in (a), and 150 GHz for (b)-(c) respectively. These frequencies are actually very high frequencies, where several diffraction lobes are expected to be propagating, and far away from typical ranges of application.

A second brief study is carried out in Fig.4.32 concerning the number of slits per unit cell, and its possible influence on the accuracy of the model. The figure shows results obtained with two different compound gratings having five and six slits per period. The slit size is $w = 0.5$ mm for all the slits. The agreement between results from HFSS and the circuit model is good up to $w/\lambda_0 \approx 0.5$, similarly to the limit deduced in the previous cases.

4.6 Conclusions

An equivalent circuit model has been rigorously deduced for compound gratings with an arbitrary number of slits per unit cell, either simmetrically or non-simmetrically distributed and illuminated with a TM-polarized normally impinging uniform plane wave. The equivalent circuit incorporates dynamical features that were absent in previous circuit models reported in the literature. All the parameters of the proposed circuit model can easily be computed using analytical expressions in such a way that a very low computational effort is required. Moreover, the equivalent circuit provides an alternative and easy way to understand the complex behavior of compound gratings working both in transmission and reflection. A detailed and simple explanation of phase resonances has been provided in terms of the behaviour of the circuit element. The influence of phase resonances in the scattering properties of the structure are also explained in a very wide frequency range. Material losses have also been added to the model in a straightforward manner. In addition, the model can be used at THz/infrared frequencies by incorporating the Drude model of metals in the circuit model. Our analytical data agree very well with HFSS simulations and

with previously reported experimental results. Finally, for oblique incidence an equivalent-admittance expression for a compound grating can be derived by using our model, but no explicit topology can be identified from such expression. The agreement with results from full wave simulations is also excellent.

Chapter 5

1-D periodic stacked arrays.

5.1 Introduction

Thus far in the present dissertation, the study of the scattering properties of periodic structures has been focused on systems containing a single 1-D periodic grating. The spectral features associated with a single array can be modified by stacking additional periodic arrays. In this sense, the interest of studying the spectral features of stacked arrays lies in the additional degrees of freedom introduced [17].

Pioneering researchers studied the electromagetic response of stacks of periodic arrays for the design of artificial dielectrics in the framework of lens antennas [121]. At certain frequency bands, the stack behaves similarly to a conventional dielectric medium. The "dielectric" properties associated with a stack can be tailored by tuning its geometrical parameters. Systems composed of stacked arrays were then conceived as a convenient substitute of solid dielectrics, not only because of their dielectric properties but also because of their low weigth and cost. Several extensions and improvements of the work reported in [121] were published in the following years [122–125]. More recently, artificial dielectrics made of stack arrays have been studied in depth and applied in the context of integrated antennas [126, 127]. Other practical applications of stacked arrays were oriented to enhance the radiation pattern of microstrip antennas

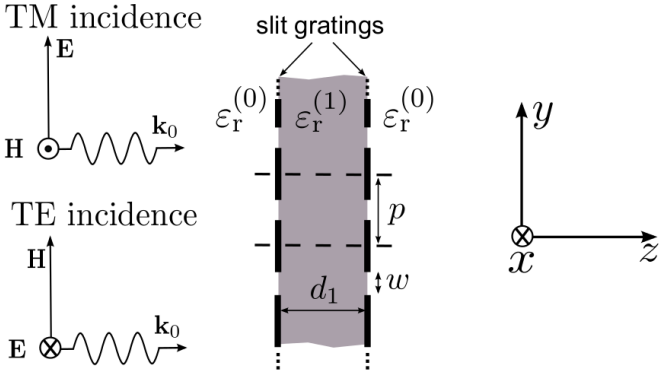

Figure 5.1: Cross-section of a pair of periodic coupled slit arrays under TM or TE normal incidence. The metal strips are infinitely thin and infinitely long along the x direction. Parameters: period of the arrays, p; slit width, w; distance between gratings (or dielectric thickness), d_1; relative permittivity of the dielectric slab, $\varepsilon_r^{(1)}$; and relative permittivity of the external medium, $\varepsilon_r^{(0)}$. ©2016 APS.

[128, 129], or to fabricate filters for radioastronomy applications [130].

The design of applications that makes use of stacked arrays requires the proposal of a theoretical and efficient design tool. Many of the theoretical analysis concerning these structures were originally based on previous results achieved in the context of single arrays [131–133]. In [134] analytical formulas are provided for the tranmission coefficient of an impinging plane wave through a single array, and are applied to more complex configurations involving stacked arrays. The authors highlight the low CPU time required to obtain the solution, but also remark the limitations of the formulas, only valid for normal incidence and assuming a long space between adjacent arrays (no reactive-field coupling between gratings is considered). In [135–137] the scattering of stacked arrays is explored by using the mutual impedance method, which includes the contribution of the near reactive field. This field is specially important for closely-spaced arrays, where the mutual coupling between gratings is actually strong. A more recent method, also including the mutual coupling between pair of arrays, is the generalized scattering matrix-method, applied in the context of stacked arrays [138–140] and multilayer structures [141]. Generally, the scattering-matrix

formulation is a quite efficient approach to evaluate the scattering of a multilayered system. The approach consists of cascading the matrices associated with each individual layer/array, resulting in a global scattering matrix. The obtaining of the individual matrices in [138–140] is carried out by a method-of-moments formulation. Other papers calculate such matrices by using an iterative method [142–144].

The analysis of stacked-gratings systems based on equivalent circuits has also been reported in the literature. For instance, applications in the fishnet-metamaterials topic[145–147] required simple models for describing negative-index materials [148, 149]. In the context of extraordinary transmission, circuit models were employed for understanding the anomalous extraordinary transmission [150, 151]. Studies with grephene-gratings were also conducted by the proposal of circuit models [152, 153].

In this chapter we will develop a method to explore the scattering properties of 1-D stacked arrays. Our method, according to the rationale followed in this dissertation, will consist of finding an equivalent circuit to reproduce the scattering response of stacked arrays. However, the analysis will be first carried out for a pair of 1-D coupled and identical slit gratings as the one sketched in Fig.5.1, which will be properly represented by an equivalent Π-topology. The resulting Π topology is readily applied to construct the equivalent circuit of a stack of several identical slit-arrays. The case of different and misaligned coupled slits gratings (having the same period) is also treated in this chapter. Varied numerical results, including comparisons with results from a in-made MoM code, from HFSS, and also with experimental results reported in [155] will be given. Finally, the limits of validity of the Π-network are studied in detail in order to evaluate the performance of the model. The issues reported in this chapter have been published in a series of two papers. The first one [154] includes the model for identical arrays. The second, considering non-identical and non-aligned coupled gratings, has recently been submitted.

5.2 Two coupled and identical slit arrays under normal incidence

In the present section the equivalent Π-circuit for a pair of coupled, identical and periodic 1D slit gratings under normal TM/TE incidence will be derived. The starting point is the equivalent circuit for a single slit array presented in Chapter 2, where fully analytical circuit models were derived for single slit gratings with an electric or magnetic wall placed at a certain distance from the slit array. These problems actually correspond to the odd/even excitation half-problems [34] of the symmetrical coupled grating. This fact is illustrated in Fig. 5.2, where the rightmost drawing shows a transmission line (representing the fundamental mode propagating in the external region) loaded with appropriate equivalent admittances. These admittances correspond to the input admittances of the slit array printed on a dielectric slab of thickness $d_1/2$ terminated with a magnetic (open-circuit, Y_{eq}^{e}) or an electric (short-circuit, Y_{eq}^{o}) wall. The superscripts "e" and "o" stand for even and odd excitation, respectively. According to the previous derivation in [66], Y_{eq}^{e} and Y_{eq}^{o} are given by the following

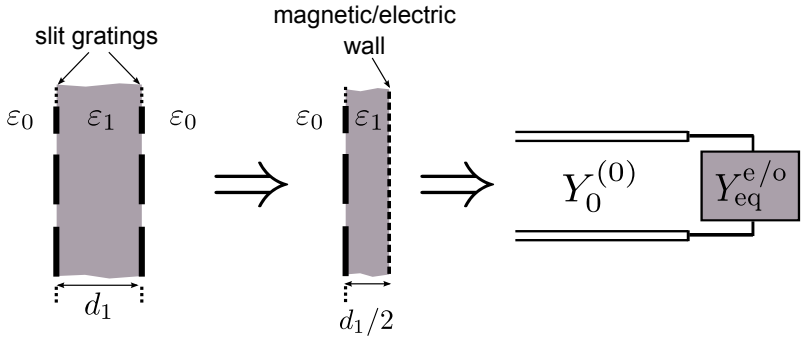

Figure 5.2: Even-odd excitation analysis using magnetic or electric walls in the symmetry plane and its circuit representation, already derived in Chapter 2. Superscript "e" stands for even excitation; "o" for odd excitation.

infinite sum of modal admittances:

$$Y_{\text{eq}}^{\text{e}} = 2\sum_{n=1}^{\infty}\left[\frac{\tilde{f}_n}{\tilde{f}_0}\right]^2 Y_n^{(0)} + 2\text{j}\sum_{n=0}^{\infty}\left[\frac{\tilde{f}_n}{\tilde{f}_0}\right]^2 Y_n^{(1)}\tan(\beta_n^{(1)}d_1/2) \tag{5.1}$$

$$Y_{\text{eq}}^{\text{o}} = 2\sum_{n=1}^{\infty}\left[\frac{\tilde{f}_n}{\tilde{f}_0}\right]^2 Y_n^{(0)} - 2\text{j}\sum_{n=0}^{\infty}\left[\frac{\tilde{f}_n}{\tilde{f}_0}\right]^2 Y_n^{(1)}\cot(\beta_n^{(1)}d_1/2) \tag{5.2}$$

where

$$\left[\frac{\tilde{f}_n}{\tilde{f}_0}\right]^2 = \begin{cases} J_0^2(k_n w/2) & \text{TM incidence} \\ \left[2\dfrac{J_1(k_n w/2)}{k_n w/2}\right]^2 & \text{TE incidence} \end{cases} \qquad n \geq 1 \tag{5.3}$$

$$Y_n^{(i)} = \frac{1}{\eta_0} \times \begin{cases} \varepsilon_{\text{r}}^{(i)} k_0/\beta_n^{(i)} & \text{TM incidence} \\ \beta_n^{(i)}/k_0 & \text{TE incidence} \end{cases} \qquad n \geq 1 \tag{5.4}$$

$$\beta_n^{(i)} = \sqrt{\varepsilon_{\text{r}}^{(i)} k_0^2 - k_n^2} \quad n \geq 1 \tag{5.5}$$

$$k_0 = \frac{\omega}{c}, \quad k_n = \frac{2\pi n}{p} \quad n \geq 1 \tag{5.6}$$

with $J_i(\cdot)$ being the Bessel function of the first kind and i-th order, $\eta_0 = \sqrt{\mu_0/\varepsilon_0}$ the intrinsic impedance of free space, ω the angular frequency, c the speed of light in free space, k_n the cutoff wavenumber of the n-th mode supported by the parallel-plate waveguide associated with the unit cell, and $\beta_n^{(i)}$ the corresponding longitudinal wavenumber of the n-th mode in medium (i). The coefficient $\left[\frac{\tilde{f}_n}{\tilde{f}_0}\right]^2$ is the nth Fourier coefficient of the electric-field profile assumed at the slit aperture ($y \in [-w/2, w/2]$, with w being the width of the slit), which according to Chapter 2, is taken as

$$E_{\text{slit}}(y) = \begin{cases} \frac{2}{\pi w}\left[1-(2y/w)^2\right]^{-1/2} & \text{TM incidence} \\ \frac{4}{\pi w}\left[1-(2y/w)^2\right]^{1/2} & \text{TE incidence} \end{cases} \tag{5.7}$$

Starting from the basic circuit models for the even- and odd-excitation-half

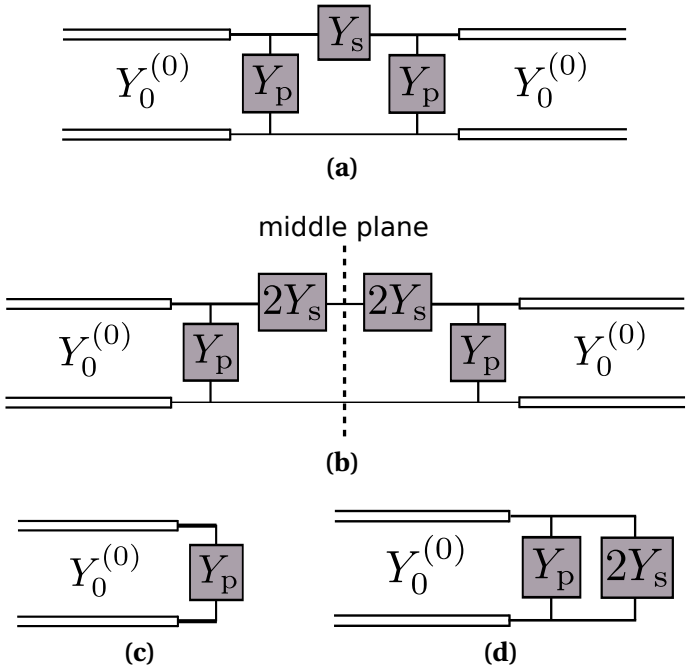

Figure 5.3: (a) Equivalent Π-circuit for a pair of coupled gratings. (b) The same circuit as in (a), showing the middle symmetry plane. (c), (d) The circuits that result from applying open or short circuit terminations (corresponding to even or odd excitations) at the middle symmetry plane. ©2016 APS.

problems shown in Fig. 5.2, our first goal next section will be to find an equivalent circuit for the pair of coupled gratings in the form of an equivalent Π-network. Then, the following section will present a detailed study of the elements in the Π-circuit, leading to a further decomposition into different elements that allows for their efficient computation and provides an insightful physical interpretation. Later, it will be presented the strategy proposed for the computation of the Π-circuit elements. Finally various numerical results will illustrate and support the previous discussion as well as demonstrate the quantitative performance of the Π-network circuit model.

5.2.1 Equivalent Π-network for coupled gratings

In order to find the equivalent Π-network that describes the behavior of the coupled screens (see Fig. 5.3a), an even-odd excitation analysis is also applied to this Π-circuit by placing open- or short-circuit terminations in the middle plane (Fig.5.3b). As a result, the half-problem circuits shown in Figs. 5.3c and 5.3d are obtained. Identifying the latter two circuits with the one in Fig.5.2, it is clear that the parallel and series admittances (Y_{p} and Y_{s}) can readily be obtained from the even and odd equivalent admittances as

$$Y_{\mathrm{p}} = Y_{\mathrm{eq}}^{\mathrm{e}} \qquad , \qquad Y_{\mathrm{s}} = \frac{1}{2}[Y_{\mathrm{eq}}^{\mathrm{o}} - Y_{\mathrm{eq}}^{\mathrm{e}}] \tag{5.8}$$

and, therefore, from (5.1) and (5.2)

$$Y_{\mathrm{p}} = \sum_{n=1}^{\infty} \left[\frac{\tilde{f}_n}{\tilde{f}_0}\right]^2 Y_n^{(0)} + \mathrm{j} \sum_{n=0}^{\infty} \left[\frac{\tilde{f}_n}{\tilde{f}_0}\right]^2 Y_n^{(1)} \tan(\beta_n^{(1)} d_1/2) \tag{5.9}$$

$$Y_{\mathrm{s}} = -\mathrm{j} \sum_{n=0}^{\infty} \left[\frac{\tilde{f}_n}{\tilde{f}_0}\right]^2 Y_n^{(1)} \csc(\beta_n^{(1)} d_1)\,. \tag{5.10}$$

It should be noted that the first summation in (5.9)

$$Y_{\mathrm{p}}^{(0)} = \sum_{n=1}^{\infty} \left[\frac{\tilde{f}_n}{\tilde{f}_0}\right]^2 Y_n^{(0)} \tag{5.11}$$

only accounts for the external field, whereas the second summation is associated with the field in region (1) (hencefort internal region):

$$Y_{\mathrm{p}}^{(1)} = \mathrm{j} \sum_{n=0}^{\infty} \left[\frac{\tilde{f}_n}{\tilde{f}_0}\right]^2 Y_n^{(1)} \tan(\beta_n^{(1)} d_1/2)\,. \tag{5.12}$$

This fact will be key in Sec. 5.3 to obtain the equivalent circuit for stacked structures involving an arbitrary number of gratings.

5.2.2 Interpretation of the admittances deduced for the Π-circuit

The analytical expressions found in previous sections for the circuit elements of the Π-network have been derived as infinite series and, certainly, these formal

expressions are not well suited for a qualitative understanding of the behavior of the fields, nor are they convenient from a computational perspective. However, it will be shown that they can easily be manipulated and rewritten in a more insightful and suitable form. First, it is convenient to split the infinite series in (5.10), (5.11) and (5.12) into two separate contributions. The first contribution comprises the low-order terms, which correspond to propagating modes at the highest frequency of interest. It is also advisable to add the first evanescent mode to this low-order group . The second contribution is formed by an infinite series of evanescent modes whose cutoff frequencies are far above the working frequency, namely, high-order ("ho") evanescent modes. Expressions in (5.10), (5.11), and (5.12) are thus regrouped as

$$Y_{\mathrm{p}}^{(0)} = \sum_{n=1}^{N} \left[\frac{\tilde{f}_n}{\tilde{f}_0}\right]^2 Y_n^{(0)} + \underbrace{\sum_{n=N+1}^{\infty} \left[\frac{\tilde{f}_n}{\tilde{f}_0}\right]^2 Y_n^{(0)}}_{Y_{\mathrm{p,ho}}^{(0)}} \tag{5.13}$$

$$Y_{\mathrm{p}}^{(1)} = \mathrm{j} \sum_{n=0}^{N} \left[\frac{\tilde{f}_n}{\tilde{f}_0}\right]^2 Y_n^{(1)} \tan(\beta_n^{(1)} d_1/2) + \underbrace{\mathrm{j} \sum_{n=N+1}^{\infty} \left[\frac{\tilde{f}_n}{\tilde{f}_0}\right]^2 Y_n^{(1)} \tan(\beta_n^{(1)} d_1/2)}_{Y_{\mathrm{p,\,ho}}^{(1)}} \tag{5.14}$$

$$Y_{\mathrm{s}} = -\mathrm{j} \sum_{n=0}^{N} \left[\frac{\tilde{f}_n}{\tilde{f}_0}\right]^2 Y_n^{(1)} \csc(\beta_n^{(1)} d_1) \underbrace{- \mathrm{j} \sum_{n=N+1}^{\infty} \left[\frac{\tilde{f}_n}{\tilde{f}_0}\right]^2 Y_n^{(1)} \csc(\beta_n^{(1)} d_1)}_{Y_{\mathrm{s,\,ho}}} \tag{5.15}$$

where N is the number of low-order ("lo") terms. According to the above-mentioned criterion, N will be given by

$$N = \left\lceil \sqrt{\varepsilon_{\mathrm{r,max}}} \, \frac{p}{\lambda_{0,\mathrm{min}}} \right\rceil \tag{5.16}$$

where $\lceil \cdot \rceil$ represents the smallest following integer (ceiling function), $\varepsilon_{\mathrm{r,max}}$ is the greater of the two surrounding permittivities, and $\lambda_{0,\mathrm{min}}$ is the minimum vacuum wavelength value of interest. Since the modes that contribute to the $Y_{\mathrm{p,ho}}^{(i)}$ and $Y_{\mathrm{s,ho}}$ high-order admittances are far below their cutoff frequencies, the

following approximation (also employed in the previous chapters) can be used

$$k_n \gg \sqrt{\varepsilon_{\mathrm{r}}^{(i)}} k_0 \quad , \quad \beta_{n,\mathrm{ho}}^{(i)} \approx -\mathrm{j}k_n \quad (i = 0, 1) \; . \tag{5.17}$$

The expressions for the TM and TE characteristic admittances of these modes then reduce to

$$Y_{n,\mathrm{ho}}^{(i)} \approx \mathrm{j}\omega \frac{\varepsilon_0 \varepsilon_{\mathrm{r}}^{(i)}}{k_n} = \mathrm{j}\omega C_n^{(i)} \qquad \text{TM case} \tag{5.18}$$

$$Y_{n,\mathrm{ho}}^{(i)} \approx \frac{1}{\mathrm{j}\omega} \frac{k_n}{\mu_0} = \frac{1}{\mathrm{j}\omega L_n} \qquad \text{TE case} \tag{5.19}$$

whose frequency dependence is readily recognized as standard reactive lumped elements (inductors and capacitors). Depending on the polarization of the impinging wave, a lumped n-order capacitor $C_n^{(i)}$ or n-order inductance L_n is defined for the n-th order mode (note that L_n does not depend on the permittivity of the medium, as expected for a standard inductance).

For TM polarization, introducing (5.18) in $Y_{\mathrm{p}}^{(i)}$ and Y_{s}, we obtain

$$Y_{\mathrm{p,\,ho}}^{(0)} = \mathrm{j}\omega \sum_{n=N+1}^{\infty} \left[\frac{\tilde{f}_n}{\tilde{f}_0}\right]^2 C_n^{(0)} = \mathrm{j}\omega C_{\mathrm{p}}^{(0)} \tag{5.20}$$

$$Y_{\mathrm{p,\,ho}}^{(1)} = \mathrm{j}\omega \sum_{n=N+1}^{\infty} \left[\frac{\tilde{f}_n}{\tilde{f}_0}\right]^2 C_n^{(1)} \tanh(k_n d_1/2) = \mathrm{j}\omega C_{\mathrm{p}}^{(1)} \tag{5.21}$$

$$Y_{\mathrm{s,\,ho}} = \mathrm{j}\omega \sum_{n=N+1}^{\infty} \left[\frac{\tilde{f}_n}{\tilde{f}_0}\right]^2 C_n^{(1)} \mathrm{csch}(k_n d_1) = \mathrm{j}\omega C_{\mathrm{s}} \tag{5.22}$$

where $C_{\mathrm{p}}^{(1)}$ and C_{s} are capacitors that account for the global effect of all the higher-order evanescent modes.

Similarly, for TE polarization the following equivalent inductances associated with the effect of all the higher-order modes are obtained:

$$Y_{\mathrm{p,\,ho}}^{(0)} = \frac{1}{\mathrm{j}\omega} \sum_{N+1}^{\infty} \left[\frac{\tilde{f}_n}{\tilde{f}_0}\right]^2 \frac{1}{L_n} = \frac{1}{\mathrm{j}\omega L_{\mathrm{p}}^{(0)}} \tag{5.23}$$

$$Y_{\mathrm{p,\,ho}}^{(1)} = \frac{1}{\mathrm{j}\omega} \sum_{N+1}^{\infty} \left[\frac{\tilde{f}_n}{\tilde{f}_0}\right]^2 \frac{1}{L_n} \tanh(k_n d_1/2) = \frac{1}{\mathrm{j}\omega L_{\mathrm{p}}^{(1)}} \tag{5.24}$$

$$Y_{\mathrm{s,\,ho}} = \frac{1}{\mathrm{j}\omega} \sum_{N+1}^{\infty} \left[\frac{\tilde{f}_n}{\tilde{f}_0}\right]^2 \frac{1}{L_n} \mathrm{csch}(k_n d_1) = \frac{1}{\mathrm{j}\omega L_{\mathrm{s}}} \, . \tag{5.25}$$

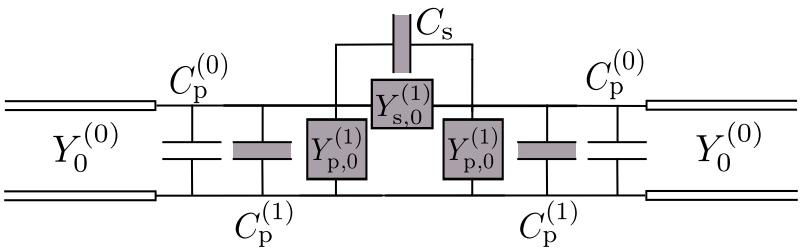

(a) TM polarization

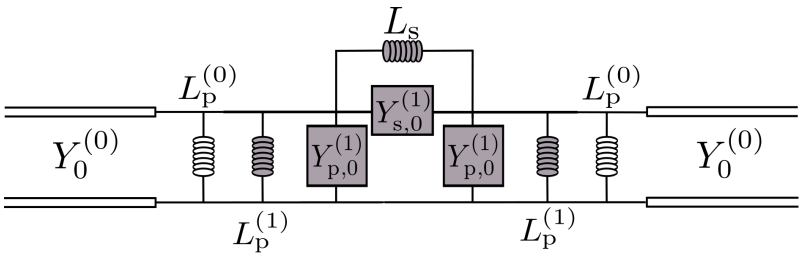

(b) TE polarization

Figure 5.4: (a) Equivalent circuit showing separately the contribution of the fundamental mode (Π-network) and the higher-order modes (lumped capacitors and inductors). ©2016 APS.

The circuit models in the form obtained thus far are depicted in Fig.5.4, with the high-order capacitances and inductances explicitly shown. For simplicity, in these drawings it is assumed $N = 0$; i.e., the frequently encountered situation in which only the fundamental zero-order term contributes to the low-order admittances that appear in the internal Π-network. All the higher-order modes are then included in the lumped elements.

As pointed out for the single-grating problem, a more specific physical interpretation of these lumped reactive elements can be found after noting that they represent the reactive field excited in the vicinity of the slit aperture (since they account for the evanescent modes). This interpretation can directly be translated to the external high-order element ($C_{\mathrm{p}}^{(0)}$ or $L_{\mathrm{p}}^{(0)}$), which represents the reactive near field around the slit in the external region. For the internal region it is also desirable to find an interpretation for both the series and the parallel reactive lumped elements. For the series element in (5.22) or (5.25), the exponential behavior of the $\mathrm{csch}(\cdot)$ function for large arguments makes this series

admittance decrease exponentially as the two coupled screens are separated, which clearly suggests that the series element is basically related to the coupling between both screens through evanescent fields. From (5.22) or (5.25) it is apparent that only the evanescent modes that reach the other screen will contribute to the series element, with the contribution of the remaining modes being negligible. On the contrary, the parallel element in (5.21) or (5.24) does not vanish for distant screens, since the $\tanh(\cdot)$ function approaches unity instead. Therefore, for coupled screens sufficiently separated (so that the reactive field around the slits does not reach the other screen), the parallel lumped element approaches its single-grating value. This suggests further splitting the parallel element as

$$C_{\mathrm{p}}^{(1)} = \underbrace{\sum_{n=N+1}^{\infty} \left[\frac{\tilde{f}_n}{\tilde{f}_0}\right]^2 C_n^{(1)}}_{C_{\mathrm{p,\,single}}^{(1)}} - \underbrace{\sum_{n=N+1}^{\infty} \left[\frac{\tilde{f}_n}{\tilde{f}_0}\right]^2 C_n^{(1)} \left[1 - \tanh(k_n d_1/2)\right]}_{C_{\mathrm{p,\,coup}}} \,. \tag{5.26}$$

The first term, $C_{\mathrm{p,\,single}}^{(1)}$ represents the value of the reactive element in the absence of coupling with a second screen (single-grating value). The second one, $C_{\mathrm{p,coup}}$, is a coupling term that accounts for the modification of the single-screen capacitance due to the presence of the other screen. The fact that this term is subtracted from $C_{\mathrm{p,\,single}}^{(1)}$ indicates that the overall parallel capacitance tends to decrease as a consequence of the coupling, and this can be interpreted as a parallel connection between the single-screen capacitance and a negative capacitance, $-C_{\mathrm{p,coup}}$. A similar decomposition can be made for the parallel inductance in the TE case as

$$1/L_{\mathrm{p}}^{(1)} = \underbrace{\sum_{n=N+1}^{\infty} \left[\frac{\tilde{f}_n}{\tilde{f}_0}\right]^2 \frac{1}{L_n}}_{1/L_{\mathrm{p,\,single}}=1/L_{\mathrm{p}}^{(0)}} - \underbrace{\sum_{n=N+1}^{\infty} \left[\frac{\tilde{f}_n}{\tilde{f}_0}\right]^2 \frac{1}{L_n} \left[1 - \tanh(k_n d_1/2)\right]}_{L_{\mathrm{p,\,coup}}} \,. \tag{5.27}$$

As found for the series coupling elements in (5.22) and (5.25), only those higher-order modes whose evanescent field significantly gets to the other screen need to be included in the parallel coupling elements in (5.26) and (5.27). A convenient criterion to determine the highest-order mode, M, to be considered in the

C_{s}, L_{s}, $C_{\mathrm{p,coup}}$ and $L_{\mathrm{p,coup}}$ summations in (5.22), (5.25) (5.26), and (5.27) is found to be

$$k_M d_1 \approx 1 \quad \Longrightarrow \quad M = \left\lceil \frac{1}{2\pi} \frac{p}{d_1} \right\rceil \ . \tag{5.28}$$

This criterion has been satisfactorily checked in situations in which coupling through evanescent modes plays a significant role.

Finally, in Fig.5.4 the contribution of the zero-order mode is accounted for by the internal Π-circuit formed by the $Y^{(1)}_{\mathrm{p},\,0}$ and $Y_{\mathrm{s},0}$ admittances. After some manipulations (with the help of the ABCD matrix [34]), it can be shown that such a low-order Π-circuit is equivalent to a transmission-line section with characteristic admittance $Y^{(1)}_0$ and length d_1.

The above ideas are illustrated in the circuits shown in Fig.5.5 with the aim of gaining a graphical insightful interpretation (it is again assumed that the zero-order mode is the only low-order term, $N = 0$). The internal transmission line with admittance $Y^{(1)}_0$ accounts for the coupling between both screens through the propagating zero-order wave. The reactive elements labeled as "single" represent the reactive field around the slits for a single grating (i.e., in the absence of coupling through evanescent fields). For TM polarization this element is obtained as the sum (parallel connection) of $C^{(0)}_{\mathrm{p}}$ in (5.20) and $C^{(1)}_{\mathrm{p,single}}$ in (5.26) (for TE polarization it is given by the parallel connection between the corresponding inductances). If the two coupled screens are distant enough so that there is not significant coupling through evanescent modes (namely, if $M = 0$ for the cases in Fig. 5.5a and Fig. 5.5b, or $M \leq N$ in general), then the reactive coupling elements can be neglected. This situation, with only one propagating mode and no reactive coupling, is obtained when the period is electrically small and the dielectric slab is electrically thick. In the literature, many authors restrict themselves to the analysis of such a situation. However, closely spaced gratings are important for many practical cases of interest and, in such cases, the coupling through evanescent fields should actually be taken into account, which can conveniently be carried out by introducing the series and parallel coupling capacitors or inductors. Furthermore, in order to extend the range of application of the model to higher frequencies where one or more higher-order

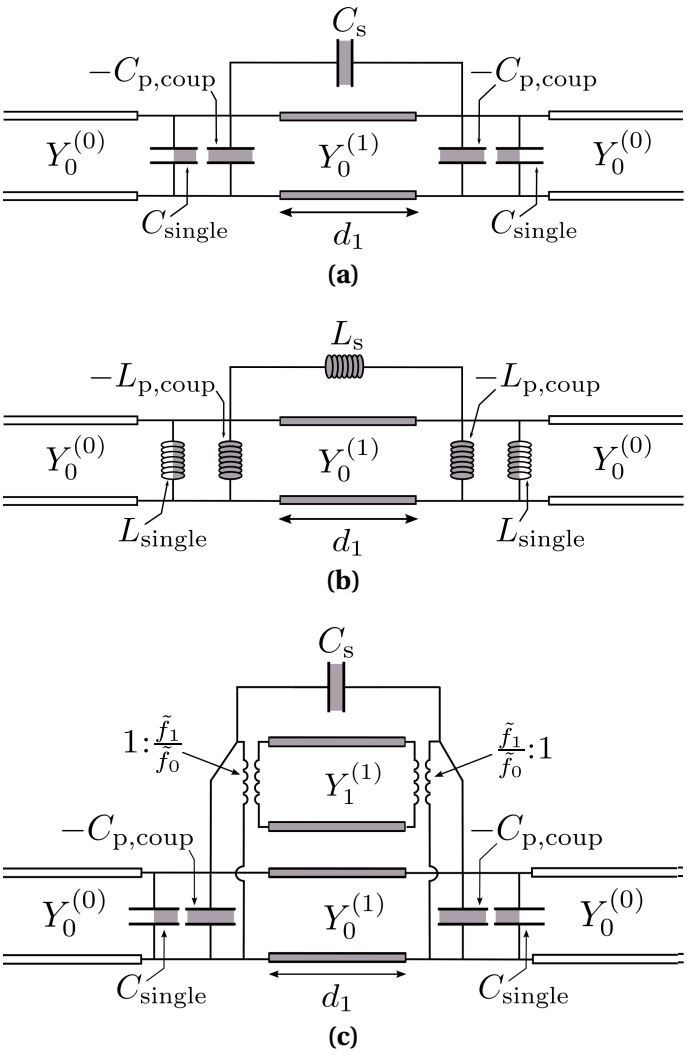

Figure 5.5: Circuit models for (a) TM and (b) TE polarizations considering the fundamental mode as the only distributed element (transmission line of admittance $Y_0^{(1)}$). The higher-order modes contribution is included in the lumped elements. (c) Circuit model for the case of two distributed modes (only the TM polarization case). ©2016 APS.

modes become propagative in the slab between the gratings, the full dynamic frequency dependence of their modal admittances and propagation wavenumbers has to be considered. As $N > 0$, these higher-order modes must contribute to the low-order sums in (5.13), (5.14) and (5.15) and their respective effect can similarly be separated from the high-order elements to form another Π-circuit, which is again equivalent to another transmission line with its corresponding admittance $Y_i^{(1)}$ and length d_1. This fact is sketched in Fig. 5.5c for $N = 1$ and TM polarization. The appearance of transformers of turn ratio $\frac{\tilde{f}_1}{\tilde{f}_0}$ placed at both ends of the transmission line is noteworthy.

5.2.3 Computation of the Π-circuit admittances

Taking into account the ideas discussed above, we now discuss the systematic strategy followed in this work to compute the $Y_{\mathrm{p}}^{(0)}$, $Y_{\mathrm{p}}^{(1)}$, and Y_{s} admittances that make up the Π-circuit. First, given the structural parameters and frequency range of interest, the value of N is computed following the criterion proposed in (5.16). Using this value of N, the $C_{\mathrm{p}}^{(0)}$ and $C_{\mathrm{p,single}}^{(1)}$ lumped elements in (5.20) and (5.26) are computed as

$$C_{\mathrm{p}}^{(0)} = w\varepsilon_0\varepsilon_{\mathrm{r}}^{(0)} \sum_{n=N+1}^{\infty} \frac{[J_0(k_n w/2)]^2}{k_n w/2} \tag{5.29}$$

$$C_{\mathrm{p,single}}^{(1)} = \frac{\varepsilon_{\mathrm{r}}^{(1)}}{\varepsilon_{\mathrm{r}}^{(0)}}\, C_{\mathrm{p}}^{(0)} \ . \tag{5.30}$$

Similarly, for the TE case, the $L_{\mathrm{p}}^{(0)}$ and $L_{\mathrm{p,single}}^{(1)}$ elements in (5.23) and (5.27) are obtained from

$$\frac{1}{L_{\mathrm{p}}^{(0)}} = \frac{1}{L_{\mathrm{p,single}}^{(1)}} = \frac{16}{w\mu_0} \sum_{n=N+1}^{\infty} \frac{[J_1(k_n w/2)]^2}{k_n w/2} \ . \tag{5.31}$$

Next, the value of M is obtained from the criterion in (5.28). If $M > N$, then the coupling reactive elements are computed as

$$C_{\text{p,coup}} = w\varepsilon_0\varepsilon_{\text{r}}^{(1)} \sum_{n=N+1}^{M} \frac{[J_0(k_n w/2)]^2}{k_n w/2} \left[1 - \tanh(k_n d_1/2)\right] \tag{5.32}$$

$$C_{\text{s}} = w\varepsilon_0\varepsilon_{\text{r}}^{(1)} \sum_{n=N+1}^{M} \frac{[J_0(k_n w/2)]^2}{k_n w/2} \operatorname{csch}(k_n d_1) \tag{5.33}$$

or

$$\frac{1}{L_{\text{p,coup}}} = \frac{16}{w\mu_0} \sum_{n=N+1}^{M} \frac{[J_1(k_n w/2)]^2}{k_n w/2} \left[1 - \tanh(k_n d_1/2)\right] \tag{5.34}$$

$$\frac{1}{L_{\text{s}}} = \frac{16}{w\mu_0} \sum_{n=N+1}^{M} \frac{[J_1(k_n w/2)]^2}{k_n w/2} \operatorname{csch}(k_n d_1)\ . \tag{5.35}$$

If $M \leq N$ these coupling elements are ignored. Once all of the above lumped elements are known, the high-order admittances in (5.13)–(5.15) are given by

$$Y_{\text{p,ho}}^{(0)} = \text{j}\omega C_{\text{p}}^{(0)} \tag{5.36}$$

$$Y_{\text{p,ho}}^{(1)} = \text{j}\omega \left(C_{\text{p,single}}^{(1)} - C_{\text{p,coup}}\right) \tag{5.37}$$

$$Y_{\text{s,ho}} = \text{j}\omega C_{\text{s}} \tag{5.38}$$

and the corresponding expressions for the TE case are obtained by replacing $\text{j}\omega C$ with $1/\text{j}\omega L$. It is important to note that none of the above lumped elements depends on frequency. Hence, they have to be evaluated only once when performing a frequency sweep. Furthermore, the elements with infinite summations in (5.29)–(5.31) do not depend on d_1 either, and therefore it is not necessary to recalculate them when varying the distance between the gratings, provided the period p or the slit width w is not modified. Finally, for each value of

frequency, the admittances in the Π-circuit are obtained as

$$Y_{\mathrm{p}}^{(0)} = \sum_{n=1}^{N} \left[\frac{\tilde{f}_n}{\tilde{f}_0}\right]^2 Y_n^{(0)} + Y_{\mathrm{p,ho}}^{(0)} \tag{5.39}$$

$$Y_{\mathrm{p}}^{(1)} = \mathrm{j} \sum_{n=0}^{N} \left[\frac{\tilde{f}_n}{\tilde{f}_0}\right]^2 Y_n^{(1)} \tan(\beta_n^{(1)} d_1/2) + Y_{\mathrm{p,\,ho}}^{(1)} \tag{5.40}$$

$$Y_{\mathrm{s}} = -\mathrm{j} \sum_{n=0}^{N} \left[\frac{\tilde{f}_n}{\tilde{f}_0}\right]^2 Y_n^{(1)} \csc(\beta_n^{(1)} d_1) + Y_{\mathrm{s,\,ho}} \ . \tag{5.41}$$

5.2.4 Results and discussion

Some numerical results are next presented in order to check the validity and accuracy of the equivalent-circuit approach for a pair of coupled gratings and to illustrate the previous discussion. Fig. 5.6 shows the transmission coefficient of a pair of coupled gratings printed on either side of a dielectric slab, for two different values of the slab thickness d_1 (separation between the gratings).

For comparison purposes, we have developed an in-house numerical code based on the Method of Moments (MoM) solution of the integral equation for the aperture field. This MoM implementation, which uses several basis functions to reproduce the aperture field, has been carefully checked and the numerical results it provides can be considered virtually "exact" for our purposes.

In the first case shown in Fig. 5.6a, the separation between the metallic screens is relatively large (the slab thickness is 2.5 times smaller than the periodicity of the slit gratings). Indeed, the value of the ratio $p/(2\pi d_1)$ is quite low (≈ 0.4) and, consequently, the coupling through evanescent fields is not expected to be relevant. Hence, the $C_{\mathrm{p,coup}}$ and C_{s} capacitors do not have to be considered in the circuit model [in other words, $M = 0$ is taken for the circuit model results shown in Fig. 5.6a, although $M = 1$ could have been taken according to our more conservative general criterion given in (5.28)]. It is shown in the figure that the circuit-model results obtained with $N = 0$ reproduce accurately the transmission spectrum at low frequencies, but they tend to deviate as the frequency increases until they become qualitatively wrong. The reason is that the

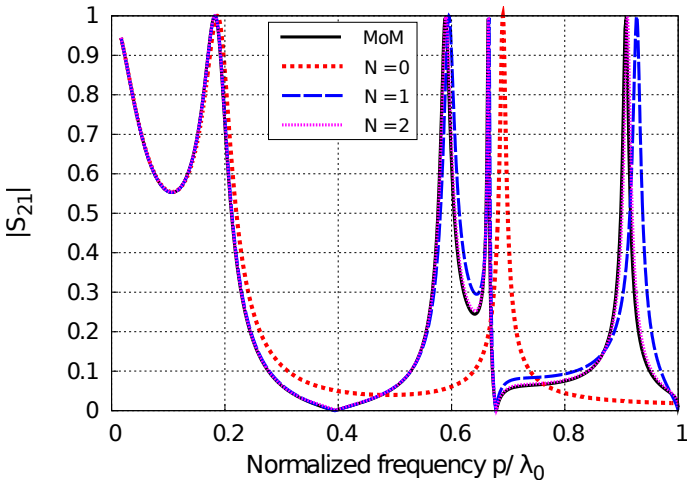

(a) $d_1 = p/2.5 = 4w$

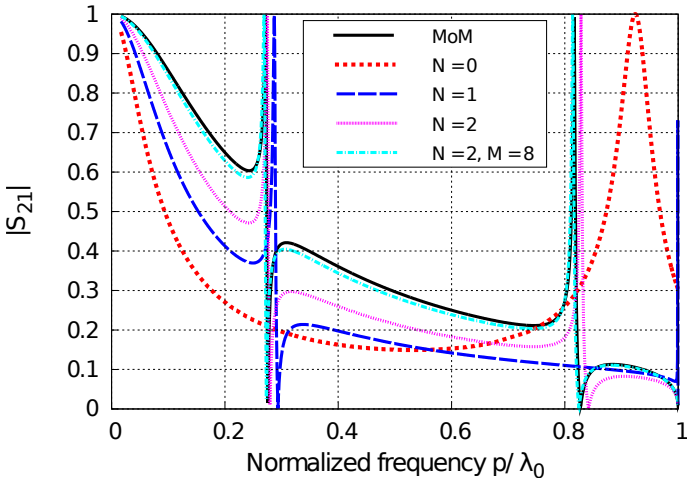

(b) $d_1 = p/50 = w/5$

Figure 5.6: Magnitude of the transmission coefficient ($|S_{21}|$) for two coupled gratings versus normalized frequency for TM incidence and for different thicknesses (d_1) of the dielectric slab between the gratings (i. e., for different values of the separation between the gratings). Parameters: $w = 0.1p$, $\varepsilon_{\mathrm{r}}^{(0)} = 1$, $\varepsilon_{\mathrm{r}}^{(1)} = 4$. (a) Relatively distant gratings. (b) Closely-spaced gratings.

first higher-order mode becomes propagative in the dielectric slab at $p/\lambda_0 = 0.5$. Thus, the $N = 0$ results start to deviate at lower frequencies ($p/\lambda_0 \gtrsim 0.2$) where the $n = 1$ evanescent mode is no longer far below its cutoff frequency and its increasingly dynamic behavior starts to have an effect on the transmission spectrum. The circuit model can accommodate this situation by simply setting $N = 1$; i.e., by incorporating the corresponding Π-network for the $n = 1$ mode (together with that for the fundamental $n = 0$ wave, which is always present). This is confirmed by the $N = 1$ results in Fig.5.6a, which show a very good agreement with the MoM curve up to $p/\lambda_0 \gtrsim 0.6$. For higher frequencies, these results show some deviation with respect to the MoM data, although still being able to reproduce the main features of the spectrum. Once again, this deviation is due to the fact that the next higher order mode ($n = 2$) is approaching its cutoff frequency inside the dielectric slab ($p/\lambda_0 = 1$). The circuit model with $N = 2$ does provide very accurate results over the whole frequency range.

Next, Fig. 5.6b shows the transmission spectrum for the same two coupled slit gratings as in Fig. 5.6a, but now with a much thinner dielectric slab ($d_1 = p/50$) and hence the gratings are tightly coupled. Two total transmission peaks are observed, each one followed by a transmission zero. If only the zero-order wave is considered as distributed element in the model through its corresponding Π-network (curve labeled as $N = 0$), the resulting equivalent circuit is not able to reproduce the transmission behavior at all. When the first higher-order mode is considered as a "low-order" mode and thus its dynamic distributed nature is taken into account through the corresponding Π-network ($N = 1$ curve), the first transmission peak and zero are captured by the circuit model, though slightly blue-shifted. The inclusion of the second higher-order mode ($N = 2$) mostly corrects this frequency shift and makes the proposed circuit model able to reproduce the second peak and zero. However, even with $N = 2$ the results are not satisfactory, since a significant difference in the transmission level with respect to MoM results is observed throughout the considered frequency range. The reason is that the circuit used to compute the $N = 0$, $N = 1$, and $N = 2$ curves in Fig.5.6b did not include the $C_{\text{p,coup}}$ and C_{s} coupling capacitors, which

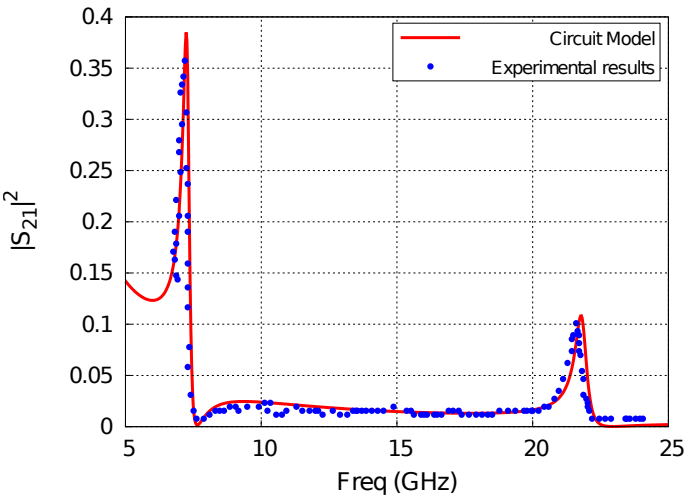

Figure 5.7: Comparison of our circuit approach data with experimental results [155] for the transmissivity coefficient ($|S_{21}|^2$) of a pair of tightly coupled 1-D gratings when a TM-polarized normally incident plane wave impinges on the structure. Parameters: $p = 10.02\,\text{mm}$, $w = 0.29\,\text{mm}$, $d_1 = 0.356\,\text{mm}$, $\varepsilon_\text{r}^{(0)} = 1$, $\varepsilon_\text{r}^{(1)} = 4.17$, $\tan(\delta) = 0.0167$. ©2016 APS.

implies that the coupling through evanescent modes is being neglected. As the gratings are now very close to one another, this coupling is expected to be significant. Indeed, for the present configuration and according to our criterion in (5.28), M should be set to 8. This means that, for the circuit model with $N = 2$, higher-order evanescent modes from $n = 3$ to $n = 8$ should contribute to the $C_\text{p,coup}$ and C_s capacitors. When these capacitors are also introduced in the circuit model (curve labeled $N = 2$, $M = 8$), the agreement with the MoM results is very good over all the frequency range shown. At this point, it is also worth highlighting the computational efficiency of the proposed equivalent circuit method. Even in this quite stringent case (with three distributed modes and up to eight modes contributing to the evanescent coupling), the CPU time needed for the computation of the ≈ 1000 values represented in Fig. 5.6b is almost negligible (it takes about $100\,\text{ms}$ in a modest laptop computer).

A second example is given in Fig.5.7, which shows a comparison between our equivalent-circuit results and experimental results reported in [155]. The transmissivity coefficient is plotted versus the frequency when a normally incident

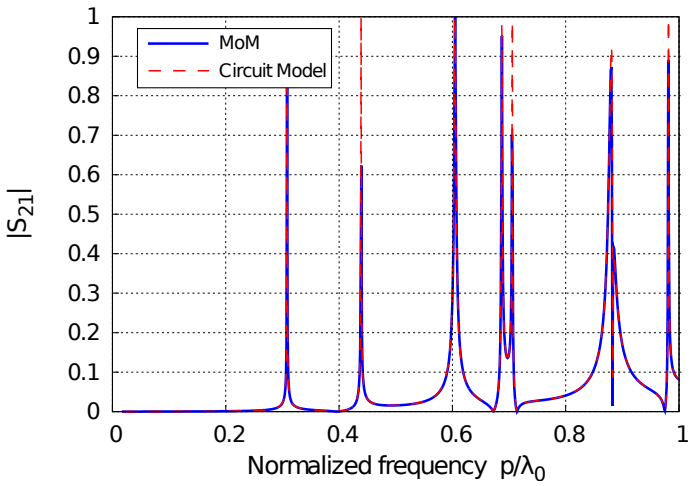

Figure 5.8: Transmission coefficient (magnitude) versus frequency for TE incidence. Parameters: $w = 0.2\,p$, $d_1 = 0.5\,p$, $\varepsilon_{\mathrm{r}}^{(0)} = 1$, $\varepsilon_{\mathrm{r}}^{(1)} = 9.8$. ©2016 APS.

TM plane wave impinges on a pair of coupled arrays. The gratings are printed on the two sides of an electrically very thin and lossy FR4 substrate. It should be pointed out that losses in the substrate can be straightforwardly incorporated in the circuit model through the admittances, (5.4), and wavenumbers, (5.5), just by replacing the lossless real value of permittivity, $\varepsilon_{\mathrm{r}}^{(i)}$, with its complex value for lossy substrates, $\varepsilon_{\mathrm{r}}^{(i)}(1 - \mathrm{j}\tan\delta^{(i)})$. According to our general criteria in (5.16) and (5.28), the circuit-model results in Fig.5.7 are computed with $N = 2$, $M = 5$. As it can be observed, the agreement with the experimental results is remarkably good.

The case of TE incidence is studied in Fig.5.8, where it is shown the frequency behavior of the transmission coefficient when a normally incident plane wave impinges on a pair of coupled gratings. For this polarization the interaction of the incident wave with the slits is weaker than for the TM case and an electrically thick medium is needed to observe transmission peaks, which are extremely frequency selective. Four low-order terms were taken as distributed elements ($N = 4$) because of the high permittivity of the substrate. These terms are associated with propagating modes in the dielectric region since the interaction through evanescent modes is almost negligible because the screens are far enough to be affected by them ($M = 0$). Once again, the accuracy shown by

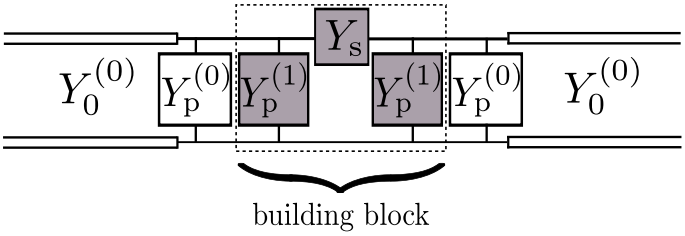

Figure 5.9: Topology of the equivalent circuit defining the internal Π-circuit (building block) and the external part. ©2016 APS.

the circuit model compared with the numerical MoM data is very good.

5.3 Stacked arrays

The previous section presented the derivation of the Π-circuit model for a pair of coupled slit gratings, together with a detailed in-depth physical interpretation of its elements. All the previous derivations and discussions will be found very pertinent for the study of stacked arrays since its corresponding equivalent circuit will be systematically built up from the Π-circuit model for a pair of coupled slit gratings. As already pointed out in Sec. 5.2.1, the key fact is that the Y_{p} admittance in the Π-network is given by the sum (parallel connection) of the external, $Y_{\mathrm{p}}^{(0)}$, and internal, $Y_{\mathrm{p}}^{(1)}$, parallel admittances. Since these admittances independently account for the field in medium (0) [external medium] and medium (1) [internal medium], there can be defined an "internal" Π-block associated with medium (1) characterized by $Y_{\mathrm{p}}^{(1)}$ and Y_{s}, as shown in Fig. 5.9. This internal Π-circuit can be employed as a "building block" to build up the equivalent circuit of a series of stacked arrays, as shown in Fig.5.10. The stacked structure amenable to be analyzed with this procedure may have the dielectric layers of different thickness and permittivity, but the slit arrays must be identical and aligned among them to preserve the periodicity in the transverse direction. It should be noted that the employed strategy is applicable to stacked structures thanks to the initial "aperture" formulation of the problem, which made it possible to define two independent sub-problems at both sides of the apertures

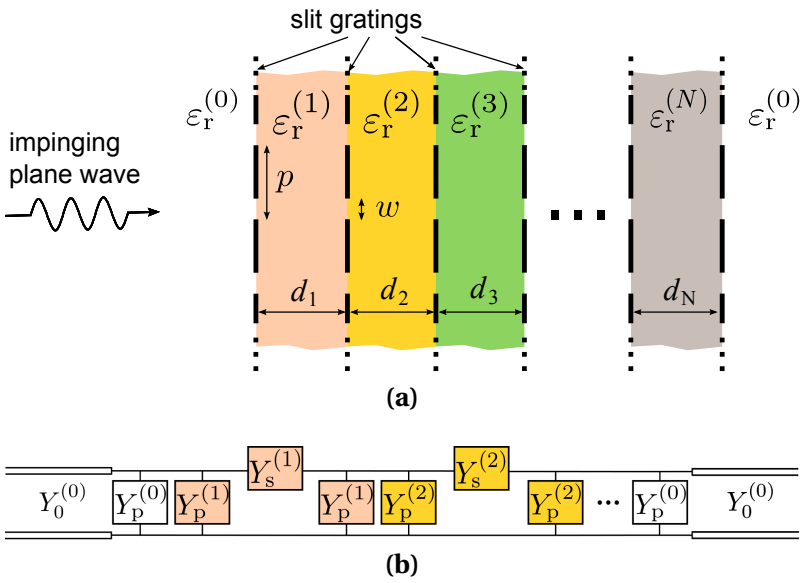

Figure 5.10: (a) Stacked structure with different dielectric slabs. (b) Equivalent circuit made by cascading Π-building blocks. ©2016 APS.

(slits).

The above rationale can also be employed to study an infinite set of periodically stacked slit gratings. In this case, the equivalent network of this longitudinally periodic structure is formed by the periodic repetition of the corresponding Π building block (the "unit cell" of the structure along the longitudinal z direction), as illustrated in Fig.5.11. As the elements of this Π building block are known in closed form, the dispersion relation of the Bloch modes of the infinite periodic stack is readily obtained as [34]

$$\cosh(\gamma d_1) = 1 + \frac{Y_\mathrm{p}}{Y_\mathrm{s}} \tag{5.42}$$

where $\gamma = \alpha + \mathrm{j}\beta$ is the complex propagation constant of the Bloch mode, with β being the phase constant and α the attenuation constant. The Bloch admittance at the longitudinal unit cell terminals is also derived immediately as [34]

$$Y_\mathrm{B} = \sqrt{Y_\mathrm{p}(Y_\mathrm{p} + 2Y_\mathrm{s})}\,. \tag{5.43}$$

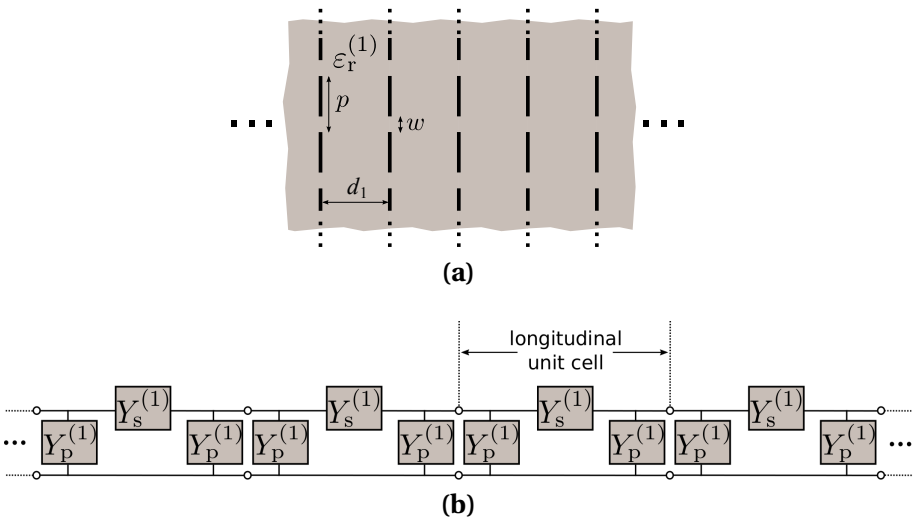

Figure 5.11: (a) Infinite periodic stack of slit gratings. (b) Equivalent circuit consisting of an infinite cascade of Π-building blocks. ©2016 APS.

5.3.1 Results and discussion

As a first example to check the validity of the circuit approach for stacked arrays, the transmission coefficient of a set of four cascaded arrays printed on three dielectric slabs under normal TM incidence is plotted in Fig.5.12. A high reflection behavior is observed at the center of the plot from $0.25p/\lambda_0$ up to about $0.7p/\lambda_0$. At low frequencies, a high level of transmission is expected because the slit gratings interact weakly with the incident wave. Additional transmission peaks are also found between $0.7p/\lambda_0$ and $0.9p/\lambda_0$. For comparison purposes, the results provided by the commercial simulator Ansys HFSS (based on the finite-element method in the frequency domain) are also shown. An excellent agreement is found between the two sets of data.

Next, the case of an infinite periodic stack of identical gratings is studied in Fig.5.13. The Brillouin diagram for the Bloch mode of this periodic structure obtained from (5.42) is plotted in Fig.5.13a, which shows four passbands separated by three stopbands (SB). It is interesting to note that the slope of the dispersion relation is positive in the first two passbands (often called *forward* passbands), whereas it is negative in the two higher-frequency bands (*backward* passbands).

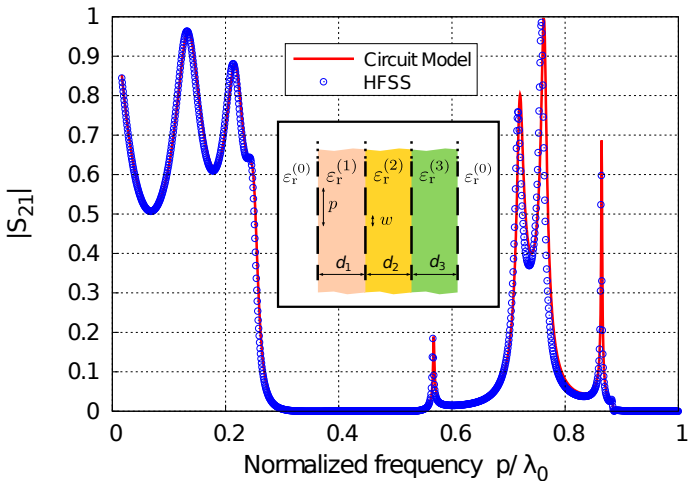

Figure 5.12: Magnitude of the transmission coefficient ($|S_{21}|$) versus normalized frequency for 4 stacked slit arrays under normal TM incidence. Parameters: $w = 0.1\,p$, $d_1 = 0.4\,p$, $d_2 = 0.3\,p$, $d_3 = 0.2\,p$, $\varepsilon_{\mathrm{r}}^{(0)} = 1$, $\varepsilon_{\mathrm{r}}^{(1)} = 2.2$, $\varepsilon_{\mathrm{r}}^{(2)} = 4$, $\varepsilon_{\mathrm{r}}^{(3)} = 3$. ©2016 APS.

Since no losses are assumed in any element of the present structure, the second member of (5.42) is always real, providing two possibilities for the propagation constant:

$$\gamma = \mathrm{j}\beta \qquad \text{if } \left[1 + \frac{Y_{\mathrm{p}}}{Y_{\mathrm{s}}}\right] \in [-1, 1] \tag{5.44}$$

$$\gamma = \alpha + \mathrm{j}\begin{cases} 0 \\ \pi d \end{cases} \qquad \text{if } \left[1 + \frac{Y_{\mathrm{p}}}{Y_{\mathrm{s}}}\right] \notin [-1, 1]\,. \tag{5.45}$$

Clearly, passbands occur when $\alpha = 0$ ($\gamma = \mathrm{j}\beta$) and stopbands when $\alpha \neq 0$ and $\beta = 0$ or πd. The existence of a passband is then subject to the following two conditions:

- (i) the reactive nature (capacitive/inductive) of Y_{s} and Y_{p} has to be different in order to satisfy $Y_{\mathrm{p}}/Y_{\mathrm{s}} < 0$
- (ii) $|Y_{\mathrm{p}}| < 2|Y_{\mathrm{s}}|$.

For instance, these conditions are satisfied if the Π-network has a relatively small capacitance as a parallel element (close to open circuit) and a small inductance as a series element (close to short circuit), which allows the power to pass

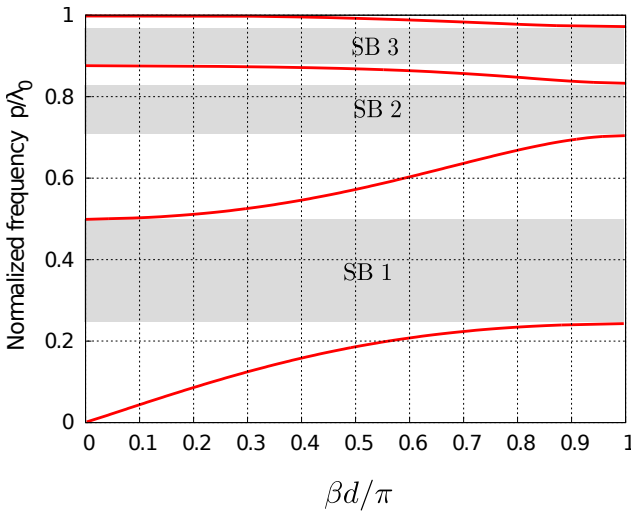

(a)

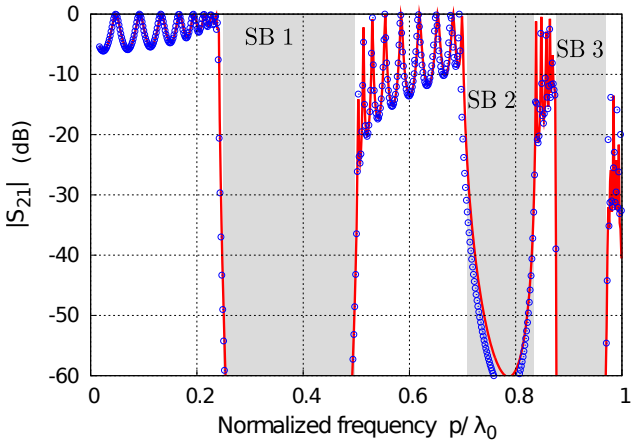

(b)

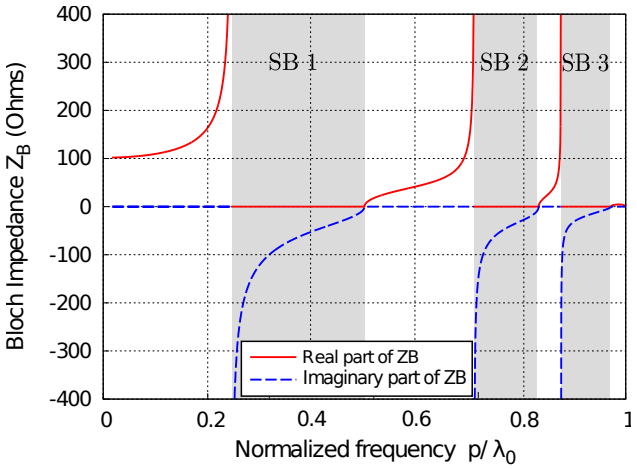

(c)

Figure 5.13: (a) Brillouin diagram of an infinite stacked structure. (b) Transmission coefficient (dB) versus normalized frequency for a truncated version (10 stacked gratings). (c) Bloch impedance of the Bloch mode represented in (a). The parameters of the unit cell are: $w = 0.15\,p$, $d_1 = 0.3\,p$, $\varepsilon_{\mathrm{r}}^{(0)} = 1$, $\varepsilon_{\mathrm{r}}^{(1)} = 4$. Frequency regions labeled SB 1, SB 2, and SB denotes stopbands.

through the structure thus obtaining a forward band [34]. On the other hand, the above two conditions can also be satisfied if Y_{s} is capacitive and Y_{p} inductive; for instance, a Π-network with a high capacitance as a series element and a high inductance as the parallel element. This would also allow the power to travel along the stacked structure, but now the passband would be of backward nature.

If a finite (truncated) version of the previous longitudinally periodic structure is now considered, a clear correspondence is expected between the Brillouin diagram and the behavior of the transmission coefficient of the finite stack. This fact is illustrated in Fig. 5.13b, which shows the transmission coefficient through a finite stack with 10 gratings. This figure shows the presence of successive passbands or stopbands that perfectly correlate with the associated Brillouin diagram in Fig.5.13a. The circuit-model results (solid lines) are compared with those provided by Ansys HFSS (circles), showing an excellent agreement. Another feature of this transmission behavior worthy to mention is the high level of ripples observed in the passbands. This is due to an impedance mismatching between the impinging wave (whose characteristic impedance is the intrinsic impedance of free space, $\eta_0 \approx 377\,\Omega$) and the Bloch input impedance (Bloch impedance) of the stack. Fig.5.13c shows the real and imaginary parts of the Bloch impedance ($Z_{\mathrm{B}} = 1/Y_{\mathrm{B}}$) obtained from (5.43). Since the considered structure is lossless, Z_{B} is real-valued at passband and purely imaginary at stopband frequencies. For the most part of the first three passbands, the Z_{B} value is much lower than the free space impedance, although it tends to grow within each band, which is consistent with the decreasing trend of the ripples. Also, Z_{B} is higher in the first (low-frequency) passband, and hence the ripples in this band are smaller than in the next two passbands. Finally, the last passband (at the higher frequencies) is the one showing by far the highest mismatching, due to the particularly low value of Z_{B} at these frequencies.

As a last example, in Fig.5.14a a lossy stack with the space between the gratings filled with resistive silicon slabs is studied. The complex effective permittivity of the slabs is given by $\varepsilon^{(1)} = \varepsilon_0 \varepsilon_{\mathrm{r}}^{(1)} - \mathrm{j}\sigma/\omega$, where σ is the dc conductivity of

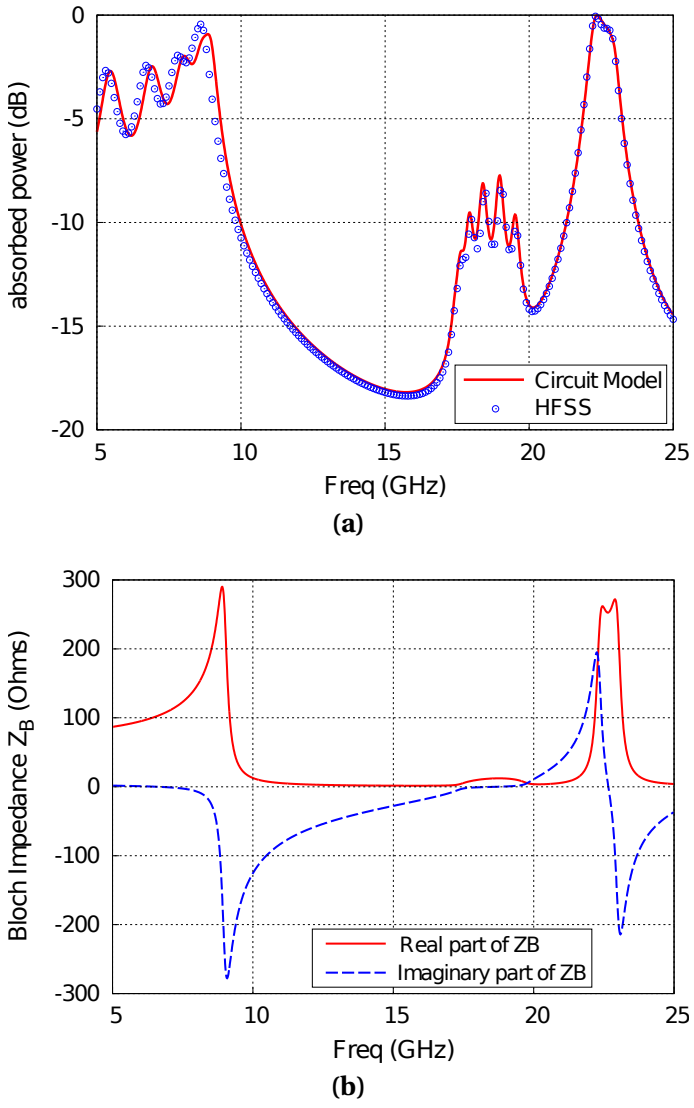

Figure 5.14: (a) Power absorbed in a lossy system formed by eight stacked arrays separated by seven resistive (ohmic) dielectric slabs ($\sigma = 0.2\,\mathrm{S/m}$). (b) Bloch impedance versus frequency. Parameters: $p = 5\,\mathrm{mm}$, $w = 1.4\,\mathrm{mm}$, $d_1 = 2.2\,\mathrm{mm}$, $\varepsilon_\mathrm{r}^{(0)} = 1$, $\varepsilon_\mathrm{r}^{(1)} = 11.9$.

the layers. Fig. 5.14a shows the power absorbed in a finite stack (normalized to the incident power), whereas the Bloch impedance of the corresponding infinite stack is plotted in Fig. 5.14b. Since the structure is lossy, the Bloch impedance takes complex values at any frequency. The most interesting feature is the high-absorption band at high frequencies, with a fractional bandwidth of 4.5% for a central frequency of $22.5\,\mathrm{GHz}$. As shown in Fig. 5.14b, this absorption band can be related to a Bloch impedance as well as a relatively constant real part that is close to the free-space impedance and with a relatively small imaginary part in the same frequency range. This behavior of the Bloch impedance has been obtained by properly adjusting the geometrical parameters and the value of the slab conductivity. Note that, for frequencies between approximately 17 and $20\,\mathrm{GHz}$, Z_B is mostly real-valued as well. However, its small value implies a strong mismatch with the incident wave that causes most of the incident power to be reflected rather than absorbed in the resistive silicon slabs.

5.4 Oblique incidence

The extension of the circuit model to the case of a plane wave that impinges obliquely with an incident angle θ is straightforward. Assuming that the incidence is in the yz plane (see Fig. 5.1), the corresponding incident wave vector is given by

$$\mathbf{k} = \sqrt{\varepsilon_\mathrm{r}^{(0)}}\, k_0(\cos\theta\,\hat{\mathbf{z}} + \sin\theta\,\hat{\mathbf{y}})\ . \tag{5.46}$$

The parallel and series admittances obtained in Sec. 5.2 are defined in terms of an infinite sum of modes. For oblique incidence, the transverse boundary conditions of the unit cell are no longer electric or magnetic walls but periodic walls, which implies that the series of modes now become series of Floquet spatial harmonics. Thus, the series and parallel admittances in Fig. 5.9 can be written

as

$$Y_{\mathrm{p}}^{(0)} = \sum_{n}{}' \left[\frac{\tilde{f}_n}{\tilde{f}_0}\right]^2 Y_n^{(0)} \tag{5.47}$$

$$Y_{\mathrm{p}}^{(1)} = \sum_{n=-\infty}^{\infty} \left[\frac{\tilde{f}_n}{\tilde{f}_0}\right]^2 Y_n^{(1)} \tan(\beta_n^{(1)} d_1/2) \tag{5.48}$$

$$Y_{\mathrm{s}} = \sum_{n=-\infty}^{\infty} \left[\frac{\tilde{f}_n}{\tilde{f}_0}\right]^2 Y_n^{(1)} \csc(\beta_n^{(1)} d_1) \tag{5.49}$$

where

$$\beta_n^{(i)} = \sqrt{\varepsilon_{\mathrm{r}}^{(i)} k_0^2 - (k_n + k_{\mathrm{t}})^2} \tag{5.50}$$

$$k_t = \sqrt{\varepsilon_{\mathrm{r}}^{(0)}}\, k_0 \sin(\theta) \tag{5.51}$$

with k_t being the transverse (to z) y-component of the wavevector. For the definition of the $\left[\frac{\tilde{f}_n}{\tilde{f}_0}\right]$ coefficients, the same field profiles as in (5.7) are considered, and therefore their expressions are similar to those in (5.3) but now incorporate the phase shift imposed by the incident plane wave,

$$[\tilde{f}_n]^2 = \begin{cases} \left[J_0((k_n + k_{\mathrm{t}})w/2)\right]^2 & \text{TM incidence} \\ \left[2\dfrac{J_1((k_n + k_{\mathrm{t}})w/2)}{(k_n + k_{\mathrm{t}})w/2}\right]^2 & \text{TE incidence} \end{cases}. \tag{5.52}$$

Regarding the criterion for the number of low-order harmonics, we now define N as the number of propagative negative harmonics ($n < 0$) plus 1 inside the highest-permittivity medium at the highest frequency of interest, namely:

$$N = \left\lceil \left(\sqrt{\varepsilon_{\mathrm{r,max}}} + \sqrt{\varepsilon_{\mathrm{r}}^{(0)}} \sin\theta\right) \frac{p}{\lambda_{0,\mathrm{min}}} \right\rceil \tag{5.53}$$

(for positive angles of incidence, the number of propagative positive harmonics is at most equal to the number of propagative negative harmonics). All the harmonics with $|n| \leq N$ are thus considered low-order harmonics whose contribution to the above sums is taken rigorously without any approximation. The

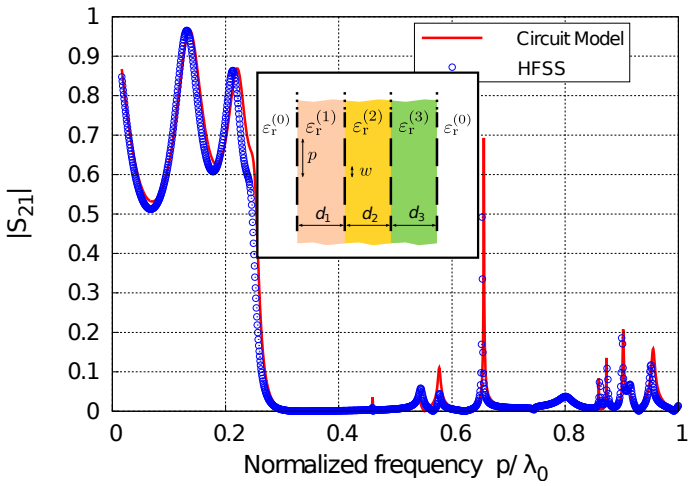

Figure 5.15: Transmission coefficient (magnitude) versus normalized frequency for a four-slit-array stacked structure under oblique TM incidence ($\theta = 20^o$). Parameters: $w = 0.1\,p$, $d_1 = 0.4\,p$, $d_2 = 0.3\,p$, $d_3 = 0.2p$, $\varepsilon_{\rm r}^{(0)} = 1$, $\varepsilon_{\rm r}^{(1)} = 2.2$, $\varepsilon_{\rm r}^{(2)} = 4$, $\varepsilon_{\rm r}^{(3)} = 3$. ©2016 APS.

harmonics with $|n| \geq N+1$ are all far below the cutoff in the frequency range of interest, and thus we can use the following approximation:

$$k_n + k_t \approx k_n \tag{5.54}$$

$$\beta_n \approx -\mathrm{j}k_{|n|} \tag{5.55}$$

which implies that, once again, their global contribution to the equivalent circuit can be accounted for by frequency-independent capacitances or inductances. Taking into account (5.55), the same criterion for M as in (5.28) can be applied here, and only those high-order harmonics with $|n| \leq M$ are considered in the elements that represent coupling through evanescent fields.

As an example of application, Fig.5.15 shows the reflection coefficient versus frequency for the case of four stacked slit arrays under oblique TM incidence with $\theta = 20^o$. As in previous comparisons, the agreement with the results from HFSS is very good.

Finally, it should be mentioned that the range of application of the model is more reduced for oblique incidence than for normal incidence, as expected. In

order to check quantitatively the limitations of both normal and oblique incidence, an exhaustive analysis of the accuracy of the model (similar to the one reported in Chapter 2) will be next carried out.

5.5 Range of validity of the model for two identical coupled slit arrays.

In this section we will establish the limits of validity of the models, both for TE and TM incidence. Since the circuit models presented in the present chapter are actually extensions of the models derived in Chapter 2, it is expected to observe, at least for largely-spaced arrays, similar limits of validity. The main point of discussion will then concern how the limits of validity are affected as the gratings separation decreases.

5.5.1 TM incidence

Pairs of coupled slits arrays under TM normal incidence are considered in this section. It is worth mentioning that the range of validity of the model deduced for a pair of gratings is also applicable to a set of stacked gratings (composed of more than two gratings). It should be reminded that, for TM normal incidence, the limit of validity deduced for a single slit grating was given by $w/\lambda = 0.4$ (according to the criterion established in Chapter 2), with w being the width of the slit aperture and λ the wavelength at the highest-permitivitty medium forming the interface where the grating is located.

In order to check whether this limit remains the same for closely spaced staked arrays, we show in Fig. 5.16 and Fig. 5.17 several results representing the transmission coefficient versus the normalized frequency. In particular, Fig.5.16 considers a pair of slit gratings in vacuum with $w/p = 0.4$. The figure is composed of four plots, each obtained for a different value of the separation between gratings. In all cases, the results provided by the model are compared

with results from a in-house MoM code. Generally, the agreement between both curves is excellent up to $w/\lambda_0 = 0.4$ although there exist sligh deviations in Fig. 5.16c and Fig. 5.16d beyond $w/\lambda \approx 0.3$. These cases account for a separation between arrays smaller than the slit width. A similar limit of validity can be extracted from the plots in Fig. 5.17, where the aperture width is $w/p = 0.2$. It is important to highlight, however, than now the agreement shown between the curves obtained from the model and the MoM is good up to $w/\lambda_0 = 0.4$ in all cases. It seems that as the slit width is becoming smaller with respect the period, the accuracy of the model is greater. Despite these minor differences, it is reasonable to conclude that the limit of validity of the model for a pair of coupled gratings is still the same as for a single grating.

This range of validity is satisfied if a dielectric slab is filling the region between gratings. In Fig. 5.18 three plots are shown representing the transmission coefficient versus normalized frequency for a pair of coupled gratings with three different values of the separation d. The dielectric slab have a permittivity of $\varepsilon_{\mathrm{r}} = 9$, so the normalized frequency is now defined as $w(\varepsilon_{\mathrm{r}})^{1/2}/\lambda_0 = w/\lambda_{\mathrm{diel}}$. We now observe how the agreement between both curves is quite good up to $w/\lambda_{\mathrm{diel}} \approx 0.4$. At higher frequencies, the degree of deterioration comparing with the case in vacuum is actually lesser. Consequently, $w/\lambda_{\mathrm{diel}} \approx 0.4$ can be stated as a reliable limit.

A final TM-incidence example is shown in Fig. 5.19. The structure parameters are identical to the previous example, but oblique incidence with 30^o incidence angle is now considered. The accuracy of the model is now restricted to frequencies below $w/\lambda_{\mathrm{diel}} \approx 0.15 - 0.2$. This reduced range is expected since the assumed electric-field profile at the aperture is symmetrical with respect the horizontal middle plane of the unit cell, whereas the actual field at the aperture is clearly non-symmetrical. In practice, it reduces the limit of accuracy to the half, as we observe in the figures in accord with that previously observed for single gratings in Chapter 2.

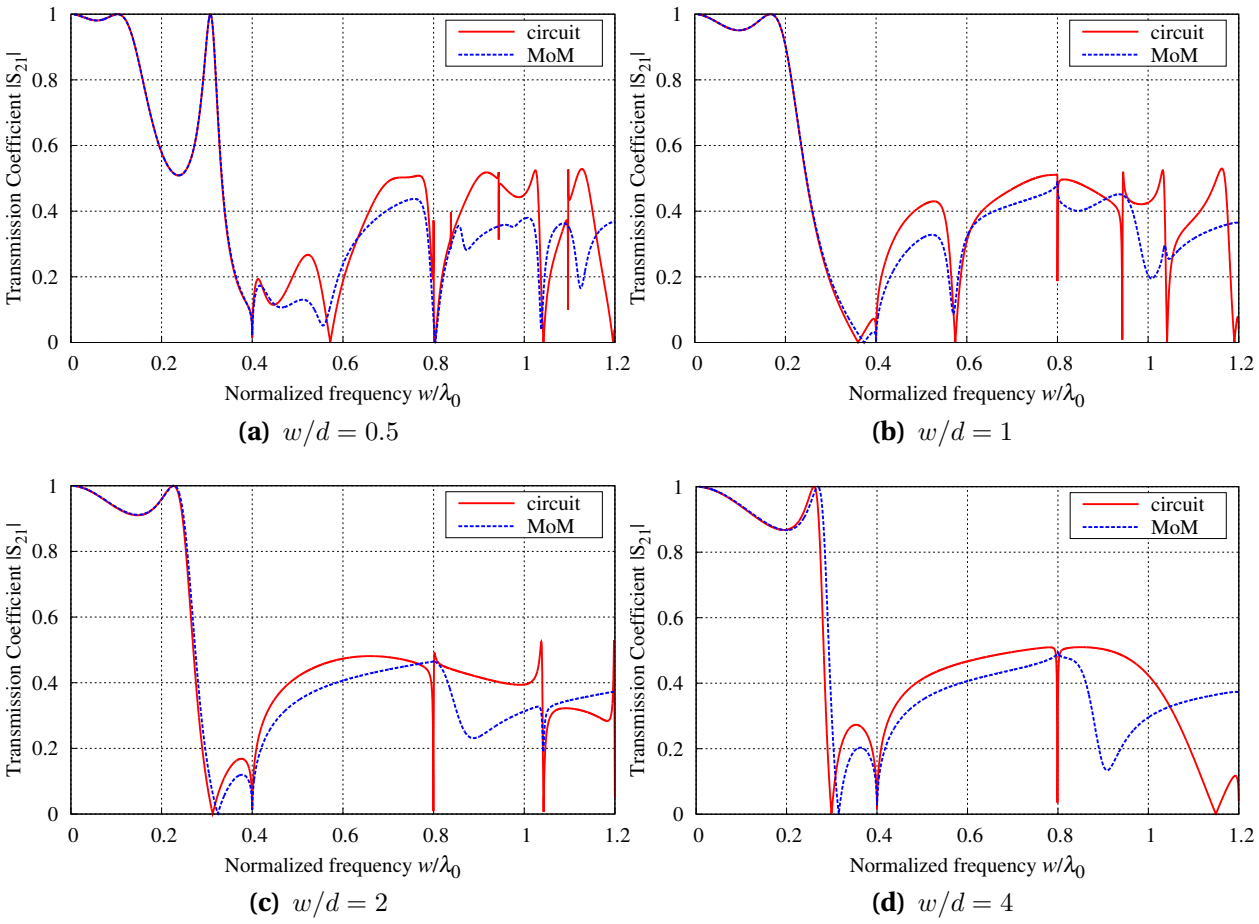

(a) $w/d = 0.5$ **(b)** $w/d = 1$

(c) $w/d = 2$ **(d)** $w/d = 4$

Figure 5.16: Magnitude of the transmission coefficient for two coupled slit gratings in vacuum under TM normal incidence for different values of the separation between the gratings. The slits are considerably wide $w/p = 0.4$.

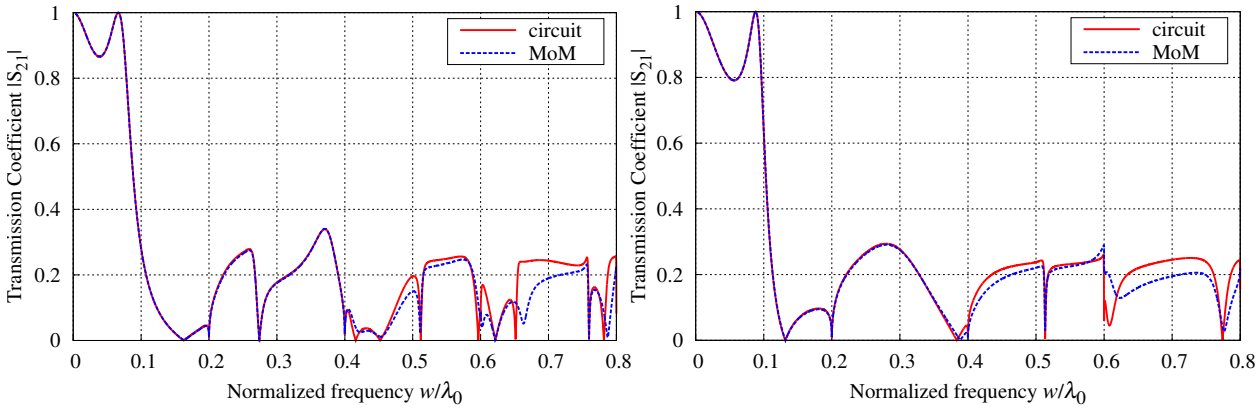

(a) $w/d = 0.5$ **(b)** $w/d = 1$

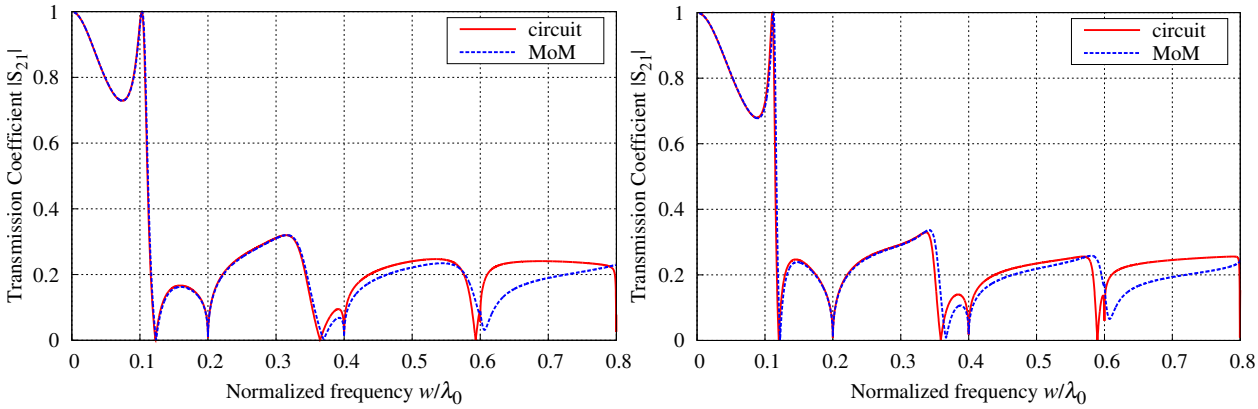

(c) $w/d = 2$ **(d)** $w/d = 4$

Figure 5.17: Same as Fig.5.16, but for a slit width $w = 0.2p$.

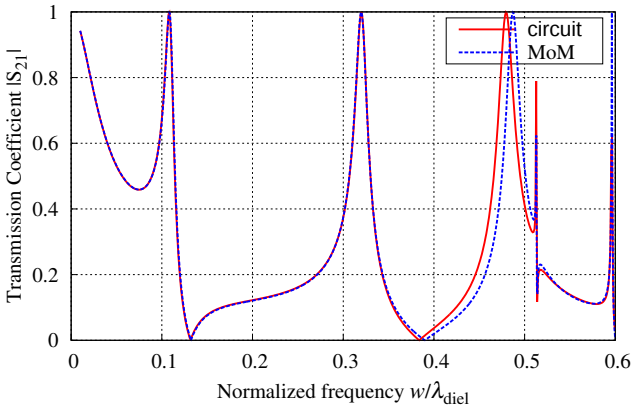

(a) $w/d = 1$

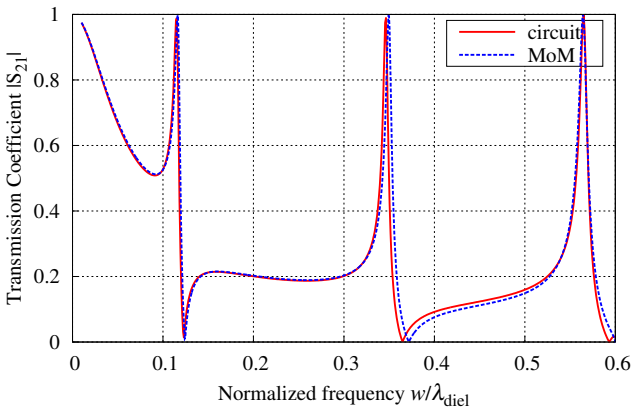

(b) $w/d = 2$

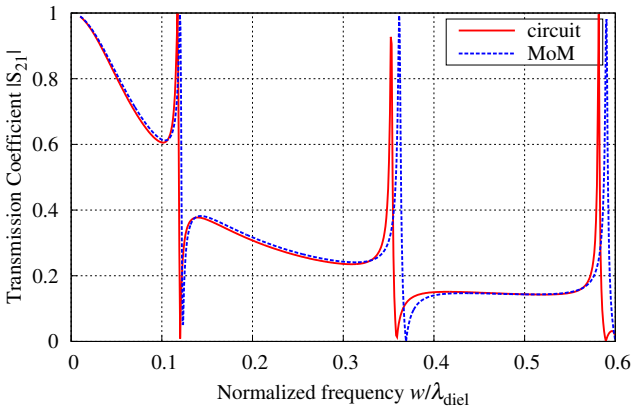

(c) $w/d = 4$

Figure 5.18: Same as Fig.5.17, but with a dielectric slab sith $\varepsilon_r = 9$ between the gratings. Note that the normalized frequency values in the abscissa now use the wavelength inside the dielectric $\lambda_{\text{diel}} = \lambda_0/\sqrt{\varepsilon_r}$.

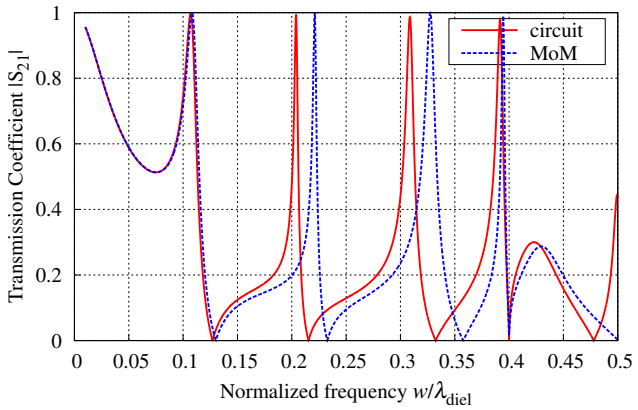

(a) $w/d = 1$

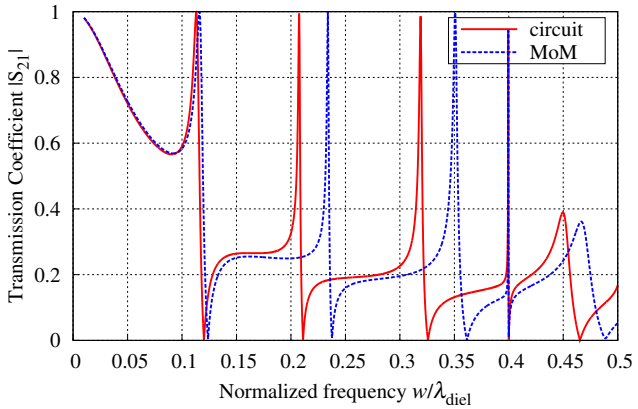

(b) $w/d = 2$

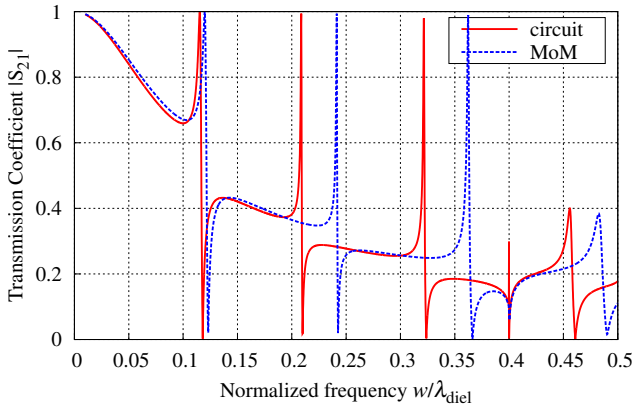

(c) $w/d = 4$

Figure 5.19: Same as Fig.5.18, but under oblique incidence with $\theta = 30°$.

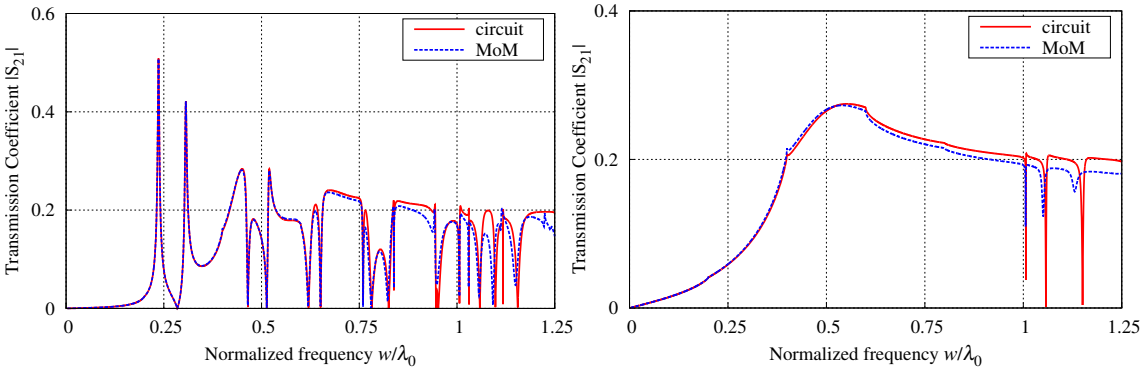

(a) $w/d = 0.5$ **(b)** $w/d = 2$

Figure 5.20: Magnitude of the transmission coefficient for two coupled slit gratings in vacuum under TE normal incidence for two different values of the separation between the gratings (d). The slits occupy 20% of the unit cell, $w/p = 0.2$.

5.5.2 TE incidence

Let us now check the accuracy of the model for TE incidence. According to the studied carried out in Chapter 2 for a single slit grating in vacuum under TE normal incidence, the limit of validity of the model was set around $w/\lambda_0 = 0.6$. Considering now a pair of coupled slits gratings, we will check how this accuracy limit is barely modified. Fig. 5.20 and Fig. 5.21 represent the transmission coefficient obtained for a pair of coupled slit gratings in vacuum under TE normal incidence. Each figure is composed of two different plots, referring to two different gratings separations. The plots in Fig. 5.20 have been obtained for $w/p = 0.2$. The agreement between the results provided by the circuit model and the MoM is excellent up to $w/\lambda_0 = 0.6$ although the deviation between both curves is not dramatic beyond this limit. Same conclusions can be inferred from the results in Fig. 5.21, where the slit width has been increased to $w/p = 0.7$ (70% of the period). The deviations beyond $w/\lambda_0 = 0.6 - 0.65$ are now, however, much more noticeable.

Placing a dielectric slab in the region between gratings, the limit of validity is

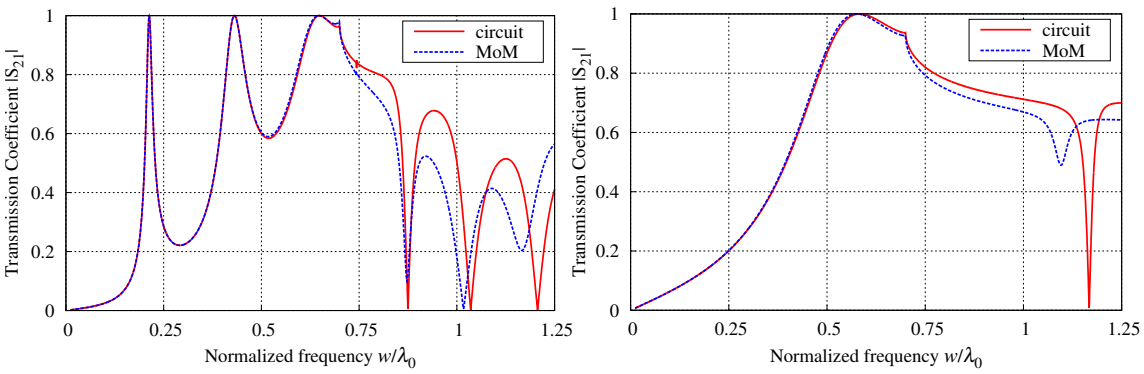

(a) $w/d = 0.5$ **(b)** $w/d = 2$

Figure 5.21: Same as Fig.5.20, but for very wide slits $w/p = 0.7$.

now governed by a normalized frequency in terms of the effective wavelength

$$\lambda_{\text{eff}} = \lambda_0/(\varepsilon_{\text{eff}})^{1/2} \tag{5.56}$$

with ε_{eff} being

$$\varepsilon_{\text{eff}} = \frac{\varepsilon_{\text{L}} + \varepsilon_{\text{R}}}{2} \tag{5.57}$$

where ε_{L} and ε_{R} are the permittivity of the medium at the left- and right-hand side of the grating. This normalization was already used for single gratings, and we will check that it is appropriate also for stacked gratings. In order to corroborate this, an example is depicted in Fig.5.22 where the transmission coefficient is represented versus the normalized frequency. The effective wavelength is calculated using the permittivity of vacuum (external medium) and $\varepsilon_{\text{r}} = 9$ (internal slab). The slit widths of both gratings are $w/p = 0.2$ for this example. A safe limit can be established at $w/\lambda_{\text{eff}} \approx 0.7 - 0.8$, although the deterioration is not dramatic beyond this limit. A final example regarding oblique incidence is represented in Fig.5.23 for $w/p = 0.7$. The limit of validity can be set around $w/\lambda_{\text{eff}} \approx 0.5 - 0.6$, as observed in Fig.5.23a. However, if the variation of the spectrum with frequency is smoother (as the one in Fig. 5.23b), the differences are appreciated around and beyond $w/\lambda_{\text{eff}} \approx 0.7$. In conclusion, no significant differences are introduced in the limit of accuracy of the model, by the presence of the second grating, and thus the limit established in Chapter 2 for slits gratings

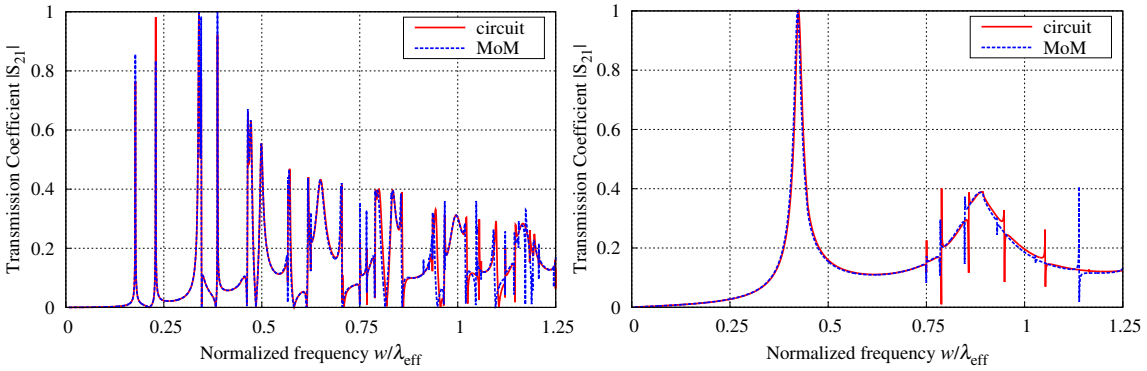

(a) $w/d = 0.5$ **(b)** $w/d = 2$

Figure 5.22: Same as Fig. 5.20, but with a high permittivity slab ($\varepsilon_r = 9$) between the gratings. The wavelength used for the normalized frequency values is $\lambda_{\text{eff}} = \lambda_0/\sqrt{\varepsilon_{\text{eff}}}$, corresponding to an effective medium with relative permittivity $\varepsilon_{\text{eff}} = (1+\varepsilon_r)/2$. In this example, $\varepsilon_{\text{eff}} = 5$.

remains practically the same for stacked gratings.

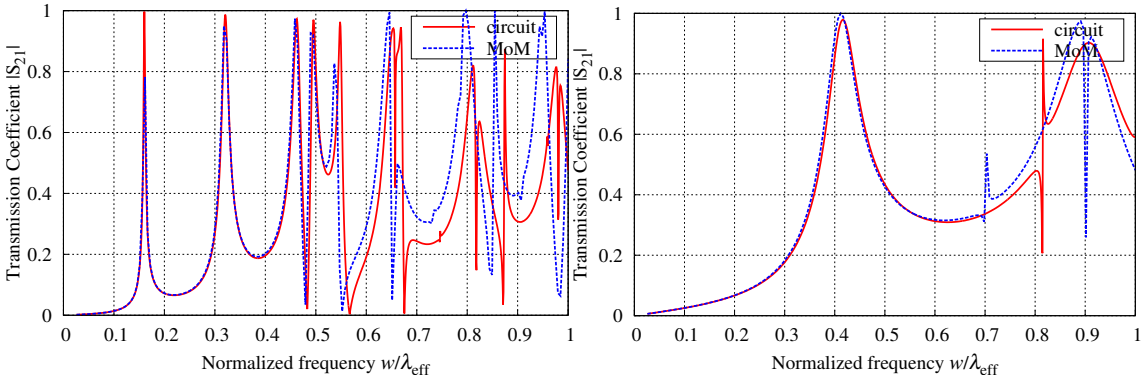

(a) $w/d = 0.5$ **(b)** $w/d = 2$

Figure 5.23: Same as Fig. 5.22, but for oblique incidence at $\theta = 30°$ and with $w/p = 0.7$.

5.6 A pair of non-aligned and different coupled arrays. Generalization of the equivalent circuit.

The equivalent Π topology derived above has been shown to exhibit a very good performance. The model is accurate for a wide frequency range, even well beyond the onset of the grating-lobes regime (if the slits are not very wide). However, the model can only be used to analyze the scattering response of a pair of identical gratings. Its derivation required the structure to be symmetric with respect the vertical middle plane of the unit cell. Under this circumstance, the problem could be treated by considering an even/odd excitation analysis, which led to an equivalent Π network according to the procedure detailed above. This symmetry condition is not satisfied when, for instance, a pair of two different coupled and *aligned* arrays are considered; the term *aligned* indicates here that the middle planes of both slit apertures are set at the same height in the unit cell [see Fig. 5.24]. In this case the methodology detailed above for deriving the Π equivalent circuit is clearly insufficient. Fortunately, next it will be shown that there exists an alternative procedure to obtain a Π-topology for different coupled slit arrays as long as they have the same period. This new procedure is based on the matrix formalism of microwave network analysis [34]. This equivalent Π circuit can also be extended to find an equivalent circuit for a pair of *non-aligned* coupled gratings, although in this latter case, an equivalent circuit with an explicit topology can only be derived for normal incidence.

5.6.1 Equivalent Π network for two different and aligned coupled gratings.

The basic structure under study is schematically shown in Fig. 5.24. Two 1-D aligned periodic arrays with different slit widths (w_1 and w_2), having the same

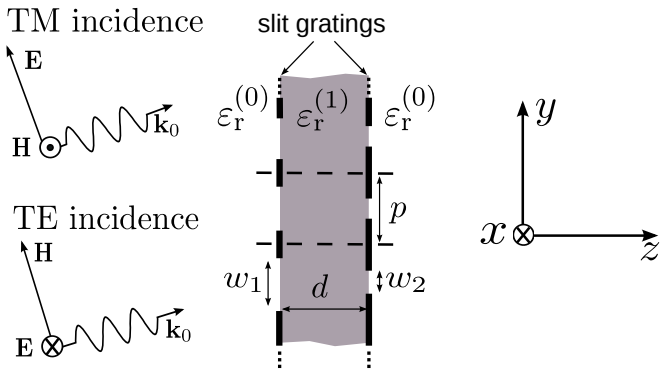

Figure 5.24: Cross-section of a pair of periodic coupled slit arrays. The metal strips are infinitely thin and infinitely long along the x direction. The slit widths of each grating are, in general, different. TM or TE incidence is considered.

lattice parameter (period p), are sandwiching a dielectric slab with permittivity $\varepsilon_r^{(1)}$ and thickness d. The lack of a vertical symmetry plane along the longitudinal z-direction clearly precludes the use of the even/odd analysis to derive the corresponding equivalent Π circuit. In this subsection a new strategy is provided to obtain an appropriate Π-network that models the scattering of a TE/TM-polarized plane wave that impinges obliquely on the structure. Before dealing with the coupled-grating case, it will be first considered the multimode equivalent network for a single-slit grating surrounded by two semi-infinite dielectric media, previously obtained in Chapter 2. The correspondig expression for the equivalent admittance of the aperture discontinuity is the following:

$$Y_{\text{eq}} = \sum_n{}' \left[\frac{\tilde{f}_n}{\tilde{f}_0}\right]^2 (Y_n^{(0)} + Y_n^{(1)}) \tag{5.58}$$

where $Y_n^{(i)}$ is the TM/TE admittance of the nth Floquet harmonic in the medium $i = 0, 1$. The corresponding schematic representation of the equivalent circuit associated with (5.58) is shown in Fig. 5.25. It consists of an interconnection among an infinite number of transmission lines, each associated with a different n-th harmonic. Let us now assume a system formed by two coupled gratings spaced a certain distance d. Taking each individual grating separately, their respective circuit models, depicted in Fig. 5.26(a), have the same representation

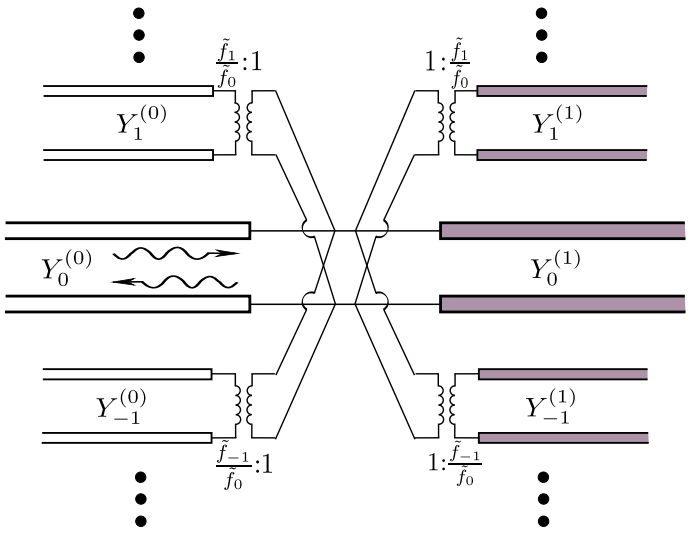

Figure 5.25: Multimode equivalent circuit for a single grating placed between two semi-infinite half spaces.

as the one in Fig.5.25. The information about the slit width of the gratings is incorporated into the tranformer-ratio expressions. For a slit discontinuity, they are given by

$$\frac{\tilde{f}_n(w_i)}{\tilde{f}_0(w_i)} = \begin{cases} \dfrac{J_0([k_n + k_\mathrm{t}]w_i/2)}{J_0(k_\mathrm{t} w_i/2)} & \text{TM incidence} \\ \dfrac{J_1([k_n + k_\mathrm{t}]w_i/2)}{J_1(k_\mathrm{t} w_i/2)} \dfrac{k_\mathrm{t}}{k_n + k_\mathrm{t}} & \text{TE incidence}\,. \end{cases} \tag{5.59}$$

Clearly, the transformer ratios for each of the two single-grating model will be different when $w_1 = w_2$. On the contrary, the charasteristic admittances and the propagation constants of the nth transmission lines in a particular medium are identical regardless of the geometry of the gratings under consideration (they basically depend on the periodicity of the structure and the permitivity of the medium). This fact allows us to construct the multimode circuit for the coupled-array system by simply connecting the transmission lines associated with harmonics of the same order within medium (1), as shown in Fig. 5.26(b). The length of each nth-order *internal* line (grey line in the figure) is precisely the dielectric thickness d. In principle, the internal circuit comprises an infinite number of internal lines. However, in practice, there are only a few propagative

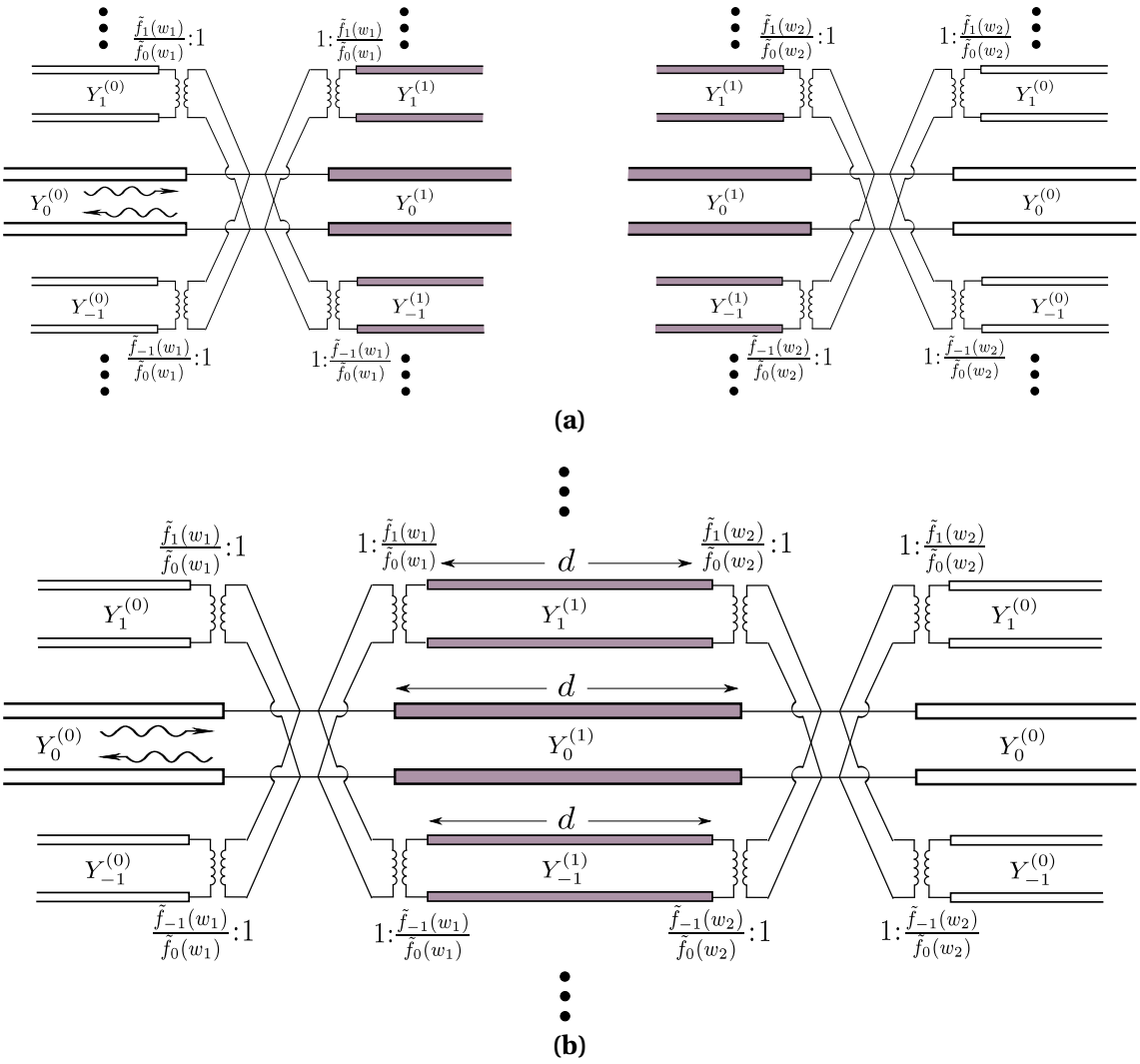

Figure 5.26: (a): Individual equivalent circuits for the slit arrays forming the coupled system. (b): Equivalent circuit of the coupled system, obtained after connecting the nth-order transmission lines of each individual circuit.

harmonics in the region between gratings, with the remaining ones being of evanescent nature. Depending on the electrical distance between screens, several evanescent harmonics could have an attenuation constant low enough to allow for a direct interaction between the two slits discontinuities. In this sense, they should be treated as propagating harmonics although the characteristic

admittance of their equivalent transmission line would be purely imaginary instead of real. As the distance between gratings decreases, more evanescent harmonics are required to be represented by transmission lines. This idea has been studied in depth in the present chapter, in Sec 5.2.2 and Sec. 5.2.3 for identical and aligned arrays, and will be similarly used below for the case under study.

Now our attention will focus on the so-called "internal" region [grey lines in Fig. 5.26(b)] in order to find an equivalent Π topology to describe the field behaviour in this region. First it will be defined a nth-order *internal block*, formed by the nth-order left tranformer, the nth-order transmission line and the nth-order right transformer. This block admits the following matrix representation in terms of the product of their associated ABCD matrices [34]:

$$
\begin{aligned}
[\mathrm{ABCD}]_n = &\begin{pmatrix} \dfrac{1}{\left[\dfrac{\tilde{f}_n(w_1)}{\tilde{f}_0(w_1)}\right]} & 0 \\ 0 & \left[\dfrac{\tilde{f}_n(w_1)}{\tilde{f}_0(w_1)}\right] \end{pmatrix} \\
&\times \begin{pmatrix} \cos(\beta_n^{(1)} d) & \mathrm{j} Z_n^{(1)} \sin(\beta_n^{(1)}) \\ \mathrm{j} Y_n^{(1)} \sin(\beta_n^{(1)} d) & \cos(\beta_n^{(1)} d) \end{pmatrix} \\
&\times \begin{pmatrix} \left[\dfrac{\tilde{f}_n(w_2)}{\tilde{f}_0(w_2)}\right] & 0 \\ 0 & \dfrac{1}{\left[\dfrac{\tilde{f}_n(w_2)}{\tilde{f}_0(w_2)}\right]} \end{pmatrix}
\end{aligned}
\tag{5.60}
$$

where the leftmost/righmost matrix represents the nth-order transformer placed at the left/right- hand termination of the line, and the middle matrix is the ABCD matrix for the nth-order transmission line. The resulting nth-order ABCD matrix is found to be

$$
[\mathrm{ABCD}]_n = \begin{pmatrix} \dfrac{\tilde{f}_n(w_2)}{\tilde{f}_0(w_2)} \dfrac{\tilde{f}_0(w_1)}{\tilde{f}_n(w_1)} \cos(\beta_n^{(1)} d) & \mathrm{j} Z_n^{(1)} \dfrac{\tilde{f}_0(w_1)}{\tilde{f}_n(w_1)} \dfrac{\tilde{f}_0(w_2)}{\tilde{f}_n(w_2)} \sin(\beta_n^{(1)} d) \\ \mathrm{j} Y_n^{(1)} \dfrac{\tilde{f}_n(w_1)}{\tilde{f}_0(w_1)} \dfrac{\tilde{f}_n(w_2)}{\tilde{f}_0(w_2)} \sin(\beta_n^{(1)} d) & \dfrac{\tilde{f}_n(w_1)}{\tilde{f}_0(w_1)} \dfrac{\tilde{f}_0(w_2)}{\tilde{f}_n(w_2)} \cos(\beta_n^{(1)} d) \end{pmatrix}.
\tag{5.61}
$$

The nth ABCD matrix is next converted into the following nth-order admittance matrix $[Y]_n$,

$$[Y]_n = \begin{pmatrix} -\mathrm{j}Y_n^{(1)} \left[\dfrac{\tilde{f}_n(w_1)}{\tilde{f}_0(w_1)}\right]^2 \cot(\beta_n^{(1)} d) & \mathrm{j}Y_n^{(1)} \dfrac{\tilde{f}_n(w_2)}{\tilde{f}_0(w_2)} \dfrac{\tilde{f}_n(w_1)}{\tilde{f}_0(w_1)} \csc(\beta_n^{(1)} d) \\ \mathrm{j}Y_n^{(1)} \dfrac{\tilde{f}_n(w_2)}{\tilde{f}_0(w_2)} \dfrac{\tilde{f}_n(w_1)}{\tilde{f}_0(w_1)} \csc(\beta_n^{(1)} d) & -\mathrm{j}Y_n^{(1)} \left[\dfrac{\tilde{f}_n(w_2)}{\tilde{f}_0(w_2)}\right]^2 \cot(\beta_n^{(1)} d) \end{pmatrix} . \quad (5.62)$$

Such a nth-admittance matrix characterizes the corresponding two-port network. Since $Y_{12} = Y_{21}$ in (5.62) and all the matrix elements are imaginary, the admittance matrix leads to a reciprocal lossless Π network in a natural way [6, 34]. The circuit elements of such a Π network [Fig.5.27(a)] are given by

$$Y_{\mathrm{s},n} = -Y_{12} = -\mathrm{j}Y_n^{(1)} \frac{\tilde{f}_n(w_1)}{\tilde{f}_0(w_1)} \frac{\tilde{f}_n(w_2)}{\tilde{f}_n(w_2)} \csc(\beta_n^{(1)} d) \quad (5.63)$$

$$Y_{\mathrm{p},n}^{\mathrm{L}} = Y_{11} + Y_{12} = -\mathrm{j}Y_n^{(1)} \left[\frac{\tilde{f}_n(w_1)}{\tilde{f}_0(w_1)}\right]^2 \cot(\beta_n^{(1)} d) + Y_{\mathrm{s},n} \quad (5.64)$$

$$Y_{\mathrm{p},n}^{\mathrm{R}} = Y_{22} + Y_{12} = -\mathrm{j}Y_n^{(1)} \left[\frac{\tilde{f}_n(w_2)}{\tilde{f}_0(w_2)}\right]^2 \cot(\beta_n^{(1)} d) + Y_{\mathrm{s},n} \, . \quad (5.65)$$

This nth-order Π circuit can now substitute the nth-order block previously defined, thus obtaining the equivalent network represented in Fig.5.27(b). Notice that the internal region is then described by an infinite number of Π blocks connected in parallel, where each block represents the contribution of a different harmonic in this region. The parallel admittances of a particular Π-block ($Y_{\mathrm{p},n}^{\mathrm{L}}$ and $Y_{\mathrm{p},n}^{\mathrm{R}}$) account for the near field around the slit regions whereas the series admittance ($Y_{\mathrm{s},n}$) accounts for the coupling field between both slit arrays associated with the nth-order harmonic (which can be of propagative or evanescent). At this point, the same rationale employed in Sec. 5.2.2 to interpret the admittances can be similarly applied. In this sense, Π blocks associated with low-order harmonics keeps the dynamical frequency dependence of the modal admittances. The number of low-order harmonics, N, necessary for the accurate representation of the electrical response is taken according to the criterion in (5.53) (namely, the number of propagative harmonics in the highest-permitivity medium plus the first evanescent one). High order harmonics, on the contrary,

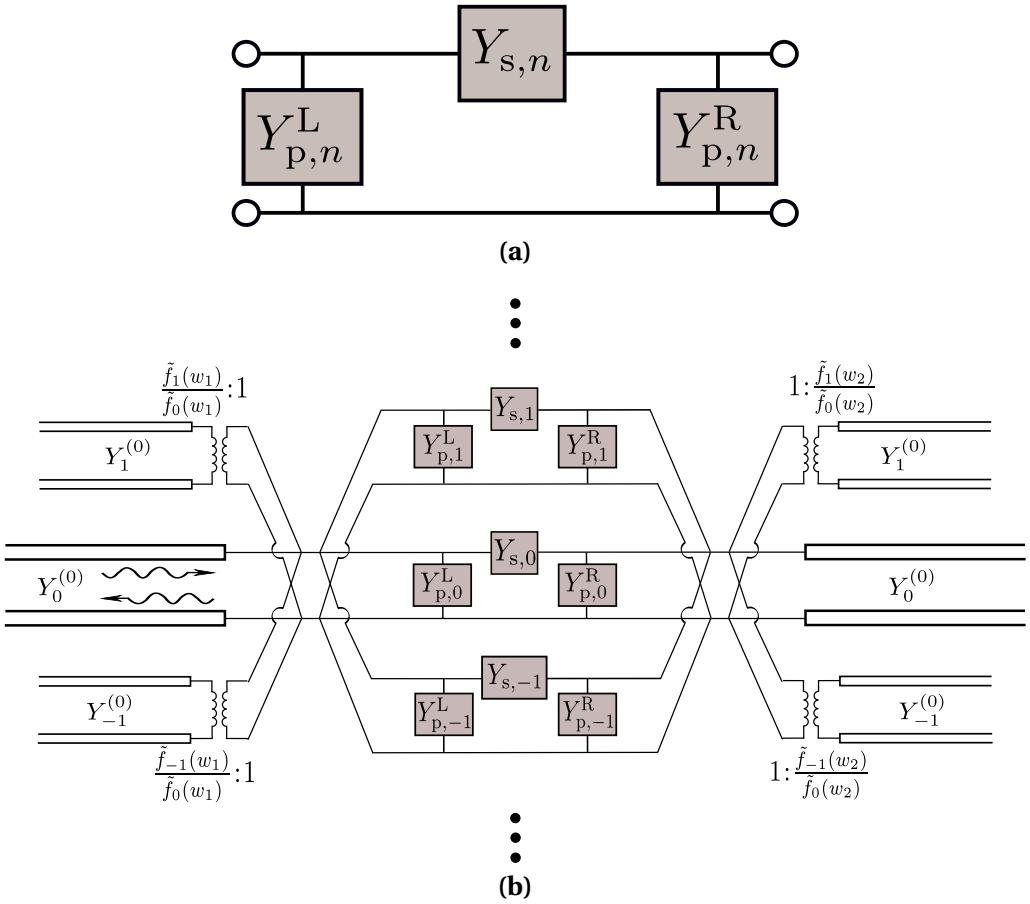

Figure 5.27: (a): nth-order Π block. (b): Equivalent circuit resulting from the subsititution of the Π blocks. In principle, the circuit consists of an infinite number of Π circuits connected in parallel.

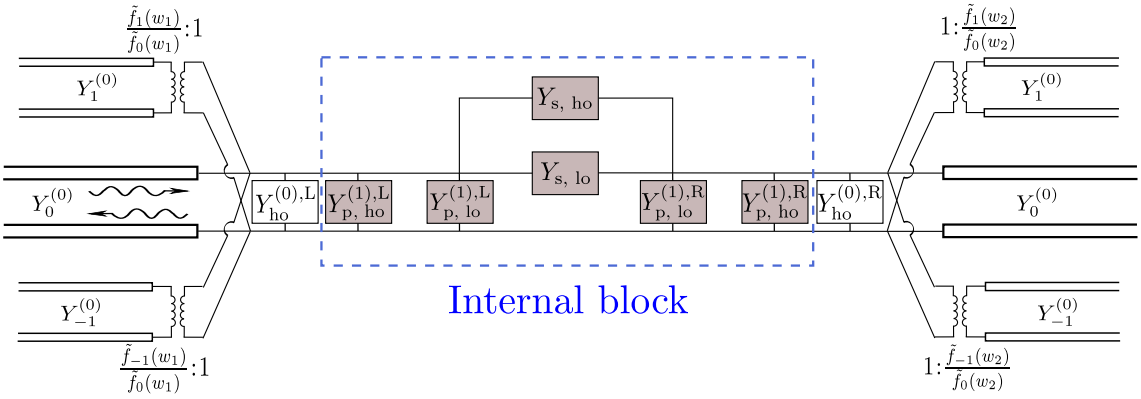

Figure 5.28: Final version of the equivalent circuit.

represent a pure reactive field. The series admittance for high-order elements accounts for a purely reactive coupling field between both screens. For largely spaced gratings the contribution of this series admittance is practically negligible for all these high-order blocks. On the contrary, for closely spaced arrays, the contribution of the series admittance associated with the lowest-order harmonics of high-order nature can be significant, and their contribution has to be explicitly taken into account. The number of high-order harmonics with significant value of $Y_{\text{s},n}$ is well established by the parameter M previously defined in (5.28).

In summary, low-order Π blocks keep the dynamical frequency dependence of the modal admittances. They all form a global Π-block whose admittances are given by

$$Y_{\text{p,lo}}^{(1),\text{L}} = \sum_{n=-N}^{n=N} Y_{\text{p},n}^{\text{L}} \tag{5.66}$$

$$Y_{\text{p,lo}}^{(1),\text{R}} = \sum_{n=-N}^{n=N} Y_{\text{p},n}^{\text{R}} \tag{5.67}$$

$$Y_{\text{s,lo}} = \sum_{n=-N}^{n=N} Y_{\text{s},n}\,. \tag{5.68}$$

High-order harmonics also form a global Π-block. The parallel admittances of

this global Π block include the contribution of the parallel admittances associated with *all* the individual nth-order Π blocks. On the contrary, the series admittance of this global high-order π-circuit is the result of the contribution of a *few* individual series admittances. It results in the following expressions:

$$Y_{\text{p, ho}}^{(1),\text{L}} = \sum_{\forall|n|\geq N+1}^{\infty} Y_{\text{p},n}^{\text{L}} \tag{5.69}$$

$$Y_{\text{p, ho}}^{(1),\text{R}} = \sum_{\forall|n|\geq N+1}^{\infty} Y_{\text{p},n}^{\text{R}} \tag{5.70}$$

$$Y_{\text{s, ho}} = \sum_{\forall|n|\geq N+1}^{|M|} Y_{\text{s},n}\,. \tag{5.71}$$

Certainly, for TM incidence, the admittances in (5.69), (5.70) and (5.71) become capacitive, and for TE incidence, they become inductive. The final version of the equivalent circuit for both TM and TE incidence is illustrated in Fig.5.28. In this figure we have boxed the block containing all the information about the internal region (internal block). The external region is characterized by the high-order admittance $Y_{\text{ho}}^{(0)}$ which accounts for the reactive field around the external face of the slit gratings, in addition to some transmission lines accounting for the low-order field. Following a similar procedure as in Sec. 5.3, internal blocks can be cascaded to build up an equivalent circuit for dealing with a stack formed by any given number of slit arrays.

5.6.2 Equivalent Π network for two different and non-aligned coupled gratings.

In Sec. 5.6.1 an equivalent circuit has been deduced for a pair of strongly-coupled non-identical but aligned arrays. Non-aligned arrays are also of interest in the literature, as reported in several works [139, 140]. The general methodology above described can still be employed to deal with the non-aligned case although the derivation of a compact Π circuit for the internal region is found to be restricted to the normal incidence case.

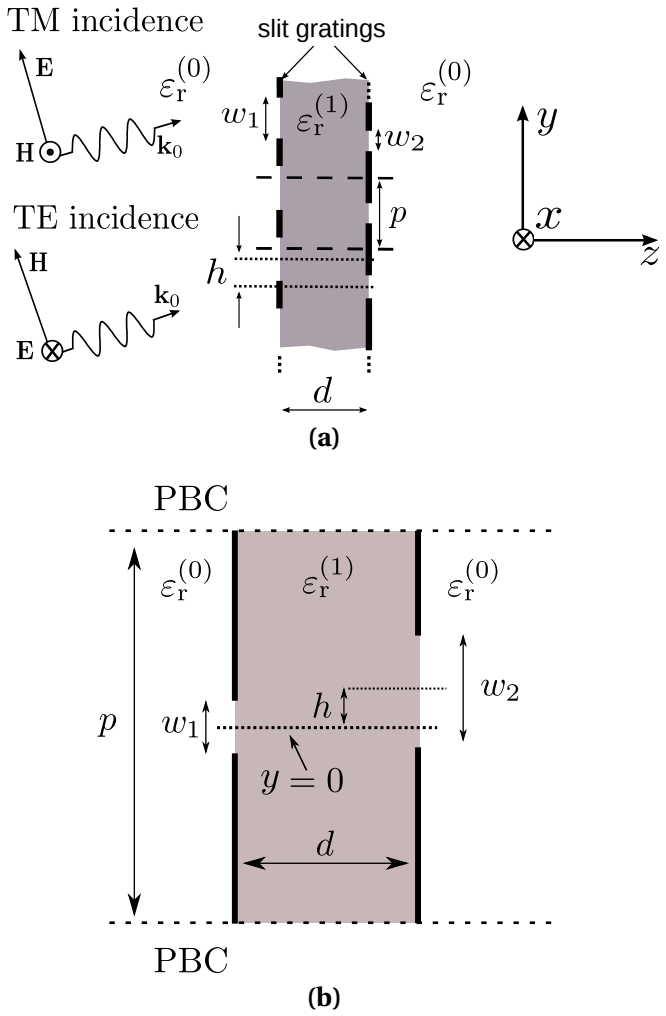

Figure 5.29: (a): Two coupled non-aligned slit gratings. (b): Unit cell of the problem.

A sketch of the system under consideration is depicted in Fig.5.29(a) together with its corresponding unit cell in Fig.5.29(b). Both arrays have the same period. The misaligment between the center of both slit apertures (within the same unit cell) is given by the variable h. The center of the left-side slit has been set to coincide with the y-axis (reference plane at $y = 0$). The corresponding equivalent

admittance of the left-side arrays is the same as in (5.58),

$$Y_{\text{eq}} = \sum_n{}' \left[\frac{\tilde{f}_n(w_1)}{\tilde{f}_0(w_1)}\right]^2 (Y_n^{(0)} + Y_n^{(1)}) \tag{5.72}$$

with $\tilde{f}_n(w_1)$ defined in (5.59). The second slit, shifted upward with respect the left one, also admits a representation by means of an equivalent circuit. As the slit center is placed at $y = h$, its corresponding equivalent admittance is expressed as

$$Y_{\text{eq}} = \sum_n{}' \left|\frac{\tilde{f}_n(w_2)}{\tilde{f}_0(w_2)}\right|^2 (Y_n^{(0)} + Y_n^{(1)}) \tag{5.73}$$

where $\dfrac{\tilde{f}_n(w_2)}{\tilde{f}_0(w_2)}$ is actually a complex number given by

$$\frac{\tilde{f}_n(w_2)}{\tilde{f}_0(w_2)} = \begin{cases} \dfrac{J_0([k_n + k_{\text{t}}]w_2/2)}{J_0(k_{\text{t}}w_2/2)} \mathrm{e}^{\mathrm{j}k_n h} & \text{TM incidence} \\ \dfrac{J_1([k_n + k_{\text{t}}]w_2/2)}{J_1(k_{\text{t}}w_2/2)} \dfrac{k_{\text{t}}}{k_n + k_{\text{t}}} \mathrm{e}^{\mathrm{j}k_n h} & \text{TE incidence}\,. \end{cases} \tag{5.74}$$

The additional term $\mathrm{e}^{\mathrm{j}k_n h}$ in (5.74) comes from the evaluation of the Fourier integral of the field in the second slit in a non-symmetric interval with respect to $y = 0$. It is worth noting that the expressions in (5.74) are related to a transformer of *complex* turn ratio. This can be interpreted as an ideal transformer which, in addition, also introduces a phase shift in the output voltage and current with respect the input magnitudes.

Once both equivalent circuits have been defined individually, the entire equivalent circuit is readily achieved by connecting their corresponding nth-order lines as showm in Fig. 5.30. In order to find an equivalent Π-topology for the whole internal region, it is first considered the admittance-matrix formalism $[Y]_n$, applied to each single nth-order block system, formed by the nth-order left tranformer, the nth-order line, and the nth-order right transformer:

$$[Y]_n = \begin{pmatrix} -\mathrm{j}Y_n^{(1)} \left|\dfrac{\tilde{f}_n(w_1)}{\tilde{f}_0(w_1)}\right|^2 \cot(\beta_n^{(1)} d) & \mathrm{j}Y_n^{(1)} \left[\dfrac{\tilde{f}_n(w_2)}{\tilde{f}_0(w_2)}\right]^* \dfrac{\tilde{f}_n(w_1)}{\tilde{f}_0(w_1)} \csc(\beta_n^{(1)} d) \\ \mathrm{j}Y_n^{(1)} \dfrac{\tilde{f}_n(w_2)}{\tilde{f}_0(w_2)} \dfrac{\tilde{f}_n(w_1)}{\tilde{f}_0(w_1)} \csc(\beta_n^{(1)} d) & -\mathrm{j}Y_n^{(1)} \left|\dfrac{\tilde{f}_n(w_2)}{\tilde{f}_0(w_2)}\right|^2 \cot(\beta_n^{(1)} d) \end{pmatrix}. \tag{5.75}$$

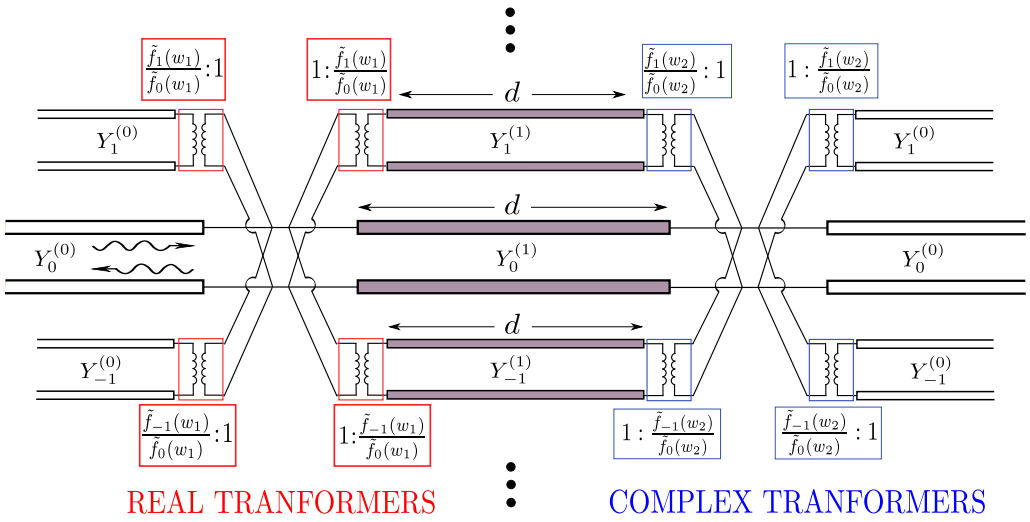

Figure 5.30: Equivalent circuit corresponding to a pair of coupled and non-aligned slits arrays. The complex transformers turn rations are given in (5.59).

Again, the matrix in (5.75) represents a two-port network. However, no equivalent Π circuit composed of regular admittances can be inferred from it since the reciprocity condition is not satisfied $Y_{12} \neq Y_{21}$ [34]. The responsible of such a "non-reciprocity" is the complex tranformer associated to right-slit discontinuity, $\dfrac{\tilde{f}_n(w_2)}{\tilde{f}_0(w_2)}$, which forces instead

$$Y_{12} \;=\; -\;\left[Y_{21}\right]^{*}. \tag{5.76}$$

It is worth mentioning that (5.76) still guarantees the lossless condition of the structure. In fact, as reported in [6, 156], a non-reciprocal lossless two-port network necessarily forces the condition in (5.76) for its corresponding admittance matrix. Furthermore this implies a further result, which ensures that the scattering parameters S_{12} and S_{21} satisfy

$$|S_{12}| = |S_{21}| \tag{5.77}$$

although the phase associated each scattering parameter does not generally coincide. A possible interpretation about the the non-recripocity associated with the circuit is outlined in Appendix A by applying the reciprocity theorem [34].

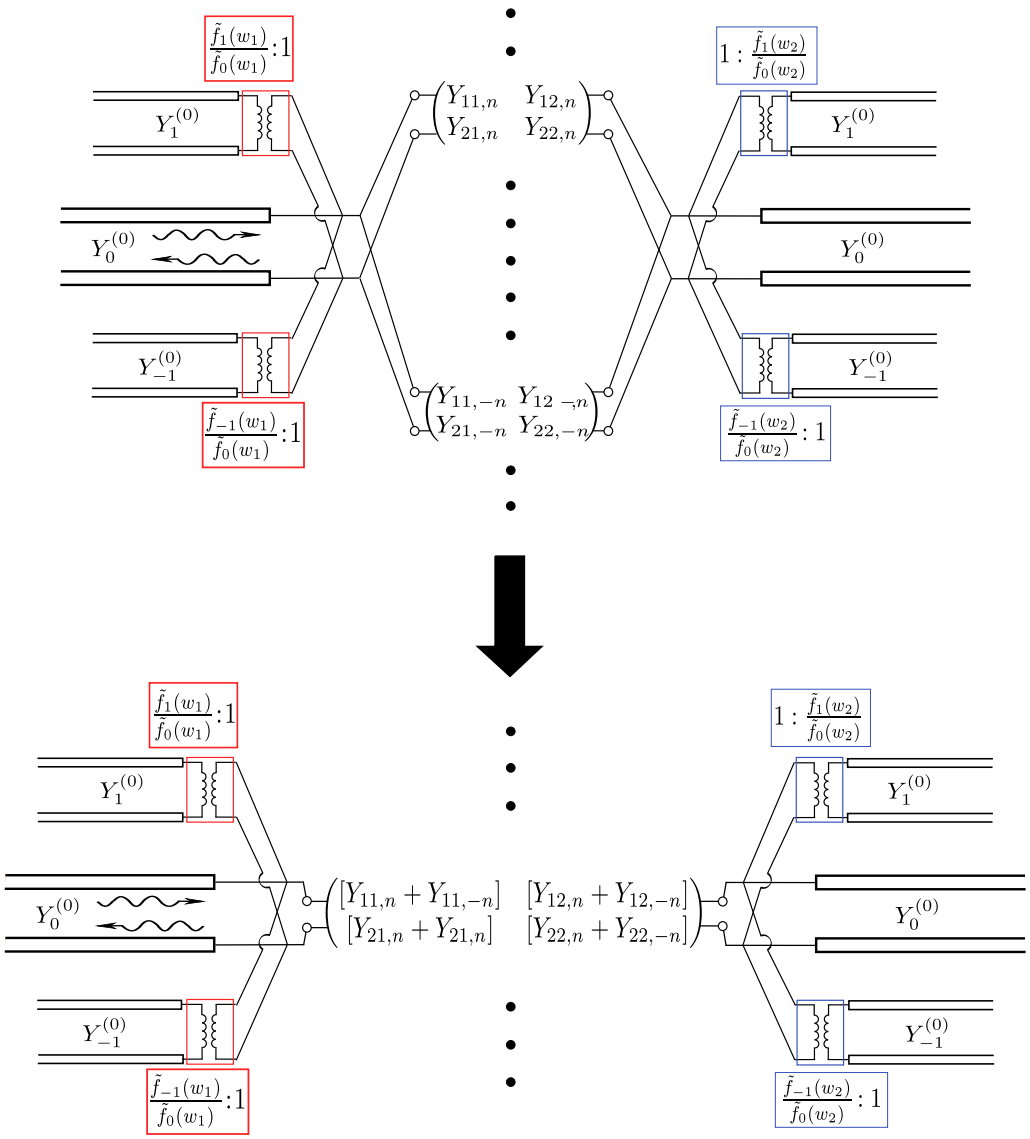

Figure 5.31: Two admittance matrices defined for two networks connected in parallel can be added to give rise to a new single matrix representing the whole system. This result is useful to find a Π topology for non-aligned arrays under normal incidence.

The non-reciprocity of the admittance matrix is not present for the case of normal incidence. In this case, harmonics of opposite orders have the following properties:

$$\beta_n^{(1)} = \beta_{-n}^{(1)} \tag{5.78}$$

$$Y_n^{(1)} = Y_{-n}^{(1)} \tag{5.79}$$

$$\frac{\tilde{f}_n(w_2)}{\tilde{f}_0(w_2)} = \left|\frac{\tilde{f}_{-n}(w_2)}{\tilde{f}_0(w_2)}\right|^* . \tag{5.80}$$

These properties can be used to construct an overall nth-order *modal* admittance matrix as a combination of two matrices associated with harmonics of opposite order. Basic circuit analysis shows that two admittance matrices representing two different networks connected in parallel can be added resulting in a single and global admittance matrix which would represent such a paralell connection. An schematic drawing is illustrated in Fig.5.31. If we construct the resulting matrix by the admittance matrices of two harmonics of opposite order, we can apply the properties in (5.78), (5.79) and (5.80). After applying these properties, the entries of the resulting admittance matrix are

$$\hat{Y}_{11,n} = Y_{11,n} + Y_{11,-n} = -2\mathrm{j}Y_n^{(1)}\left|\frac{\tilde{f}_n(w_1)}{\tilde{f}_0(w_1)}\right|^2 \cot(\beta_n^{(1)}d) \tag{5.81}$$

$$\hat{Y}_{22,n} = Y_{22,n} + Y_{22,-n} = -2\mathrm{j}Y_n^{(1)}\left|\frac{\tilde{f}_n(w_2)}{\tilde{f}_0(w_2)}\right|^2 \cot(\beta_n^{(1)}d) \tag{5.82}$$

$$\hat{Y}_{12,n} = Y_{12,n} + Y_{12,-n} = 2\mathrm{j}Y_n^{(1)}\frac{\tilde{f}_n(w_1)}{\tilde{f}_0(w_1)}\mathrm{Re}\left[\frac{\tilde{f}_n(w_2)}{\tilde{f}_0(w_2)}\right] \csc(\beta_n^{(1)}d) \tag{5.83}$$

$$\hat{Y}_{21,n}^{\mathrm{ov}} = Y_{21,n} + Y_{21,-n} = 2\mathrm{j}Y_n^{(1)}\frac{\tilde{f}_n(w_1)}{\tilde{f}_0(w_1)}\mathrm{Re}\left[\frac{\tilde{f}_n(w_2)}{\tilde{f}_0(w_2)}\right] \csc(\beta_n^{(1)}d) \tag{5.84}$$

Since this resulting matrix represents the field of two harmonics of opposite order, it can be called as *modal* matrix. Since this modal matrix is symmetric, it represents a reciprocal network for which a Π topology can be straighforwardly

derived [6, 34] as follows:

$$Y_{\mathrm{s},n} = -Y_{12,n}^{\mathrm{ov}} = -2\mathrm{j}Y_n^{(1)} \frac{\tilde{f}_n(w_1)}{\tilde{f}_0(w_1)} \mathrm{Re}\left[\frac{\tilde{f}_n(w_2)}{\tilde{f}_0(w_2)}\right] \csc(\beta_n^{(1)} d) \tag{5.85}$$

$$Y_{\mathrm{p},n}^{\mathrm{L}} = Y_{11,n}^{\mathrm{ov}} + Y_{12,n}^{\mathrm{ov}} = -2\mathrm{j}Y_n^{(1)} \cot(\beta_n^{(1)} d) \left|\frac{\tilde{f}_n(w_1)}{\tilde{f}_0(w_1)}\right|^2 + Y_{\mathrm{s},n} \tag{5.86}$$

$$Y_{\mathrm{p},n}^{\mathrm{R}} = Y_{22,n}^{\mathrm{ov}} + Y_{12,n}^{\mathrm{ov}} = -2\mathrm{j}Y_n^{(1)} \cot(\beta_n^{(1)} d) \left|\frac{\tilde{f}_n(w_2)}{\tilde{f}_0(w_2)}\right|^2 + Y_{\mathrm{s},n}\,. \tag{5.87}$$

From this point, the same procedure as in the previous sections can be applied. The infinite number of Π blocks admits a decomposition into low-order blocks and high-order blocks. Low order blocks keep the Π-topology and the admittances composing the network elements retain their dynamical frequency dependence. The parallel connection of the low-order Π-blocks gives rise to a global Π-block whose elements are defined as

$$Y_{\mathrm{p,\,lo}}^{(1),\mathrm{L}} = \sum_{n=0}^{N} Y_{\mathrm{p},n}^{\mathrm{L}} \tag{5.88}$$

$$Y_{\mathrm{p,\,lo}}^{(1),\mathrm{R}} = \sum_{n=0}^{N} Y_{\mathrm{p},n}^{\mathrm{R}} \tag{5.89}$$

$$Y_{\mathrm{s,\,lo}} = \sum_{n=0}^{N} Y_{\mathrm{s},n}\,. \tag{5.90}$$

The Π-blocks associated with high order harmonics also give rise to a global Π circuit whose parallel admittances are the result of the contribution of all the individual parallel admittances of the high-order Π blocks. The series admittance of the global high-order Π-circuit is the result of the contribution of a few series admittances.

$$Y_{\mathrm{p,\,ho}}^{(1),\mathrm{L}} = \sum_{n=N+1}^{\infty} Y_{\mathrm{p},n}^{\mathrm{L}} \tag{5.91}$$

$$Y_{\mathrm{p,\,ho}}^{(1),\mathrm{R}} = \sum_{n=N+1}^{\infty} Y_{\mathrm{p},n}^{\mathrm{R}} \tag{5.92}$$

$$Y_{\mathrm{s,\,ho}} = \sum_{n=N+1}^{M} Y_{\mathrm{s},n}\,. \tag{5.93}$$

The admittances in (5.91), (5.92) and (5.93) are purely capacitive for TM incidence and purely inductive for TE incidence (in absence of dielectric losses). The resulting equivalent circuit has the same topology as the one depicted in Fig.5.28.

For oblique incidence, no Π-topology can be derived from the matrix formalism. However according to Fig.5.31, it is still feasible to build a global admittance matrix resulting from the summation of all the individual nth-admittance matrices (both high- and low-order),

$$[Y]_{\text{global}} = \begin{pmatrix} -\mathrm{j}\sum_{n=-\infty}^{\infty} Y_n^{(1)} \left|\frac{\tilde{f}_n(w_1)}{\tilde{f}_0(w_1)}\right|^2 \cot(\beta_n^{(1)} d) & \mathrm{j}\sum_{n=-\infty}^{\infty} Y_n^{(1)} \left[\frac{\tilde{f}_n(w_2)}{\tilde{f}_0(w_2)}\right]^* \frac{\tilde{f}_n(w_1)}{\tilde{f}_0(w_1)} \csc(\beta_n^{(1)} d) \\ \mathrm{j}\sum_{n=-\infty}^{\infty} Y_n^{(1)} \frac{\tilde{f}_n(w_2)}{\tilde{f}_0(w_2)} \frac{\tilde{f}_n(w_1)}{\tilde{f}_0(w_1)} \csc(\beta_n^{(1)} d) & -\mathrm{j}\sum_{n=-\infty}^{\infty} Y_n^{(1)} \left|\frac{\tilde{f}_n(w_2)}{\tilde{f}_0(w_2)}\right|^2 \cot(\beta_n^{(1)} d) \end{pmatrix}. \tag{5.94}$$

The global matrix in (5.94) keeps on being non-reciprocal, $Y_{12} = -[Y_{21}]^*$. If we convert the matrix $[Y_{\text{global}}]$ into its associated scattering matrix [34], its corresponding cross terms S_{12} and S_{21} can be written as

$$S_{12} = \frac{-2Y_{12}Y_0^{(0)}}{\Delta[Y]_{\text{global}}} \tag{5.95}$$

$$S_{21} = \frac{-2Y_{21}Y_0^{(0)}}{\Delta[Y]_{\text{global}}} \tag{5.96}$$

with

$$\Delta[Y]_{\text{global}} = (Y_{11} + Y_0^{(0)})(Y_{22} + Y_0^{(0)}) - Y_{12}Y_{21}\,. \tag{5.97}$$

Note that according to (5.95) and (5.96), $S_{12} = [S_{21}]^*$, which indicates that the magnitude of the transmission coefficient is "reciprocal" whereas the phase of the scattering parameters is "non-reciprocal", as was expected according to the results reported in [156].

5.6.3 Numerical results.

In order to check the performance of the model, some results are shown next. A first example is shown in Fig. 5.32 where three plots represent the reflection

coefficient obtained for three different structures under normal TM incidence. Fig. 5.32(a) corresponds to a pair of two aligned and identical coupled arrays sandwiching a lossy FR4-dielectric layer of thickness $d = 2$ mm (remember that dielectric losses are readily taken into account by introducing the complex-valued permittivity associated with the dielectric under consideration into the corresponding admittance expressions). Assuming this same structure, but modifying the slit width of the right array, w_2, its reflection coefficient is plotted in Fig. 5.32(b). The third structure analyzed in Fig. 5.32(c) is the same as the one in Fig. 5.32(b), but shifting the right array 1 mm upward. It can be observed the influence of the geometrical modifications in the reflection spectra, especially at higher frequencies. There is a reflection minimum close to 10 GHz appearing for all these structures. At higher frequencies the differences are more noticeable, specially in the non-aligned case. The aligned cases in Fig. 5.32(a) and Fig. 5.32(b) show four reflections dips above 30 GHz located, approximately, at the same frequencies. On the contrary, the non-aligned case provides an additional reflection minimum. The agreement with HFSS results is quite good in all cases.

A second example is shown in Fig. 5.33 and consists of a stack of three different and non-aligned slit arrays (Fig. 5.33(a)) excited by a normally-incident TM plane wave. This configuration provides a complex transmission spectrum, as shown in Fig. 5.33(b). It is remarkable that the analytical equivalent circuit matches the numerical results provided by HFSS. It is worth mentioning that, for frequencies above 30 GHz, there are two propagative modes within the denser dielectric slab($\varepsilon_{\mathrm{r}}^{(2)} = 4$).

Fig.5.35 shows a comparison between the results provided by our model and experimental data reported in [155]. The plotted transmissivity coefficient corresponds to a pair of identical non-aligned slit arrays under TM normal incidence (the gratings are printed on both faces of a lossy FR4-dielectric slab). Even though two transmission maxima appear around 13 and 26 GHz, no full transmission is achieved due to the losses associated with the dielectric layer. The agreement shown between both curves is excellent.

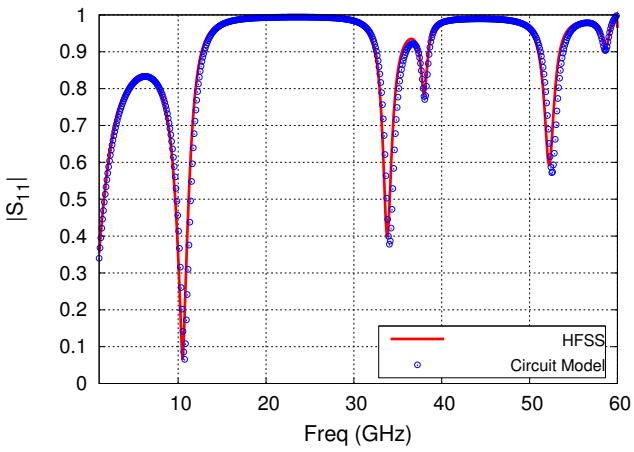

(a)

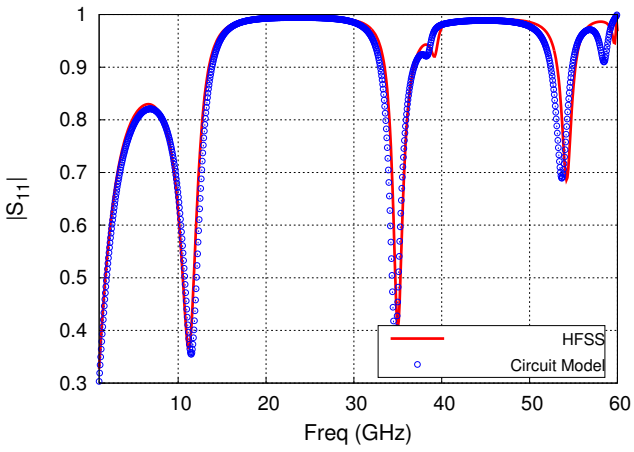

(b)

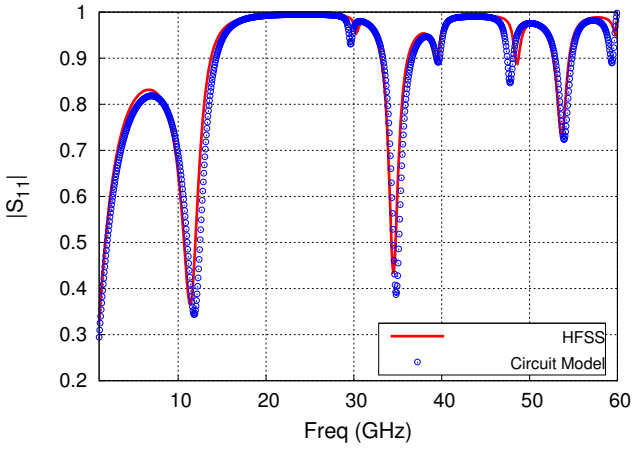

(c)

Figure 5.32: Reflection coefficient magnitude versus frequency under TM normal incidence. (a): coupled and aligned pair of identical slit arrays. Structure parameters: $p = 5\,\text{mm}$, $w_1 = w_2 = 0.5\,\text{mm}$, $\varepsilon_\text{r}^{(0)} = 1$, $\varepsilon_\text{r}^{(1)} = 4.4 - \text{j}0.088$, $d = 2\,\text{mm}$, $h = 0\,\text{mm}$. (b): coupled and aligned pair of different slit arrays. Structure parameters: same as (a) excepting $w_2 = 1\,\text{mm}$. (c): coupled and non-aligned pair of different slit arrays. Structure parameters: same as (b) excepting $h = 1\,\text{mm}$.

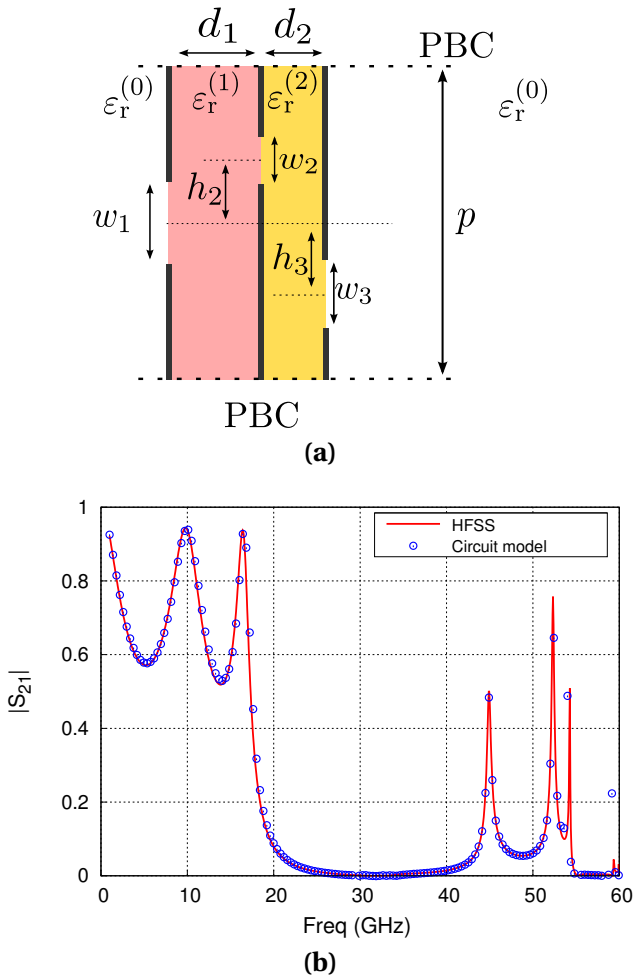

Figure 5.33: (a): Unit cell of the structure under analysis. (b): Transmission coefficient versus frequency for the structure in (a) for TM normal incidence. Structure parameters: $p = 5\,\text{mm}$, $w_1 = 0.5\,\text{mm}$, $w_2 = 1\,\text{mm}$, $w_3 = 0.8\,\text{mm}$, $d_1 = 2\,\text{mm}$, $d_2 = 1.5\,\text{mm}$, $h_2 = 0\,\text{mm}$, $h_3 = 1.5\,\text{mm}$, $\varepsilon_r^{(0)} = 1$, $\varepsilon_r^{(1)} = 2.2$, $\varepsilon_r^{(2)} = 4$.

Finally, a last example is given in Fig. 5.35 for a pair of non-identical and non-aligned coupled gratings illuminated by TM/TE oblique impinging waves (structure in Fig.5.29(b)). In this situation, as explained previously, there is not an equivalent Π circuit for the structure. Thus the scattering parameters of the structure are obtained after calculating the matrix in (5.94). In the figure it is plotted the magnitude of the transmission coefficient. The results from HFSS

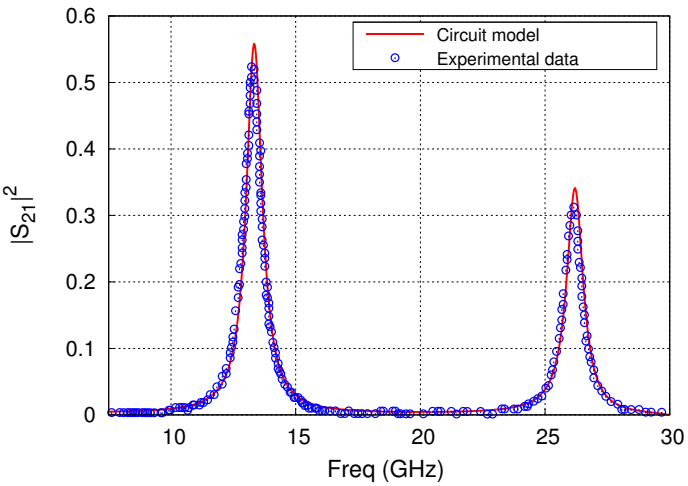

Figure 5.34: Transmissivity versus frequency. Comparison of the results from the model with experimental data extracted from [155]. Results obtained for a pair of two coupled and non-aligned slit arrays under TM normal incidence. Structure parameters: $p = 10.01\,\text{mm}$,$w_1 = w_2 = 0.33\,\text{mm}$, $h = p/2$, $d = 0.356\,\text{mm}$, $\varepsilon_\text{r}^{(0)} = 1$, $\varepsilon_\text{r}^{(1)} = 4.17 - \text{j}0.07$.

and the circuit model shown in Fig.5.35(a) fit quite well for the frequency range under consideration. This particular plot deals with TE incidence, where the structure is practically opaque except for some narrow frequency intervals, associated with the excitation of higher-order modes and Fabry-Pérot resonances in the dielectric medium, with $\varepsilon_\text{r}^{(1)}$. The case of TM incidence plotted in Fig.5.35(b) also shows a good agreement with results from HFSS although some differences appear in the frequency interval between 48 and 53 GHz approximately.

5.7 Conclusions

A wideband equivalent Π-circuit has been derived for a pair of coupled, different and not aligned slit arrays illuminated by TM or TE normally incident plane waves. Fully analytical expressions are derived for the Π-circuit elements, which are valid both for slightly and tightly coupled gratings. The numerical series defining the circuit components are physically interpreted in terms of distributed (low-order-mode) and lumped (high-order-mode) contributions, in

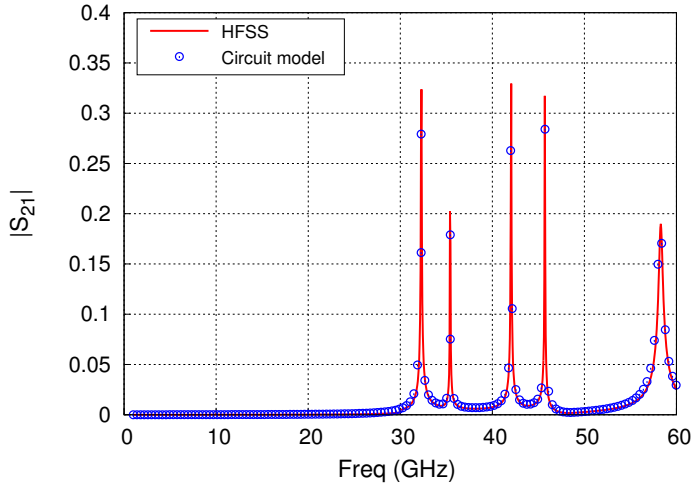

(a)

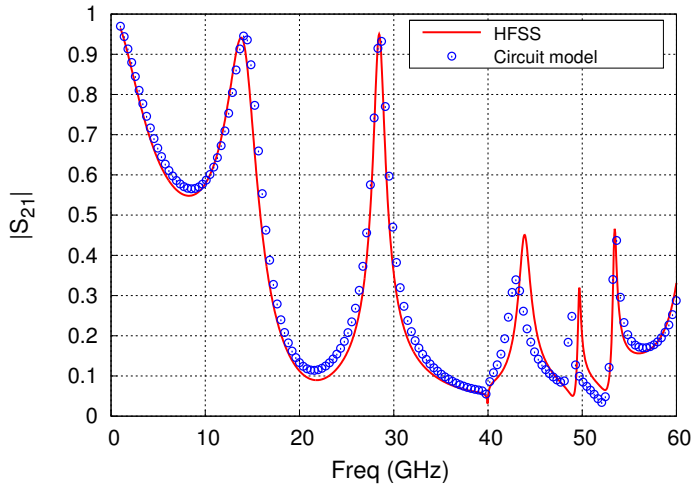

(b)

Figure 5.35: Transmission coefficient versus frequency for an obliquely-incident wave. (a): TE incidence. Structure parameters: $p = 5\,\text{mm}$, $w_1 = 1\,\text{mm}$, $w_2 = 0.5\,\text{mm}$, $d = 1.5\,\text{mm}$, $h = 1\,\text{mm}$, $\varepsilon_{\text{r}}^{(0)} = 1$, $\varepsilon_{\text{r}}^{(1)} = 4$, $\theta = 30^o$. (b): TM incidence. Structure parameters: Same as (a) excepting $\varepsilon_{\text{r}}^{(1)} = 9$.

such a way that explicit networks can be obtained for each specific configuration and a wide frequency band. The deduced Π-circuit model shows separate contributions of the internal and external fields to the parallel elements, which allows for a straightforward extension of the circuit model to the case of stacked structures with an arbitrary number of slit gratings separated by dielectric slabs. Specifically, the equivalent circuit is obtained just by cascading the elementary internal Π-building blocks. The model can also be used for the dispersion analysis of the Bloch modes of infinitely long periodic stacks. The validity of the derived circuit models has been systematically checked by comparison with numerical data generated by the MoM code, the commercial simulator HFSS, and also some available experimental results. Specifically, for the case of non-aligned slit arrays, the obtaining of the equivalent circuit is not possible for oblique incidence, due to the complex tranformers which naturally appear in the derivation of the model. The non-aligned structure is actually reciprocal, and can be demostrated by using the reciprocity theorem.

Appendix A

About the non-reciprocity of the circuit model

The reciprocity theorem for the electromagnetic field in a source-free region states that

$$\oint_S (\mathbf{E}^{(a)} \times \mathbf{H}^{(b)} - \mathbf{E}^{(b)} \times \mathbf{H}^{(a)}) \cdot \mathrm{d}\mathbf{S} = 0 \tag{A.1}$$

where S is the surface enclosing the considered region and the superscripts refer to two independent excitations "a" and "b". If the considered region is a given waveguide section, then we can split the integration surface into the input and output ports (P) and the lateral walls of the waveguide (L):

$$\int_P (\mathbf{E}^{(a)} \times \mathbf{H}^{(b)} - \mathbf{E}^{(b)} \times \mathbf{H}^{(a)}) \cdot \mathrm{d}\mathbf{S} + \int_L (\mathbf{E}^{(a)} \times \mathbf{H}^{(b)} - \mathbf{E}^{(b)} \times \mathbf{H}^{(a)}) \cdot \mathrm{d}\mathbf{S} = 0\,. \tag{A.2}$$

For an actual metallic waveguide or a virtual waveguide bounded by perfect electric or magnetic walls (discontinuities may exist within the considered waveguide section), the lateral integrals vanish because the tangential electric field, or magnetic field in the case of a virtual magnetic wall, is zero. In this case, reciprocity guarantees that the integrals of the "a" and "b" fields at the two ports P_1

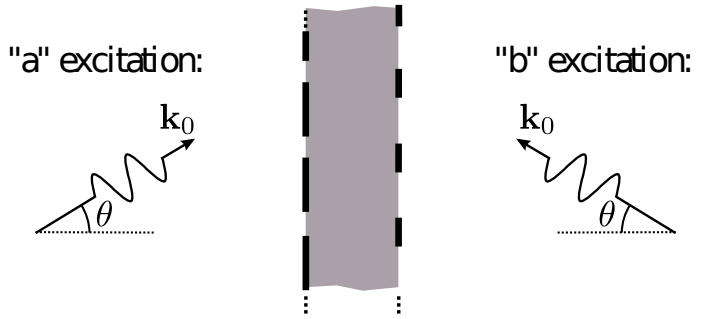

Figure A.36: Two plane-wave excitations of the coupled gratings, impinging from different sides but with the same incidence angle θ. For $\theta \neq 0$, the transmission coefficients for the "a" and "b" excitations have the same magnitude but different phase.

and P_2 satisfy

$$\int_{P_1} (\mathbf{E}^{(\mathrm{a})} \times \mathbf{H}^{(\mathrm{b})} - \mathbf{E}^{(\mathrm{b})} \times \mathbf{H}^{(\mathrm{a})}) \cdot \mathrm{d}\mathbf{S} + \int_{P_2} (\mathbf{E}^{(\mathrm{a})} \times \mathbf{H}^{(\mathrm{b})} - \mathbf{E}^{(\mathrm{b})} \times \mathbf{H}^{(\mathrm{a})}) \cdot \mathrm{d}\mathbf{S} = 0 \,. \quad \text{(A.3)}$$

It is easy to show (see, for instance, [34]) that (A.3) directly implies that the transmission coefficients between the two ports are the same in either direction ($S_{12} = S_{21}$) and thus the considered waveguide problem can be modeled, in principle, using a reciprocal equivalent circuit.

In the case under study in this work, the virtual waveguide is not bounded by perfect electric or magnetic walls but by periodic boundary conditions that, for a given incidence angle, impose a fixed phase shift between the fields at the boundaries of the unit cell waveguide. Thus, let us consider excitations "a" and "b" as plane waves impinging with an incidence angle θ from either side of the structure, as shown in Fig.A.36. For both excitations, the fields at the lower (say $y = 0$) and upper ($y = p$) unit cell boundaries are related in the following way:

$$\mathbf{A}^{(\mathrm{a/b})}|_{y=p} = \mathrm{e}^{-\mathrm{j}k_{\mathrm{t}}p} \mathbf{A}^{(\mathrm{a/b})}|_{y=0} \,, \quad \text{(A.4)}$$

where $\mathbf{A}$ stands for either $\mathbf{E}$ or $\mathbf{H}$. Each term in the lateral integrals (per unit

length in the x direction) can then be written as

$$\int_{y=0} (\mathbf{E}^{(\mathrm{a/b})} \times \mathbf{H}^{(\mathrm{b/a})}) \cdot (-\hat{\mathbf{y}})\, \mathrm{d}z + \int_{y=p} (\mathbf{E}^{(\mathrm{a/b})} \times \mathbf{H}^{(\mathrm{b/a})}) \cdot \hat{\mathbf{y}}\, \mathrm{d}z = (\mathrm{e}^{-2\mathrm{j}k_{\mathrm{t}}p} - 1) \int_{y=0} (\mathbf{E}^{(\mathrm{a/b})} \times \mathbf{H}^{(\mathrm{b/a})}) \cdot \hat{\mathbf{y}}\, \mathrm{d}z \quad \text{(A.5)}$$

In general, the contribution of the lateral integrals is not zero, which implies that (A.3) is not satisfied and, consequently, $S_{21} \neq S_{12}$. Nevertheless, it is not possible that the transmission coefficients of a lossless structure have different *magnitude*. Necessarily, $|S_{21}| = |S_{12}|$ and only *phase* nonreciprocity is allowed [156]. This fact causes the appearance of the phase-shifting (complex) transformers in our circuit model. For normal incidence, however, $k_{\mathrm{t}} = 0$ and therefore (A.5) is identically zero. In this case equation (A.3) does hold and it is indeed possible to derive a reciprocal circuit model.

Finally, it is interesting to consider the case in which the structure is excited by plane waves that impinge with *opposite* angles, as shown in Fig. A.37. This might seem a more natural scenario when considering reciprocity in the complete electromagnetic problem. In this situation we have

$$\mathbf{A}^{(\mathrm{a})}|_{y=p} = \mathrm{e}^{-\mathrm{j}k_{\mathrm{t}}p} \mathbf{A}^{(\mathrm{a})}|_{y=0} \quad \text{(A.6)}$$

$$\mathbf{A}^{(\mathrm{b})}|_{y=p} = \mathrm{e}^{+\mathrm{j}k_{\mathrm{t}}p} \mathbf{A}^{(\mathrm{b})}|_{y=0} \quad \text{(A.7)}$$

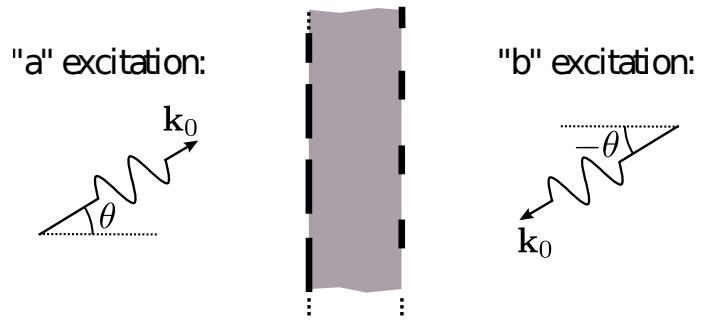

Figure A.37: Two plane-wave excitations impinging from different sides and with opposite incidence angle. The transmission coefficients for the “a” and “b” excitations have the same complex value (magnitude and phase).

which, because of the different signs in the phase shifts, clearly implies that

$$[\mathbf{E}^{(\mathrm{a/b})} \times \mathbf{H}^{(\mathrm{b/a})}]_{y=p} = [\mathbf{E}^{(\mathrm{a/b})} \times \mathbf{H}^{(\mathrm{b/a})}]_{y=0} \tag{A.8}$$

and hence the lateral integrals in the upper and lower unit cell boundaries cancel out and (A.3) is satisfied once again. In consequence, the transmission coefficients for the "a" and "b" excitations in Fig.A.37 have the same complex value (magnitude and phase). The reader can verify that our model is consistent with this observation since it implies $S_{21}(\theta) = S_{12}(-\theta)$. A relevant consequence of this fact is that, for the aligned coupled gratings, the transmission coefficients for the "a" and "b" excitations in Fig. A.36 also have the same complex value. Indeed, for vertically aligned gratings, the symmetry of the structure with respect to the slits' middle plane (see Fig.5.1 and Fig.5.24) clearly implies that the problem is invariant with respect to a change of sign in the incidence angle, and therefore $S_{21}(\theta) = S_{12}(-\theta) = S_{12}(\theta)$. This is consistent with the reciprocal nature of their corresponding circuit models for oblique incidence.

Bibliography

[1] David and Julia Bart , "Sir William Thompson, on the 150th anniversary of the atlantic cable," *Antique Wireless Association Review*, vol. 21, 2008. Cited in page 1.

[2] O. Heaviside, *Electrical papers*, New York and London: Macmillan and co., 1984. Cited in page 2.

[3] J. C. Maxwell, *A treatise on electricity and magnetism*, Oxford: Clarendon Press, 1873. Cited in page 2.

[4] A. A. Oliner, "Historical perspectives on microwave field theory," *IEEE Trans. Microw. Theory Techn.*, vol. 32, no. 9, pp. 1022-1045, Sept. 1984. Cited in page 2.

[5] S. A. Schelkunoff, "The impedance concept and its application to problems of reflection, refraction, shielding and power absorption," *Bell System Technical Journal*, vol. 17, pp. 17-48, Jan. 1938. Cited in page 2.

[6] C. G. Montgomery, R. H. Dicke, and E. M. Purcell, *Principles of Microwave Circuits*, McGraw-Hill Book Company, New York, 1948. Cited in pages 3, 19, 205, 211, and 214.

[7] N. Marcuvitz, *Waveguide handbook*, McGraw-Hill Book Company, 1951. Cited in pages 3 and 10.

[8] J. R. Whinnery and H. W. Jamieson, "Equivalent circuits for discontinuities

in transmission lines," *Proceedings of the Institute of Radio Engineers*, 1944. Cited in pages 3 and 10.

[9] G. G. Macfarlane, "Quasi-stationary field theory and its application to diaphrams and juctions in transmission lines and wave guides," *Proceedings of the Institute of Radio Engineers*, 1946. Cited in pages 3 and 10.

[10] L. Brilloin, *Wave propagation in periodic structures*, McGraw-Hill Book Company, 1946. Cited in page 3.

[11] A. W. Lines, G. R. Nicoll, and A. M. Woodward, "Some properties of waveguides with periodic structures," *Proc. IEE-Part III*, vol. 97, pp. 263-276, July. 1950. Cited in page 3.

[12] A. F. Harvey, "Periodic and guiding structures at microwave frequencies," *IRE Trans. Microw. Theory Techn.*, vol. 8, no 1, pp. 30-61, Jan. 1960. Cited in pages 3 and 79.

[13] C. Palmer, *Diffraction grating handbook*, Newport Corporation, 2005. Cited in page 4.

[14] D. Rittenhouse, "An optical problem proposed by Mr. Hopkitson, and solved by Mr. Rittenhouse," *Trans. Amer. Phil. Soc.*, vol. 2, pp. 201-206, 1786. Cited in page 4.

[15] R. W. Wood, "On a remarkable case of uneven distribution of light in a diffraction grating spectrum," *Proc. Phys. Soc. London*, vol. 18, pp. 269-276, 1902. Cited in pages 4, 11, and 39.

[16] A. K. Rashid, B. Li, and Z. Shen, "An overview of three-dimensional frequency-selective structures," *IEEE Antennas Propag. Magazine*, vol. 56, no. 3, pp. 43-67, June 2014. Cited in page 4.

[17] B. A. Munk, *Frequency Selective Surfaces: Theory and Design*, John Wiley, 2000. Cited in pages 4, 9, 39, and 161.

[18] C. H. Tsao, and R. Mittra, "A spectral-iteration approach for analyzing scattering from frequency selective surfaces," *IEEE Trans. Antennas Propag.*, vol. 30, no. 2, pp. 303-308, March 1982. Cited in page 5.

[19] G. Floquet, "Sur le équations différentielles linéaires à coefficients périodiques ," *Ann. Sci. Ec. Norm. Sup.*, vol. 12, pp. 47-88, 1883. Cited in page 4.

[20] T. W. Ebbesen, H. J. Lezec, H. F. Ghaemi, T. Thio, and P. A. Wolff, "Extraordinary transmission through sub-wavelength hole arrays," *Nature*, vol. 391, pp. 667-669, Feb. 1998. Cited in pages 5 and 41.

[21] H. A. Bethe, "Theory of diffraction by small holes," *Phys. Rev.*, vol. 66, no 7/8, pp. 163-182, Oct. 1944. Cited in pages 5 and 41.

[22] M. Beruete, M. Sorolla, I. Campillo, J. S. Dolado, L. Martín-Moreno, J. Bravo-Abad, and F. J. García-Vidal, "Enhanced millimiter-wave transmission through subwavelength hole arrays," *Opt. Lett.*, vol. 29, no. 21, pp. 2500-2502, Nov. 2004. Cited in pages 5 and 41.

[23] F. Medina, F. Mesa, and R. Marqués, "Extraordinary transmission through arrays of electrically small holes from a circuit theory perspective," *IEEE Trans. Microw. Theory Techn.*, vol. 56, no. 12, pp. 3108-3120, Dec. 2008. Cited in pages 5, 42, and 80.

[24] F. Medina, F. Mesa, and D. C. Skigin, "Extraordinary transmission through arrays of slits: a circuit theory model," *IEEE Trans. Microw. Theory Techn.*, vol. 58, no. 1, pp. 105-115, Jan. 2010. Cited in pages 5, 42, 92, 111, 120, 142, 143, and 148.

[25] ANSYS High Frequency Structure Simulator (HFSS). http://www.ansys.com/Product/Electronics/ANSYS-HFSS. Cited in page 6.

[26] D. Sievenpiper, L. Zhang, R. F. Jiménez-Broas, N. G. Alexópoulos, and

E. Yablonovitch, "High-impedance electromagnetic surfaces with a forbidden frequency band ," *IEEE Trans. Microw. Theory Techn.*, vol. 47, no 11, pp. 2059-2074, Nov. 1999. Cited in pages 7 and 79.

[27] A. N. Fantino, S. I. Grosz, and D. C. Skigin, "Resonant effects in periodic gratings comprising a finite number of grooves in each period," *Phys. Rev. E*, vol. 64, pp. 016605, Jun. 2001. Cited in pages 7, 110, 132, 145, and 146.

[28] R. Mittra, C. H. Chan and T. Cwik , "Techniques for analyzing frequency surfaces - a review," *Proc. IEEE*, vol. 76, no. 12, pp. 1593-1615, Dec. 1998. Cited in page 9.

[29] L. Stark , "Electromagnetic waves in periodic structures," *Technical report No. 208, Research Laboratory of Electronics, M. I. T.*, Dec. 1952. Cited in page 9.

[30] J. C. Slater, "The design of linear accelerators," *Technical report No. 47, Research Laboratory of Electronics, M. I. T*, Sept. 1947. Cited in page 10.

[31] R. E. Collin, *Field theory of guided waves*, Second edition, IEEE Press, 1991. Cited in pages 10 and 44.

[32] J. E. Page de la Vega, *Propagación de ondas guiadas*, Departamento de teoría electromagnética, Universidad Politécnica de Madrid, 1983. Cited in page 10.

[33] S. Edelberg, and A. A. Oliner, "Mutual coupling effects in large antenna arrays, Part I," *IRE Trans. Antennas Propag.*, vol. AP-8, pp. 286-297, May 1960. Cited in page 10.

[34] D. M. Pozar *Microwave engineering*, John Wiley & Sons Inc, 2005. Cited in pages 11, 12, 19, 84, 87, 125, 164, 172, 182, 186, 200, 204, 205, 211, 214, 215, and 224.

[35] R. E. Collin *Foundations for microwave engineering*, McGraw-Hill international edition, 1992. Cited in pages 11 and 79.

[36] I. S. Gradshteyn, and I. M. Ryzhik *Table of integrals, series and products*, Seventh edition, Elsevier, 2007. Not cited.

[37] V. O. Byelobrov, T. L. Zinenko, K. Kobayashi, and I. Nosich "Periodicity matters. Grating or lattice resonances in the scattering by sparse arrays of subwavelength strips and wires," *IEEE Antennas Propag. Magazine*, pp. 34-45, Dec. 2015. Cited in page 39.

[38] B. Gimeno, J. L. Cruz, E. A. Navarro, and V. Such, "A polarizer rotator system for three-dimensional oblique incidence, " *IEEE Trans. Antennas Propag.*, vol. 42, pp. 912-919, 1994. Cited in page 39.

[39] G. F. Brand, "The strip grating as a circular polarizer, " *Am. J. Phys.*, vol. 71, pp. 452-456, 2003. Cited in page 39.

[40] M. A. Hiranandani, A. B. Yakovlev and A. A. Kishk, "Artificial magnetic conductors realised by frequency-selective surfaces on a grounded dielectric slab for antenna applications, " *IEE Proc. Microw. Antennas Propag.*, vol. 153, no. 5, pp. 487-493, Oct. 2006. Cited in page 39.

[41] O. Luukkonen, C. Simovski, G. Granet, G. Goussetis, D. Lioubtchenko, A. V. Raisanen, and S. A. Tretyakov, "Simple and accurate analytical model of planar grids and high-impedance surfaces comprising metal strips or patches," *IEEE Trans. Antennas Propag.*, vol. 56, no. 6, pp. 1624-1632, June 2008. Cited in page 39.

[42] A. Foroozesh, and L. Shafai, "On the characteristics of the highly directive resonant cavity antenna having metal strip grating superstrate, " *IEEE Trans. Antennas Propag.*, vol. 60, pp. 78-91, 2012. Cited in page 39.

[43] R. Ulrich, "Far-infrared properties of metallic mesh and its complementary structure," *Infrared Phys.*, vol. 7, pp. 37-55, 1967. Cited in pages 39 and 57.

[44] R. Ulrich, "Effective low-pass filters for far infrared frequencies," *Infrared Phys.*, vol. 7, pp. 65-74, 1967. Cited in pages 39 and 57.

[45] G. Dolling, M. Wegener, C. M. Soukoulis, and S. Linden, "Negative-index metamaterial at 780 nm wavelength," *Opt. Lett.*, vol. 32, pp. 53-55, 2007. Cited in page 39.

[46] J. Zhang, W. Bai, L. Cai, Y. Xu, G. Song, and Q. Gan, "Observation of ultranarrow band plasmon induced transparency based on large-area hybrid plasmon-waveguide systems," *Appl. Phys. Lett.*, vol. 99, pp. 181120, 2011. Cited in page 39.

[47] P. Patoka, T. Sun, M. Giersig, Z. Ren, and K. Kempa, "Nanoribbon plasmonic gratings and their anomalous interaction with electromagnetic waves," *Adv. Materials*, vol. 24, pp. 3042-3045, 2012. Cited in page 39.

[48] H. Lamb, "On the reflection and transmission of electric waves by a metallic grating," *Proc. London Math Soc.*, vol. 1, no 1, pp. 523-546, 1897. Cited in page 39.

[49] L. Raileigh, "On the dynamical theory of gratings," *Proc. Roy. Soc London*, vol. 79, pp. 399-418, 1907. Cited in page 39.

[50] L. Raileigh, "Note on the remarkable case of diffraction spectra described by Prof. Wood," *Phylos. Mag.*, vol. 14, pp. 60-65, 1907. Cited in pages 39 and 40.

[51] U. Fano, "The theory of anomalous diffraction gratings and of quasi-stationary waves on metallic surfaces," *J. Opt. Soc. Am.*, vol. 31, pp. 213-222, 1941. Cited in page 40.

[52] A. Hessel, and A. A. Oliner, "A new theory of Wood's anomaly on optical gratings," *App. Opt.*, vol. 4, pp. 1275-1297, 1965. Cited in page 40.

[53] S. Enoch, and N. Bonod, *Plasmonics. From basics to advanced topics*, Springer, 2012. Cited in page 40.

[54] J. A. Porto, F. J. Garcá-Vidal, and J. B. Pendry, "Transmission resonances on metallic gratings with very narrow slits," *Phys. Rev. Lett.*, vol. 83, no 14, pp. 2845-2848, Oct. 1999. Cited in page 40.

[55] Y. Takakura, "Optical resonance in a narrow slit in a thick metallic screen," *Phys. Rev. Lett.*, vol. 86, no 24, pp. 5601-5603, Jun. 2001. Cited in page 40.

[56] F. Yang, and J. R. Sambles, "Resonant transmission of microwaves through a narrow metallic slit," *Phys. Rev. Lett.*, vol. 89, no 6, pp. 063901-1 – 063901-4, Aug. 2002. Cited in page 40.

[57] J. R. Sambles, "More than transparent," *Nature*, vol. 391, pp. 641-642, Feb. 1998. Cited in page 41.

[58] H. F. Ghaemi, T. Thio, D. E. Grupp, T. W. Ebbesen, and H. J. Lezec, "Surface plasmons enhance opticl transmission through subwavelength holes," *Phys. Rev. B Condens. Matter*, vol. 58, no. 15, pp. 6779-6782, Sep. 1998. Cited in page 41.

[59] D. E. Grupp, H. J. Lezec, T. W. Ebbesen, K. M. Pellerin, and T. Thio, "Crucial role of metal surfaces in enhanced transmission through subwavelength apertures," *Appl. Phys. Lett.*, vol. 77, pp. 1569-1571, Sep. 2000. Cited in page 41.

[60] L. Martín-Moreno, F. J. García-Vidal, H. J. Lezec, K. M. Pellerin, T. Thio, J. B. Pendry, and T. W. Ebbesen, "Theory of extraordinary optical transmission through subwavelength hole arrays," *Phys. Rev. Lett.*, vol. 86, pp. 1114-1117, Feb. 2001. Cited in page 41.

[61] S. A. Maier, *Plasmonics: fundamentals and applications*, Springer, New York, 2017. Cited in pages 41 and 124.

[62] M. Beruete, M. Sorolla, I. Campillo, J. S. Dolado, L. Martín-Moreno, J. Bravo-Abad, and F. J. García-Vidal, "Enhanced millimiter-wave transmission through quasi-optical subwavelength perforated plates,"

IEEE. Trans. Antennas Propag., vol. 53, no. 6, pp. 1897-1903, Jun. 2005. Cited in page 41.

[63] F. J. G. d. Abajo, and J. J. Sáenz, "Electromagnetic surfaces modes in structured perfect-conductor surfaces," *Phys. Rev. Lett.*, Dec. 2005, Article ID 233901-1. Cited in page 41.

[64] R. Rodríguez-Berral, F. Medina, and F. Mesa, "Circuit model for a periodic array of slits sandwiched between two dielectric slabs," *Appl. Phys. Lett.*, vol. 96, pp. 161104, April 2010. Cited in page 42.

[65] R. Rodríguez-Berral, F. Medina, F. Mesa, and M. García-Vigueras, "Quasi-analytical modelling of transmission/reflection in strip/slit gratings loaded with dielectric slabs," *IEEE Trans. Microw. Theory Techn.*, vol. 60, pp. 405-418, March. 2012. Cited in pages 42, 53, and 80.

[66] R. Rodríguez-Berral, C. Molero, F. Medina, and F. Mesa, "Analytical wideband model for strip/slit gratings loaded with dielectric slabs," *IEEE Trans. Microw. Theory Techn.*, vol. 60, no. 12, pp. 3908-3918, Dec. 2012. Cited in page 164.

[67] L. Brilloin, "Wave guides for slow waves," *J. Appl. Phys.*, vol. 19, pp. 1023, 1948. Cited in page 77.

[68] W. Rotman, "A study of single-surface corrugated guides," *Proc. IRE*, vol. 39, pp. 952-959, Aug. 1951. Cited in page 77.

[69] L. O. Goldstone, and A. A. Oliner, "A note on surface waves along corrugated structures," *IRE Trans. Antennas Propag.*, vol. 7, no. 3, pp. 274-276, 1959. Cited in page 77.

[70] G. Piefke, "The transmission characteristic of a corrugated guide," *IRE Trans. Antennas Propag.*, vol. 7, no. 5, pp. 183-190, 1959. Cited in page 77.

[71] H. E. M. Barlow, and A. E. Karbowiak, "An experimental investigation of the properties of corrugated cylindrical surface waveguides," *Proc. IEE Part III: Radio Commun. Eng.*, vol. 101, pp. 182-188, 1953. Cited in page 77.

[72] R. S. Elliot, "On the theory of corrugated plane surfaces," *IRE Trans. Antennas Propag.*, vol. 2, pp. 71-81, Jan. 1954. Cited in page 77.

[73] V. H. Rumsey, "Horn antennas with uniform power patterns around their axes," *IEEE Trans. Antennas Propag.*, vol. 14, pp. 656-658, Jan. 1966. Cited in page 77.

[74] H. C. Minnet, and B. MacA. Thomas, "A method of synthesizing radiation patterns with axial symmetry," *IEEE Trans. Antennas Propag.*, vol. 14, pp. 654-656, Jan. 1966. Cited in page 77.

[75] C. A. Mentzer, and L. Peters. Jr, "Properties of cutoff corrugated surfaces for corrugates horn design," *IEEE Trans. Antennas Propag.*, vol. 22, no 2, pp. 191-196, March 1974. Cited in page 77.

[76] P. S. Kildal, "Definitions of artificially soft and hard surfaces for electromagnetic waves," *Electron Lett.*, vol. 24, no 3, pp. 168-170, Feb. 1988. Cited in page 78.

[77] P. S. Kildal, "Artificially soft and hard surfaces in electromagnetic," *IEEE Trans. Antennas Propag.*, vol. 38, no 3, pp. 1537-1544, Oct. 1990. Cited in page 78.

[78] G. Manara, G. Perosi, A. Monorchio, and A. R. Coccioli, "Plane-wave scattering from with cylinders with transverse corrugations," *Electron. Lett.*, vol. 31, no 6, pp. 437-438, March 1995. Cited in page 78.

[79] A. A. Kishk, and P. S. Kildal, "Electromagnetic scattering from circular cylinder with an anisotropic surface impedance due to an obliquely incident

plane wave," *Microw. Optical Tech. Lett.*, vol. 10, pp. 162-165, 1995. Cited in page 78.

[80] A. A. kishk, P. S. Kildal, A. Monorchio, and G. Manara, "Asymptotic boundary conditions for strip-loaded and corrugated surfaces," *Microw. Optical Tech. Lett.*, vol. 14, no 2, pp. 99-101, Feb. 1997. Cited in page 78.

[81] W. V. T. Rusch, J. Appel-Hansen, C. A. Klein, and R. Mittra, "Forward scattering from square cylinders in the resonance region with application to aperture blockage," *IEEE Trans. Antennas Propag.*, vol. 24, no 2, pp. 182-189, March 1976. Cited in page 78.

[82] T. López-Rios, D. Mendoza, F. J. García-Vidal, J. Sánchez-Dehesa and B. Pannetier, "Surface shape resonances in lamellar metallic gratings," *Phys. Rev. Lett.*, vol. 81, no 3, pp. 665-668, July 1998. Cited in page 78.

[83] E. Rajo-Iglesias, M. Caiazzo, L. Inclán-Sánchez, and P. S. Kildal, "Comparisons of bandgaps of mushroom-type EGB surface and corrugated and strip-type soft surfaces ," *IET Trans. Microw. Antennas Propag.*, vol. 1, pp. 184-189, 2007. Cited in page 79.

[84] E. Rajo-Iglesias, O. Quevedo, and L. Inclán-Sánchez, "Planar soft surfaces and their application to mutual coupling reduction," *IEEE Trans. Antennas Propag.*, vol. 57, no 12, pp. 3852-3859, Dec. 2009. Cited in pages 79 and 97.

[85] G. Goussetis, A. P. Feresidis, and J. C. Vardaxoglou, "Tailoring the AMC and EGB characteristics of periodic metallic arrays printed on grounded dielectric substrates," *IEEE Trans. Antennas Propag.*, vol. 54, no 1, pp. 82-89, Jan. 2006. Cited in page 79.

[86] E. Alfonso, A. Valero-Nogueira, J. I. Herranz, and F. Vico, "Moment Method analysis of corrugated surfaces using the aperture integral equation," *IEEE Trans. Antennas Propag.*, vol. 57, no 7, pp. 2208-2212, July 2009. Cited in page 80.

[87] I. Hanninen, and K. Nikoskinen, "Implementation of method of moments for numerical analysis of corrugated surfaces with impedance boundary conditions," *IEEE Trans. Antennas Propag.*, vol. 56, no 1, pp. 278-281, Jan. 2008. Cited in page 80.

[88] T. M. Uusitapa, "Usability studies on approximate corrugation models in scattering analysis," *IEEE Trans. Antennas Propag.*, vol. 54, no 9, pp. 2486-2496, Sep. 2006. Cited in page 80.

[89] N. N. M. Kehn, "Moment method analysis of plane-wave scattering from planar corrugated surfaces using parallel-plate cavity Green's function and derivation of analytic reflection-phase formulas for both polarizations and oblique azimut planes," *Radio Sci.*, vol. 47, pp. RS3008, Jun. 2012. Cited in pages 80, 89, and 91.

[90] N. N. M. Kehn, "Rapid surface-wave dispersion and plane-wave reflection analyses of planar corrugated surfaces by asymtotic corrugations boundary conditions even for oblique azimut planes," *IEEE Trans. Antennas. Propag.*, vol. 61, no. 5, pp. 2695-2707, May. 2013. Cited in pages 80 and 91.

[91] D. W. Woo, S. J. Muhn, and W. S. Park, "Simple analytical model of propagation through thick periodic slots," *IEEE Trans. Antennas. Propag.*, vol. 60, no. 11, pp. 5329-5335, Nov. 2012. Cited in pages 80, 89, and 92.

[92] D. C. Skigin, V. V. Veremey, and R. Mittra, "Superdirective radiation from finite gratings of rectangular grooves," *IEEE Trans. Antennas Propag.*, vol. 47, no. 2, pp. 376-383, Feb. 1999. Cited in pages 109 and 110.

[93] S. A. Schelkunoff, "A mathematical theory of linear arrays," *Bell System Tech. J.*, vol. 22, no. 22, pp. 80-107, 1943. Not cited.

[94] A. I. Uzkov, "An approach to the problem of optimum directive antenna design," *C. R. Dokl. Acad. Sci. USSR*, vol. 53, no. 1, pp. 35-38, 1946. Cited in page 109.

[95] E. Shamonina, and L. Solymar, "Maximum directivity of arbitrary dipole arrays," *IET Microw. Antennas Propag.*, vol. 9, no. 2, pp. 101-107, 2015. Cited in page 109.

[96] A. Bloch, R. G. Medhurst, S. D. Pool, and W. E. Nock, "Superdirectivity," *Proc. Inst. Elect. Eng.*, vol. 48, pp. 1164, 1960. Cited in page 109.

[97] J. R. Andrewartha, J. R. Fox, and I. J. Wilson, "Resonance anomalies in lamellar gratings," *Opt. Acta*, vol. 26, pp. 69-89, 1977. Cited in page 109.

[98] S. Jovicevic, and S. Sesnic, "Diffraction of a parallel- and perpendicular-polarized wave from an echelette grating," *J. Opt. Soc. Amer.*, vol. 62, pp. 865-877, 1972. Cited in page 109.

[99] J. R. Andrewartha, G. H. Derric, and R. C. McPhedran, "A modal theory solution to diffraction from a gratings with semi-circular grooves," *Opt. Acta*, vol. 28, pp. 1177-1193, 1981. Cited in page 109.

[100] R. A. Depine, and D. C. Skigin, "Scattering from metallic surfaces having a finite number of rectangular grooves," *J. Opt. Soc. Amer.*, vol. 11, no. 11, pp. 2844-2850, 1994. Cited in page 109.

[101] D. C. Skigin, and R. A. Depine, "The multilayer modal method for electromagnetic scattering for surfaces with several arbitrarily shaped grooves," *J. Mod. Opt.*, vol. 44, pp. 1023-1036, 1997. Cited in page 109.

[102] V. V. Veremey, and R. Mittra, "Scattering from structures formed by resonant elements," *IEEE Trans. Antennas Propag.*, vol. 46, pp. 494-501, 1998. Cited in pages 109 and 110.

[103] S. I. Grosz, D. C. Skigin, and A. N. Fantino, "Resonant effects in compound diffraction gratings: Influence of the geometrical parameters of the surface," *Phys. Rev. E*, vol. 65, pp. 056619, May 2002. Cited in pages 110, 146, and 148.

[104] R. A. Depine, A. N. Fantino, S. I. Grosz, and D. C. Skigin, "Phase resonances in obliquely illuminated compound gratings," *BIB*, July 2005. Cited in pages 110 and 156.

[105] M. Beruete, M. Navarro-Cía, D. C. Skigin, and M. Sorolla, "Millimeter-wave phase resonances in compound reflection gratings with subwavelength grooves," *Opt. Express*, vol. 18, no. 23, pp. 23957-23964, Nov 2010. Cited in page 110.

[106] D. C. Skigin, and R. A. Depine, "Transmission resonances of metallic compound gratings with subwavelength slits," *Phys. Rev. Lett.*, vol. 95, pp. 217402, Nov 2005. Cited in page 111.

[107] D. C. Skigin, and R. A. Depine, "Narrow gaps for transmission through metallic structured gratings with subwavelength slits," *Phys. Rev. E.*, vol. 74, pp. 046606, 2006. Cited in page 111.

[108] S. Chen, S. Jin, and R. Gordon, "Super transmission from a finite subwavelength arrangement of slits in a metal film," *Opt. Express*, vol. 22, no. 11, pp. 209015, May 2014. Cited in page 111.

[109] A. P. Hibbins, I. R. Hooper, M. J. Lockyear, and J. R. Sambles, "Microwave transmission of a compound metal gratings ," *Phys. Rev. Lett.*, vol. 96, pp. 257402, 2006. Cited in pages 111, 148, and 150.

[110] M. Navarro-Cía, D. C. Skigin, M. Beruete, and M. Sorolla, "Experimental demostration of phase resonances in metallic compound gratings with subwavelength slits in the millimeter wave regime," *App. Phys. Lett.*, vol. 94, pp. 091107, March 2009. Cited in page 111.

[111] Y. G. Ma, X. S. Rao, G. F. Zang, and C. K. Ong, "Microwave transmission modes in compound metallic gratings," *Phys. Rev. B*, vol. 76, pp. 085413, 2007. Cited in page 111.

[112] R. Gordon, "Near-field interference in a subwavelength double slit in a perfect conductor," *J. Opt. A*, vol. 8, pp. L1-L3, 2006. Cited in page 111.

[113] P. Lalanne, J. P. Hugonin, and J. C. Rodier, "Theory of surface plasmon generation at nanoslit apertures," *Phys. Rev. Lett.*, vol. 95, pp. 263902, 2005. Cited in page 111.

[114] D. Xiang, L.-L. Wang, X.-F. Li, L. Wang, X. Zhai, Z.-H. Liu, and W.-W. Zhao, "Transmission resonances of compound metallic gratings with two subwavelength slits in each period," *Opt. Express*, vol. 19, no. 3, pp. 2187-2192, 2011. Cited in page 111.

[115] I. M. Mandel, A. B. Golovin, and D. T. Crouse, "Analytical description of the dispersion relation for phase resonances in compound transmission gratings," *Phys. Rev. A.*, vol. 87, pp. 053833, 2013. Cited in page 111.

[116] L. Verslegers, Z. Yu, Z. Ruan, P. B. Catrysse and S. Fan, "From electromagnetically induced transparency to superscattering with a single structure: a coupled-mode theory for doubly resonant structures," *Phys. Rev. Lett.*, vol. 108, pp. 083902, 2012. Cited in page 111.

[117] F. Medina, D. C. Skigin, and F. Mesa, "Extraordinary transmission through slits from a microwave engineering perspective," *Proc. 38th European Microw. Conf.*, vol. 108, pp. 702-705, Oct. 2008. Cited in page 111.

[118] C. Molero, R. Rodríguez-Berral, F. Mesa and F. Medina, "Wideband equivalent circuit for 1-D periodic compound gratings," *9th European Conf. Antennas Propag.*, April 2015, Lisbon. Not cited.

[119] A. W. Sanders, "Optical properties of metallic nanostructures," *Dissertation*, Yale University, 2007. Cited in pages 124 and 140.

[120] W. H. Press, B. P. Flannery, S. A. Teukolsky, and W. T. Vetterling, *Numerical recipes in C: the art of scientific computing*, Cambridge University Press, 1988. Cited in page 125.

[121] W. E. Kock, "Metallic delay lenses," *Bell System Tech. Journal*, vol. 27, pp. 58-82, 1948. Cited in page 161.

[122] S. B. Cohn, "Analysis of the metal strip delay structure," *Journal of Appl. Phys.*, vol. 20, pp. 257-262, 1949. Cited in page 161.

[123] J. Brown, "The design of metallic delay dielectrics," *Proceedings IEE-Part III*, vol. 97, pp. 45-48, 1950. Cited in page 161.

[124] M. M. Z. El-Kharadly, and W. Jackson, "The properties of artificial dielectrics comprising arrays of conducting elements," *Proceedings IEE-Part 3*, vol. 100, pp. 199-212, 1953. Cited in page 161.

[125] J. Brown, and W. Jackson, "The properties of artificial dielectrics at centimetre wavelengths," *Proceedings IEEE-Part B*, vol. 102, pp. 11-16, Jan. 1955. Cited in page 161.

[126] D. Cavallo, W. H. Syed, and A. Neto, "Closed-form analysis of artificial dielectric layers – Part I: properties of a single layer under plane-wave incidence," *IEEE Trans. Antennas Propag.*, vol. 62, no. 12, pp. 6256-6264, Dec. 2014. Cited in page 161.

[127] D. Cavallo, W. H. Syed, and A. Neto, "Closed-form analysis of artificial dielectric layers – Part II: extension to multiple layers and arbitrary illumination ," *IEEE Trans. Antennas Propag.*, vol. 62, no. 12, pp. 6265-6273, Dec. 2014. Cited in page 161.

[128] A. Sabban, "A new broadband stacked two-layer microstrip antenna," *Antennas and Propag. Soc. Int. Symp.*, vol. 21, pp. 63-66, 1983. Cited in page 162.

[129] H. J. Stalzer Jr, Y. Lubin, A. Hessel, and J. Shmoys, "Microstrip stacked strip element phased array," *IEEE Trans. Antennas Propag.*, vol. 38, no. 5, pp. 770-773, May 1990. Cited in page 162.

[130] H. Aroudaki, V. Hansen, H.-P. Gemund, and E. Kreysa, "Analysis of low-pass filters consisting of multiple stacked FSS's of different periodicities with applications in the submillimeter radioastronomy," *IEEE Trans. Antennas Propag.*, vol. 43, no. 12, pp. 1486-1491, Dec 1995. Cited in page 162.

[131] C. C. Chen, "Transmission through a conducting screen perforated periodically with apertures," *IEEE Trans. Microw. Theory Techn.*, vol. 18, pp. 627-632, 1970. Cited in page 162.

[132] S. W. Lee, "Scattering by a dielectric-loaded screen," *IEEE Trans. Antennas Propag.*, vol. 19, pp. 656-665, 1971. Cited in page 162.

[133] C. C. Chen, "Transmission of microwave through perforated flat plates of finite thickness," *IEEE Trans. Microw. Theory Techn.*, vol. 21, pp. 1-6, 1973. Cited in page 162.

[134] S. W. Lee, G. Zarrillo, and C. L. Law "Simple formulas for transmission through periodic metal grids or plates," *IEEE Trans. Antennas Propag.*, vol. 30, no. 5, pp. 904-909, Sept. 1982. Cited in page 162.

[135] B. A. Munk, R. G. Kouyoumjian, and L. Peters Jr, "Reflection properties of periodic surfaces of loaded dipoles," *IEEE Trans. Antennas Propag.*, vol. 19, pp. 612-617, Sept. 1971. Cited in page 162.

[136] B. A. Munk, and R. J. Luebbers, "Reflection properties of two-layers dipole arrays," *IEEE Trans. Antennas Propag.*, vol. 22, no. 6, pp. 766-773, Nov. 1974. Cited in page 162.

[137] B. A. Munk, R. J. Luebbers, and R. D. Fulton, "Transmission through a two-layer array of loaded slots," *IEEE Trans. Antennas Propag.*, vol. 22, no. 6, pp. 804-809, Nov. 1974. Cited in page 162.

[138] T. Cwik, and R. Mittra, "The cascade connection of planar periodic surfaces and lossy dielectric layers to form and arbitrary periodic screen,"

IEEE Trans. Antennas Propag., vol. 35, no. 12, pp. 1397-1405, Dec. 1987. Cited in pages 162 and 163.

[139] J. D. Vacchione, and R. Mittra, "A generalized scattering matrix analysis for cascading FSS of different periodicities," *Antennas Propag. Soc. Int. Symp.*, vol. 1, pp. 92-95, May 1990. Cited in pages 162, 163, and 208.

[140] C. Wan, and J. A. Encinar, "Efficient computation of generalized scattering matrix for analyzing multilayer periodic structures," *IEEE Trans. Antennas Propag.*, vol. 43, no. 11, pp. 1233-1242, Nov. 1995. Cited in pages 162, 163, and 208.

[141] J. D. Vacchione, and R. Mittra, "Cascade analysis of power distribution in a multilayered dielectric/frequency selective surface system," *Antennas Propag. Soc. Int. Symp.*, vol. 2, pp. 1080-1083, June 1989. Cited in page 162.

[142] E. A. Hajlaoui, H. Travelsi, H. Zairi, A. Gharsallah, and H. Baudrand, "Analysis of multilayer substrates by a multilayer contribution of wave concept iterative process," *Microw. Optical Techn. Lett.*, vol. 49, no. 6, pp. 1439-1445, Jun. 2007. Cited in page 163.

[143] E. A. Hajlaoui, H. Travelsi, A. Gharsallah, and H. Baudrand, "Analysis of Novel Dual-Resonant and Dual-Polarized Frequency Selective Surface using Periodic contribution of Wave Concept Iterative Process: PPMS-WCIP ," *ICTAA*, pp. 1-6, April 2008. Cited in page 163.

[144] E. A. Hajlaoui, H. Travelsi, and H. Baudrand, "Periodic Planar Multilayered Substrates Analysis Using Wave Concept Iterative Process ," *Journal Electromagnetic Analysis Applications*, vol. 4, pp. 118-128, March 2012. Cited in page 163.

[145] A. Mary, S. G. Rodrigo, F. J. García-Vidal, and L. Martín-Moreno, "Theory of negative-refractive index response of double-fishnet structures," *Phys. Rev. Lett.*, vol. 101, pp. 103902, Sept. 2008. Cited in page 163.

[146] R. Ortuño, C. García-Meca, F. J. Rodríguez-Fortuño, J. Martí, and A. Martínez, "Role of surface plasmons polaritons on optical transmission through double layer metallic hole arrays," *Phys. Rev. B*, vol. 79, pp. 075425, 2009. Cited in page 163.

[147] J. Yang, C. Sauvan, H. T. Liu, and P. Lalanne, "Theory of fishnet negative-index optical metamaterials," *Phys. Rev. Lett.*, vol. 107, pp. 043903, July 2011. Cited in page 163.

[148] M. Beruete, I. Campillo, M. Navarro-Cía, F. Falcone, and M. Sorolla-Ayza, "Molding left- or right-handed metamaterials by stacked cutoff metallic hole arrays," *IEEE Trans. Antennas Propag.*, vol. 55, no. 6, pp. 043903, June 2007. Cited in page 163.

[149] M. Beruete, I. Campillo, M. Navarro-Cía, F. Falcone, and M. Sorolla-Ayza, "Accurate circuit modeling of fishnet structures for negative-index-medium applications," *IEEE Trans. Microw. Theory Techn.*, vol. 64, no. 1, pp. 15-26, Jan 2016. Cited in page 163.

[150] M. Beruete, M. Navarro-Cía, S. A. Kuznetzov, and M. Sorolla-Ayza, "Circuit approach to the minimal configurations on terahertz anomalous extraordinary transmission," *Appl. Phys. Lett.*, vol. 98, pp. 014106, 2011. Cited in pages 41, 61, and 163.

[151] M. Beruete, M. Navarro-Cía, and M. Sorolla-Ayza, "Understanding anomalous extraordinary transmission from equivalent circuit and grounded slab concept," *IEEE. Trans. Microw. Theory Techn.*, vol. 59, no. 9, pp. 2180-2188, Sept. 2011. Cited in pages 41 and 163.

[152] C. S. R. Kaipa, A. B. Yakovlev, F. Medina, F. Mesa, C. A. M. Butler and A. P. Hibbins, "Circuit modeling of the transmissivity of stacked two-dimensional metallic meshes," *Optics Express*, vol. 18, no. 13, pp. 13309-13320, 2010. Cited in page 163.

[153] Y. R. Padooru, A. B. Yakovlev, C. S. R. Kaipa, G. W. Hanson, F. Medina, and F. Mesa, "Dual capacitive-inductive nature of graphene metasurface: transmission characteristics at low-terahertz frequencies," *Antennas Propag. Soc. Int. Symp.*, pp. 1598-1599, July 2013. Cited in page 163.

[154] C. Molero, R. Rodríguez-Berral, F. Mesa, F. Medina, and A. B. Yakovlev, "Wideband analytical equivalent circuit for one-dimensional periodic stacked arrays," *Phys. Rev. E*, Jan 2016. Cited in page 163.

[155] A. P. Hibbins, J. R. Sambles, C. R. Lawrence, and J. R. Brown, "Squeezing millimeters waves into microns," *Phys. Rev. Lett.*, vol. 92, pp. 143904, April 2004. Cited in pages 163, 179, 216, and 219.

[156] Q. Zhang, T. Guo, B. A. Khan, T. Kodera and C. Caloz, "Coupling matrix Synthesis of nonreciprocal lossless two-port networks using gyrators and inverters," *IEEE Trans. Microw. Theory Techn.*, vol. 62, pp. 2782, Sept 2015. Cited in pages 211, 215, and 225.

List of publications

Internation journal papers

- R. Rodríguez-Berral, C. Molero, F. Medina and F. Mesa, "Analytical wideband model for strip/slit gratings with dielectrics slabs ", *IEEE Trans. Microw. Theory Techn.*, vol. 60, pp. 3908-3918, Dec. 2012.

- C. Molero, R. Rodríguez-Berral, F. Mesa and F. Medina, "Analytical circuit model for 1-D periodic T-shaped corrugated surfaces ", *IEEE Trans. Antennas Propag.*, vol. 62, pp. 794-803, Feb. 2014.

- C. Molero, R. Rodríguez-Berral, F. Mesa, F. Medina, A. B. Yakovlev, "Wideband analytical equivalent circuit for 1-D periodic stacked arrays ", *Phys. Rev. E*, vol. 1, pp. 013306, Jan. 2016.

- C. Molero, R. Rodríguez-Berral, F. Mesa and F. Medina, "Dynamical equivalent circuit for 1-D periodic compound gratings ", *IEEE Trans. Microw. Theory Techn.*, vol. 64, pp. 1195-1208, April 2016.

- C. Molero, R. Rodríguez-Berral, F. Mesa and F. Medina, "Making metal transparent: a circuit model approach ", *Opt. Express*, vol. 24, pp. 259951, May 2016.

- C. Molero, R. Rodríguez-Berral, F. Mesa and F. Medina, "Wideband analytical equivalent circuit for coupled asymmetrical non-aligned slit arrays ", submitted to *Phys. Rev. E*

International conference contributions

- C. Molero, R. Rodríguez-Berral, F. Mesa, and F. Medina "Analytical circuit model for stacked slit gratings ", International Microwave Simposium (IMS), Tampa Bay (Florida, USA), June 2014.

- C. Molero, R. Rodríguez-Berral, F. Mesa, and F. Medina "Wideband equivalent circuit for 1-D periodic compound gratings ", European Conference Antennas and Propagation (EUCAP), Lisbon (Portugal), April 2015.

- R. Rodríguez-Berral, F. Mesa, F. Medina and C. Molero,"Enhanced analytical models for periodic electromagentic structures ", X iberian meeting on computational electromagnetics (EIEC), Baeza (Jaén, Spain), May 2015.

- C. Molero, R. Rodríguez-Berral, F. Mesa, and F. Medina "Wideband equivalent circuit for non-aligned 1-D periodic metal strips coupled gratings ", European Microwave Conference (EuMC), Paris (France), September 2015.

- C. Molero, F. Medina, R. Rodríguez-Berral, and F. Mesa, "Making metal transparent: a circuit model approach ", metamaterials 2015, Oxford (United Kingdom), September 2015.

- C. Molero, F. Medina, R. Rodríguez-Berral, and F. Mesa, "Making gratings with slits and grooves for transmission control: an analytical approach ", metamaterials 2015, Oxford (United Kingdom), September 2015.

- F. Medina, F. Mesa, R. Rodríguez-Berral, and C. Molero, "Circuit modeling of periodic structures, ", The Exeter Microwave Metamaterials Meeting, Exeter (United Kingdom), December 2015.

- C. Molero, R. Rodríguez-Berral, F. Mesa, and F. Medina, "Study of the electromagnetic response of some periodic structures via equivalent circuits ", The Exeter Microwave Metamaterials Meeting, Exeter (United Kingdom), December 2015.

- F. Medina, C. Molero, R. Rodríguez-Berral, and F. Mesa, "Accurate circuit models for the analysis of stacked metal gratings ", International Conference on Mathematical Methods in Electromagnetic Theory (MMET), Lviv (Ukraine), July 2016.

- C. Molero, R. Rodríguez-Berral, F. Mesa, and F. Medina, "Analytical modelling of non-symmetric and non-uniform compound gratings ", European Microwave Conference (EuMC), London (United Kingdom), September 2016.

National conference contributions

- C. Molero, R. Rodríguez-Berral, F. Medina, and F. Mesa, "Analytical circuit model for coupled slit/strip gratings printed on dielectric slabs", XXVII Symposium Nacional de la Unión científica Internacional de Radio (URSI), Elche (Spain), September 2012.

- C. Molero, R. Rodríguez-Berral, F. Mesa, and F. Medina, "Analytical circuit model for 1-D periodic T-shaped corrugated surfaces", XXVIII Symposium Nacional de la Unión científica Internacional de Radio (URSI), Santiago de Compostela (Spain), September 2013.

- C. Molero, R. Rodríguez-Berral, F. Mesa, F. Medina, and A. B. Yakovlev, "High-frequency equivalent circuit for finite-stacked slit gratings", XXIX Symposium Nacional de la Unión científica Internacional de Radio (URSI), Valencia (Spain), September 2014.

- C. Molero, R. Rodríguez-Berral, F. Mesa, and F. Medina, "Wideband analytical circuit model for 1-D compound gratings", XXIX Symposium Nacional de la Unión científica Internacional de Radio (URSI), Valencia (Spain), September 2014.

- F. Mesa, R. Rodríguez-Berral, F. Medina, and C. Molero, "Consideraciones

sobre las limitaciones de los circuitos equivalentes para el análisis de scattering por estructuras periódicas", XXX Symposium Nacional de la Unión científica Internacional de Radio (URSI), Pamplona (Spain), September 2015.

- F. Medina, F. Mesa, R. Rodríguez-Berral, and C. Molero, "Circuitos equivalentes para estructuras periódicas y metamateriales", XXX Symposium Nacional de la Unión científica Internacional de Radio (URSI), Pamplona (Spain), September 2015.
- C. Molero, R. Rodríguez-Berral, F. Mesa and F. Medina, "Modelo circuital para rejillas de difracción acopladas no alineadas", XXXI Symposium Nacional de la Unión científica Internacional de Radio (URSI), Madrid (Spain), September 2016.
- C. Molero, R. Rodríguez-Berral, F. Mesa and F. Medina, "Modelo de circuito para rejillas de difracción compuestas con ranuras no uniformes ", XXXI Symposium Nacional de la Unión científica Internacional de Radio (URSI), Madrid (Spain), September 2016.

Awards

- **Young engineer prize** obtained at "European Microwave Conference (EuMC)" in Paris, France, for the paper and oral presentation "Wideband equivalent circuit for non-aligned 1-D periodic metal strips coupled gratings". 2015
- **Accessit** obtained at "Simposium nacional de la unión científica de radio (URSI)" in Valencia, Spain, for the paper and oral presentation "Wideband equivalent circuit for 1-D compound gratings". 2014
- **Accessit** obtained at "Simposium nacional de la unión científica de radio (URSI)" in Santiago de Compostela, Spain, for the paper and oral presentation "Analytical circuit model for 1-D periodic T-shaped corrugated surfaces". 2013

- **Accessit** obtained at "Simposium nacional de la unión científica de radio (URSI)" in Elche, Spain, for the paper and oral presentation "Analytical circuit model for coupled slit/strip gratings printed on dielectric slabs". 2012